FOSSIL ENERGY

DOE/BC/15172-1
(OSTI ID: 761985)

AN INVESTIGATION FOR DISPOSAL OF DRILL CUTTINGS INTO UNCONSOLIDATED SANDSTONES AND CLAYEY SANDS

Final Report
September 14, 1998—June 15, 2000

By
Ali Mese
Jack Dvorkin
John Shillinglaw

Date Published: September 2000

Work Performed Under Contract No. DE-FG26-98BC15172

Westport Technology Center International
Houston, Texas

National Petroleum Technology Office
U.S. DEPARTMENT OF ENERGY
Tulsa, Oklahoma

DOE/BC/15172-1
Distribution Category UC-122

An Investigation for Disposal of Drill Cuttings Into Unconsolidated Sandstones and Clayey Sands

By
Ali Mese
Jack Dvorkin
John Shillinglaw

September 2000

Work Performed Under Contract No DE-FG26-98BC15172

Prepared for
U.S. Department of Energy
Assistant Secretary for Fossil Energy

John K. Ford, Project Manager
National Petroleum Technology Office
P.O. Box 3628
Tulsa, OK 74101

Prepared by
Westport Technology Center International
6700 Portwest Drive
Houston TX 77024

Petrophysical Consulting Inc.
730 Glenmere Way
Redwood City, CA 94062

TABLE OF CONTENTS

TABLE OF CONTENTS (Cont'd)

LISTS OF GRAPHICAL MATERIALS

TABLES

LISTS OF GRAPHICAL MATERIALS (Cont'd)

TABLES (Cont'd)

LISTS OF GRAPHICAL MATERIALS (Cont'd)

TABLES (Cont'd)

LISTS OF GRAPHICAL MATERIALS (Cont'd)

TABLES (Cont'd)

LISTS OF GRAPHICAL MATERIALS (Cont'd)

FIGURES

LISTS OF GRAPHICAL MATERIALS (Cont'd)

FIGURES (Con't)

LISTS OF GRAPHICAL MATERIALS (Cont'd)

FIGURES (Con't)

LISTS OF GRAPHICAL MATERIALS (Cont'd)

FIGURES (Con't)

LISTS OF GRAPHICAL MATERIALS (Cont'd)

FIGURES (Con't)

LISTS OF GRAPHICAL MATERIALS (Cont'd)

FIGURES (Con't)

LISTS OF GRAPHICAL MATERIALS (Cont'd)

FIGURES (Con't)

ABSTRACT

Disposing of oily drill cuttings and fluids from oil and gas operations imposes major costs on producers, particularly those operating offshore. New environmental regulations are restrictive for discharging oil base drill cuttings and related waste both in onshore and offshore operations. Producers in the Gulf of Mexico, for example, commonly must barge wastes to onshore disposal sites for treatment. This expense can often make economically marginal oil and gas formations unprofitable, and for the United States, this leads to increasing reliance on oil imports.

Injection of these oily cuttings and associated wastes into unconsolidated and poorly consolidated sand formations offer an economical disposal mechanism. Injection of a significant volume slurry of oily drill cuttings and water into unconsolidated and clayey sand formations requires fracturing the formation by increasing the downhole pressure above the minimum principle stress.

Westport Technology Center International and professors from Stanford University, doing business as Petrophysical Consulting Inc., worked together to develop the algorithms for a computer model designed to predict the influence of changes in the stress state on elastic moduli and plastic properties of these formations. These models, when verified by field data, should provide a means to more accurately assess the conditions for environmentally safe injection of oily cuttings and associated wastes into unconsolidated and clayey sand formations.

The deliverables of the project include experimental data and a set of models for relating elastic moduli/porosity/texture and static-to-dynamic moduli to strength and failure relationships for unconsolidated sands and clayey sands. The results of the project should provide the industry with a basis for wider use of oil base drilling fluids in water sensitive formations by implementing drill cutting injection into existing wells at abandoned formations and controlling fracture geometry to prevent ground water contamination.

INTRODUCTION

Disposing of oily drill cuttings and fluids from oil and gas operations imposes major costs on producers, particularly those operating offshore. New environmental regulations are restrictive for discharging oil base drill cuttings and related waste both in onshore and offshore operations. Producers in the Gulf of Mexico, for example, commonly must barge wastes to onshore disposal sites for treatment. This expense can often make economically marginal oil and gas formations unprofitable, and for the United States, this leads to increasing reliance on oil imports.

Injection of these oily cuttings and associated wastes into unconsolidated and poorly consolidated sand formations offer an economical disposal mechanism. Injection of a significant volume slurry of oily drill cuttings and water into unconsolidated and clayey sand formations requires fracturing the formation by increasing the downhole pressure above the minimum principle stress.

It is well known that most materials indicate elastic behavior at low stresses. As stress is increased, the material will begin to yield at some point if it is ductile, while it will fracture at some point without appreciable yielding if the material is brittle. It is also noted that the behavior of a material varies significantly with saturation, deviatoric stress and rate of strain. It has been known for decades that the physical properties of rocks depend on the stress state at which they exist. Therefore, the mechanical properties of rocks should be studied under simulated downhole conditions. Simple tension or compression tests of rocks at atmospheric pressure cannot provide adequate data to define the mechanism of rock failure in various stability problems.

Although many consolidation studies on unconsolidated materials have been performed for more than 70 years, these tests have been limited largely to a low-pressure range. Most investigators used mainly well-indured sandstones or limestones in their laboratory experiments. Carpenter and Spencer (1940) measured the "pseudo-bulk" compressibility of various consolidated sandstones in an attempt to investigate effect of production on subsidence.

Fatt (1958) studied the relationship between compressibility and rock composition. He reported that unconsolidated sediments, which are poorly sorted and contain clay, have higher compressibility than do consolidated and well-sorted sands, also he found out that the C_b's of sandstones are a function of rock composition for a given grain shape

and sorting. The procedure used in the laboratory by Fatt (1958) was similar to that of Carpenter and Spencer (1940), but in the former case the fluid was expelled under constant hydrostatic pressure with a reduction in pore pressure rather than an increase in the external stress. This method is believed duplicate reservoir conditions.

Van der Knaap (1959) noted that pore compressibility (Cp) increases with decreasing porosity. It has been suggested that certain minimum and maximum pressures, the relationship between C_p and the logarithm of pressure, can be approximated by a straight line. This relationship has been found to exist between the log of the C_b and the log of the effective pressure, which in this case was equal to the applied axial load. Van der Vlis concluded that clay and sand layers compact almost to the same extend, the main difference being that the low permeability to fluid of the clay prevents instantaneous compaction and time effects become important.

The vertical in-situ stress in a formation reflects the weight of the overburden material resting on top. Part of the vertical stress is carried by the reservoir pore pressure. The remainder is supported by the matrix. During depletion, the reservoir pressure decreases. As the weight of the overburden does not change, the effective stress increases accordingly. This leads to compression of the formation and a reduction in volume. In general, the volume change corresponds to a diminished porosity. Besides porosity, parameters such as permeability, resistivity and acoustic properties are also effected. Reservoir compaction is predicted on the basis of core measurements. The experiments are carried out using vertical core samples. The stress in the axial direction is specified equal to the in situ vertical effective stress in the axial direction is specified equal to the in situ vertical effective stress during depletion. Similarly, the stress in the radial direction should simulate the in situ horizontal stress. Usually, the horizontal stress change is not known. Instead, the radial stress is controlled to maintain a limited radial deformation, or it is taken equal to the axial effective stress. Depletion leads to a modest decrease of permeability due to the reduction in throat size. The part of the reduction in permeability is associated with core damage, as coring has led the creation of microfractures. The concept of effective stress can be expressed as follows:

$$\sigma_{\mathbf{eff}} = \sigma - \mathbf{P} \qquad \mathbf{(1)}$$

where $\sigma_{\mathbf{eff}}$ is the effective normal stress,

σ is the total normal stress and

P denotes the fluid pressure.

The pore fluid can not sustain shear stress. Therefore the effective shear stress is the same as the total shear stress i.e.

$$\tau_{eff} = \tau \qquad (2)$$

Equation (1) is called Terzaghi's effective stress law and was originally designed for saturated soil materials. The relationship has been verified for a wide variety of porous materials by Skempton. The deformation of rock material is largely due to effective stress as defined above. However, the fluid pressure contributes to the deformation as well since the hydrostatic pressure compresses the grain material. One may choose to incorporate the pore pressure contribution in the definition of effective stress as follows

$$\sigma_{eff} = \sigma - \beta \mathbf{P} \qquad \mathbf{(3)}$$

where $\beta = \mathbf{1 - K/Ks}$ is Biot's constant and **K/Ks** is the ratio between the rock bulk stiffness and the solid material bulk stiffness. This ratio generally ranges between 0.0 and 0.3; also, 0< □ < 1.0. Equation (3) is exact where linear elastic rock deformation is concerned; Biot's constant may assume different values when considering non-linear, non-elastic deformation.

With the foregoing in mind, Westport Technology Center International ("Westport") and Petrophysical Consulting Inc. ("PCI") undertook the study to predict porosity, texture, and large-strain deformational properties of rock from well-log data. The approach was to investigate how the lithology, pore fluid, pore pressure and the concentration of drill cutting waste in the pore space and fractures affected:

- Small strain elastic properties (dynamic elastic moduli)
- Large strain elastic and plastic properties (static moduli)
- The failure envelope
- Storage (porosity), and
- Permeability.

The goal was then to develop physics based elasticity-plasticity-failure-storage-transport models for rocks subject to cuttings injection. The work consisted of four (4) major tasks:

1. Conduct stress deformation and acoustic property measurements in unconsolidated and poorly consolidated sands;
2. Review and evaluate the theoretical models for dynamic and static moduli develop a mathematical model for failure and velocity-strength relations of these sands;
3. Determine the strengths and accompanying velocity measurements of these sands; and
4. Apply the theoretical models and methods developed in the project to develop a mathematical model for failure and velocity-strength relations.

Tasks 1 and 3, which involved laboratory measurements, were performed by Westport. Tasks 2 and 4, which involved the development of mathematical models, were performed by PCI.

Investigation for Disposal of Drill Cuttings into Unconsolidated Sandstones and Clayey Sands

EXECUTIVE SUMMARY

The new environmental requirements are very strict for discharging oil base drill cuttings and related waste both in onshore and offshore operations. Injection of these oily cuttings and associated wastes into unconsolidated and poorly consolidated sand formations offer an economical disposal mechanism. There have been several successful injection operations conducted by major oil companies like ARCO, British Petroleum, Shell and Mobil both onshore and offshore fields of Alaska, Gulf of Mexico and North Sea. These operations proved that the injection of drill cuttings is technically feasible, and confirmed that unconsolidated zones provide cost effective areas for disposal. In addition, the procedure eliminates discharge for onshore as well as offshore disposal in a cost-effective manner.

In order to inject significant volume of slurry that is a mixture of drill cuttings and water into the unconsolidated sand formation, it is necessary to fracture the formation by increasing the downhole pressure above the minimum principal stress. A number of fracture mechanisms are possible during the injection of the slurry. The dominating mechanism depends on the leak characteristics of the disposal formation, the direction of minimum principal stress in the formation, and the injection sequence of the cuttings.

Periodic fracturing injections are expected to change the in situ closure stress of the formation, resulting in some associated casing problems. Not all of the injection attempts tried in the field have been successful. Operations failed in several cases where shallow drilling problems were encountered near the shallow casing shoe cluster. Issues that need to be addressed in planning for drill cutting injection operations are:

1) the amount of waste generated during drilling;
2) which well(s) and formation(s) should the waste injected into; and
3) how much waste could be injected into each well without adversely affecting the environment and field management strategy.

There are also several principal operational considerations that need to be considered during the injection:

1) possible migration of the slurry into neighboring producers;
2) pressure interference of induced fractures with drilling activity;
3) the likelihood of breach of the surface or fresh water aquifers;
4) casing and wellhead ratings for injection at the required pumping pressures; and
5) stress distribution around the wellbore.

A recent study has shown that the state of stress has significant influence on the elastic and plastic behavior of unconsolidated sand formations. Experimental results indicate that loosely consolidated and clayey sands experience plastic deformation almost with the initiation of loading. In other words, if the sample is unloaded from a given state of stress during loading, it does not return to its original configuration and experiences inelastic or plastic deformation. This plastic behavior of the unconsolidated sand causes significant amount of fracturing fluid leak off into these high permeability formations, resulting in more difficult and expensive fracturing operations in such formations.

One of the major successes of this study is to observe and understand the storage and transport properties in unconsolidated sands and to predict the role of change in the in situ stress conditions on the stability and failure behavior of clayey sand formations. The study, the stress-deformation profiles, ultrasonic wave velocities, permeability and pore volume changes of the consolidated and loosely consolidated and clayey sandstones with respect to increasing and decreasing pore pressure were simultaneously monitored. From the experimental study it was concluded that unconsolidated sands respond as a strain hardening material at high strain rates.

The role of cementation material and the amount of cement on elastic moduli has been reported by others. Using this published data, a relevant cementation model in high porosity sands was developed to explain the stress dependence of the elastic moduli as a part of the current study.

The experimental investigation conducted during this study indicates strong plasticity in these loose sands. A new model was then developed to take into consideration this plastic behavior in unconsolidated sands to predict the influence of changes in the stress state on the plastic and elastic moduli in these formations.

The work accomplished during this study should be followed by pilot field tests of drill cutting injection. The theoretical models can be used to estimate the storage and transport properties of the reservoir subject to injection. Selected samples from the well will be taken to conduct static and dynamic moduli tests and obtain field information (wire log). Based on these results, we should be able to provide the needed input for designing the cutting injection process. Special attention should be paid to the properties of depleted and clayey sands, as these will be the primary targets for drill cuttings injection.

EXPERIMENTAL

1.0 EXPERIMENTAL STUDIES

The objectives of the experimental part of the program were to obtain static and dynamic P and S wave velocity as a function of effective stress on twenty 1½' diameter core samples from the North Sea, twelve 1½' diameter core samples from Clearfolk, seventeen 1½ diameter core samples from GOM, six 1½' diameter Berea core samples, and twelve 1½ ' diameter Barnett shale samples.

The variation of elastic static, acoustic moduli and electrical properties were determined at the first phase of the experimental study. The second phase of the experimental study was involved to measure porosity and permeability change as a function of hydrostatic stress at zero pore pressure. Bulk compressibility, elastic moduli, elastic and residual deformations, acoustic compressional and shear velocity, change in porosity and permeability have been calculated and presented in tabular and graphical form.

1.1 TEST PROCEDURES

The testing procedures used were designed to obtain the maximum amount of information from each test.

1.1.1 Effective Stress Cycling Test Procedure

The Effective Stress Cycling Test involved simultaneous measurement of compressional and shear wave acoustic travel time, volumetric strain was made at each stress level and this data was used to compute the static and acoustic bulk moduli, stress state, P and S wave velocities, static and dynamic values of moduli.

1.1.2 Isostatic Compression Test Procedure

Samples are subjected to an isostatic stress $\sigma_1 = \sigma_2 = \sigma_3$ and simultaneous measurement of volumetric strain, expelled pore fluid, and upstream and down stream pressure changes were made at each stress level and this data was used to compute the static bulk compressibility, change of porosity and permeability as tabulated in Appendix.

1.1.3 Biaxial or Confined Compression Test Procedure

The biaxial compression test is the most frequent rock mechanical test, which gives, among others, values for elastic moduli. In reality, rock rarely behaves in purely linear elastic fashion. For increasing axial stress the slope of σ_{axial} versus ε_{axial} first increases then reaches a more or less constant value and subsequently starts to decrease. The increase at low stress is usually attributed to closure of coring induced microcracks or increasing contact area between grains; the reduction at high stress indicates the onset of permanent, plastic deformation. The slope of the stress-strain curves is used to calculate moduli leads to the following definition:

$$E = \frac{\partial \sigma_{axial}}{\partial \varepsilon_{axial}} \quad \text{AND} \quad \nu = \frac{\partial \varepsilon_{radial}}{\partial \varepsilon_{axial}} \qquad (4)$$

Experiments indicate that the first loading elastic parameters differ from the unloading elastic parameters. Both sets of parameters are useful depending on the specific applications. For example, first loading is most representative of reservoir compaction, while unloading best characterizes formation stiffness during hydraulic fracturing.

1.2 EXPERIMENTAL SET-UP

The equipment used in this study consists of four components: the pressure manifold, the deformation system, the acoustic assembly, and the signal processing hardware and software.

1.2.1 The Pressure Manifold

The equipment used for these tests includes two interactive systems. One system applies axial load and includes a load frame, a load cell, and a displacement transducer. The overburden load is provided by means of a high-stiffness, rock mechanics load frame which is consist of an actuator with a heavy, one piece, U shaped upper frame bolted directly to the base plate. This arrangement provides a maximum compressive capacity of 0.5 million pounds.

The actuator is single ended, double acting, and has large bearing surfaces to enable the piston rod to withstand large side loads. An upper platen is mounted to the lower surface of the transverse portion of the U shaped frame, and a lower platen is attached to the top end of the actuator piston rod. A linear variable differential transformer displacement transducer is mounted coaxially inside the lower part of the actuator.

The end caps made of polished steel are coated with resin, used to eliminate friction between the end caps and the specimen. The second system consists of a pressure vessel, a digital pressure gauge with 1 psi

resolution, and a motor driven hydraulic pump. Mineral oil is used as confining fluid to produce a homogeneous horizontal stress.

1.2.2 The Deformation System

Both the axial and radial deformations are recorded using 350-ohm foil CEA type cantilever strain gages connected into a four arm Wheatstone bridge circuit, in order to provide temperature compensation.

1.2.3 The Acoustic Assembly

Two dual mode (compressional and shear) transducers with center frequencies of about 0.8 MHz are used in a pulse transmission type arrangement. The transducers are enclosed in cells in order to isolate them from high pressure applied to the pressure vessel during testing. The transducer placed at the bottom acts as a transmitter and the top transducer acts as a receiver. Travel time of compressional and shear waves are determined under pressure by measuring the face to face delay times of the transmitter-receiver set. Their delays are then subtracted from the measured arrival times for the samples in order to obtain the transit time within the sample.

1.2.4 The Signal Processing Hardware and Software

This consists of two Panametric ultrasonic analyzers, a computer controller, a programmable digitizer, an oscilloscope, and a computer. The ultrasonic analyzers are connected to electronic gates in order to transfer only the required part of the signals for processing.

1.3 SAMPLE TESTING AND DATA REDUCTION

This report contains the completion of static and ultrasonic data on total 49 core samples. The sample inventory is displayed in Tables 1.1 through 1.4, following. These tables also indicate which measurements were completed in this study. Static moduli were determined from the effective stress-volumetric strain curves.

$$\mathrm{K} = \frac{\partial \sigma_{eff}}{\partial \varepsilon_{volum}}\bigg|_{\sigma_{hyd}} \; ; \; E = \frac{\partial \sigma_{axial}}{\partial \varepsilon_{axial}} \quad \text{and} \quad \nu = \frac{\partial \varepsilon_{radial}}{\partial \varepsilon_{axial}} \qquad (5)$$

The dynamic Young's modulus and Poisson's ratio values are calculated using the length of sample corrected for axial deformation and the wave arrival time data. Well-known equations for elastic materials are used for the calculation of these dynamic properties.

$$E = \frac{V_s^2 \rho \left[3(V_p/V_s)^2 - 4\right]}{(V_p/V_s)^2 - 1} \quad \text{and} \quad \nu = 0.5\frac{(V_p/V_s)^2 - 2}{(V_p/V_s)^2 - 1} \quad (6)$$

Where ρ is the density of sample, and V_s and V_p are S and P wave velocities respectively.

Table 1.1: Berea Sandstone Sample Inventory.

Permeability mD	Mechanical (Dry and Saturated)			ϕand Grain Density	Acoustic (Dry and Saturated)			Resistivity
75	x	x	x	x	x	x	x	x
100	x	x	x	x	x	x	x	x
200	x	x	x	x	x	x	x	x
300	x	x	x	x	x	x	x	x
400	x	x	x	x	x	x	x	x
750	x	x	x	x	x	x	x	x

Table 1.2: Clearfolk Sample Inventory.

Sample #	Depth ft	Static (Dry and Saturated) Confining Pressure (psi)				Permeability and Porosity	Acoustic (Dry and Saturated) Confining Pressure (psi)			
		4000	4500	5000	5500		4000	4500	5000	5500
1	6349.00	x	x	x	x	x	x	x	x	x
3	6854.00	x	x	x	x	x	x	x	x	x
5	6354.00	x	x	x	x	x	x	x	x	x
18	6416.00	x	x	x	x	x	x	x	x	x
19	7082.50	x	x	x	x	x	x	x	x	x
20	7155.20	x	x	x	x	x	x	x	x	x
22	6422.00	x	x	x	x	x	x	x	x	x
24	6946.50	x	x	x	x	x	x	x	x	x
27	7136.00	x	x	x	x	x	x	x	x	x
30	7177.50	x	x	x	x	x	x	x	x	x
34	7188.00	x	x	x	x	x	x	x	x	x
36	7222.00	x	x	x	x	x	x	x	x	x

Table 1.3: GOM Sample Inventory.

Sample #	Depth ft	Static (Dry) Confining Pressure (psi)			Permeability and Porosity	Acoustic (Dry) Confining Pressure (psi)		
		0	500	2000		0	500	2000
A1	10117.90	x			x	x		
A2	10118.90		x		x		x	
A3	10119.30			x	x			x
B1	10123.40	x			x	x		
B2	10121.11		x		x		x	
B3	10122.60			x	x			x
C1	10137.60	x			x	x		
C2	10136.00		x		x		x	
C3	10136.80			x	x			x
D1	10156.90	x			x	x		
D2	10157.70		x		x		x	
D3	10157.70			x	x			x
E1	10165.50	x			x	x		
E2	10166.00		x		x		x	
E3	10165.90			x	x			x
F1	10199.50	x			x	x		
F2	10197.70		x		x		x	

Table 1.4: North Sea Sample Inventory.

Sample #	Depth ft	Mechanical Properties Under Hydrostatic Stress Condition (Dry)	Acoustic Properties Under Hydrostatic Stress Condition (Dry)	XRD	k, ϕ and Grain Density	Resistivity
12	13259.68	x	x	x	x	x
14	13261.15	x	x	x	x	x
18	13264.44	x	x	x	x	x
26	13271.16	x	x	x	x	x
37	13284.28	x	x	x	x	x
60	13435.04	x	x	x	x	x
76	13448.16	x	x	x	x	x
92	13461.29	x	x	x	x	x
104	13471.13	x	x	x	x	x
116	13480.97	x	x	x	x	x
120	13484.25	x	x	x	x	x
127	13589.24	x	x	x	x	x
143	13602.36	x	x	x	x	x
147	13605.64	x	x	x	x	x
155	13612.20	x	x	x	x	x
187	13638.45	x	x	x	x	x
215	13661.42	x	x	x	x	x
xxx	13314.47	x	x	x	x	x
158	13595.05	x	x	x	x	x
162	13590.72	x	x	x	x	x

"x" represents completed measurements

2.0 THEORETICAL STUDIES

2.1 Theoretical Model Development

In this part of the study, we developed explicit theoretical models that link the porosity, mineralogy, sorting, and texture of sands to their elastic properties. The main goal of this development is to be able to predict, from non-destructive acoustic measurements, the storage and transport properties of sands. The models also link the elastic properties of sands to the amount of fine particles placed between the framework grains. As such, the models developed here can serve as diagnostic tools for identifying the amount of drill cuttings in the framework sand. A special attention is paid to the so-called "binary" mixtures of grains. The new theory of the elasticity of binary mixtures can be directly applied to sands with drill cuttings.

First, we will describe the "critical porosity" and "critical concentration" concepts and show how they can be used to build effective medium models for sands. Next, we will introduce the "rock physics diagnostic" concept and show how it cam be used to derive the textural rock properties, and, eventually, strength and permeability, from well log measurements. Finally, we will introduce the new binary mixture theory and show how it can be used to model the elastic moduli of mixtures of sands and smaller particles. The binary mixture theory is applicable to the system that includes sand grains and injected drill cuttings and as such can be used to deduce the porosity and texture of the sand/cuttings system from remote acoustic measurements.

2.2. Critical Porosity Concept

Porosity is one of the parameters required for reservoir characterization and management. It can be derived, in principle, from seismic and sonic data by using relations between the elastic-wave velocity (impedance) and porosity. Critical porosity is the porosity above which the rock can exist only as a suspension. In sandstones the critical porosity is 36% - 40%, that is the porosity of a random close pack of well-sorted rounded quartz grains. This pack is often the starting point for the formation of consolidated sandstones. We show how by using this staring point for effective medium

modeling, rational models can be built that relate velocity to porosity depending on rock texture and lithology.

In order to derive porosity from such seismic observables as impedance and velocity, a velocity-porosity relation has to be used. Such relations vary depending on lithology and rock texture. To appreciate the effect of texture on velocity, consider Figure 1.2.1 where P- and S-wave velocity is plotted versus the total porosity for relatively clay-free gas-saturated sands at the differential pressure (confining minus pore pressure) of about 20 MPa.

All sandstone data points in Figure 2.2.1 represent rock that is mainly quartz with clay content not exceeding 10%. Yet, in the same porosity range, the P-wave velocity may span from 1.5 to over 3 km/s, and the S-wave velocity from 1 to over 2 km/s. One apparent reason for this large velocity difference between mineralogically similar samples is rock texture -- the arrangement of the sand grains and pore-filling material in the pore space. In the Strandenes (1991) sandstone samples, the grains appear to be slightly cemented at their contacts while the Blangy (1992) samples are friable sands.

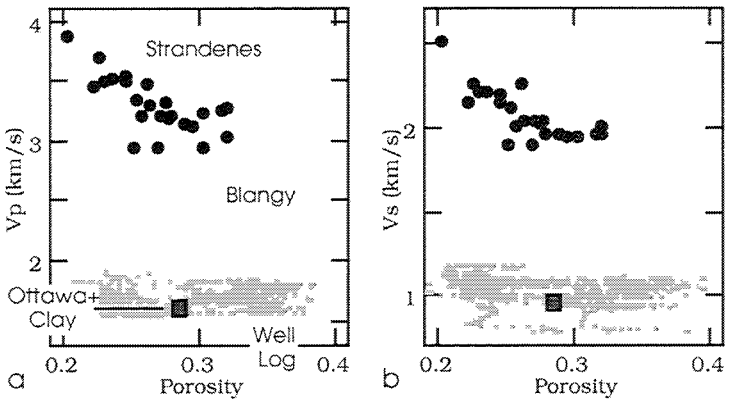

Figure 2.2.1. P- and S-wave velocity in rocks with gas at 20 MPa differential pressure. Circles represent laboratory data obtained on high-porosity "fast" (Strandenes, 1991) and "slow" (Blangy, 1992) sands, both data sets are from the North Sea. Gray symbols are from a Gulf Coast gas well. The filled square is for a hand-made mixture of Ottawa sand and 10% kaolinite (Yin's, 1993). Clay content for these data does not exceed 10%.

The velocity in the well log data (Dvorkin et al., 1999) is even smaller than that in the friable sands. These rocks are elastically equivalent to a hand-made mixture of

Ottawa sand and kaolinite where the small kaolinite particles fill the pore space without noticeably affecting the velocity.

In order to create rational effective medium models that can explain and predict the observed velocity-porosity behavior, let us examine the textural nature of sandstones. Consider Figure 2.2.2a where the compressional modulus (bulk density times the compressional-wave velocity squared) of water-saturated clean sandstones and quartz marine sediment (suspensions) is plotted versus porosity. The porosity of 36 - 40% is the point where the modulus-porosity trend abruptly changes. The reason is that this porosity is the porosity of well-sorted quartz sand. In the lower porosity domain, the stiffness of the sandstone is determined by the framework of contacting quartz grains. , In the higher-porosity domain the grains are not in contact anymore and are suspended in water. In this case, the stiffness of the sediment is determined by the pore fluid. We call this threshold porosity "critical porosity" (Nur et al., 1998).

The rocks where the solid phase is spatially continuous and dominates the stiffness of the rock have porosity that is smaller than the critical porosity. This fact is illustrated in Figure 2.2.2b where the compressional and shear moduli of many sandstone samples (room-dry at 30 - 40 MPa differential pressure) are plotted versus porosity. The data used are discussed in Nur et al. (1998).

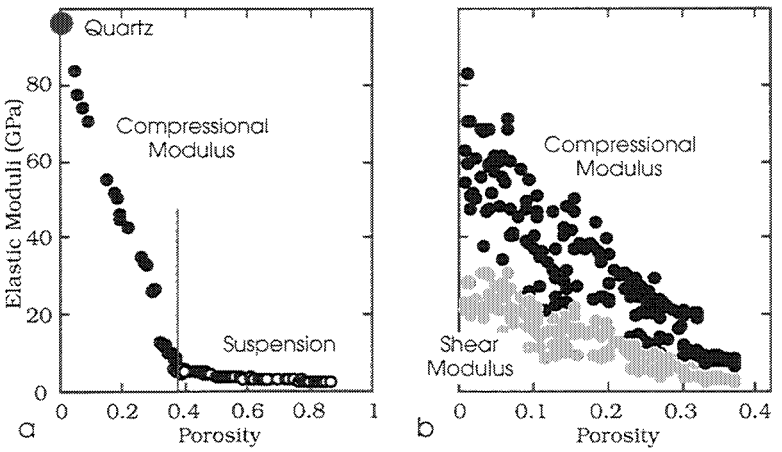

Figure 2.2.2. a. Compressional modulus versus porosity in clean sandstones and marine sediment versus porosity. b. Compressional and shear modulus of sandstones versus porosity.

The critical porosity concept is valid not only for sandstones but also for other natural and artificial rocks. An example is given in Figure 2.2.3 where the compressional modulus is plotted versus porosity for cracked igneous rocks and pumice (Nur et al., 1998). In the first case, the critical porosity is as small as 6% while in the second case it reaches 70%. The reason is the peculiar microstructural topology of the rocks under examination. The igneous rocks are permeated by cracks that percolate and make the solid phase loose its spatial continuity at very small porosity. In the pumice, the honeycomb structure of the solid ensures its spatial continuity at high porosity values.

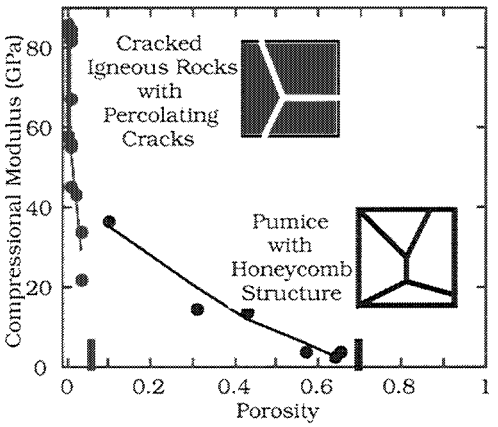

Figure 2.2.3. Compressional modulus versus porosity in cracked igneous rocks and pumice. The data used are discussed in Nur et al. (1998).

Nur et al. (1998) summarize the critical porosity values for various rocks as follows:

Material	Critical Porosity
Sandstones	40%
Limestones	40%
Dolomites	40%
Pumice	80%
Chalks	65%
Rock Salt	40%
Cracked Igneous Rocks	5%
Oceanic Basalts	20%
Sintered Glass Beads	40%
Glass Foam	90%

2.2.3 Critical Concentration Concept.

The critical porosity concept leads to the "critical concentration" concept of Marion (1990) and Yin (1993) used to describe the properties of sands with shale. Consider the experimental data from Yin (1993) obtained on samples hand-made by mixing Ottawa

sand and kaolinite. The volumetric clay content in the samples varied from 0 to 100%. The total porosity at 20 MPa differential pressure is plotted versus the volumetric clay content in Figure 1.2.4a. The two end members of the data set are the porosity of Ottawa sand at zero clay content and porosity of kaolinite at 100% clay content. The porosity of the mixture reaches its minimum at the point where the volumetric concentration of clay equals the porosity of Ottawa sand which is closer to the critical porosity for sandstones. This clay content is called "critical clay concentration."

The critical concentration is important not only for the total porosity but also for the elastic moduli of the mixture (Figure 2.2.4b). The stiffness of the mixture is maximum at the critical concentration and decreases as the clay content increases or decreases from the critical concentration value. Poisson's ratio behaves in a similar way (Figure 2.2.4c). Elastic properties of the Ottawa sand and kaolinite mixture are plotted versus the total porosity in Figure 2.2.5. The non-uniqueness of the elastic moduli, and, especially, Poisson's ratio in the cross-plots is due to the grain-scale texture of the rock.

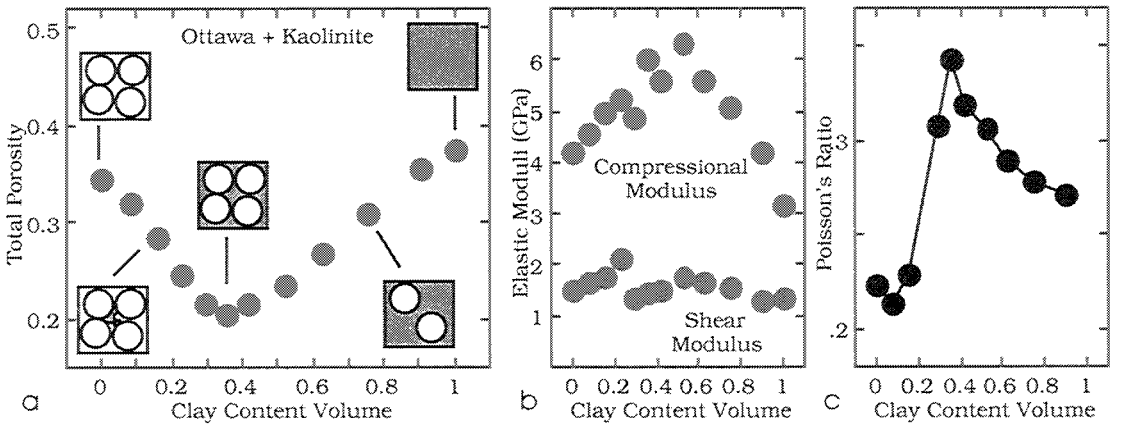

Figure 2.2.4. Porosity (a), elastic moduli (b), and Poisson's ratio (c) versus volumetric clay content in room-dry Ottawa sand mixed with kaolinite at 20 MPa differential pressure (after Yin, 1993).

This effect has to be considered when examining well-log data. In Figure 2.2.6a and 2.2.6b, we plot the bulk density and P-wave impedance versus the gamma-ray values for a well in Colombia (Gutierrez, 1998). The trends have the low-gamma-ray and the high-gamma-ray branches. They produce non-uniqueness as the impedance is plotted versus the bulk density and porosity (Figure 2.2.6c and 2.2.6d).

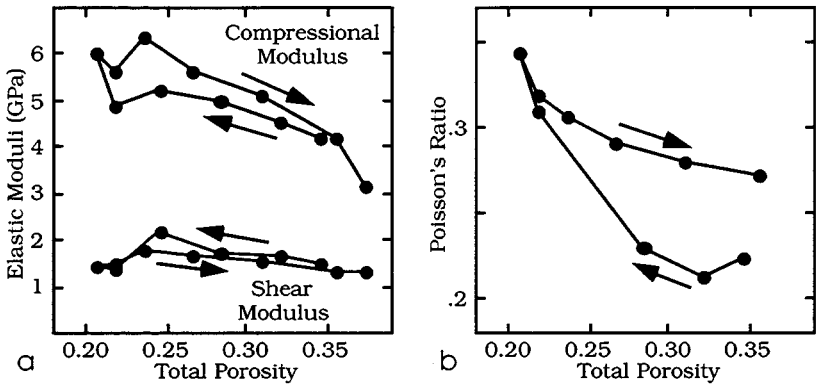

Figure 2.2.5. Elastic moduli (a) and Poisson's ratio (b) versus total porosity in room-dry Ottawa sand mixed with kaolinite at 20 MPa differential pressure (after Yin, 1993). The arrows show increasing clay content.

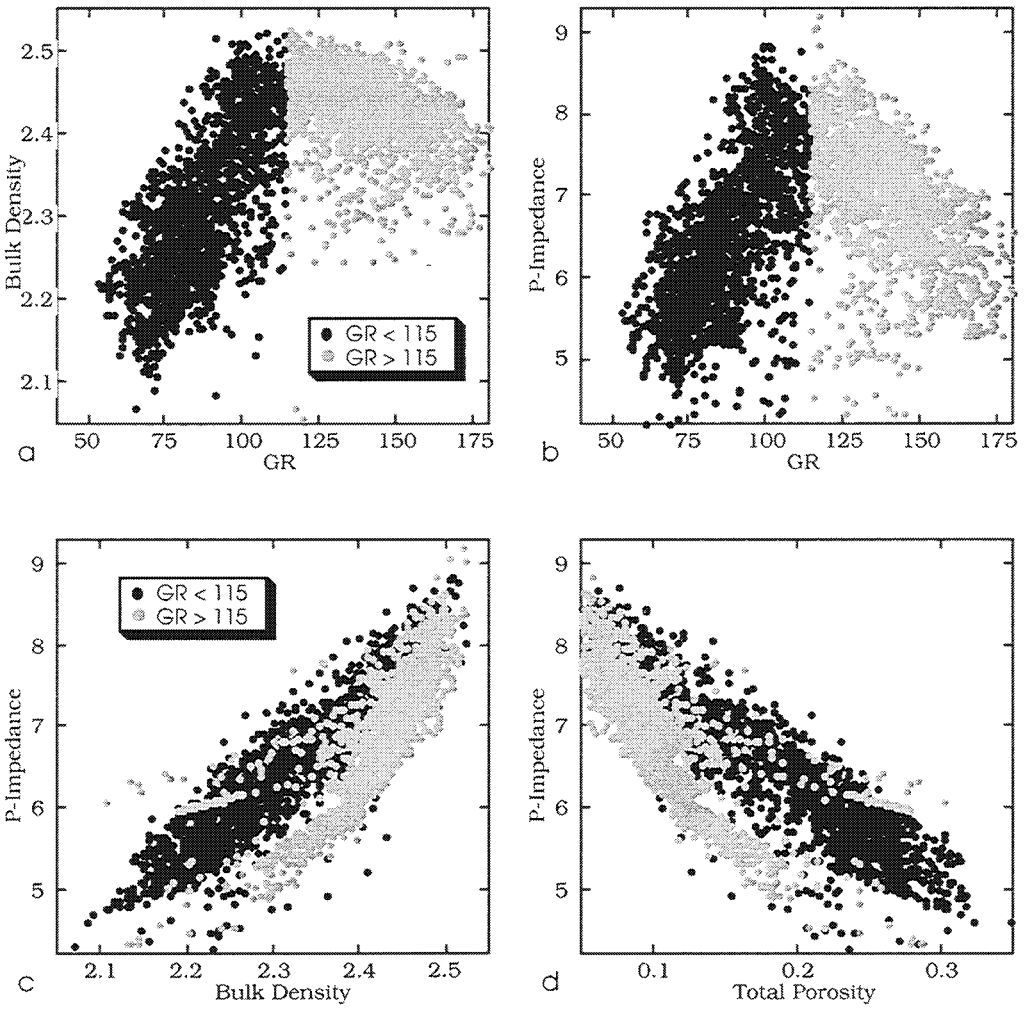

Figure 2.2.6. Well log data. Bulk density and P-impedance versus gamma-ray (a and b); P-impedance versus bulk density and total porosity (c and d).

2.2.4. Models For High-Porosity Sandstones.

The initial building point for effective medium models that describe high-porosity sandstones should be unconsolidated well-sorted sand, as proposed by the critical porosity concept. In mathematical modeling, such sand is approximated by a dense pack of identical elastic spheres (Figure 2.2.7).

The contact-cement model (Dvorkin and Nur, 1996) assumes that porosity reduces from the initial critical porosity value due to uniform deposition of cement layers on the surface of the grains. This cement may be diagenetic quartz, calcite, or reactive clay (e.g., illite). The diagenetic cement dramatically increases the stiffness of the sand by reinforcing the grain contacts (Figure 2.2.8). The mathematical model, shown in Exhibit A, is based on a rigorous contact-problem solution by Dvorkin et al. (1994).

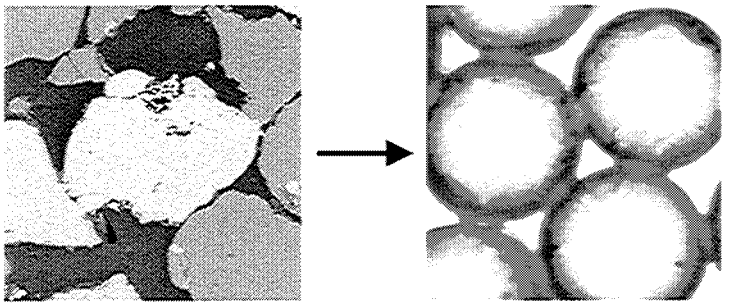

Figure 2.2.7. Approximating sand by a sphere pack (microphotographs of well-sorted sand, left, and a glass-bead pack, right).

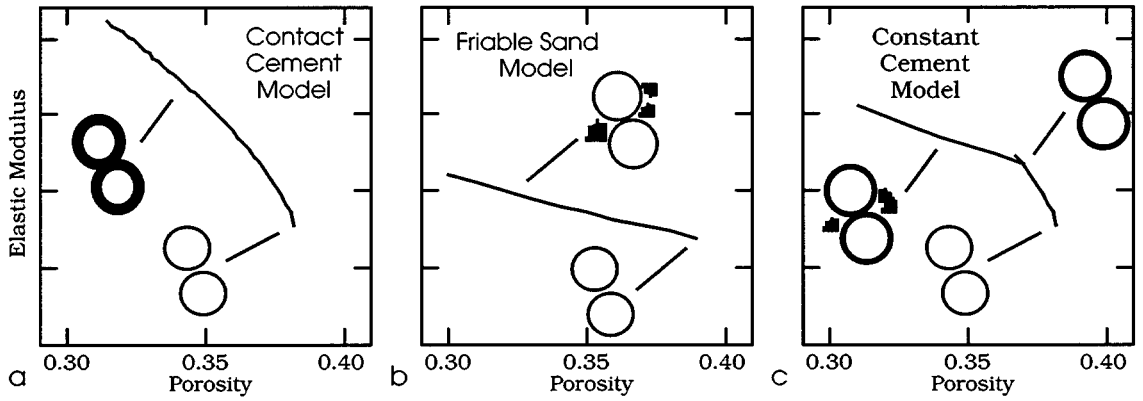

Figure 2.2.8. Schematic depiction of three effective-medium models for high-porosity sandstones and corresponding diagenetic transformations.

The contact cement theory allows one to accurately model the velocity in fast high-porosity sands (Figure 2.2.9). One may find that the contact-cement model is appropriate for describing sands in high-energy depositional environment where the grains are well-sorted and not covered by organic matter.

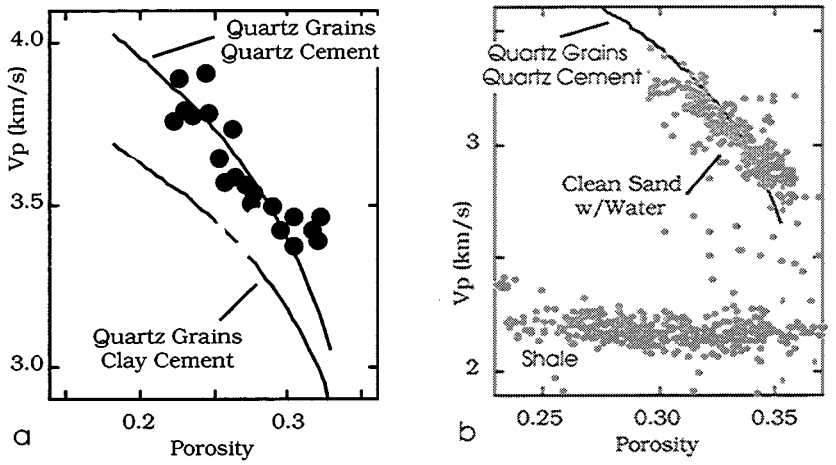

Figure 2.2.9. P-wave velocity versus porosity. a. Water-saturated-rock data based on laboratory measurements of fast high-porosity North Sea sandstones by Strandenes (1991). Solid circles are for very clean samples. Open circles are for samples with some clay. The curves are from the contact cement model for pure quartz grains with quartz and clay cement. b. Well-log data. The clean sand interval is saturated with water. The curve is from the contact cement theory for pure quartz grains with quartz cement.

The friable sand model (Dvorkin and Nur, 1996) assumes that porosity reduces from the initial critical porosity value due to the deposition of the solid matter away from the grain contacts. Such a diagenetic process of porosity reduction may correspond to deteriorating grain sorting. This non-contact additional solid matter weakly affects the stiffness of the rock (Figure 2.2.8b).

The theoretical effective-medium model connects two end-points in the elastic-modulus-porosity plane. One end point is at critical porosity. The elastic moduli of the dry rock at that point are assumed to be the same as of an elastic sphere pack subject to confining pressure. The other end-point is at zero porosity and has the bulk and shear moduli of the pure solid phase. These two points in the porosity-moduli plane are connected with the curves that have the algebraic expressions of the lower Hashin-Shtrikman (1963) bound (bulk and shear moduli) for the mixture of two components:

the pure solid phase and the phase that is the sphere pack. The reasoning is that in unconsolidated sediment, the softest component (the sphere pack) envelopes the stiffest component (the solid) in the Hashin-Shtrikman fashion (Figure 2.2.10). The equations are given in Appendix A.

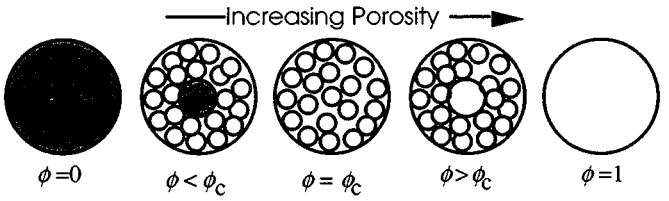

Figure 2.2.10. Hashin-Shtrikman arrangements of sphere pack, solid, and void.

The friable sand model allows one to accurately predict velocity in soft high-porosity sands (Figure 2.2.11). This model is appropriate for describing sands where contact cement deposition was inhibited by organic matter deposited on the grain surface.

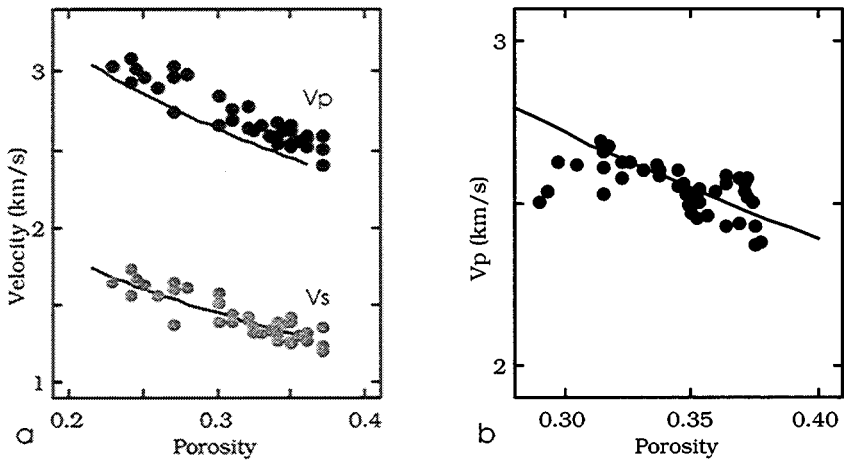

Figure 2.2.11. Velocity versus porosity. a. Water-saturated-rock data based on laboratory measurements of soft high-porosity North Sea sandstones by Blangy (1992). b. Well-log data (Avseth et al., 1998) for oil-saturated pay zone. The curves are from the friable sand model.

The constant-cement model (Avseth et al., 1998) assumes that the initial porosity reduction from critical porosity is due to the contact cement deposition. At some high porosity, this diagenetic process stops and after that porosity reduces due to the deposition of the solid phase away from the grain contacts as in the friable sand model (Figure 2.2.8c). This model is mathematically analogous to the friable sand model

except that the high-porosity end point bulk and shear moduli are calculated at some "cemented" porosity from the contact-cement model. An example of applying this model to well-log data is given in Figure 2.2.12. See equations in Appendix A.

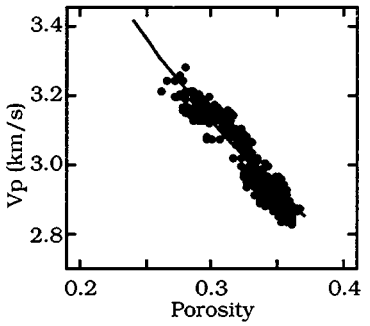

Figure 2.2.12. Velocity versus porosity. Well-log data (Avseth et al., 1998) for oil-saturated pay zone. The curve is from the constant cement model.

The marine sediment model (Dvorkin et al., 1999) is analogous to the friable sand model but covers the porosity range above critical porosity. One end point is the critical porosity where the elastic moduli of the sphere pack depend on effective pressure. To arrive at higher porosity, we add empty voids to the sphere pack (Figure 2.2.9). In this case the voids are placed inside the pack in the Hashin-Shtrikman fashion. Now the pack is the stiffest component, so we have to use the upper Hashin-Shtrikman limit. The saturated-rock elastic moduli can be calculated using Gassmann's (1951) equation.

An example of applying this model to log data is given in Figure 2.2.13 (Dvorkin et al, 1999). A good agreement between the model and the data is apparent. At the same time, the often used suspension model fails to correctly mimic the data. This model's departure from the data increases with depth which is due to the effect of confining pressure that adds stiffness to the dry frame of the sediment thus making the suspension model inadequate. See equations in Appendix A.

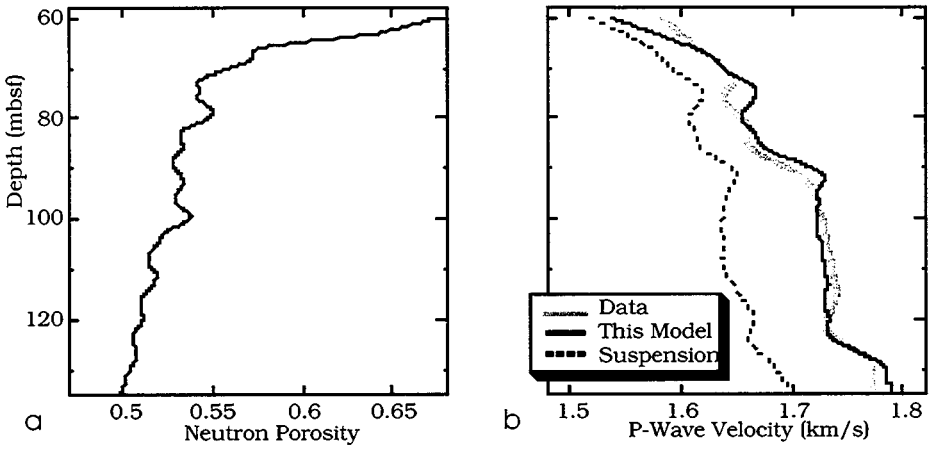

Figure 2.2.13. DSDP Well 974. a. Porosity versus depth. b. Velocity versus depth.

The critical porosity and critical concentration concepts allow the geophysicist to better understand the diversity of well log and core elastic data. Effective-medium models built on the basis of the critical porosity concept can accurately model data. By superimposing theoretical model curves on velocity-porosity and elastic-moduli-porosity crossplots, one may mathematically diagnose rock, i.e., determine the texture of the sediment (e.g., contact-cemented versus friable). Examples of rock diagnostic are given in Figure 2.2,14. Such diagnostic has implications for fluid detection (Avseth et al., 1998), and strength and permeability (Dvorkin and Brevik, 1999).

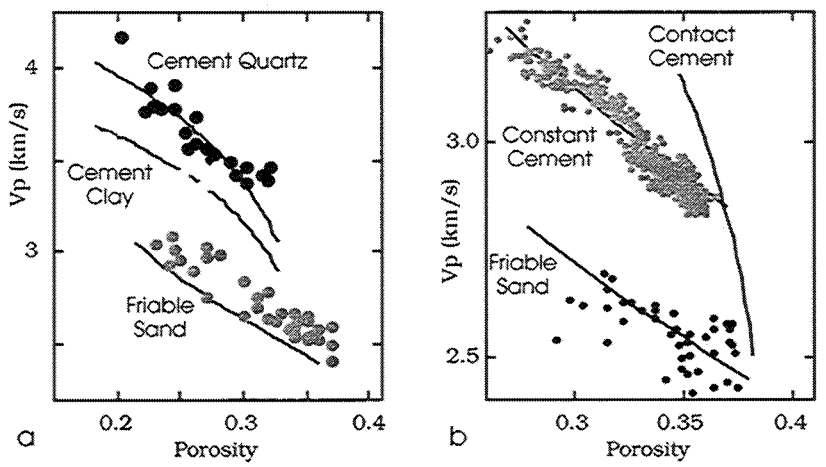

Figure 2.2.14. Velocity versus porosity. Theoretical curves superimposed on data allow one to identify the rock type. a. Data from Figures 2.2.9a and 2.2.11a.
b. Data from Figures 2.2.11b and 2.2.12.

2.3. ROCK PHYSICS DIAGNOSTIC TECHNIQUE

Rock physics laws that relate porosity, mineralogy (shale content), saturation, and pore-fluid properties to the elastic rock properties -- elastic-wave velocity and impedance -- give the connection between seismic impedance and velocity inversion and physical reservoir properties. They can also be used to produce synthetic seismic images from flow simulation results.

Often, an earth volume under examination has to be described by more that one rock physics law: different depth intervals may have distinctively different velocity-porosity trends due to variations in depositional and diagenetic history. When building a rock physics model, one has to single out various velocity-porosity trends from the entire volume of data and assign these separate trends to appropriate depth intervals and depositional sequences. This procedure is called **rock physics diagnostic**. Rock physics diagnostic is typically conducted on well log and core data.

Rock physics diagnostic allows not only to produce useful relations between seismic observables and porosity. It allows one to describe the texture of rock: the position of diagenetic cement; grain size sorting; effect of clay, etc. This texture description in turn can be linked to the depositional and stratigraphic features of the subsurface. For example, well-sorted grains with small amount of intergranular cement may correspond to a high-energy stream whereas deteriorating sorting is likely to be found in a low-energy depositional environment downstream. Sorting and cementation in turn determine permeability and strength.

2.3.1 Rock Physics Diagnostic

Rock physics laws can be obtained from: (a) core measurements where velocity, mineralogy, density, and porosity are measured simultaneously on a suite of rock samples representative of the earth volume subject to modeling; and (b) well log data that include velocity, mineralogy (gamma-ray), saturation, density, and porosity curves. The work space for rock physics diagnostic is the **rock physics plane** that may be (a)

velocity-porosity; (b) impedance-porosity; and/or (c) modulus-porosity plane.

The P- (Ip) and S-impedance (Is) are defined, respectively, as

$$I_p = V_p \rho_b, \quad I_s = V_s \rho_b,$$

where V_p and V_s are the P- and S-wave velocity, respectively; and ρ_b is the bulk density.

The compressional (M) and shear (μ) moduli are defined, respectively, as

$$M = V_p^2 \rho_b, \quad \mu = V_s^2 \rho_b.$$

Below, we show how log data measured in a continuous depth interval (Figure 2.3.1) can be separated into three distinctively different trends (Figure 2.3.2). It also follows from Figure 2.3.2 that the rock physics trends appear to be "sharper" in the impedance-porosity or modulus-porosity plane than they are in the velocity-porosity plane. This is why we recommend using impedance or elastic modulus instead of velocity.

During rock diagnostic, it is important to eliminate from consideration as many factors affecting velocity as possible. One of such factors, that can be easily eliminated, is saturation. Velocity may strongly depend on saturation and/or pore fluid compressibility that, in turn, may vary with depth. Because of varying saturation or fluid properties, the same rock type may appear to have no velocity-porosity trend at all (Figure 2.3.3). In fact, identical samples of rock (especially soft rock) will have very different velocity, impedance, and moduli, if saturated with different fluids. To eliminate this additional complication, one has to bring the entire interval to common pore fluid saturation. This common saturation process consists of three steps:

Step 1: Use well log data to calculate the elastic moduli of the dry rock.

Step 2: Use the dry-rock elastic moduli thus obtained to calculate those of rock saturated with the same fluid for the entire interval or data set.

Step 3: Use the common-fluid rock moduli to calculate velocity and impedance as needed.

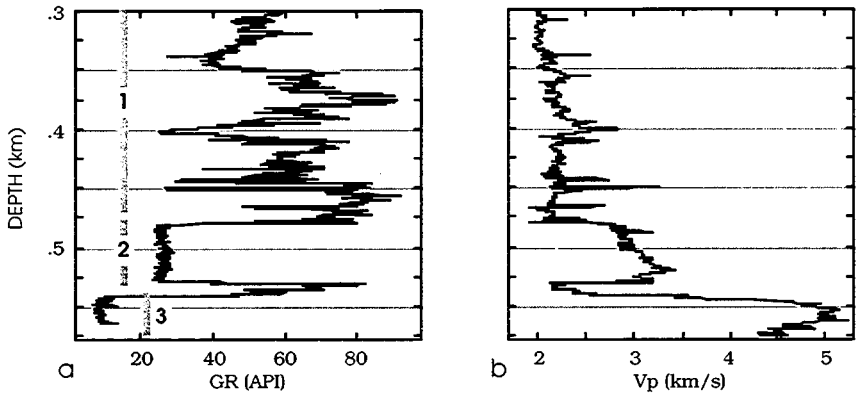

Figure 2.3.1. Well log data versus depth (fictitious). a. Gamma-ray; b. velocity.

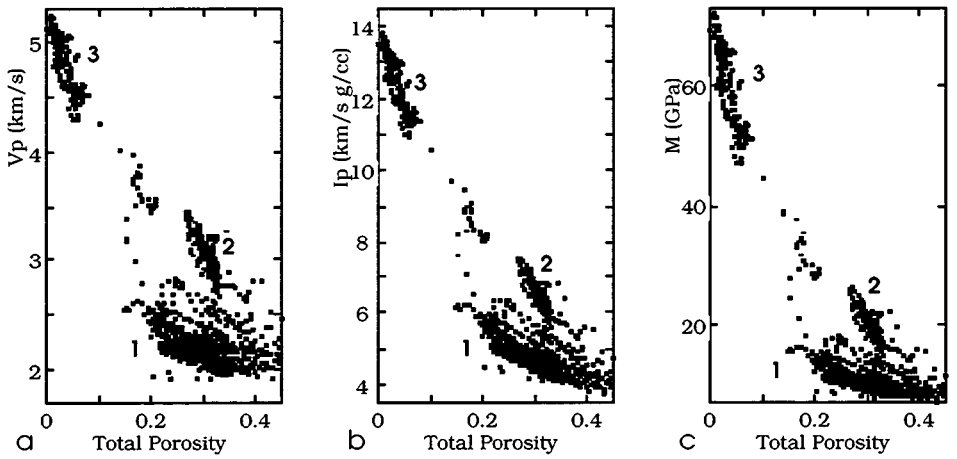

Figure 2.3.2. Cross-plotting well-log data in the rock physics plane. a. Velocity versus porosity; b. impedance versus porosity; c. modulus versus porosity. The trends marked correspond to the depth intervals shown in Figure 2.3.1a.

The details of fluid substitution needed for these tasks are given below.

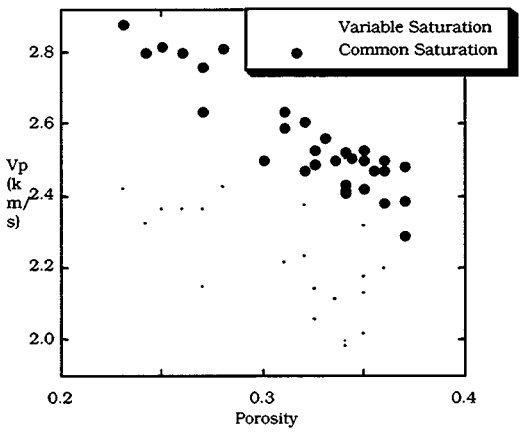

Figure 2.3.3. Velocity versus porosity for a soft rock dataset, with variable and common saturation.

2.3.2. Three Types of Rock Physics Diagnostic

We define rock physics diagnostic as the procedure of establishing elastic moduli versus porosity relations for the volume of earth under examination. The principal data source for rock physics diagnostic are well logs and/or core measurements. Once the moduli-porosity relations are established, it is easy to transform them into impedance-porosity and velocity-porosity relations. The three types of rock physics diagnostic are:

Type 1: Finding a theoretical modulus-porosity relation that describes the dataset.

Type 2: Finding a data set that is elastically analogous to the dataset under investigation.

Type 3: Finding an empirical fit from the data.

It is understood in the second case that the analog has been well studied and some of its properties (e.g., a relation between Vp and Vs) can be used for the data set under investigation. The three types of rock physics diagnostic can be used separately or simultaneously since they complement each other.

Diagnostic Type 1: Theoretical Modulus-Porosity Relations. This procedure consists of the following steps:

STEP 1: Bring the entire interval under examination, or the suite of core data, to common pore fluid saturation. Calculate the elastic moduli at this common saturation. This step includes the following sub-steps:

Substep 1.1: Calculate the effective bulk moduli of pore fluid components in the interval. Based on these, calculate the effective bulk modulus $\overline{K}_{fluid}$ of the pore fluid mixture as

$$\frac{1}{\overline{K}_{fluid}} = \frac{S_{gas}}{K_{gas}} + \frac{S_{oil}}{K_{oil}} + \frac{S_{br}}{K_{br}},$$

where $S_{gas,oil,br}$ and $K_{gas,oil,br}$ are the saturations and bulk moduli of the gas, oil, and brine, respectively.

Substep 1.2: Calculate the rock bulk modulus K_{log} from the well log (or core) data as

$$K_{log} = \rho_b (V_p^{\,2} - 4V_s^{\,2} / 3).$$

If the shear-velocity data are not available, calculate the compressional modulus M_{log} as

$$M_{log} = \rho_b V_p^{\,2}.$$

Tips to Substep 1.2: (1) Even if the shear-wave data are available, calculate the compressional modulus anyway since the shear-wave data may be of low quality.

Substep 1.3: Calculate the dry-rock bulk modulus from the rock bulk modulus as

$$K_{dry} = K_{mineral} \frac{1 - (1-\phi) K_{log} / K_{mineral} - \phi K_{log} / \overline{K}_{fluid}}{1 + \phi - \phi K_{mineral} / \overline{K}_{fluid} - K_{log} / K_{mineral}},$$

where ϕ is the total porosity, and $K_{mineral}$ is the bulk modulus of the mineral phase (for calculating $K_{mineral}$.

If the shear-velocity data are not available, calculate the dry-rock compressional modulus M_{dry} as

$$M_{dry} = M_{mineral} \frac{1 - (1-\phi) M_{log} / M_{mineral} - \phi M_{log} / \overline{K}_{fluid}}{1 + \phi - \phi M_{mineral} / \overline{K}_{fluid} - M_{log} / K_{mineral}},$$

where $M_{mineral} = K_{mineral} + 4\mu_{mineral} / 3$, and $\mu_{mineral}$ is the shear modulus of the mineral phase (for calculating $\mu_{mineral}$.

Tips to Substep 1.3: (1) Even if the shear-wave data are available, calculate the dry-rock compressional modulus anyway since the shear-wave data may be of low quality. (2) If the elastic moduli of the dry rock have unreasonable (e.g., negative) values for some data points, this may be due to small errors in input parameters (porosity, mineral's elastic moduli, etc.). These errors will be corrected in Substep 1.4 below.

Substep 1.4: Calculate the bulk modulus K_{common} of the rock saturated with common

(uniform for the entire interval or data set) pore fluid:

$$K_{common} = K_{mineral}\frac{\phi K_{dry} - (1+\phi)K_{cf}K_{dry}/K_{mineral} + K_{cf}}{(1-\phi)K_{cf} + \phi K_{mineral} - K_{cf}K_{dry}/K_{mineral}},$$

where K_{cf} is the bulk modulus of the common fluid. As common fluid use the stiffest pore-fluid component (formation water or mud filtrate). We emphasize that K_{cf} has to be the same for the entire interval or data set.

Next, calculate the compressional modulus M_{common} of the rock saturated with common (uniform for the entire interval or data set) pore fluid:

$$M_{common} = K_{common} + \rho_b 4V_s^2/3.$$

If the shear-velocity data are not available, calculate the compressional modulus M_{common} of the rock saturated with common pore fluid as

$$M_{common} = M_{mineral}\frac{\phi M_{dry} - (1+\phi)K_{cf}M_{dry}/M_{mineral} + K_{cf}}{(1-\phi)K_{cf} + \phi M_{mineral} - K_{cf}M_{dry}/M_{mineral}}.$$

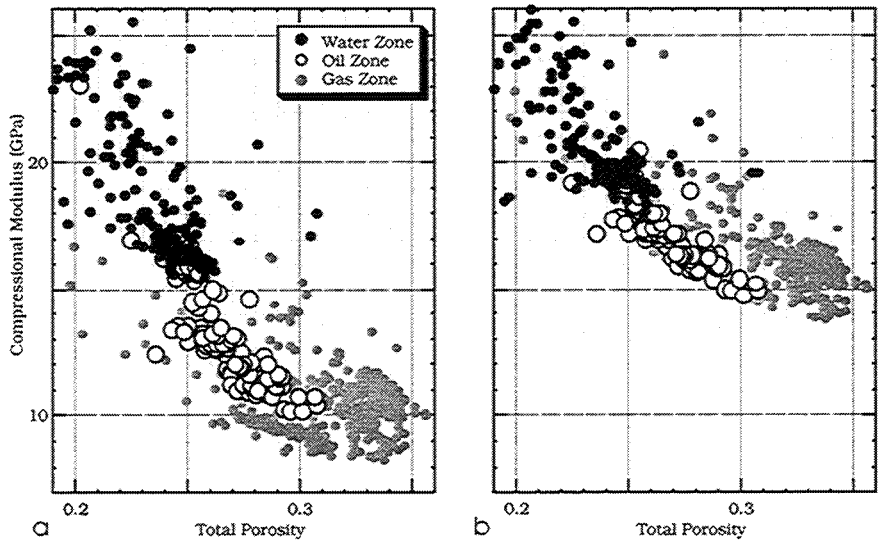

Figure 2.3.4. Example of bringing an interval to a common saturation. a. Compressional modulus directly from log data plotted versus porosity. Trends seem to be different for water, oil, and gas zones. b. Data at common saturation (formation water). Most of the data exhibit a single trend.

Tips to Substep 1.4: (1) Even if the shear-wave data are available, use the last equation

to calculate the compressional modulus of the rock saturated with common pore fluid anyway since the shear-wave data may be of low quality. Compare it to the modulus obtained from the previous equation for quality control.

STEP 2: Cross-plot the compressional modulus at common saturation versus porosity and fit appropriate theoretical modulus-porosity models.

Substep 2.1: Plot the compressional modulus versus porosity for the entire interval or data set or for selected parts of it. Use plotting package where you can easily superimpose theoretical model curves or other datasets. Some candidates are Excel, KaleidaGraph, Matlab. An example in Figure 2.3.5 shows how the well-log data from an interval where a very clean (low gamma ray) interval is present, separates into two parts when the compressional modulus is plotted versus total porosity. The upper branch of the data is form the low-GR interval whereas the lower branch is from the rest of the interval where shale is present.

Substep 2.2: Select the appropriate rock physics theory (theories) and superimpose on the modulus-porosity cross-plot. When using a theoretical relation, make sure that the pore fluid is the same as the common pore fluid used in Step 1. It is not easy to select the appropriate theory. Below, we give equations for existing theoretical and empirical modulus-porosity equations and recommend applying them depending on porosity range and rock type. The more models the user superimposes on the modulus-porosity cross-plot the better is the chance of finding the appropriate theory.

Example: Consider the log data in Figure 2.3.5. The rock is high-porosity sandstone. Appropriate theories to try are: (a) cementation theory; and (b) unconsolidated rock theory. Both provide the dry-rock elastic moduli. We use Gassmann's equation to theoretically saturate these dry rocks with the common pore fluid. The results are shown in Figure 2.3.6a. We can see that the unconsolidated rock theory describes the part of the interval where shale is present, and the cementation

theory approximately describes the clean (low-GR) interval.

Substep 2.3: Adjust the theory selected. Practically every rock physics modulus-porosity model has adjustable parameters. They may mineral elastic moduli, critical porosity, etc. (see below in model description). As we see in Figure 2.3.6a, the Model A curve computed with default input parameters does not fit the data precisely. Our next attempt is to refine the fit between the theory and the data by adjusting some input parameters (of course, within reasonable ranges). This procedure is illustrated in Figure 2.3.6b where we changed the critical porosity value from 0.38 (default mode) to 0.36 to fit the data.

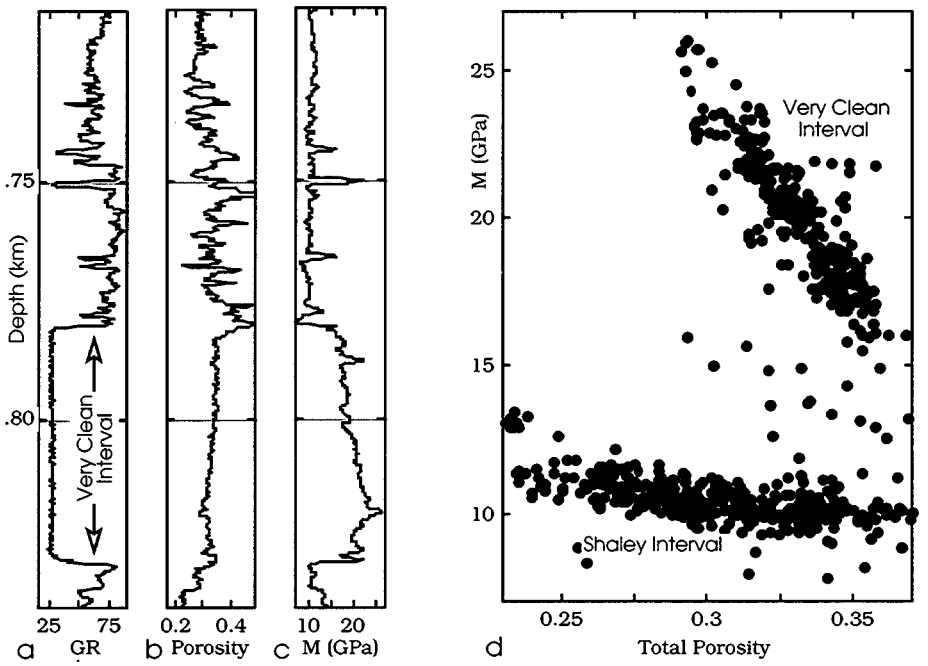

Figure 2.3.5. Example of cross-plotting compressional modulus versus porosity. a. Gamma-ray versus depth in the interval under investigation. b. Total porosity versus depth. c. Compressional modulus at common saturation versus depth. d. Compressional modulus at common saturation versus porosity.

As a result of Step 2, we will have modulus-porosity models that describe the data set under examination on the interval basis. Now these models are ready to be applied to the entire volume of rock.

As we move in space, porosity and saturation may change, but the models (we assume) will remain the same. It is very important to know (or assume) the spatial extension of the intervals to which specific models have been fitted.

For example, in the above-discussed case, one has to know the spatial configuration of clean cemented rocks that give very low gamma-ray signature (Figure 2.3.5).

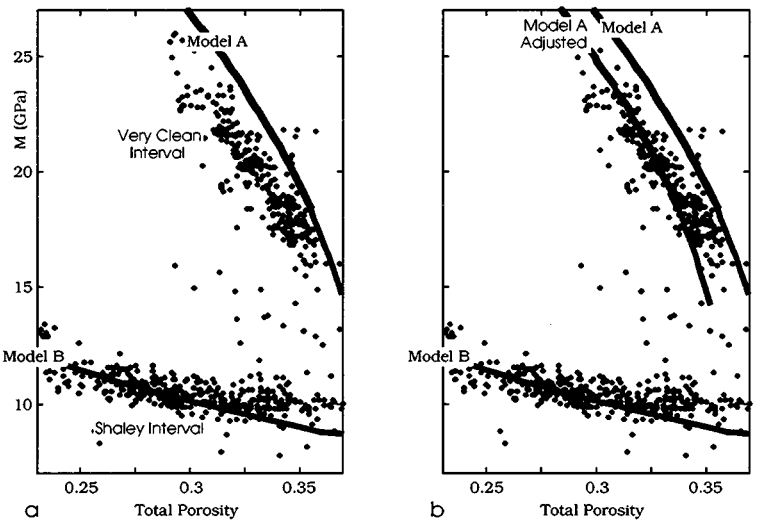

Figure 2.3.6. a. Selecting the appropriate rock physics models. b. Adjusting the models. Model A is from cementation theory; Model B is from unconsolidated rock theory.

A rock diagnostic flowchart is shown in Figure 2.3.7, following.

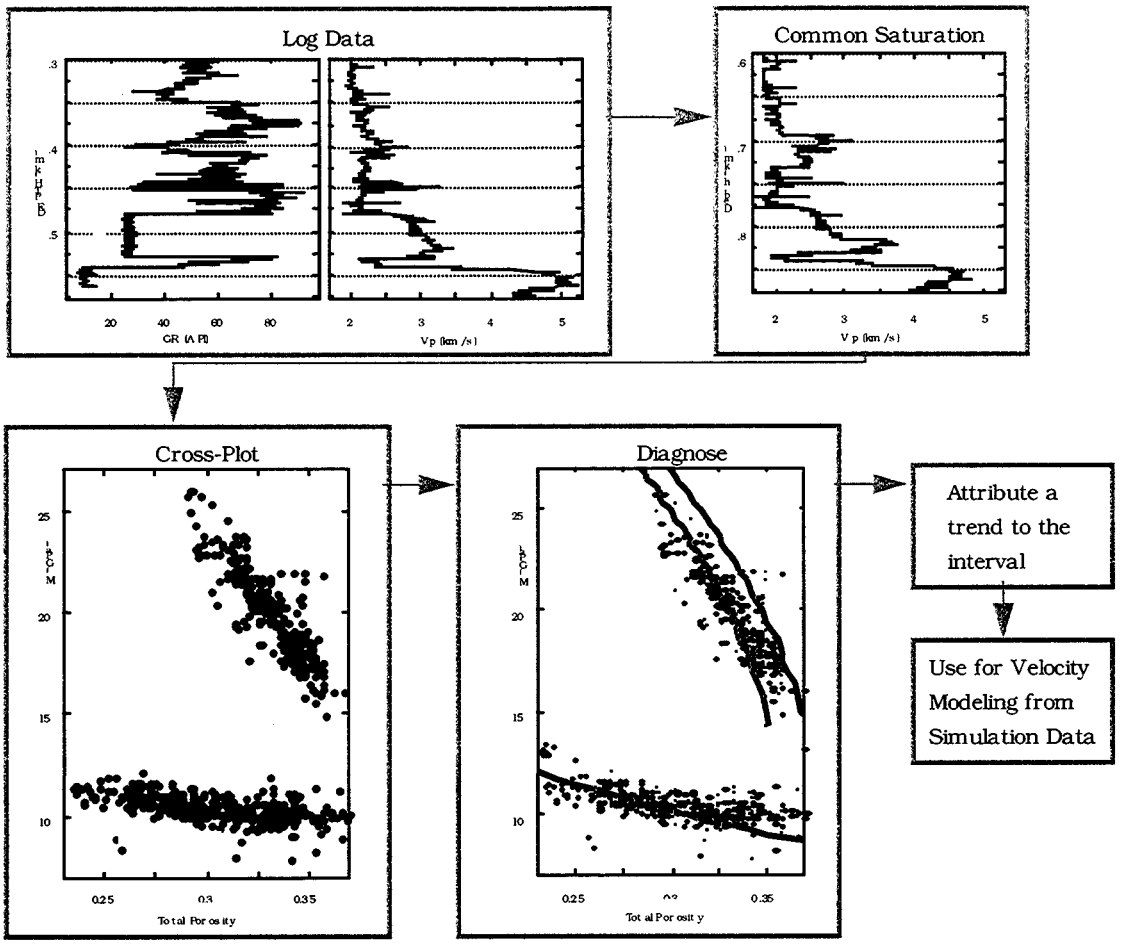

Figure 2.3.7. Rock physics diagnostic flowchart.

Diagnostic Type 2: Finding Analogous Data Set.

STEP 1: Bring the entire interval under examination, or the suite of core data, to common pore fluid saturation and calculate the elastic moduli. Same as in Type 1.

STEP 2: Cross-plot the compressional modulus at common saturation versus porosity and add on top of this cross-plot well-understood data that may be elastically close to the data set to be diagnosed. The moduli of the analogous data set should be recalculated to have the same common fluid as the data set under examination. This data set should be taken at the same effective pressure as the data set under examination. This step requires calibration datasets.

In Figure 2.3.8 we show a set of well log measurements in a vertical well drilled through

deep consolidated sandstones. Figure 2.3.8a (GR versus depth) indicates that these sandstones are very clean, especially in the lower part of the interval, with only a few thin shaley layers. Only compressional-wave measurements are available.

The goal is to diagnose these rocks and establish velocity-porosity relations for both P- and S-waves. We choose the common saturation fluid as a mixture of oil and formation water and cross-plot (Figure 2.3.9) P-impedance versus density-porosity (total porosity calculated from the bulk density data). In Figure 2.3.9a we plot the data from the entire interval under examination.

These data show a fairly tight impedance-porosity trend that can be used for further modeling. Even better trend appears if we plot only the cleanest sandstone data points versus porosity (Figure 2.3.9b). In Figure 2.3.10, we replot the same data as in Figure 2.3.9 with laboratory data set plotted on top. These superimposed data points are from Han's (1986) data set.

We can see now that for the entire interval trend (Figure 2.3.10a) can be approximated by that of a subset of Han's data set where the volumetric clay content is between 2% and 14%. The cleanest-sand trend (Figure 2.3.10b) can be approximated by that of a subset of Han's data set where the volumetric clay content in the rock is between 2% and 7%. Based on this similarity between the well log data under examination and Han's data, we speculate that all rock physics relations valid for the selected Han's data points hold for the well log data. The desired Vs versus Vp relations are plotted in Figure 2.3.11. They can be used for the well log data under examination.

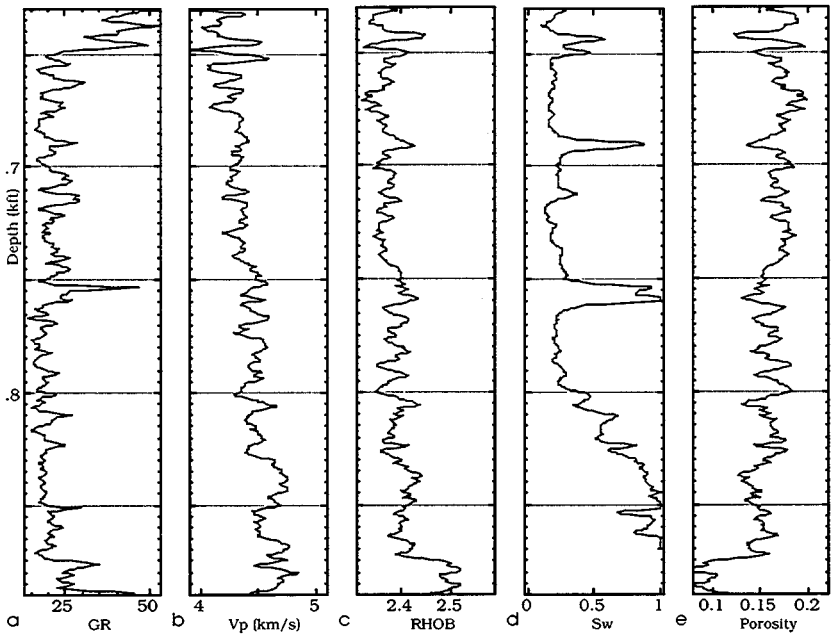

Figure 2.3.8. Log curves versus depth: gamma ray; velocity; density; saturation; and porosity.

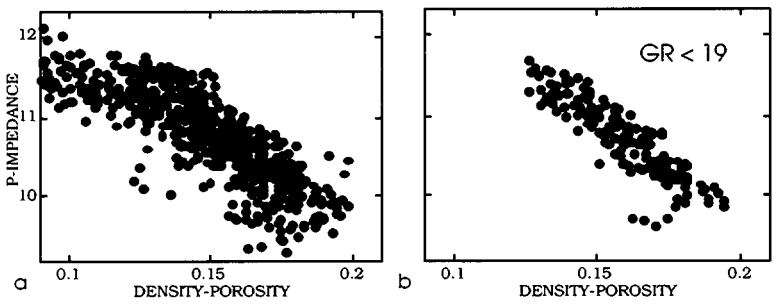

Figure 2.3.9. P-impedance versus porosity. a. For the entire interval. b. For the cleanest parts where gamma-ray count is below 19 API.

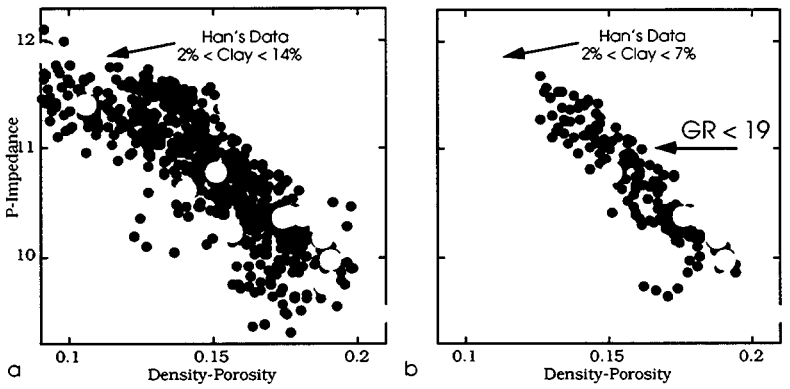

Figure 2.3.10. P-impedance versus porosity. a. Entire interval. b. Cleanest parts where gamma-ray count is below 19 API. Superimposed are data points from Han's (1986) dataset. a. Clay content between 2% and 14%. b. Clay content between 2% and 7%.

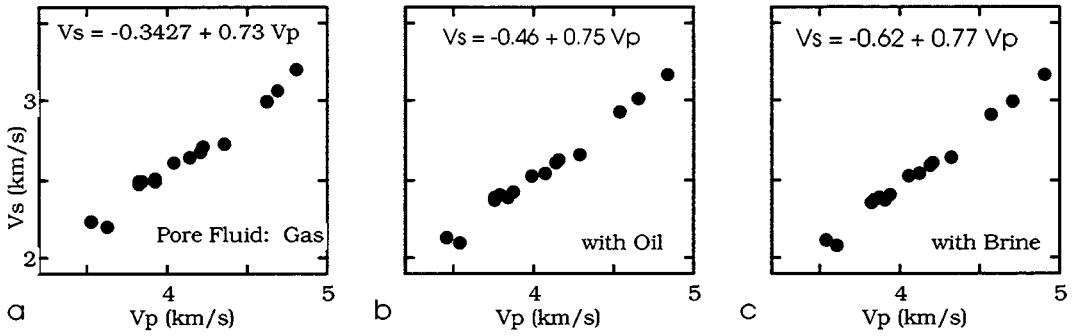

Figure 2.3.11. Vp versus Vs for Han's dataset for (a) gas-saturated rocks; (b) oil-saturated rocks; and (c) brine-saturated rocks. The relations can be used for the well log data under examination.

Diagnostic Type 3: Finding Empirical Trends.

STEP 1: Bring the entire interval under examination, or the suite of core data, to common pore fluid saturation. Calculate the elastic moduli at this common saturation.

STEP 2: Cross-plot the compressional modulus at common saturation versus porosity, identify trends and relate them to specific depth intervals and depositional sequences. As an example, we apply this diagnostic type to well log curves from a North Sea well. Several velocity-porosity trends are present in the well which are likely to be related to the vertical variation of intergranular cement type and clay content.

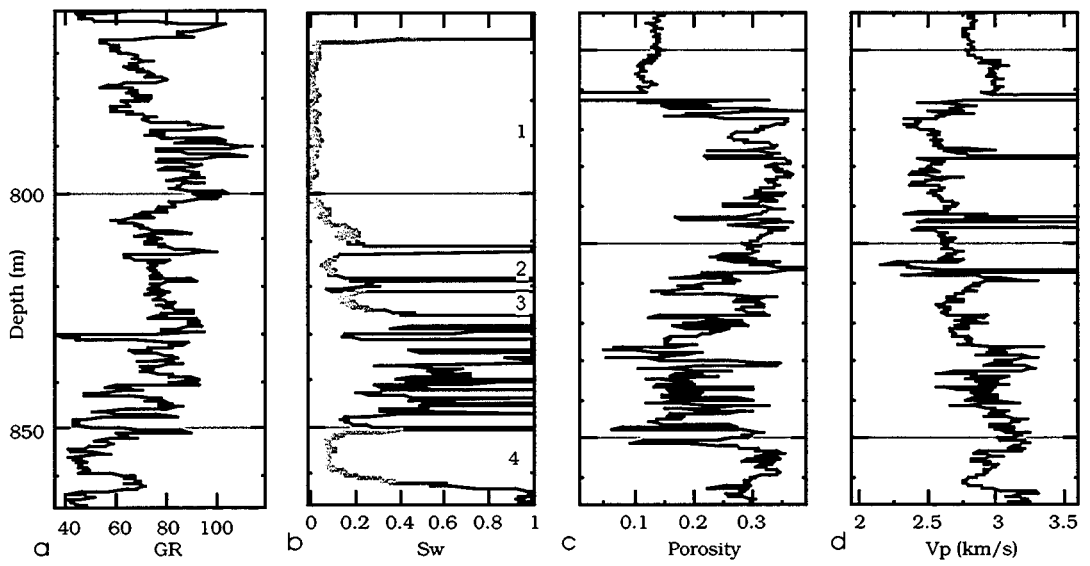

Figure 2.3.12. Gamma-ray (a), water saturation (b), porosity (c), and P-wave velocity (d) versus depth. Depth is counted not from the surface.

The gamma-ray, water saturation, porosity, and P-wave velocity curves are given in Figure 2.3.12. Porosity has been calculated from bulk density. It's values are very close to those directly measured on several core plugs. The depth interval under examination can be subdivided into four pay zones (Figure 2.3.12b).

We use the velocity, porosity, and saturation data and the Vp-only fluid substitution equation to calculate the compressional modulus of the rock fully saturated with formation water. This modulus is plotted versus log-derived porosity in Figure 2.3.13.

Four data clusters are present in Figure 2.3.13. One is associated with part of the deepest Zone 4 and falls on the cementation theoretical curve (Zone 4a). Another also belongs to Zone 4 and is grouped to the left of the cementation curve (Zone 4b). The data from Zone 2 and 3 form a linear modulus-porosity trend. The data from the shallowest Zone 1 form a low-velocity, high-porosity cluster. The data points from Zone 2 and 3 do not fall on any of the theoretical lines. The observed modulus-porosity trend is probably due to deteriorating sorting. A simple linear least-square line can be calculated that will fit those data. This line can be used as a modulus-porosity relation for rock physics transformations required in reservoir characterization.

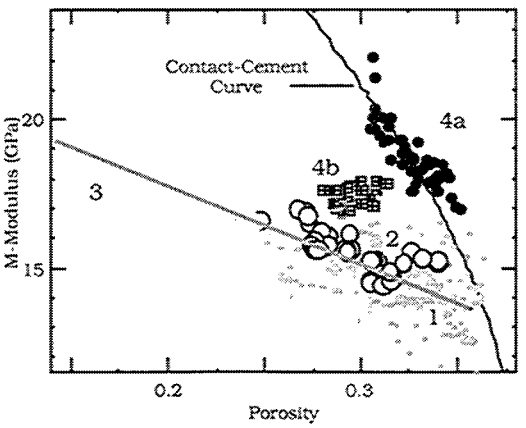

Figure 2.3.13. Compressional modulus versus porosity.

Note that a group of datapoints from Zone 4 (4b) forms a cluster in the modulus-

porosity plane that is separate from the contact-cement Zone 4a trend. At a fixed porosity, the modulus in this cluster is smaller than that predicted by the contact-cement theory and larger than that in the other zones. To analyze Zone 4b, consider the gamma-ray, porosity, and compressional-modulus curves for Zone 4 only (Figure 2.3.13). The Zone 4a datapoints correspond to the thin black lines whereas those from Zone 4b are shown by the bold gray lines.

It is clear from Figure 2.3.13 that the low-velocity Zone 4b cluster correspond to the relatively high gamma-ray 2 meter long interval at the bottom of Zone 2 and to a very thin interval in the middle. These two intervals also have relatively small porosity. Apparently here clay fills the pore space and reduces porosity without affecting the stiffness of the contact-cemented frame.

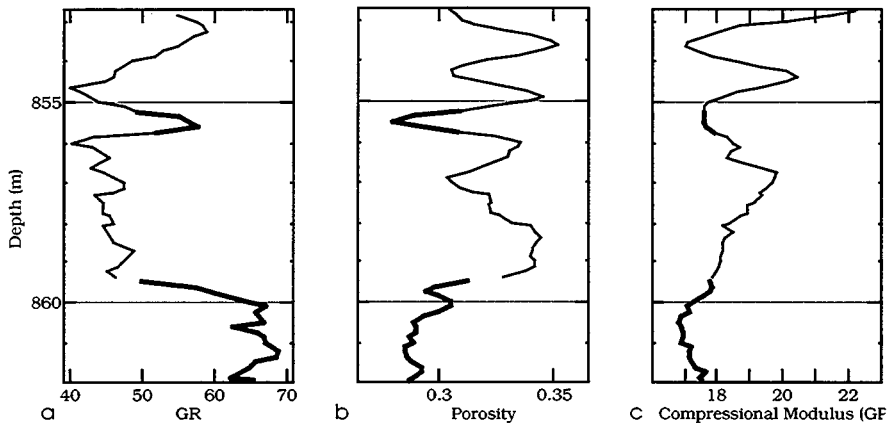

Figure 2.3.13. Gamma-ray (a), porosity (b), and compressional modulus (c) versus depth for Zone 4. Thin black curves correspond to the data points that lie along the contact-cement line in Figure 2.3.12. Bold gray lines correspond to the Zone 4b cluster in Figure 2.3.12. Depth is counted not from the surface.

The three diagnostic methods discussed above have been designed to help one to establish a rock physics model for relating reservoir simulation data to the elastic reservoir parameters for creating synthetic seismic data. One does not have to be limited by any of these three approaches. It is beneficial if all three of them are used simultaneously to establish a relation, understand its physical basis, and calibrate it by using comparable data sets.

2.4. BINARY MIXTURE THEORY

The constant cement and unconsolidated sand models (see Appendix A) mimic the process of deteriorating sorting in sands. Core analysis supports the hypothesis that in the constant cement model the data and the theoretical curve deviate from the contact cement curve because grain sorting starts to deteriorate at the cemented porosity point. The same reason produces the unconsolidated sand model: smaller particles fall between the larger well-sorted grains (Figure 2.4.1).

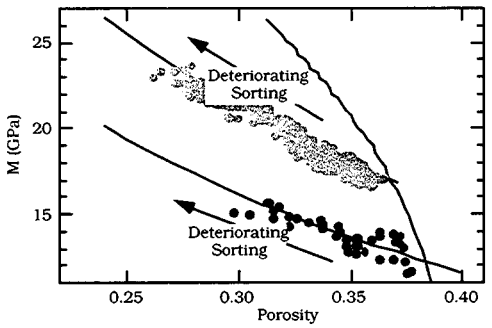

Figure 2.4.1. Porosity reduction in sands due to deteriorating sorting.

2.4.1 Geometry of a Bimodal Grain Mixture.

Assume that there are two grain sizes present in a mixture: large grains and significantly smaller grains. Depending on the volumetric fraction of the large and small grains, various configurations are possible, as shown in Figure 2.4.2, where on the left we have only large particles and on the right only small particles. Let the number of large particles in a representative volume be L and that of small particles be l (Figure 2.4.3). The radii are R (for large particles) and r (for small particles).

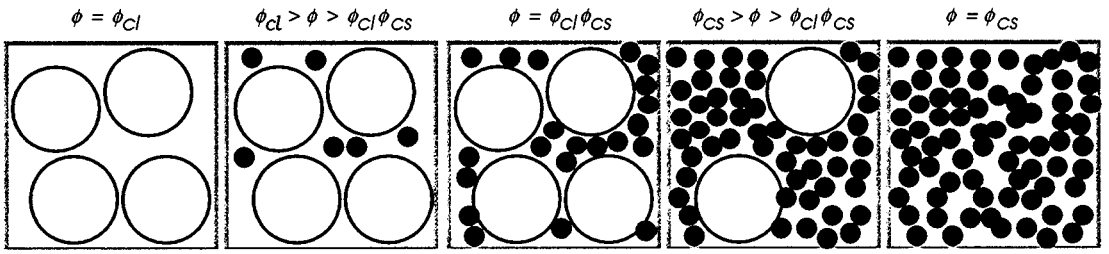

Figure 2.4.2. Porosity reduction in sands due to deteriorating sorting. It is assumed here that the porosity of the large particle pack is the same for large and small grain packs.

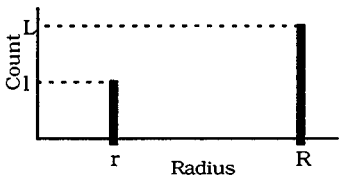

Figure 2.4.3. Size distribution in a binary particle mixture.

The total volume of the small grains when they are packed together at porosity ϕ_{cs}, which is the critical porosity for the small grains, (as in Figure 2.4.2, right) is

$$\frac{4}{3}\frac{\pi r^3 l}{1-\phi_{cs}}. \tag{2.4.1}$$

That of the large grains when they are packed together at porosity ϕ_{cl}, which is the critical porosity for the large grains, (as in Figure 2.4.2, left) is

$$\frac{4}{3}\frac{\pi R^3 L}{1-\phi_{cl}}. \tag{2.4.2}$$

The pore-space volume of the large grains packed together is

$$\frac{4}{3}\frac{\phi_{cl}\pi R^3 L}{1-\phi_{cl}}. \tag{2.4.3}$$

If the volume of the small grains in a pack is smaller than the pore-space volume of the large grains in a pack, all small grains can be accommodated inside the pore space of the large grains pack. Then we have a configuration shown in Figure 2.4.2, second frame from left. The condition for this geometry is

$$\frac{4}{3}\frac{\pi r^3 l}{1-\phi_{cs}} \le \frac{4}{3}\frac{\phi_{cl}\pi R^3 L}{1-\phi_{cl}} \Rightarrow \left(\frac{r^3 l}{1-\phi_{cs}}\right)/\left(\frac{R^3 L}{1-\phi_{cl}}\right) \le \phi_{cl} \Rightarrow \beta \le \phi_{cl}, \tag{2.4.4}$$

where

$$\beta \equiv \left(\frac{r^3 l}{1-\phi_{cs}}\right)/\left(\frac{R^3 L}{1-\phi_{cl}}\right). \tag{2.4.5}$$

The total porosity ϕ of this mixture is

$$\phi = \phi_{cl} - \beta(1-\phi_{cs}). \tag{2.4.6}$$

If the volume of the small grain pack equals that of the pore-space volume of the large grain pack, then $\beta = \phi_{cl}$ and

$$\phi = \phi_{cl}\phi_{cs}, \tag{2.4.7}$$

as in Figure 2.4.2, middle frame.

In the case of $\beta > \phi_{cl}$, the large grains will be suspended in the pack of the small grains (Figure 2.4.2, fourth frame). The total volume of the composite is

$$\frac{4}{3}\pi R^3 L + \frac{4}{3}\frac{\pi r^3 l}{1-\phi_{cs}} \tag{2.4.8}$$

and the pore volume is that of the small grain pack:

$$\frac{4}{3}\frac{\phi_{cs}\pi r^3 l}{1-\phi_{cs}}. \tag{2.4.9}$$

As a result, the total porosity of the composite is

$$\phi = \frac{\phi_{cs}}{1+(1-\phi_{cl})/\beta}. \tag{2.4.10}$$

If $\beta = \phi_{cl}$, then the large grains touch each other and $\phi = \phi_{cl}\phi_{cs}$. If $\beta = \infty$, which means that only the small grains are present, the porosity of the composite is ϕ_{cs}. The summary of these results is:

$$\begin{aligned}
&\phi = \phi_{cl} \quad \Leftarrow \beta = 0;\\
&\phi = \phi_{cl} - \beta(1-\phi_{cs}) \quad \Leftarrow \beta < \phi_{cl};\\
&\phi = \phi_{cl}\phi_{cs} \quad \Leftarrow \beta = \phi_{cl};\\
&\phi = \phi_{cs} / (1+(1-\phi_{cl})/\beta) \quad \Leftarrow \beta > \phi_{cl};\\
&\phi = \phi_{cs} \quad \Leftarrow \beta = \infty.
\end{aligned} \tag{2.4.11}$$

The graph of the total porosity of the composite is given in Figure 2.4.4.

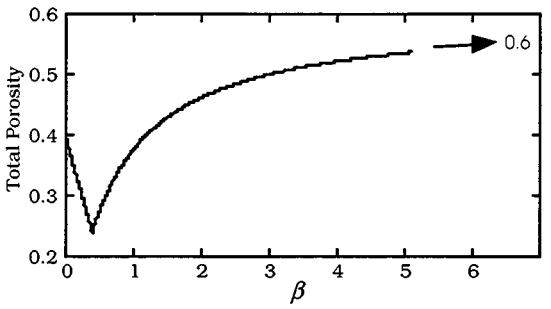

Figure 2.4.4. Total porosity versus the ratio of the small grain pack volume to the large grain pack volume. The critical porosity for large grains is 0.4 and that for small grains is 0.6.

2.4.2. Elasticity of a Bimodal Grain Mixture.

Let us first assume that $\beta \geq \phi_{cl}$, i.e., the small grains fill the entire pore space of the large grain pack, or the large grains are suspended in the small grain pack (Figure 2.4.2, third, fourth, and fifth frame). Let us also assume that the elastic moduli of the large grain material are much larger that those of the small grain pack. In this case, and because the small grain pack (soft) envelopes the large grains (stiff), we propose to model the effective elastic moduli of the composite as the lower Hashin-Shtrikman bound of two elastic components: (1) the soft component that is the small grain pack and (2) the stiff components that is the large grain material.

For $\beta \geq \phi_{cl}$, the total volume of the composite is given by Equation (2.4.8) and the volume of the small grain pack is $4\pi r^3 l / (3(1-\phi_{cs}))$. Therefore, the volumetric concentration of the small grain pack (the soft component) in the composite is

$$f_{Soft} = \frac{1}{1+(1-\phi_{cl})/\beta}. \tag{2.4.12}$$

Then, the Hashin-Shtrikman lower bound gives the following effective-medium elastic moduli of the dry composite:

$$\begin{aligned} K_{EM} &= \left(\frac{f_{Soft}}{K_{Soft}+(4/3)G_{Soft}} + \frac{1-f_{Soft}}{K_l+(4/3)G_{Soft}}\right)^{-1} - \frac{4}{3}G_{Soft}, \\ G_{EM} &= \left(\frac{f_{Soft}}{G_{Soft}+Z_{Soft}} + \frac{1-f_{Soft}}{G_l+Z_{Soft}}\right)^{-1} - Z_{Soft},\ Z_{Soft} = \frac{G_{Soft}}{6}\frac{9K_{Soft}+8G_{Soft}}{K_{Soft}+2G_{Soft}}, \end{aligned} \tag{2.4.13}$$

where K_l and G_l are the bulk and shear moduli of the large grain material, respectively; and K_{Soft} and G_{Soft} are the bulk and shear moduli of the small grain pack, respectively.

If the small grain pack can be approximated by a random dense pack of identical elastic spheres, its elastic moduli can be calculated from the Hertz-Mindlin contact theory as

$$K_{Soft} = \left(\frac{n_s^2(1-\phi_{cs})^2 G_s^2}{18\pi^2(1-\nu_s)^2} P\right)^{\frac{1}{3}},\ G_{Soft} = \frac{5-4\nu_s}{5(2-\nu_s)}\left(\frac{3n_s^2(1-\phi_{cs})^2 G_s^2}{2\pi^2(1-\nu_s)^2} P\right)^{\frac{1}{3}};$$
$$\nu_s = \frac{1}{2}\left(\frac{K_s}{G_s} - \frac{2}{3}\right) / \left(\frac{K_s}{G_s} + \frac{1}{3}\right). \qquad (2.4.14)$$

where K_s and G_s are the bulk and shear moduli of the small grain material, respectively; P is the differential pressure; and n_s is the coordination number (the average number of contacts per grain) for the pack of small grains. This approximation may not be appropriate if the small grain pack is a pack of, e.g., clay particles.

Consider now the case $\beta \le \phi_{cl}$ (Figure 2.4.2, first three panels). The two elastic end-members are: (1) $\beta = 0$, i.e., the pack of the large grains (without small grains present in the pore space, Figure 2.4.2, first panel) with porosity ϕ_{cl}; and (2) $\beta = \phi_{cl}$, i.e., the small grains fill the entire pore space of the large grain pack (Figure 2.4.2, third panel).

The elastic moduli of the first end-member (at $\beta = 0$) can be calculated from the Hertz-Mindlin contact theory by assuming that the large grains are identical elastic spheres with bulk modulus K_l, shear modulus G_l, and coordination number n_l.

Then the bulk modulus K_1 and the shear modulus G_1 are:

$$K_1 = \left(\frac{n_l^2(1-\phi_{cl})^2 G_l^2}{18\pi^2(1-\nu_l)^2} P\right)^{\frac{1}{3}},\ G_1 = \frac{5-4\nu_l}{5(2-\nu_l)}\left(\frac{3n_l^2(1-\phi_{cl})^2 G_l^2}{2\pi^2(1-\nu_l)^2} P\right)^{\frac{1}{3}};$$
$$\nu_l = \frac{1}{2}\left(\frac{K_l}{G_l} - \frac{2}{3}\right) / \left(\frac{K_l}{G_l} + \frac{1}{3}\right). \qquad (2.4.15)$$

The bulk and shear moduli of the second end-member are given by Equations (13)

where f_{Soft} has to be replaced by ϕ_{cl}:

$$K_2 = \left(\frac{\phi_{cl}}{K_{Soft} + (4/3)G_{Soft}} + \frac{1-\phi_{cl}}{K_l + (4/3)G_{Soft}}\right)^{-1} - \frac{4}{3}G_{Soft},$$
$$G_2 = \left(\frac{\phi_{cl}}{G_{Soft} + Z_{Soft}} + \frac{1-\phi_{cl}}{G_l + Z_{Soft}}\right)^{-1} - Z_{Soft},\ Z_{Soft} = \frac{G_{Soft}}{6}\frac{9K_{Soft} + 8G_{Soft}}{K_{Soft} + 2G_{Soft}}. \quad (2.4.16)$$

We will connect these two end points by a lower Hashin-Shtrikman bound curve. In order to calculate the volumetric fractions of the two end members in the composite, let us assume that the two end-members added together result in the given numbers of small and large grains (Figure 2.4.5).

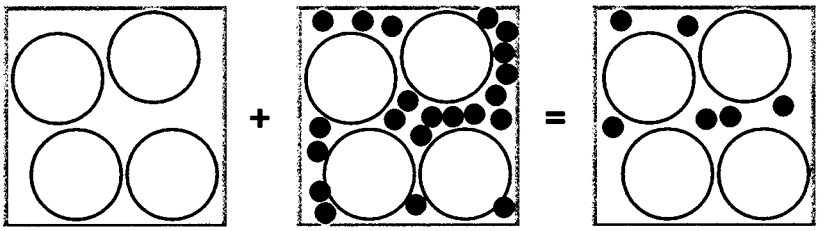

Figure 2.4.5. Two end members added provide required configuration.

If the volume fraction of the first end member in the composite is f_1 and that of the second end member is $f_2 = 1 - f_1$ then the number of the small grains in a unit volume of the composite is

$$l = \frac{f_2\phi_{cl}(1-\phi_{cs})}{4\pi r^3/3} \quad (2.4.17)$$

and the number of the large grains is

$$L = \frac{1-\phi_{cl}}{4\pi R^3/3}. \quad (2.4.18)$$

Then

$$\beta \equiv \left(\frac{r^3 l}{1-\phi_{cs}}\right) / \left(\frac{R^3 L}{1-\phi_{cl}}\right) = f_2\phi_{cl}. \quad (2.4.19)$$

As a results, we have:

$$f_2 = \beta / \phi_{cl},\ f_1 = 1 - f_2, \tag{2.4.}$$

Then, the Hashin-Shtrikman lower bound of the mixture of the elastic end me with the bulk and shear moduli K_1 and G_1, and K_2 and G_2, respectively, and fractions f_1 and f_2, respectively, is

$$\begin{aligned} K_{EM} &= \left(\frac{f_1}{K_1 + (4/3)G_1} + \frac{f_2}{K_2 + (4/3)G_1}\right)^{-1} - \frac{4}{3}G_1, \\ G_{EM} &= \left(\frac{f_1}{G_1 + Z_1} + \frac{f_2}{G_2 + Z_1}\right)^{-1} - Z_1,\ Z_1 = \frac{G_1}{6}\frac{9K_1 + 8G_1}{K_1 + 2G_1}, \end{aligned} \tag{2.4.21}$$

and it is assumed that the first end member is softer than the second end me Equations (2.4.13) and (2.4.21) provide the elastic moduli of the composite's dry i In the low-frequency limit, the shear modulus of the saturated composite is the sa that of the dry frame. The bulk modulus of the saturated composite K_{Sat} c calculated from that of the dry composite using Gassmann's equation

$$K_{Sat} = K_{Solid}\frac{\phi K_{EM} - (1+\phi)K_{Fluid}K_{EM} / K_{Solid} + K_{Fluid}}{(1-\phi)K_{Fluid} + \phi K_{Solid} - K_{Fluid}K_{EM} / K_{Solid}}, \tag{2.4.22}$$

where K_{Fluid} is the bulk modulus of the pore fluid and K_{Solid} is that of the com solid.

K_{Solid} can be calculated by mixing the material of the large grains with that of tl grains and using, e.g., Hill's average. The volume of the solid material in the grains is $4\pi R^3 L / 3$ and that in the small grains is $4\pi r^3 l / 3$. Then the volume fr f_l of the large grain material in the entire solid phase of the composite is

$$f_l = \frac{R^3 L}{R^3 L + r^3 l} = \frac{1}{1 + r^3 l / (R^3 L)} = \frac{1}{1 + \beta(1-\phi_{cs}) / (1-\phi_{cl})}. \tag{2.4.23}$$

The resulting Hill's average is

$$K_{Solid} = \frac{1}{2}\left(f_l K_l + (1-f_l)K_s + \left(\frac{f_l}{K_l} + \frac{1-f_l}{K_s}\right)^{-1}\right). \tag{2.4.24}$$

2.4.3. Example of Applying the Theory.

We use the theory to simulate well log data from Well 1879 in La Cira field in Colombia. The log data span the depth interval from 414 ft to 2258 ft with sands and shales represented in the section. The average bulk density is 2.36 g/cm^3. The pore fluid density is about 1 g/cm^3. Therefore, the differential pressure is about 1.7 MPa at the top and 9.4 MPa at the bottom of the interval, respectively.

The compressional modulus is plotted versus the density-derived porosity in Figure 2.4.6. The lower branch of the trend corresponds to shallow formations with high GR values and, apparently, large clay content. The upper branch corresponds to higher GR values and deeper intervals where sand starts to dominate.

In order to model the effect of changing effective pressure, we used the model twice, with 2 MPa and 10 MPa differential pressure as input. Other inputs are:

$$\phi_{cl} = .3;\ \phi_{cs} = .2;\ n_l = 11;\ n_s = 14;$$
$$K_l = 37\text{GPa};\ G_l = 45\text{GPa};\ K_s = 21\text{GPa};\ G_s = 8\text{GPa};\ K_f = 2.5\text{GPa}.$$

The results (Figure 2.4.6) show that the theory can reasonably well mimic the data. Some laboratory data on binary mixtures of sand and clay are presented in Appendix A, Section 5.

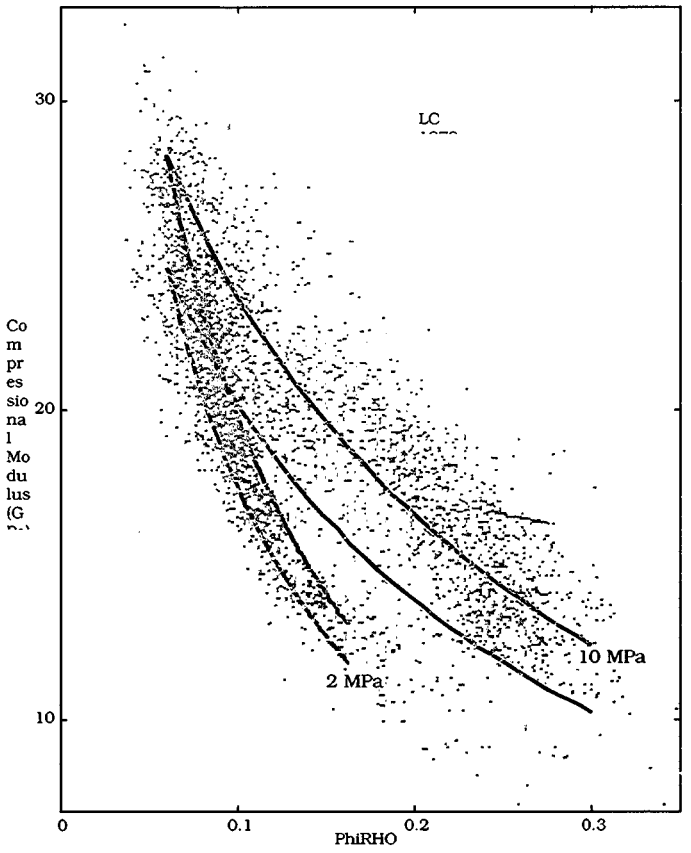

Figure 2.4.6. Well log data and model curves.

1.0 STATIC AND DYNAMIC MODULI, DEFORMATION AND FAILURE MODELS

1.1 Clayey Sandstone Core Data

New laboratory data have been obtained on a sandstone core with large amounts of clay spanning depth interval from 10118 ft to 10197 ft. The data have been analyzed to establish relations between the static and dynamic elastic moduli of the rock and its failure characteristics. Relations have been established between the *static Young's modulus and Poisson's ratio* on the one hand and the dynamic shear modulus on the other hand (the dynamic properties are those that are calculated from the elastic-wave velocity measurements). These relations will allow one to predict the static moduli from velocity well log data. The relations are:

E_Static = -0.34 + 0.59 G_Dynamic; R= 0.96,
PR_Static = 0.37 - 0.0208 G_Dynamic; R= 0.99;

where E_Static and PR_Static are the static Young's modulus and Poisson's ratio, respectively, and G_Dynamic is the dynamic shear modulus. All moduli are in GPa. The dynamic shear modulus is the product of the bulk density times the shear-wave velocity squared (Figure 1.1.1).

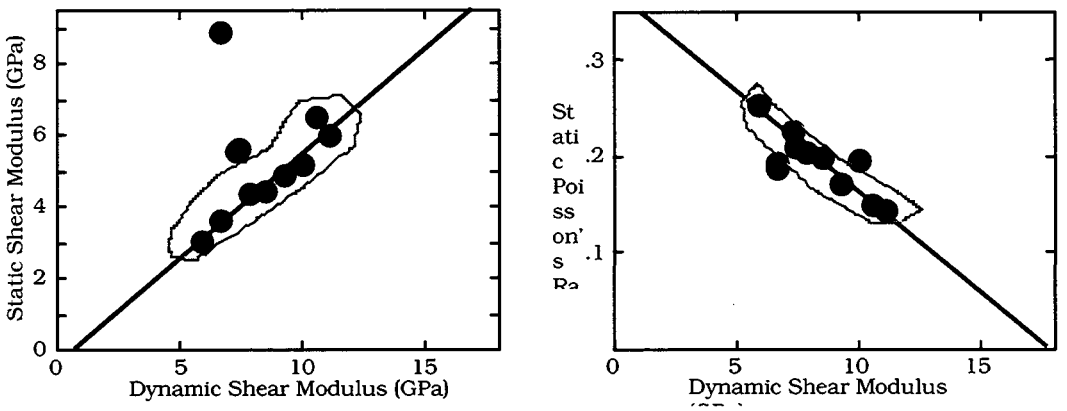

Figure 1.1.1. Static shear modulus and static Poisson's ratio versus dynamic shear modulus.

It has been established that the *failure* envelope for the samples can be adequately modeled by the Drucker-Prager and CAP model. The hardening law can be approximated by either CAP equation or linear equation that are fairly close to each

other in the case under examination. The resulting fixed and moving yield surfaces are shown in Figure 1.12.

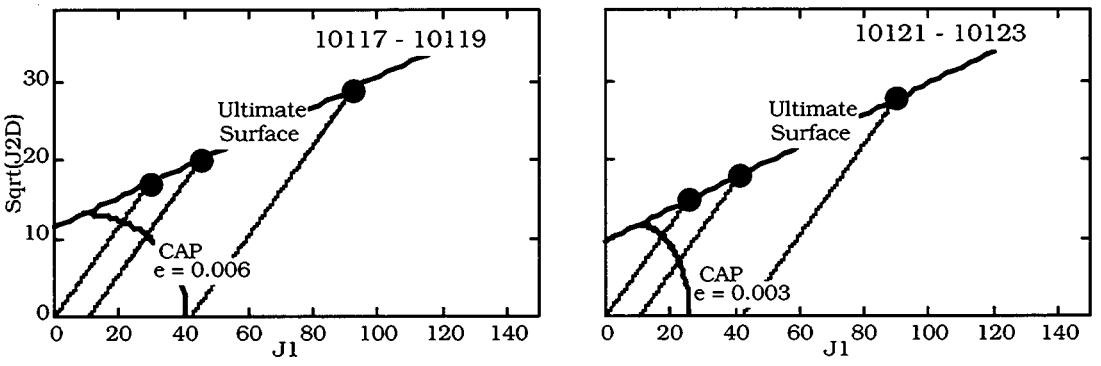

Figure 1.1.2. Fixed and moving yield surfaces.

All results are implemented as Matlab applets that can be used by the engineer.

1.2 Shaley Sandstone Core Data

New laboratory data have been obtained on a sandstone core with large amounts of clay spanning depth interval from 10118 ft to 10197 ft. The total of 28 experiments have been conducted on rock plugs from six separate portions of the core. The experiments included the elastic-wave velocity measurements under hydrostatic and axial-load conditions, and the static axial deformation measurements with and without hydrostatic confining stress.

The porosity, permeability, and mineralogy of the plugs are summarized in Table 1.2.1. The porosity and permeability measured at 4000 psi are plotted versus the values measured at 400 psi in Figure 1.2.1a and 1.2.1b, respectively. As we can see, the pressure-induced changes of these reservoir properties are not very significant.

The permeability is plotted versus porosity in Figure 1.2.2 at 400 and 4000 psi. There is no clear permeability-porosity trend in the samples under examination. The velocity versus pressure data obtained on room-dry plugs are given in Figure 1.2.3.

Table 1.2.1. Properties of the shaley samples tested (10118 - 10197 ft)

Sample Depth	Grain Density	Porosity @ 400 psi	Porosity @ 4000 psi	Permeability @ 400 psi	Permeability @ 4000 psi	Quartz	F-Spar	Clay
10117.90	2.65	0.267	0.243	17.8	14.5	0.22	0.15	0.63
10118.90	2.67	0.242	0.226	15.2	10.4	0.22	0.19	0.59
10119.30	2.67	0.237	0.216	4.78	3.77	0.41	0.21	0.38
10121.11	2.62	0.235	0.212	18.9	15.46	0.34	0.15	0.51
10122.60	2.66	0.228	0.228	5.34	4.15	0.45	0.06	0.49
10123.40	2.66	0.168	0.168	3.12	2.74	0.4	0.13	0.47
10136.00	2.68	0.278	0.247	3.57	2.05	0.3	0.17	0.53
10136.80	2.64	0.165	0.137	11.0	8.0	0.16	0.18	0.66
10137.60	2.66	0.172	0.146	2.1	1.60	0.2	0.15	0.65
10156.90	2.68	0.16	0.138	3.73	2.48	0.29	0.14	0.57
10157.70	2.68	0.108	0.103	2.5	1.12	0.59	0.08	0.33
10157.70	2.66	0.202	0.177	15.9	15.0	0.45	0.1	0.45
10165.50	2.64	0.151	0.129	3.45	2.8	0.43	0.03	0.54
10165.90	2.65	0.162	0.162	18.23	14.8	0.62	0.05	0.33
10166.00	2.67	0.112	0.11	9.92	7.9	0.31	0.1	0.59
10197.00	2.67	0.122	0.118	52.3	30.5	0.43	0.09	0.48
10199.50	2.65	0.162	0.162	19.6	14.7	0.59	0.06	0.35

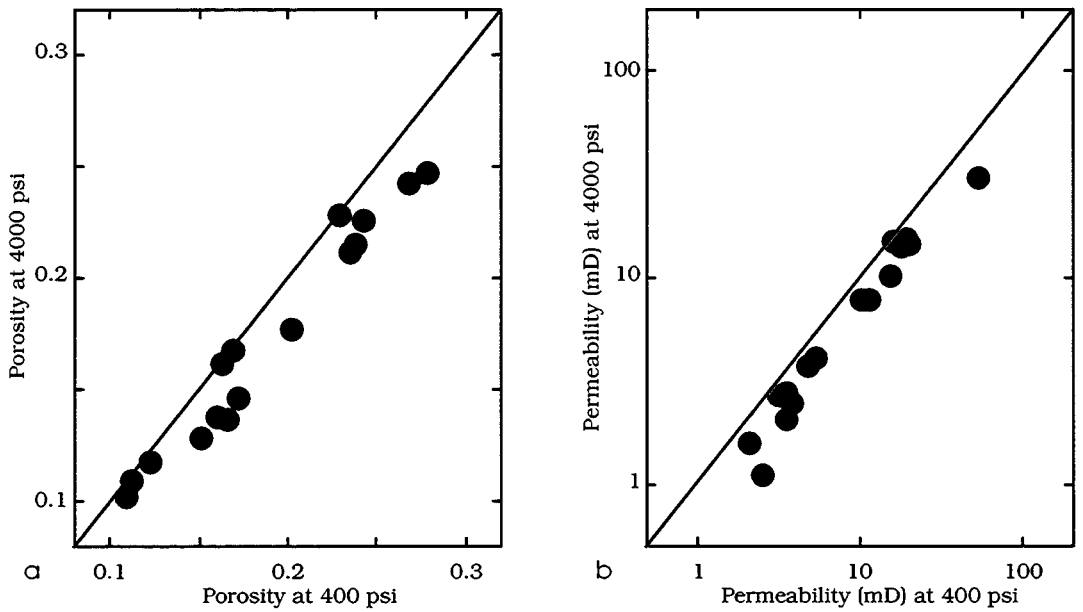

Figure 1.2.1. Porosity (a) and permeability (b) at 4000 psi versus the values at 400 psi for the shaley sandstone core.

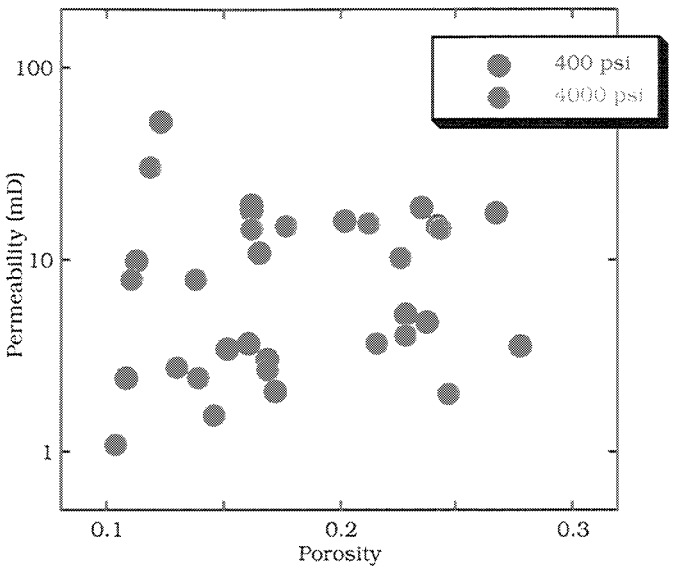

Figure 1.2.2. Permeability versus porosity at 400 and 4000 psi.

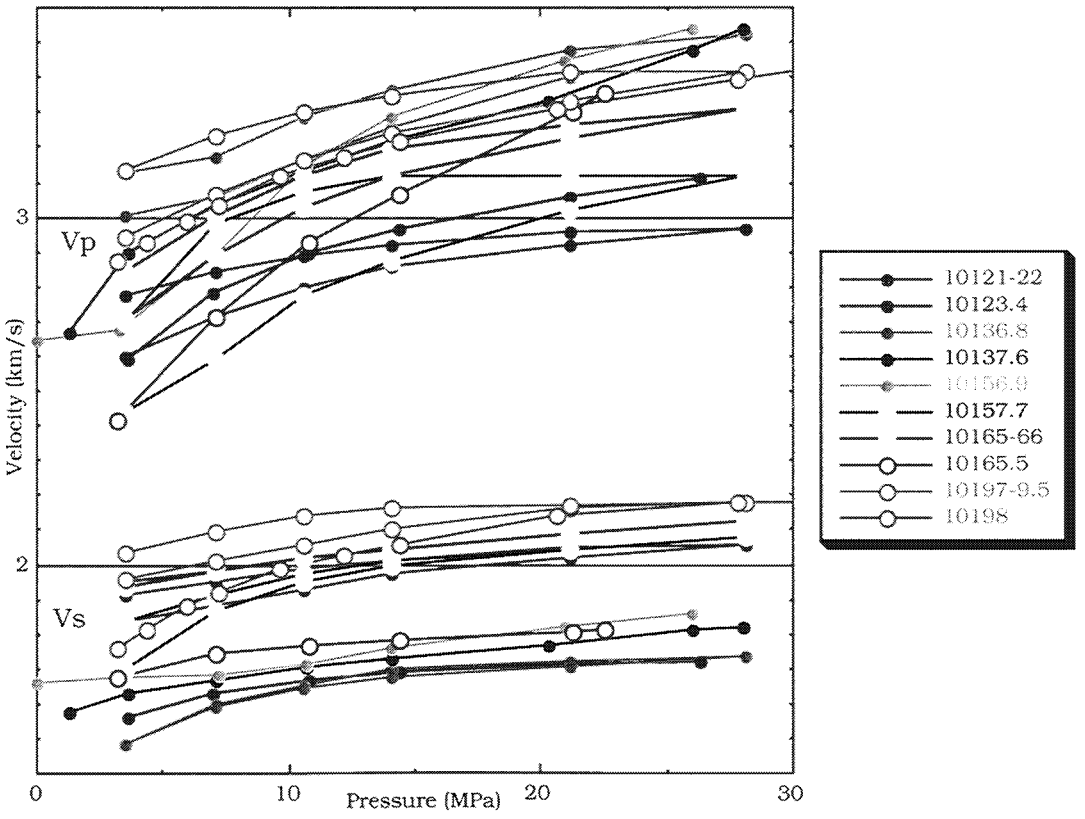

Figure 1.2.3. Velocity versus pressure from 10 experiments.
The legend gives the plug ID (see Table 1.2.1).

1.3. Elastic-Wave (Dynamic) Data Analysis

Below, we display the elastic-wave velocity measurement results for the six separate portions of the core. All samples were room-dry. The stress conditions of the experiments are indicated on the graphs. It is impossible to conclude whether the velocity difference between the hydrostatic-loading experiments and uniaxial-loading experiments is due to the difference in the loading conditions or to the porosity and mineralogy difference between the samples. Below, we will compare the results of these experiments to each other disregarding whether the loading was hydrostatic or uniaxial.

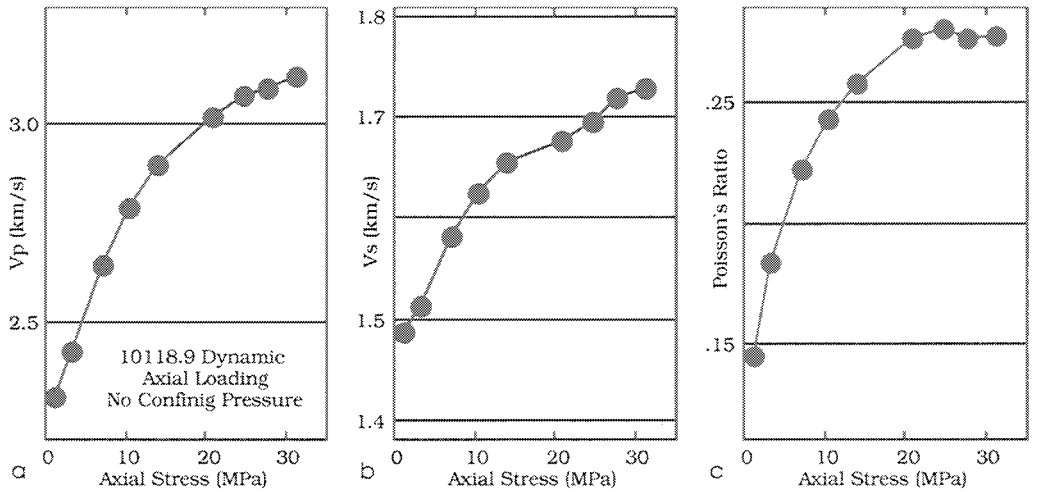

Figure 1.3.1. P- and S-wave velocity and Poisson's ratio versus axial stress in sample 10118.9. The experiment is axial loading without confining pressure.

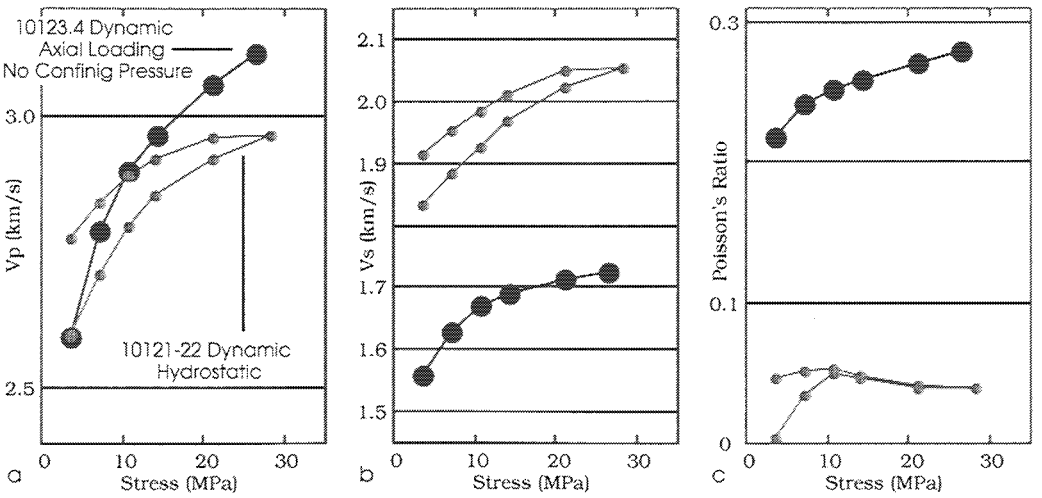

Figure 1.3.2. P- and S-wave velocity and Poisson's ratio versus pressure in samples 10123.4 and 10121-22. The experiment is axial loading without confining pressure in 10123.4 and hydrostatic loading and unloading in 10121-22.

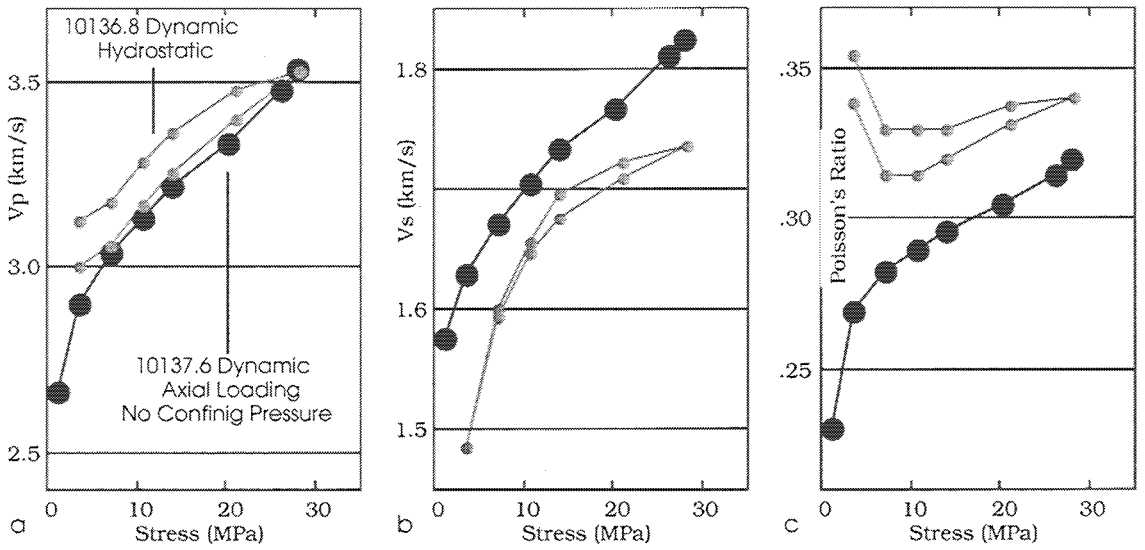

Figure 1.3.3. P- and S-wave velocity and Poisson's ratio versus pressure in samples 10136.8 and 10137.6. The experiment is axial loading without confining pressure in 10136.8 and hydrostatic loading and unloading in 10137.6.

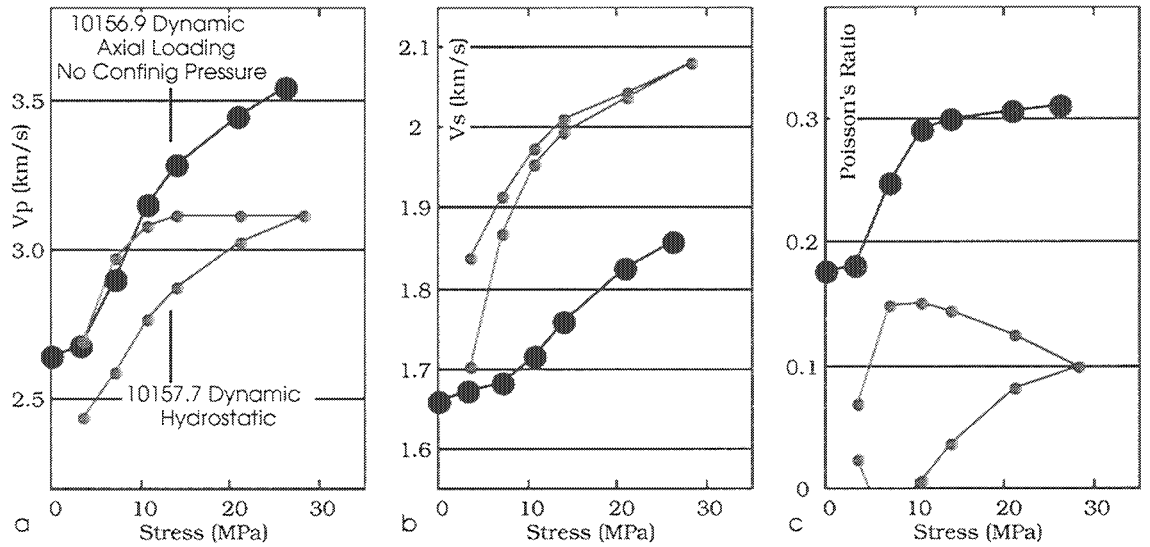

Figure 1.3.4. P- and S-wave velocity and Poisson's ratio versus pressure in samples 10156.9 and 10157.7. The experiment is axial loading without confining pressure in 10156.9 and hydrostatic loading and unloading in 10157.7.

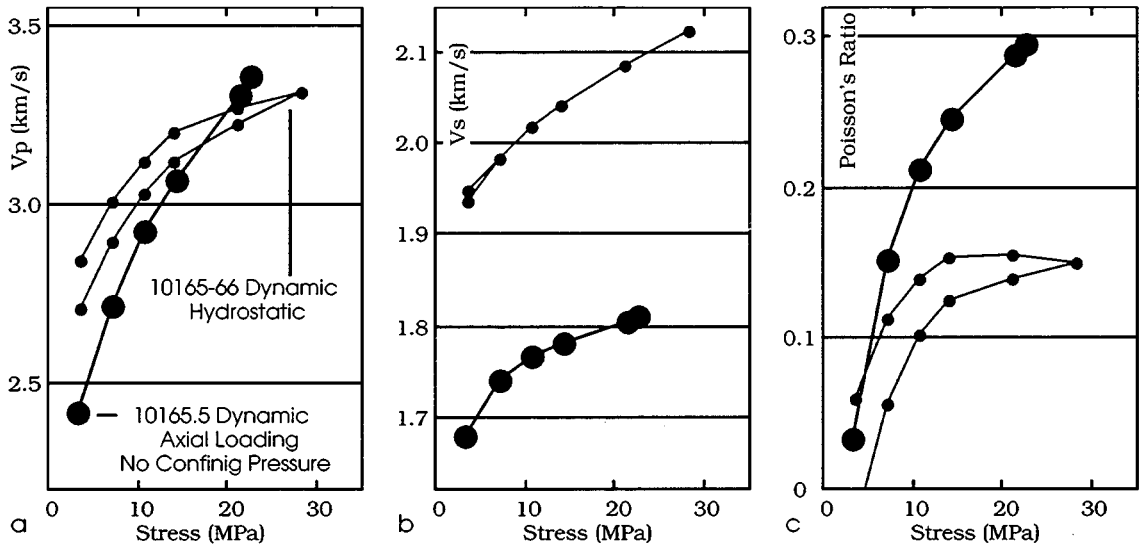

Figure 1.3.5. P- and S-wave velocity and Poisson's ratio versus pressure in samples 10165.5 and 10165-66. The experiment is axial loading without confining pressure in 10165.5 and hydrostatic loading and unloading in 10165-66.

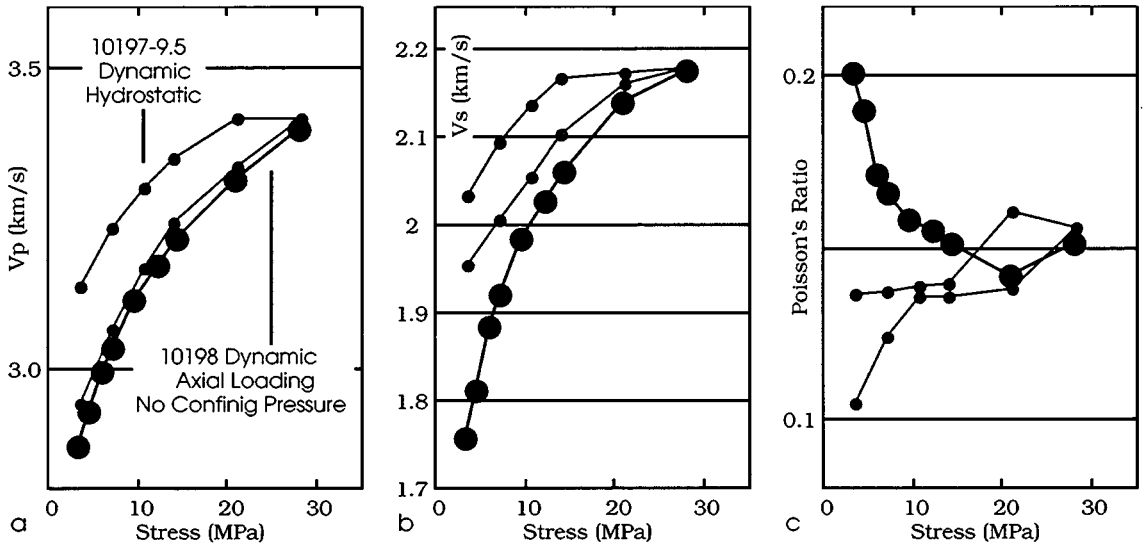

Figure 1.3.6. P- and S-wave velocity and Poisson's ratio versus pressure in samples 10198 and 10197-9.5. The experiment is axial loading without confining pressure in 10198 and hydrostatic loading and unloading in 10197-9.5.

By plotting velocity versus porosity in the samples under examination, we observe that a velocity-porosity trends exist. In Figure 1.3.7, we compare the new velocity data presented here with the velocity data from Han's (1986). In the latter, only the samples with the volumetric clay content between 28 and 45% are shown. The Han data lie on the same velocity-porosity trend as the new data. The position of the samples with clay

among cleaner rock samples is shown in Figure 1.3.8 where the new data and the Han shaley-rock data are plotted together with the Han low-clay (below 6%).

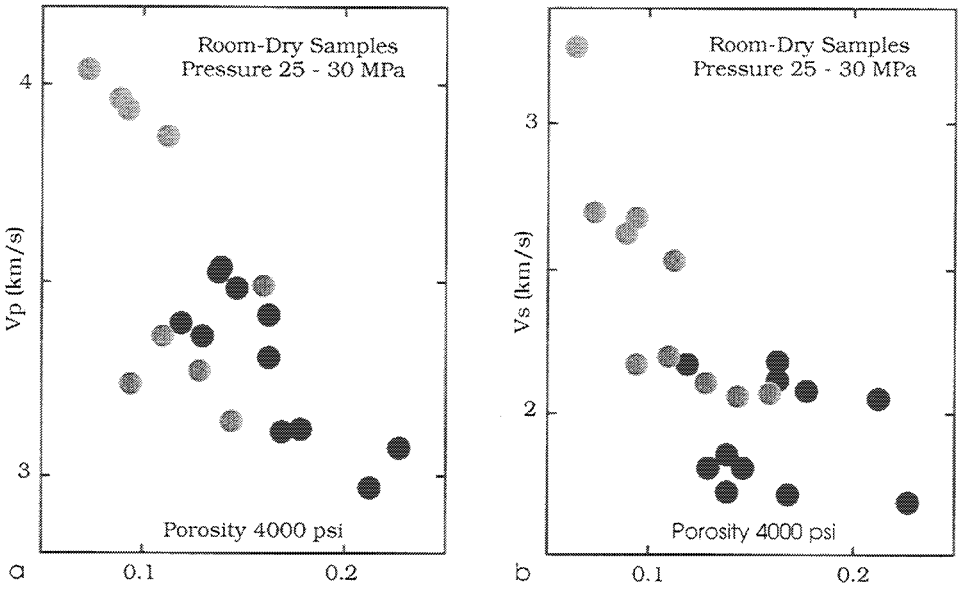

Figure 1.3.7. P- (a) and S-wave (b) velocity versus porosity (at 4000 psi) in the shaley core under examination (red symbols). The data are compared to Han's (1986) shaley sandstone (clay content between 28 and 45%) data (blue symbols). All data are for room-dry samples at 25 - 30 MPa confining or axial pressure. Han's data collected at hydrostatic loading.

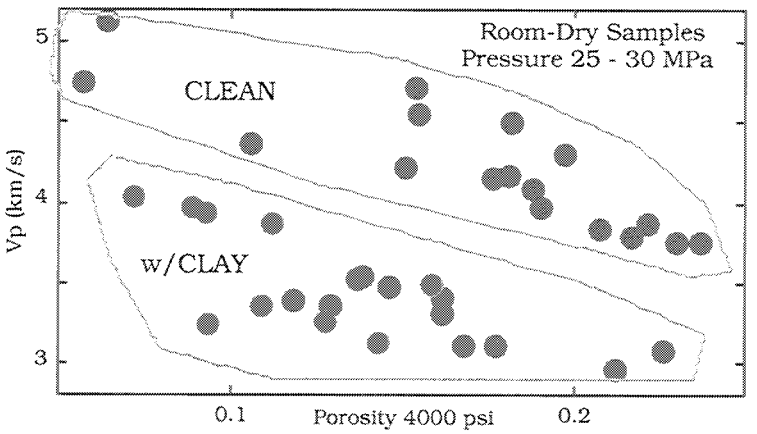

Figure 1.3.8. P-wave velocity versus porosity (at 4000 psi) in the shaley core under examination (red symbols). The data are compared to Han's (1986) shaley sandstone (clay content between 28 and 45%) data (light-blue symbols) and clean sandstone (clay content below 6%) data (blue symbols). All data are for room-dry samples at 25 - 30 MPa confining or axial pressure. Han's data collected at hydrostatic loading.

1.4. Static Measurement Analysis

The static test results for the six separate locations of the core are displayed in Figures 1.4.1 – 1.4.6. In these graphs, the axial and radial deformation is plotted versus the axial stress. The conditions of the experiment are shown in the graphs. The elastic moduli calculated from the static tests are shown in Figures 1.4.7 – 1.4.23. They are compared to the dynamic moduli in Figures 1.4.24 – 1.4.29.

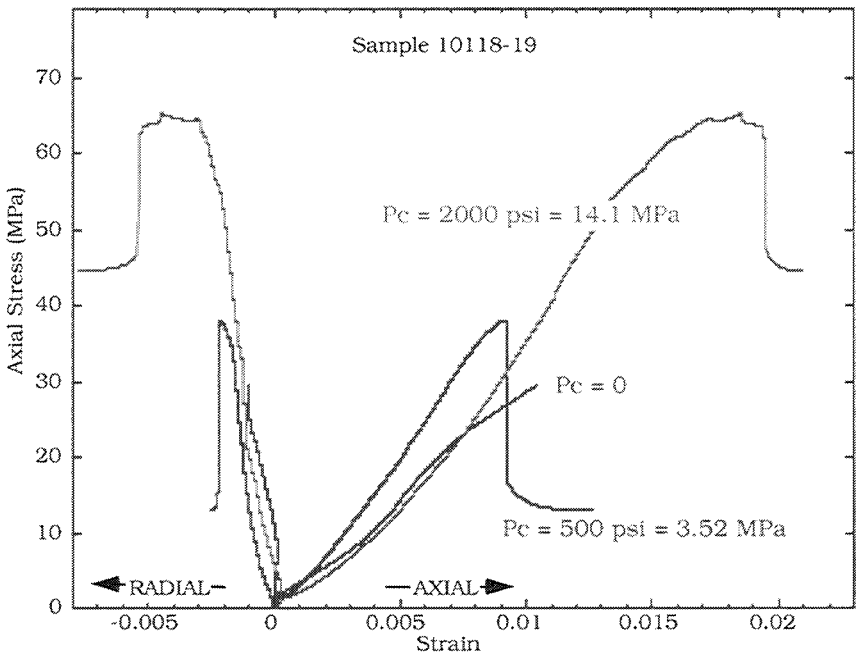

Figure 1.4.1. Stress-strain curves for the 10118-19 plugs.

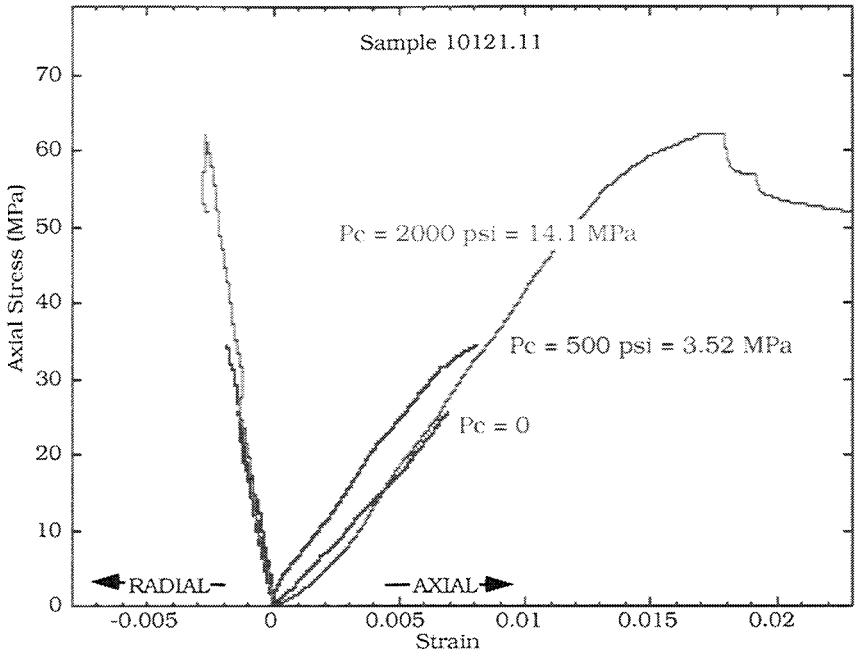

Figure 1.4.2. Stress-strain curves for the 10121-22 plugs.

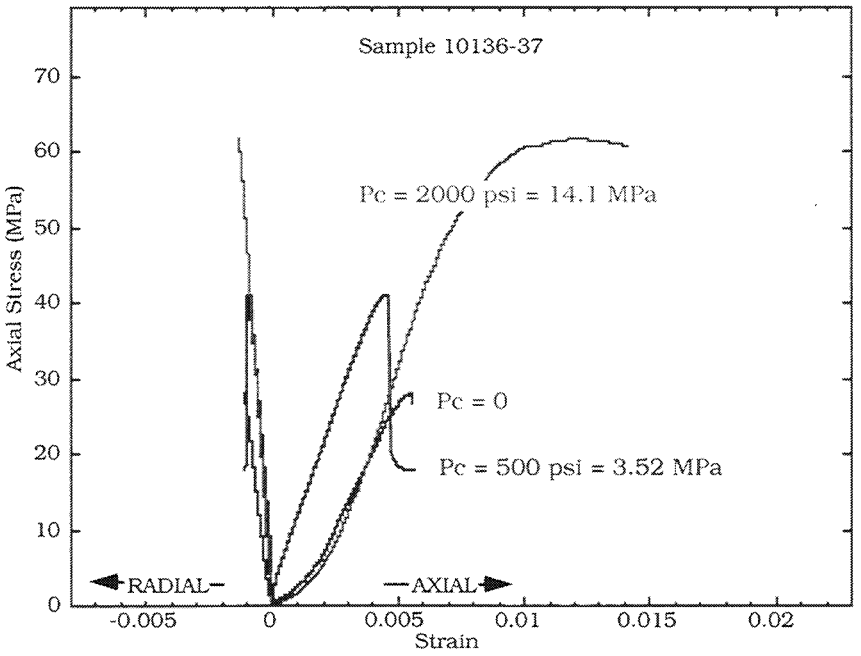

Figure 1.4.3. Stress-strain curves for the 10136-37 plugs.

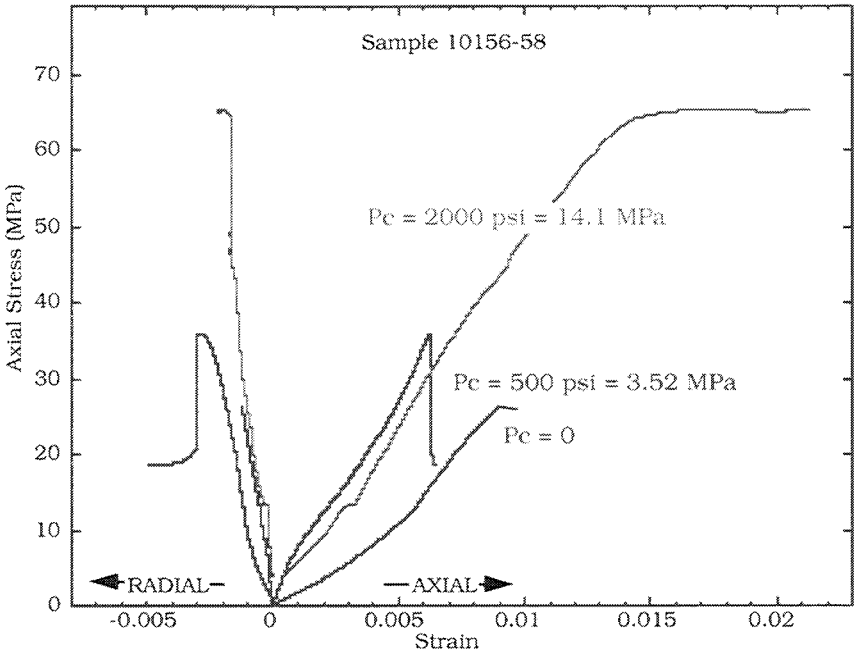

Figure 1.4.4. Stress-strain curves for the 10156-58 plugs.

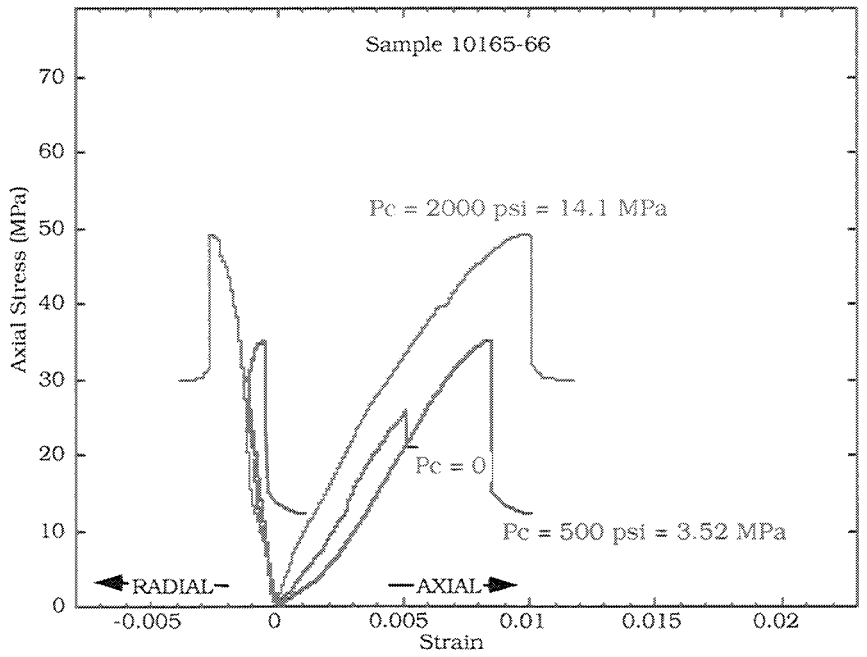

Figure 1.4.5. Stress-strain curves for the 10165-66 plugs.

Figure 1.4.5. Stress-strain curves for the 10165-66 plugs.

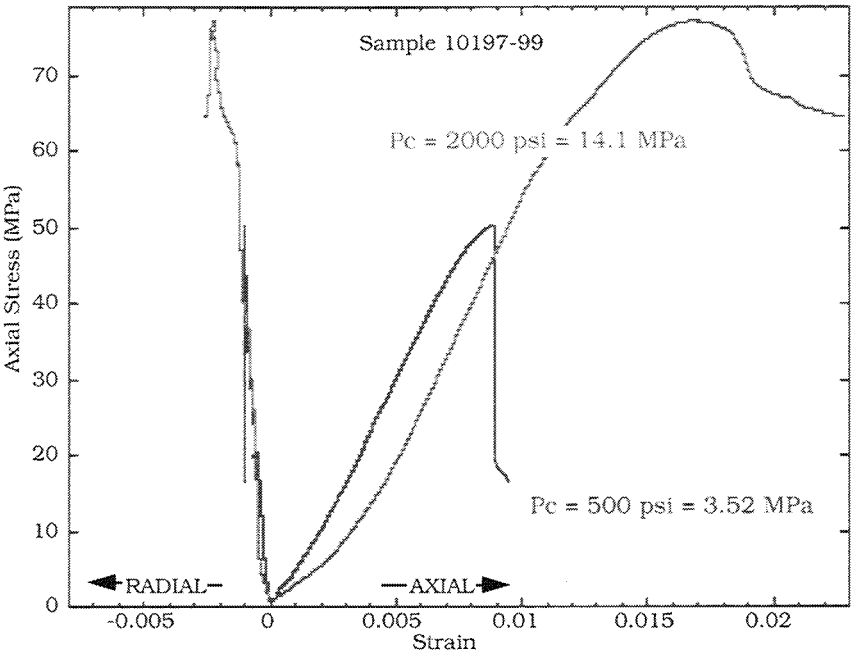

Figure 1.4.6. Stress-strain curves for the 10197-99 plugs.

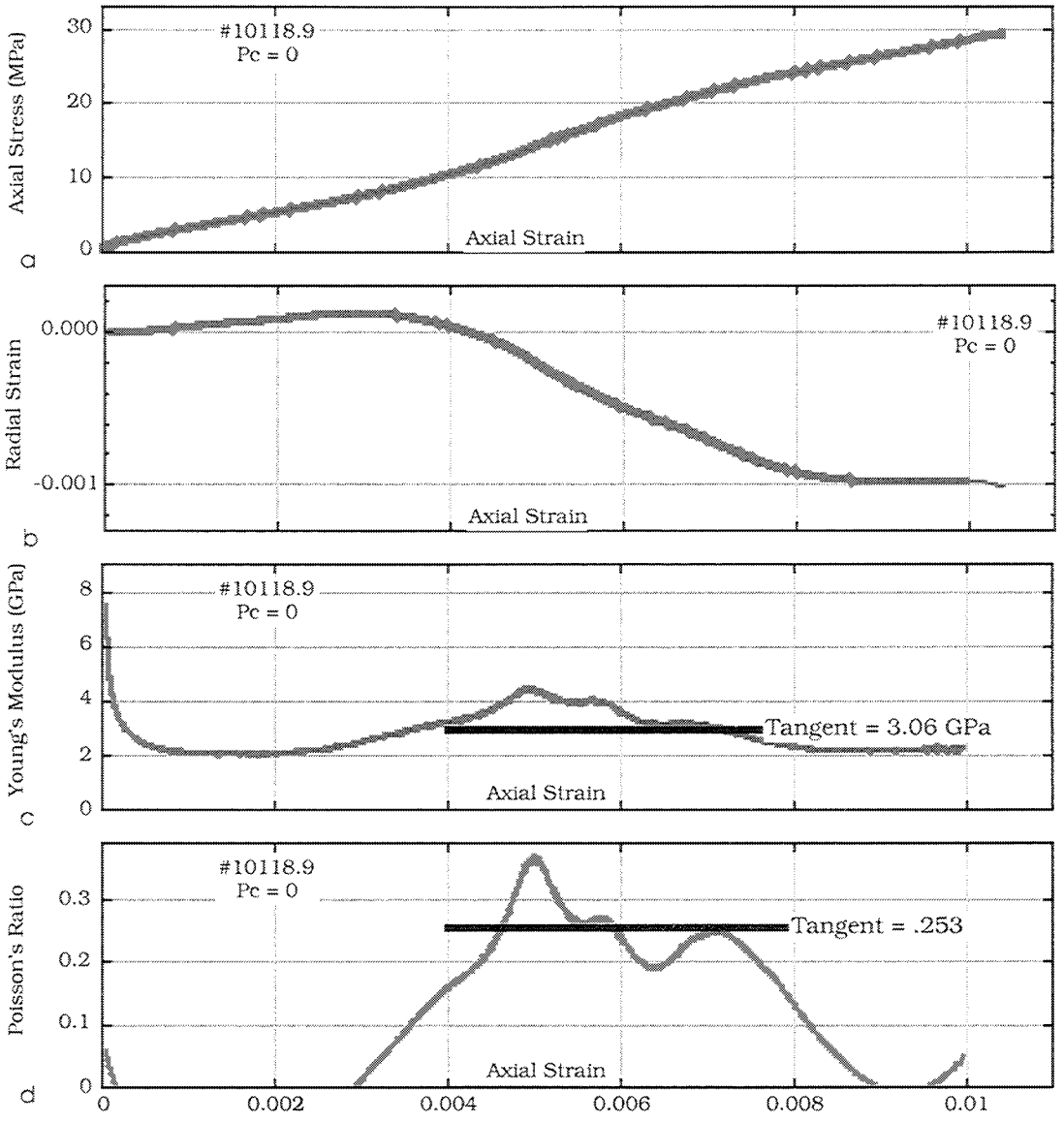

Figure 1.4.7. Loading curves and Young's modulus and Poisson's ratio for plug 10118.9.

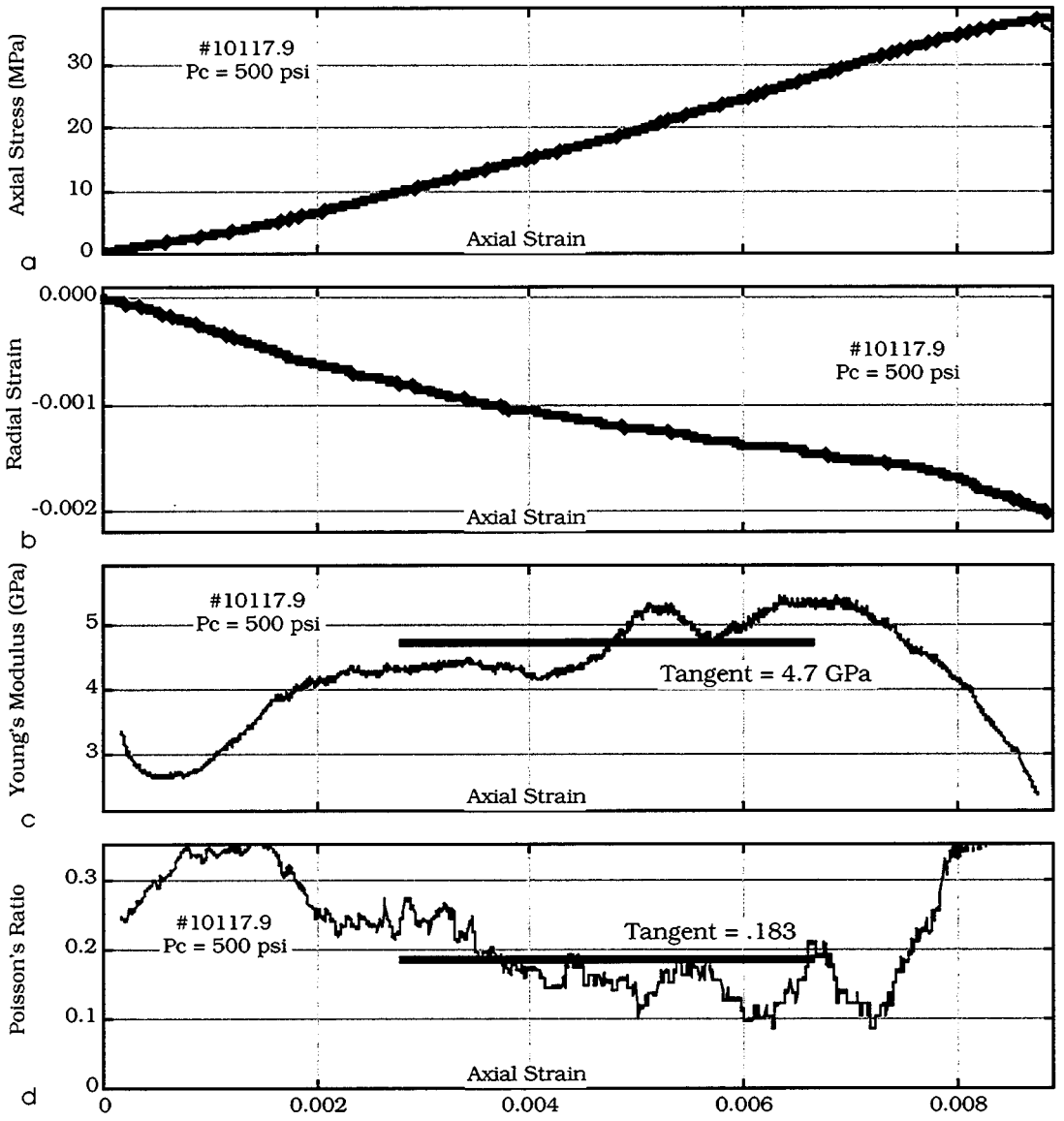

Figure 1.4.8. Loading curves and Young's modulus and Poisson's ratio for plug 10117.9.

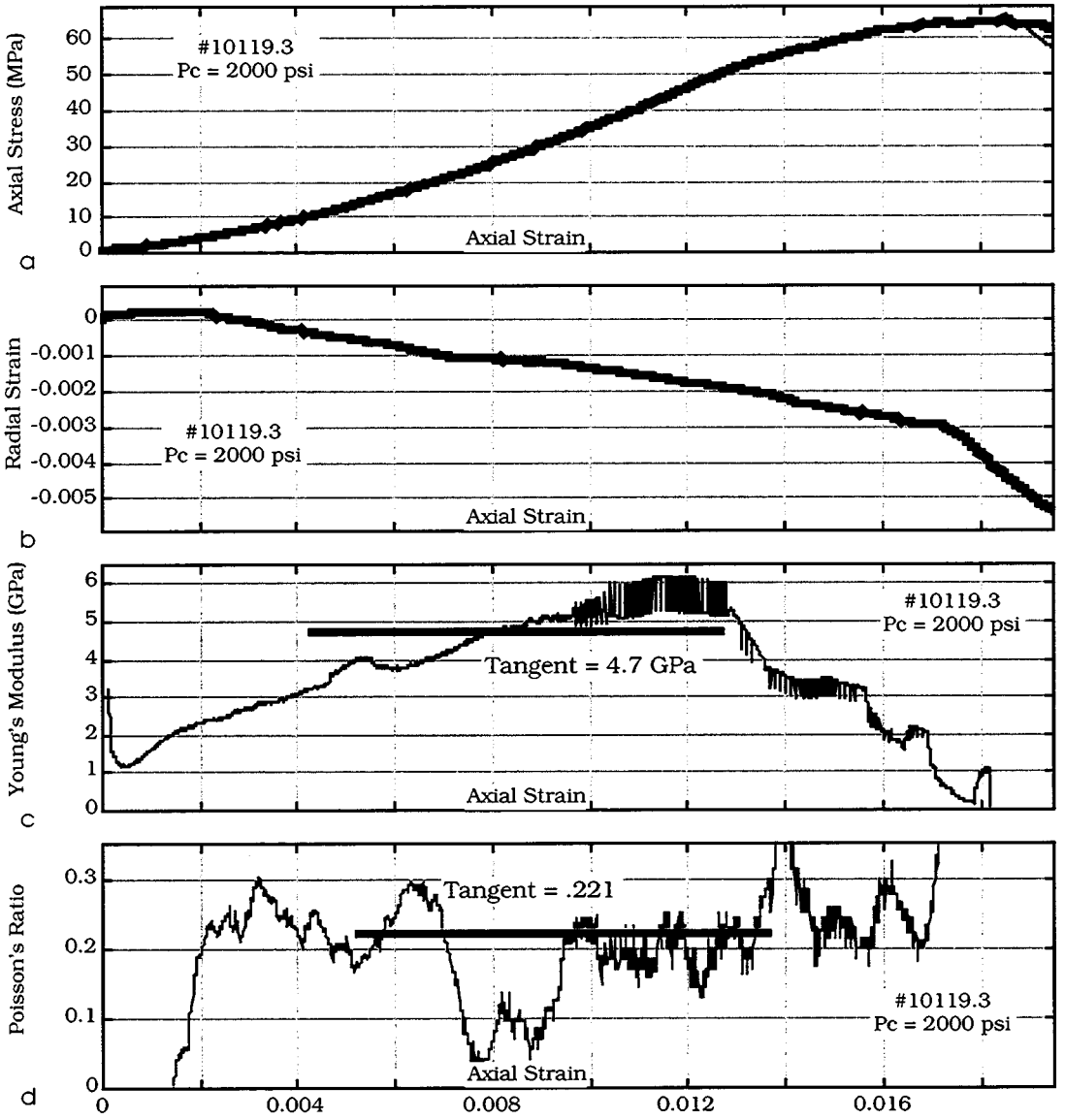

Figure 1.4.9. Loading curves and Young's modulus and Poisson's ratio for plug 10119.3.

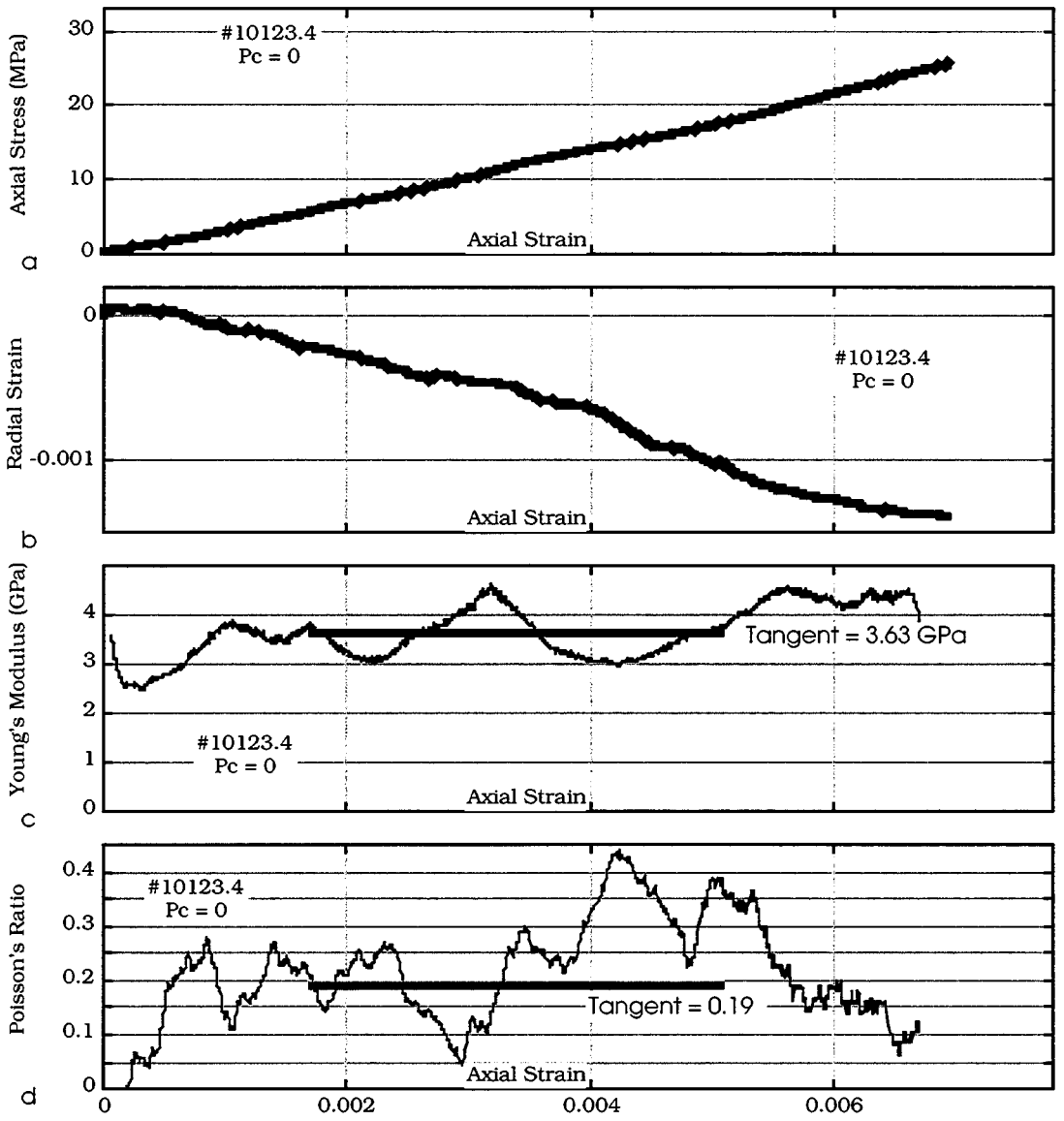

Figure 1.4.10. Loading curves and Young's modulus and Poisson's ratio for plug 10123.4.

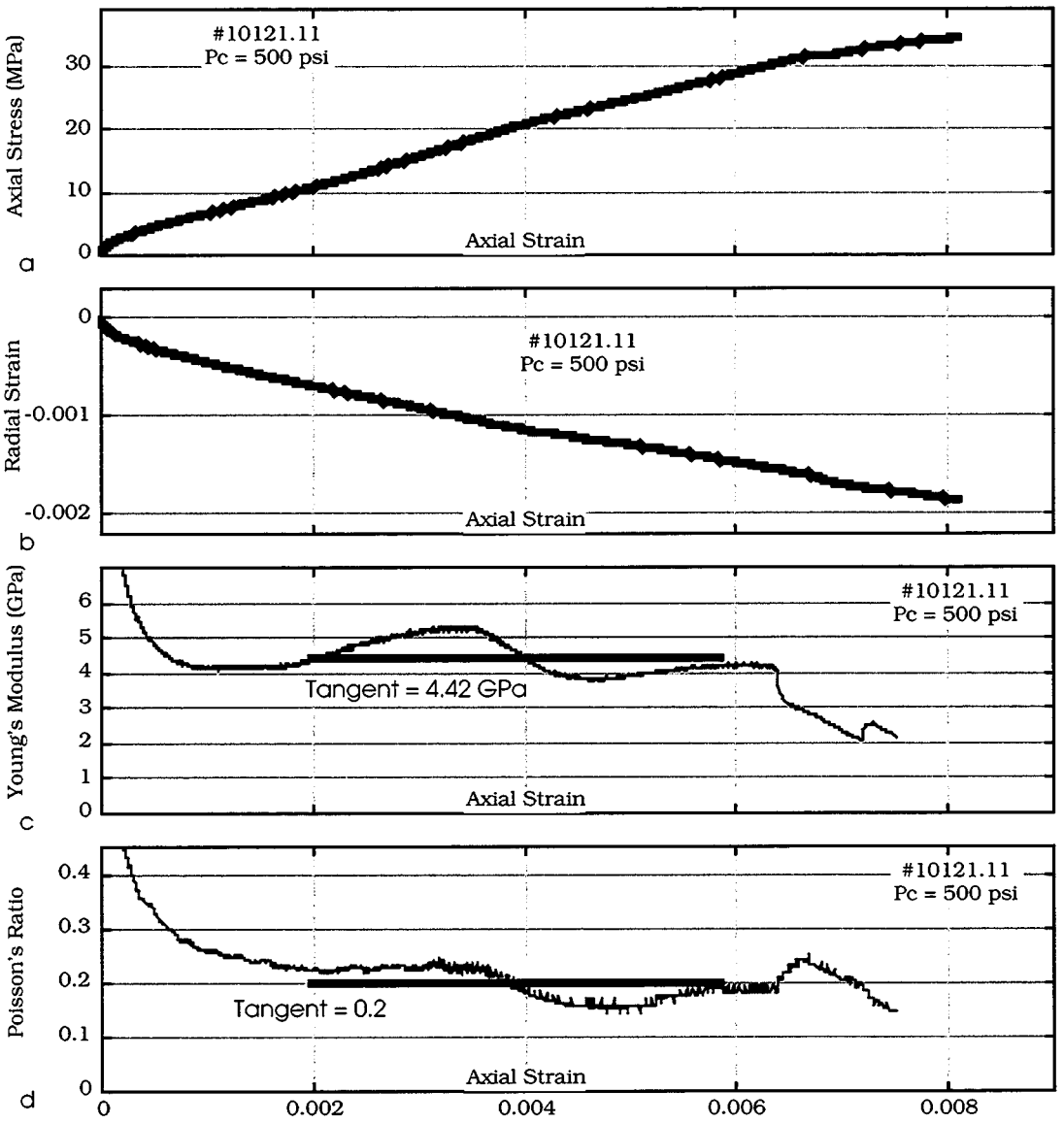

Figure 1.4.11. Loading curves and Young's modulus and Poisson's ratio for plug 10121.11.

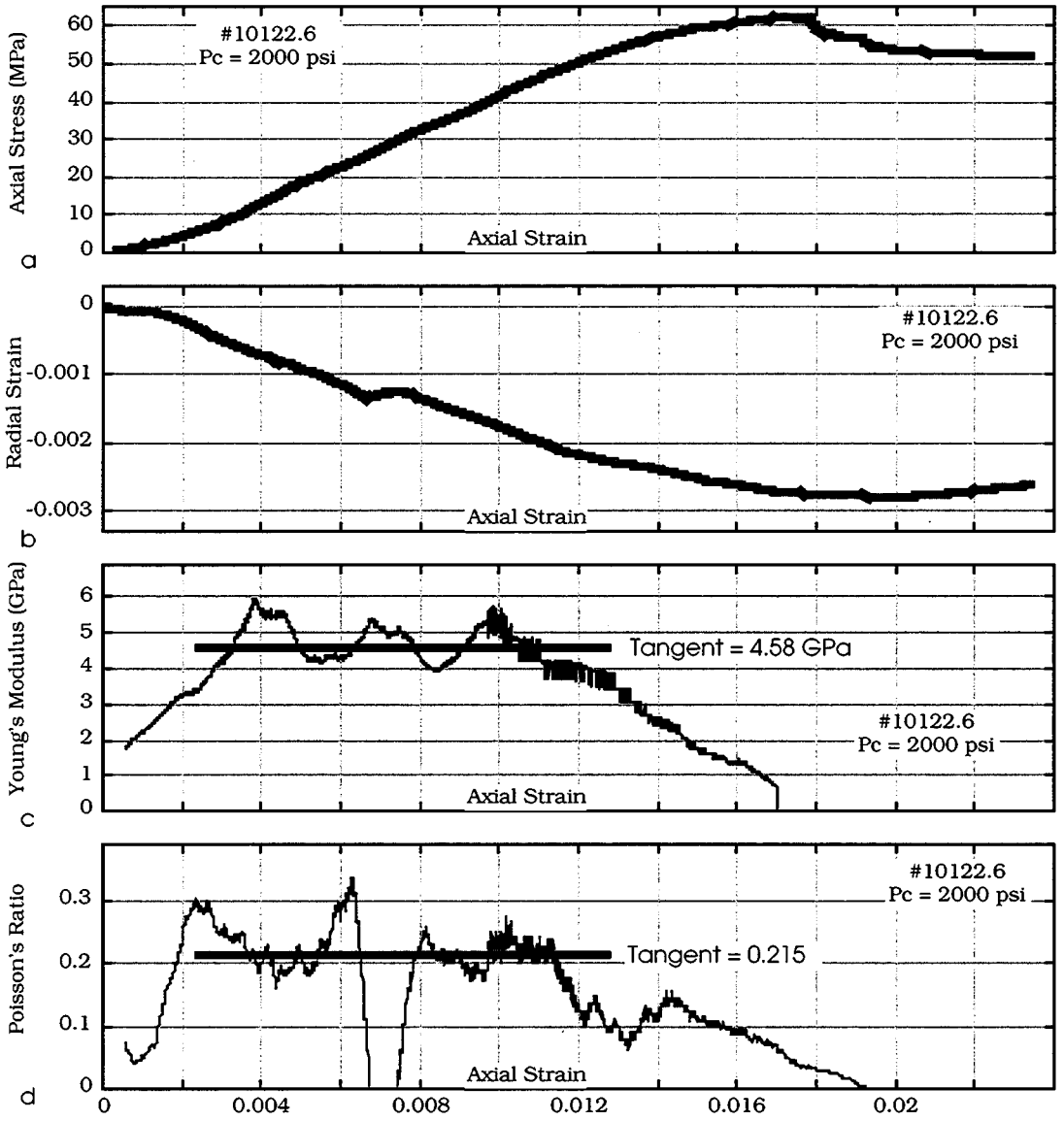

Figure 1.4.12. Loading curves and Young's modulus and Poisson's ratio for plug 10122.6.

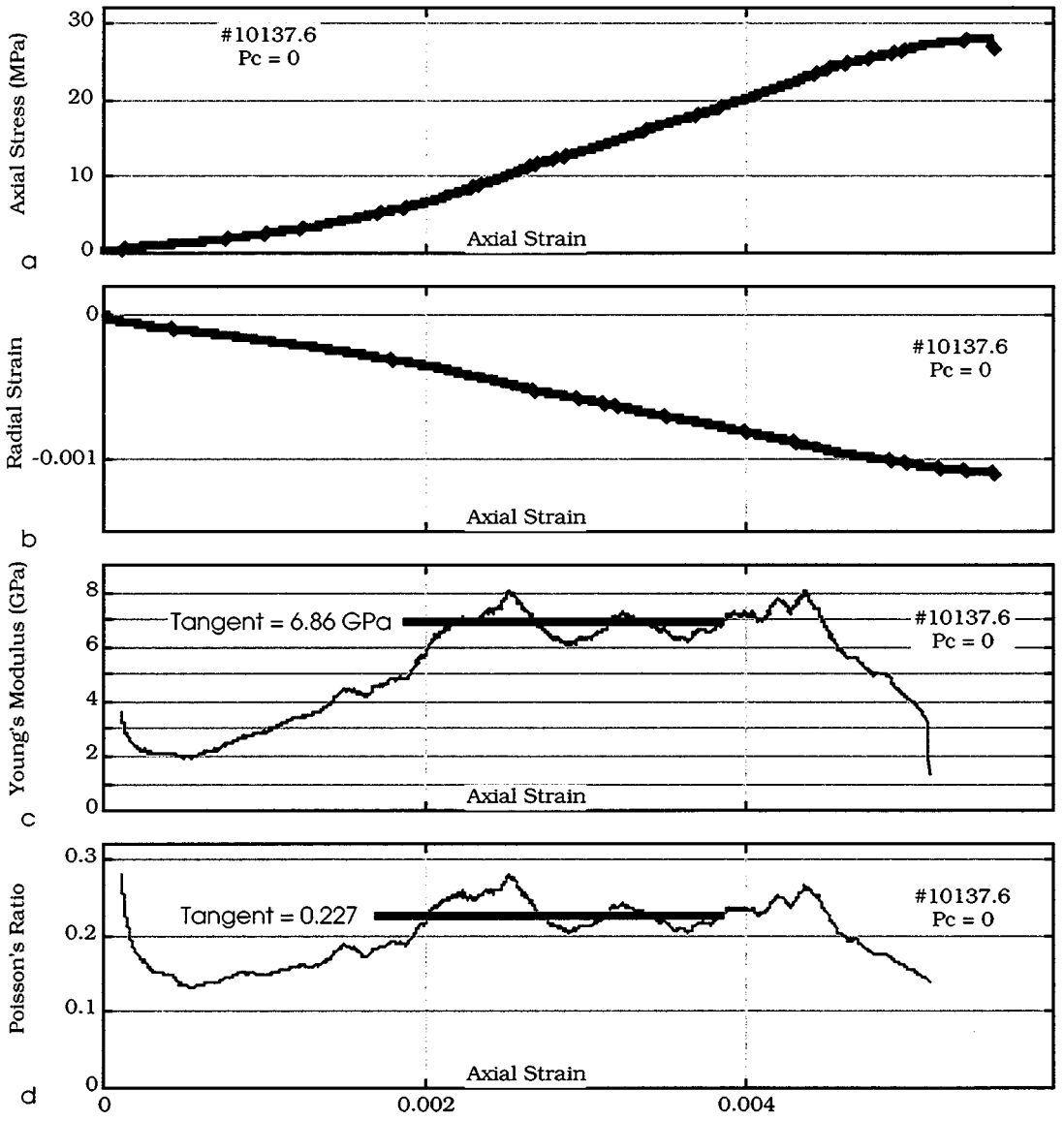

Figure 1.4.13. Loading curves and Young's modulus and Poisson's ratio for plug 10137.6.

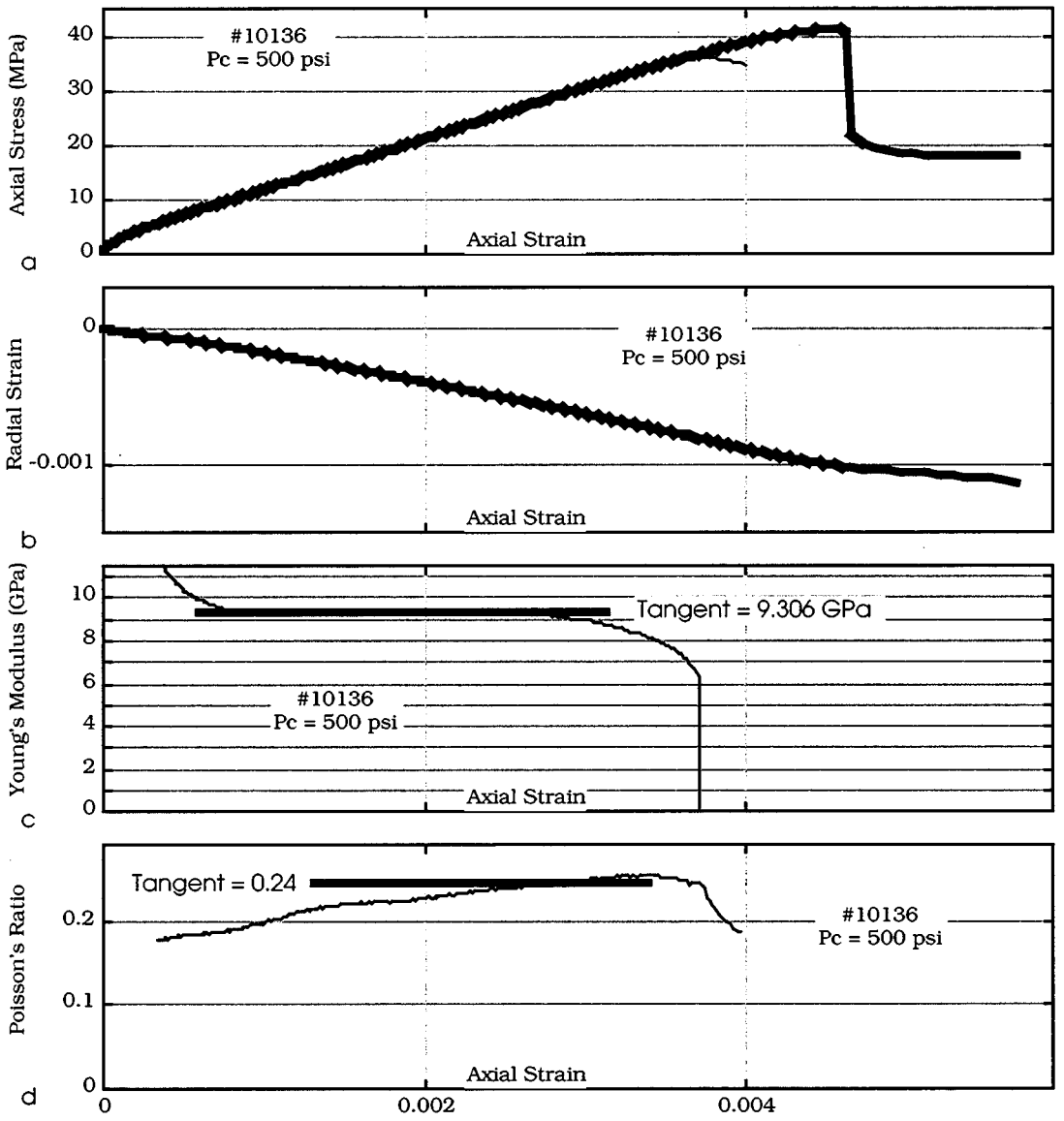

Figure 1.4.14. Loading curves and Young's modulus and Poisson's ratio for plug 10136.

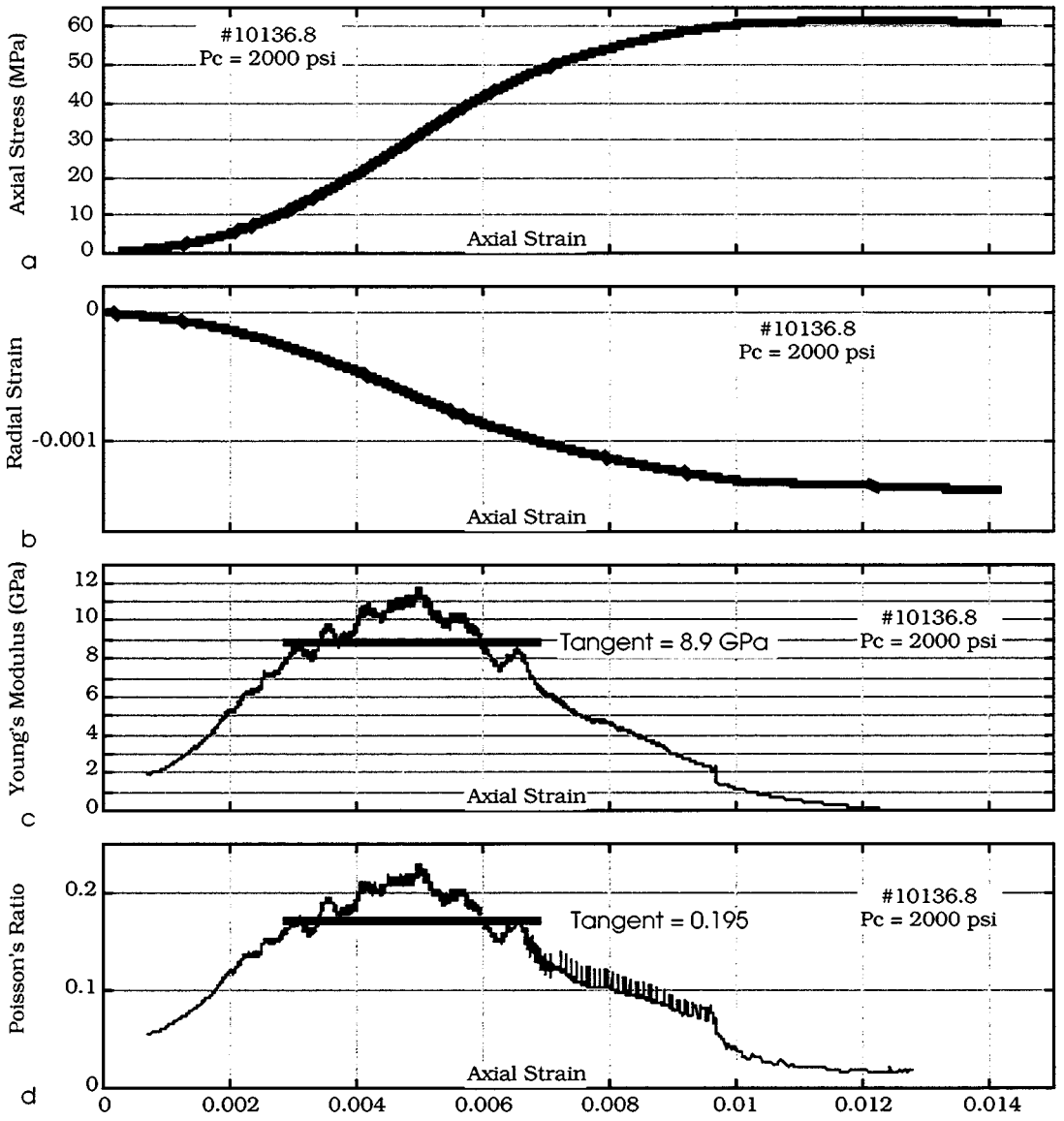

Figure 1.4.15. Loading curves and Young's modulus and Poisson's ratio for plug 10136.8.

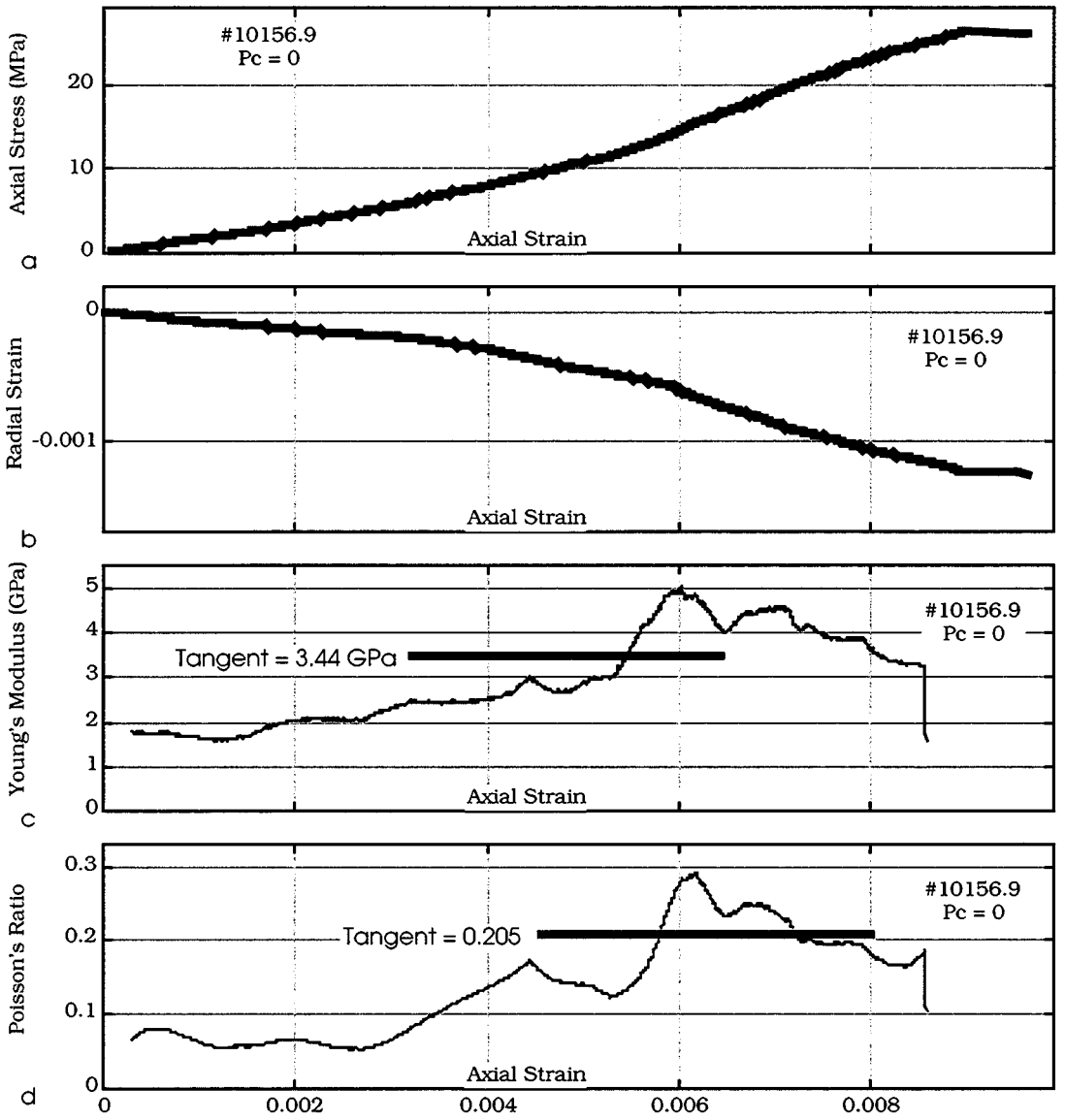

Figure 1.4.16. Loading curves and Young's modulus and Poisson's ratio for plug 10156.9.

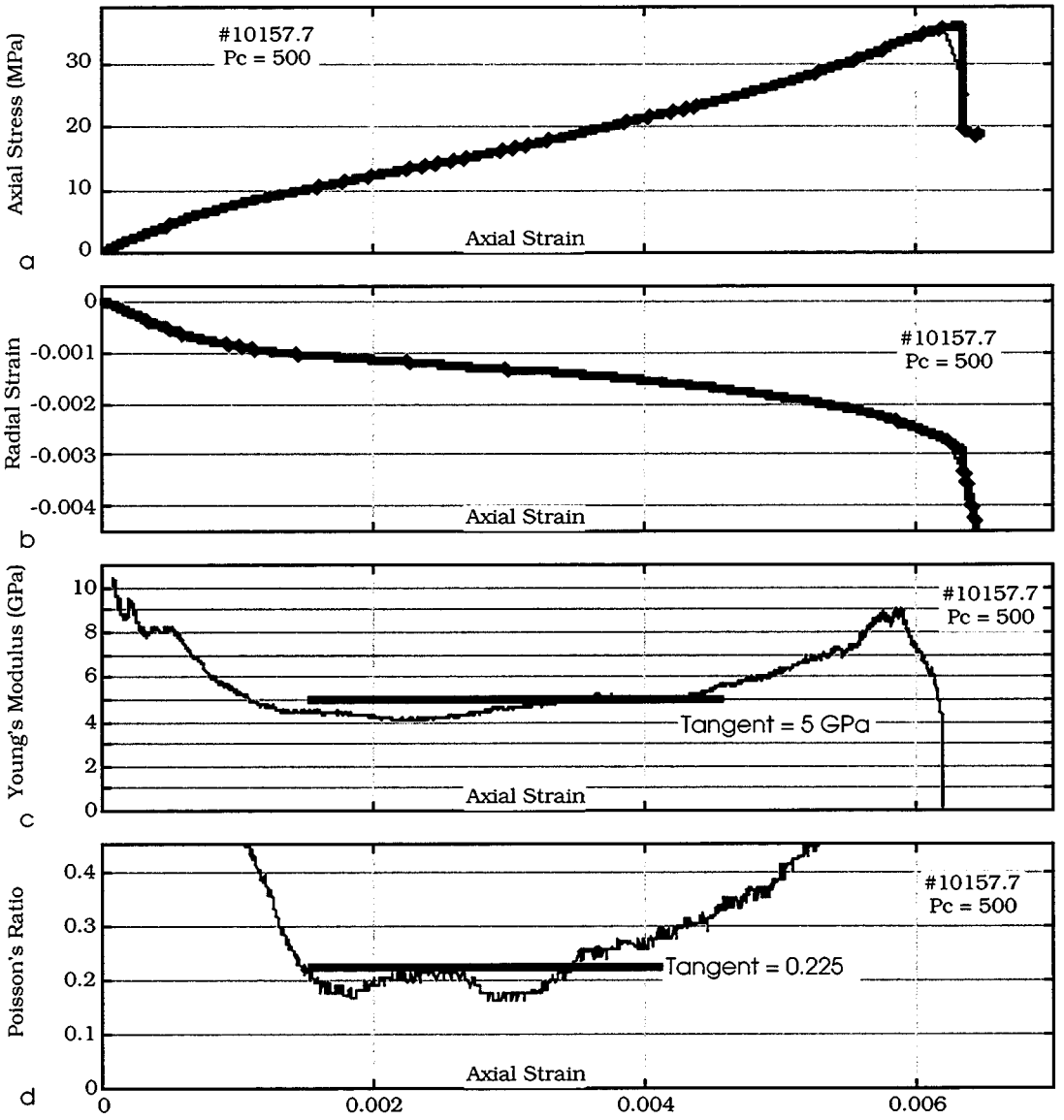

Figure 1.4.17. Loading curves and Young's modulus and Poisson's ratio for plug 10157.7.

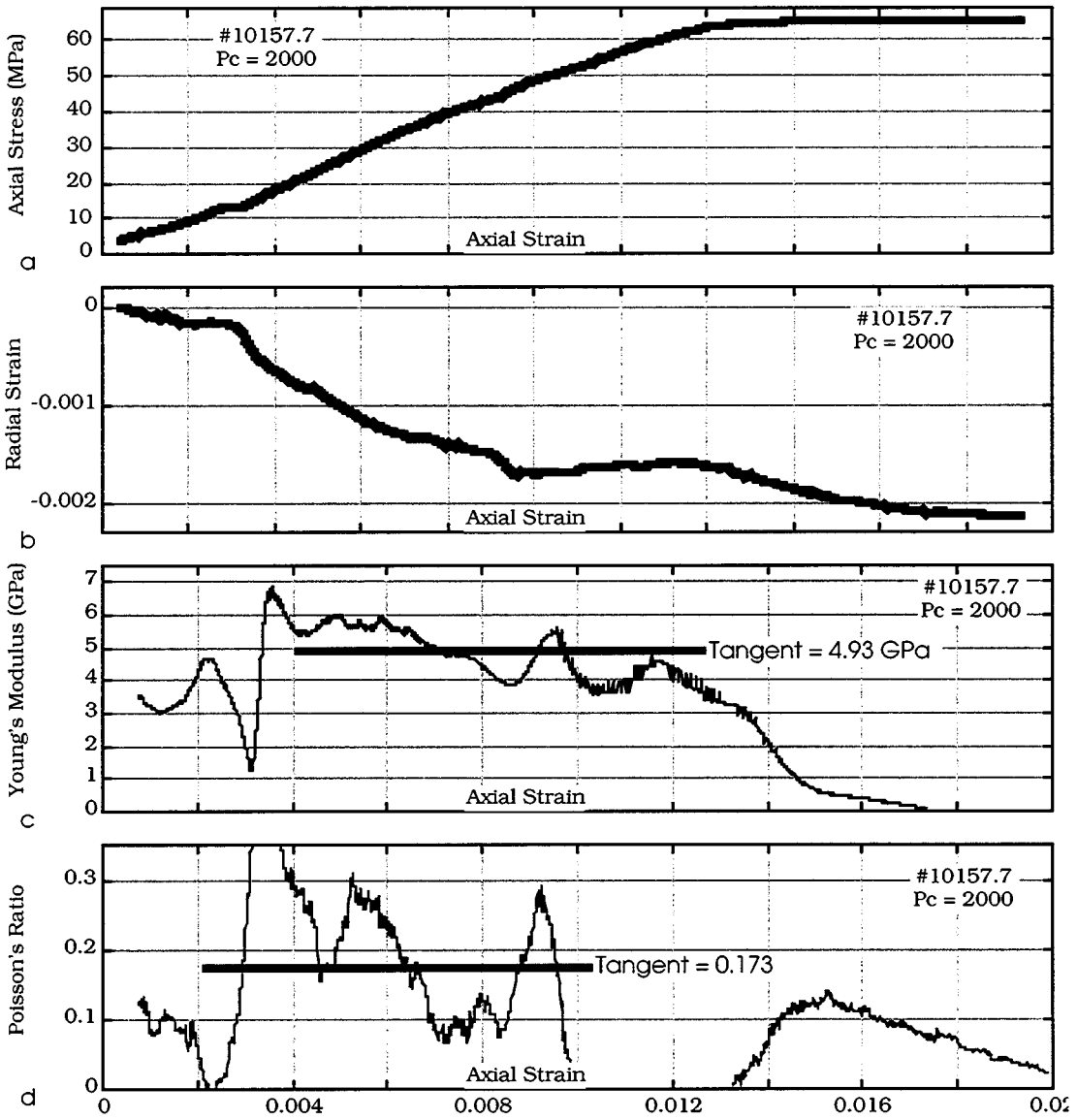

Figure 1.4.18. Loading curves and Young's modulus and Poisson's ratio for plug 10157.7.

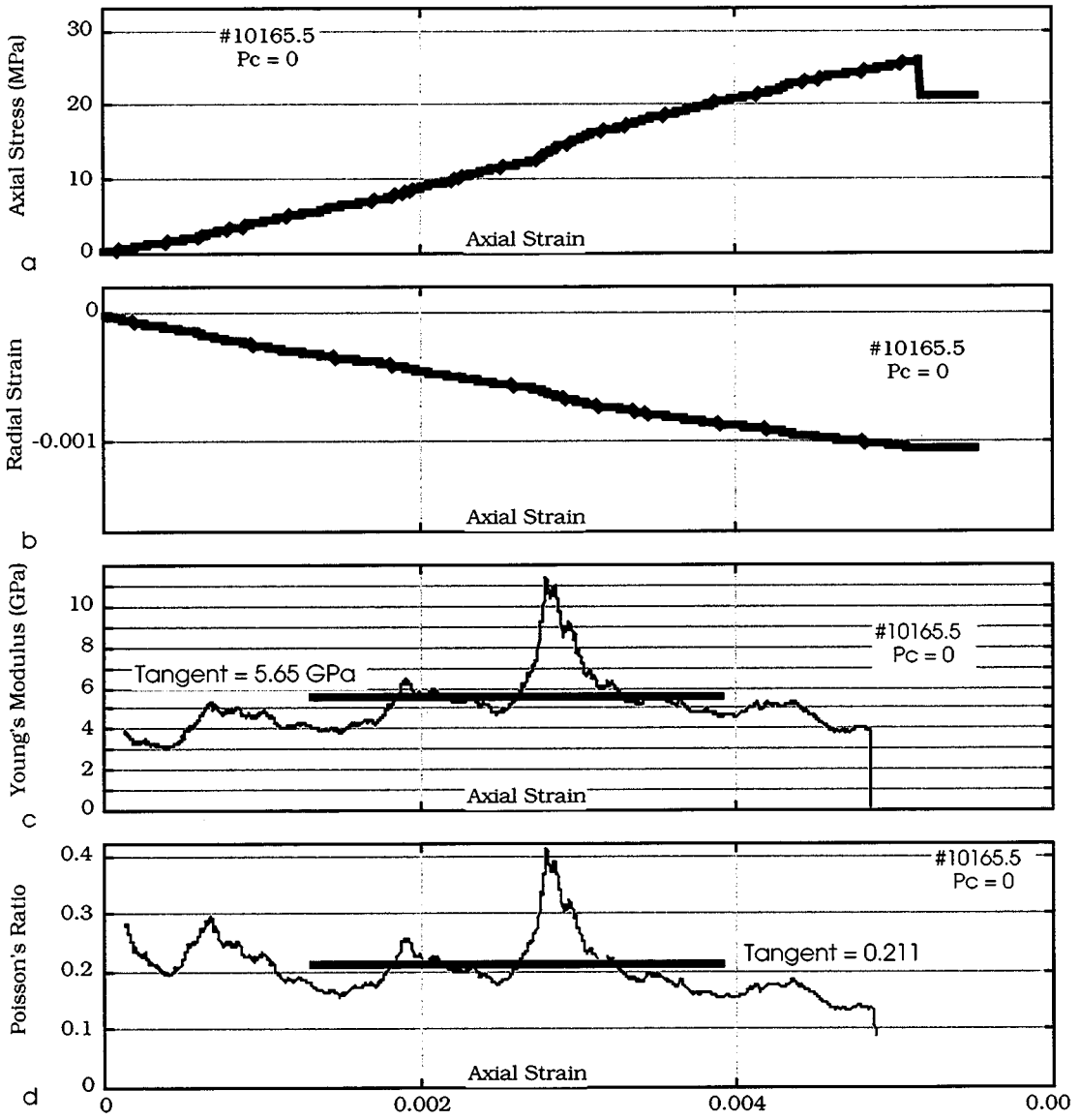

Figure 1.4.19. Loading curves and Young's modulus and Poisson's ratio for plug 10165.5.

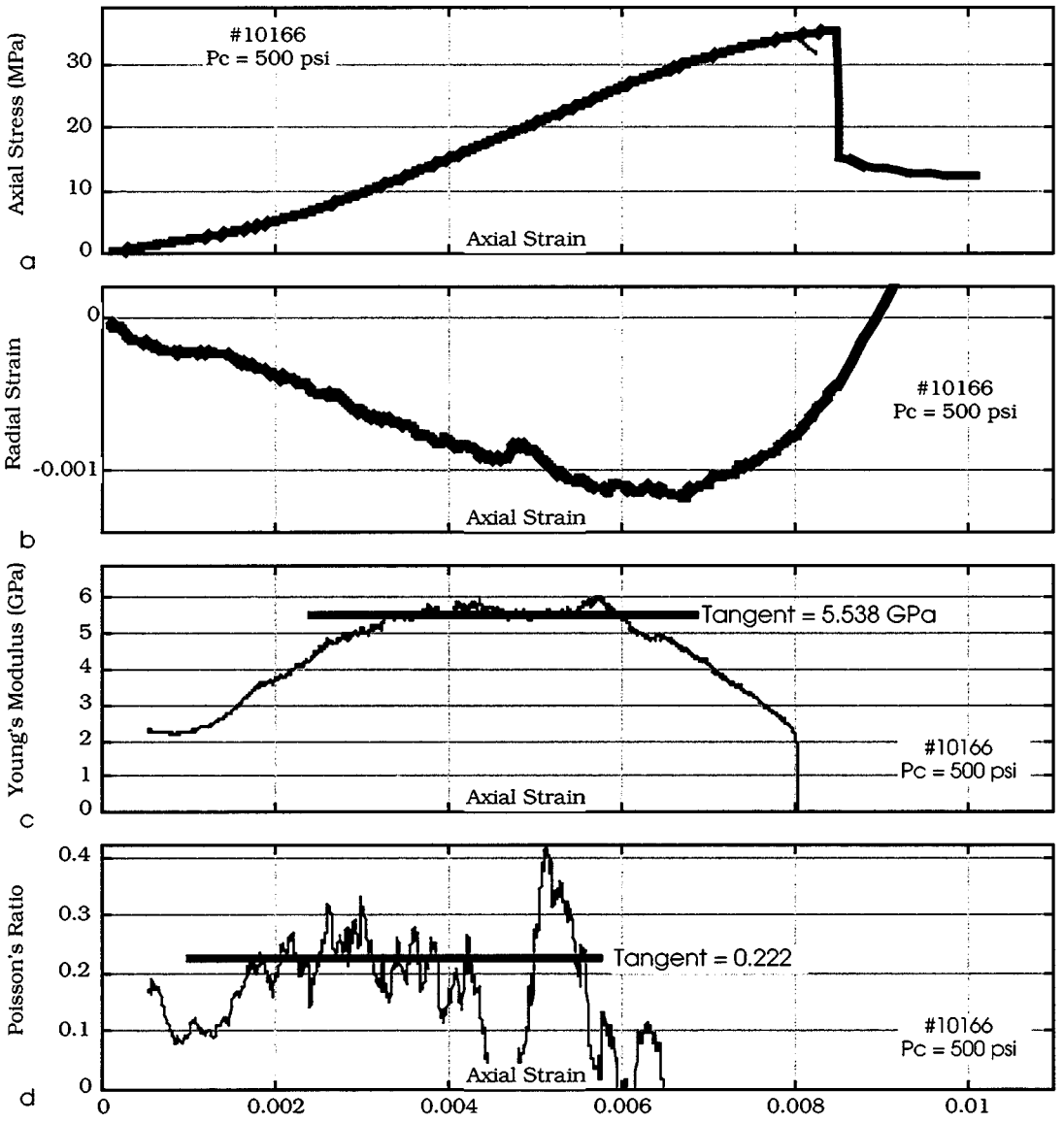

Figure 1.4.20. Loading curves and Young's modulus and Poisson's ratio for plug 10166.

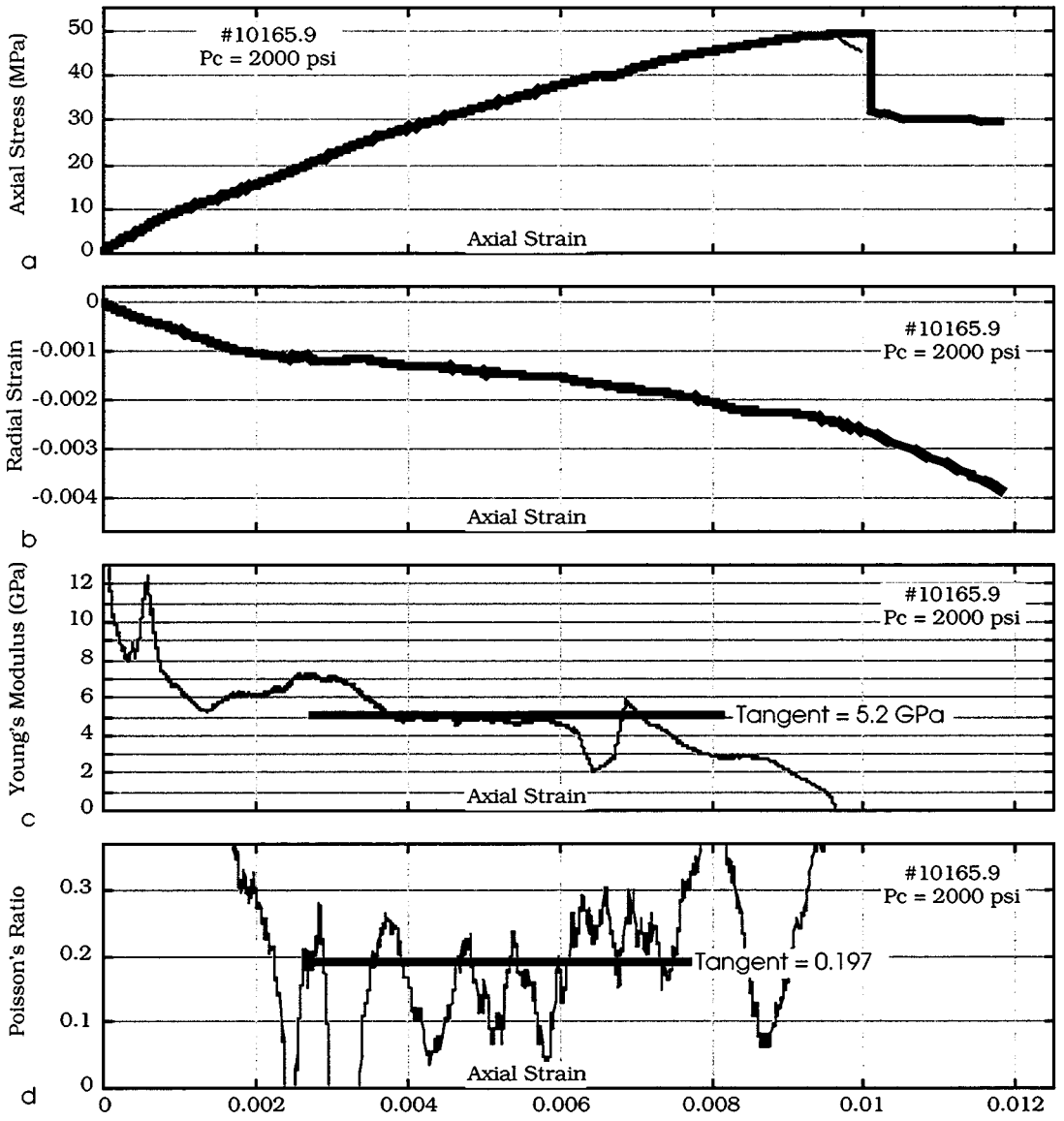

Figure 1.4.21. Loading curves and Young's modulus and Poisson's ratio for plug 10165.9.

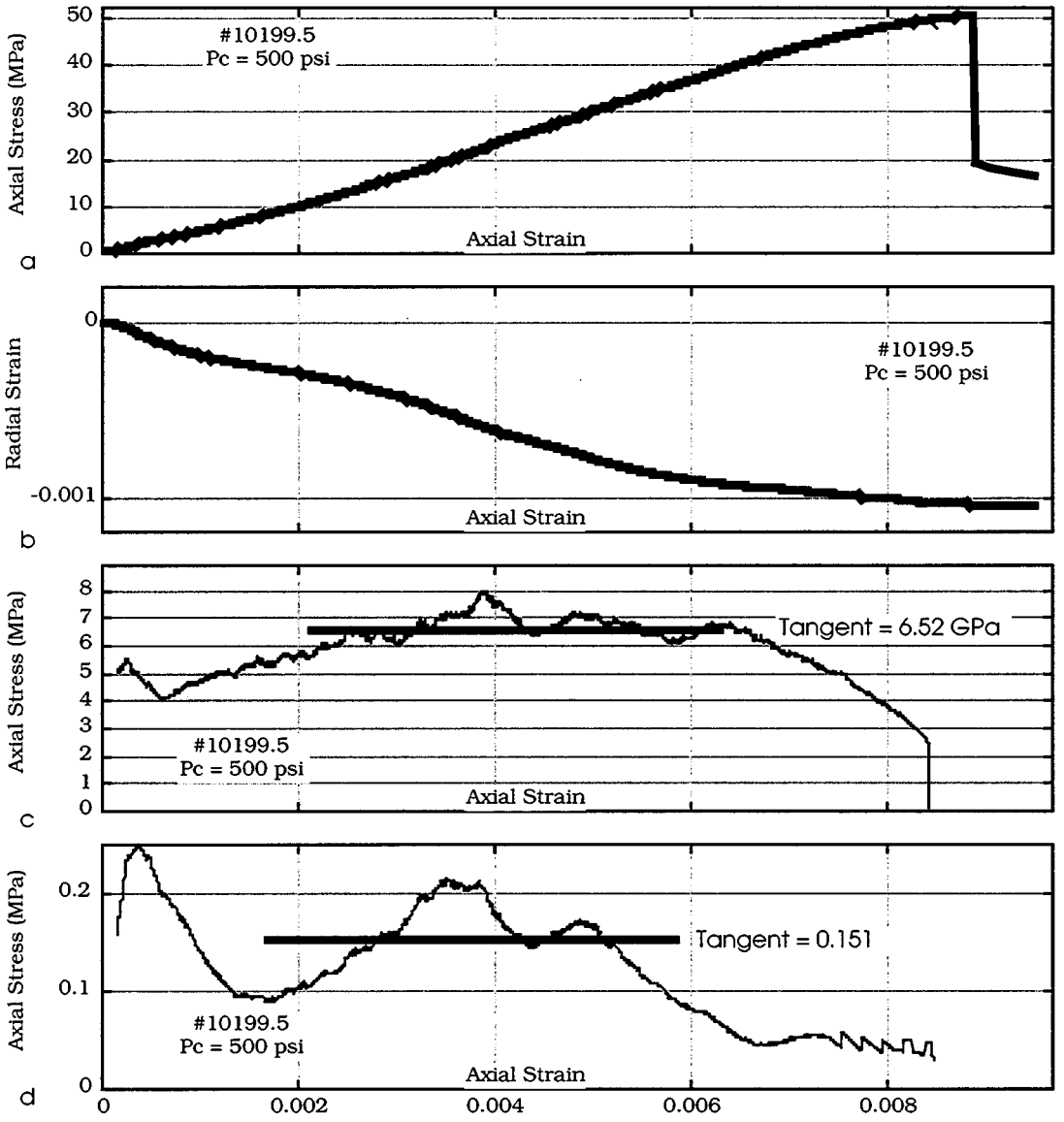

Figure 1.4.22. Loading curves and Young's modulus and Poisson's ratio for plug 10199.5.

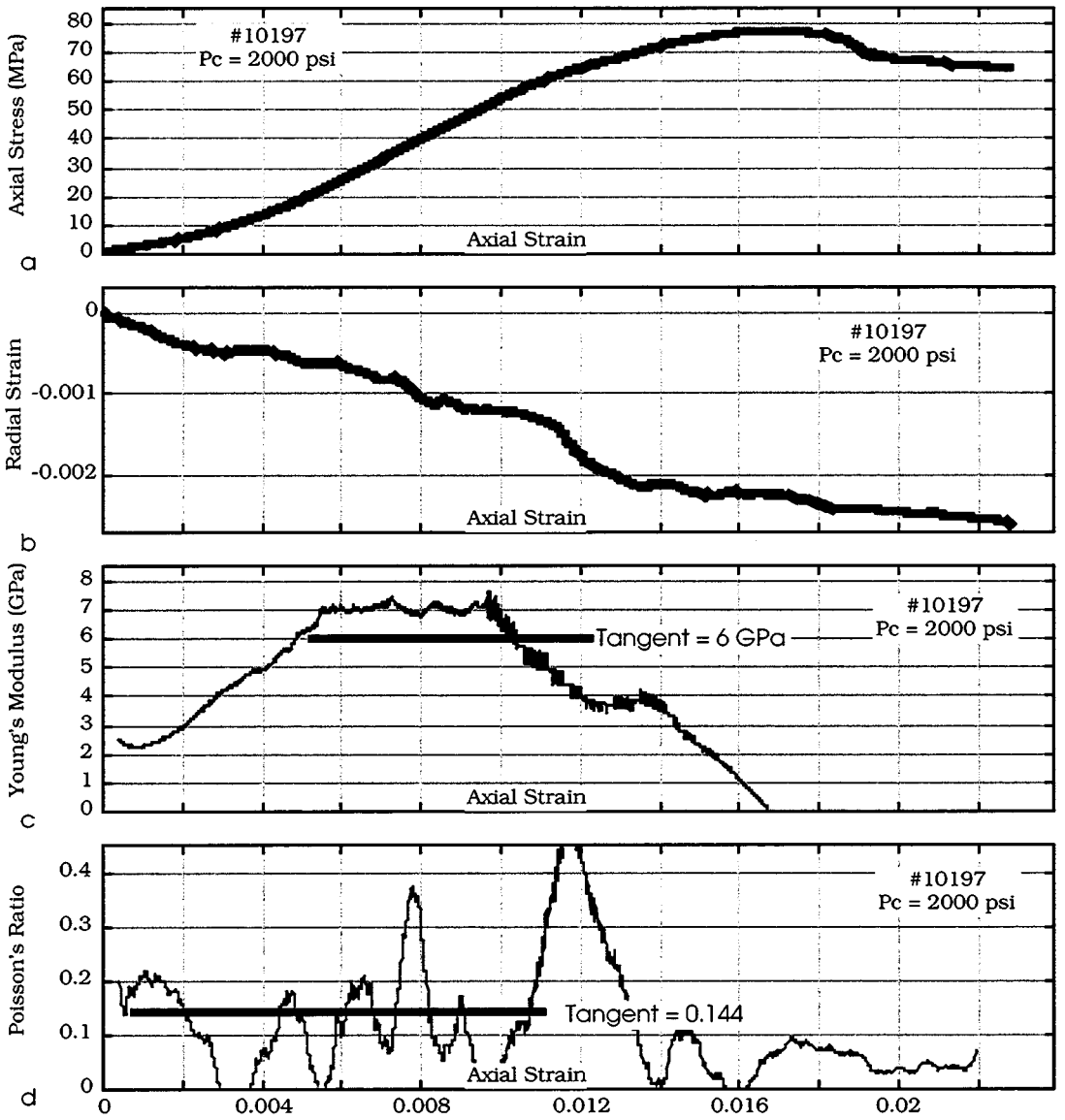

Figure 1.4.23. Loading curves and Young's modulus and Poisson's ratio for plug 10197.

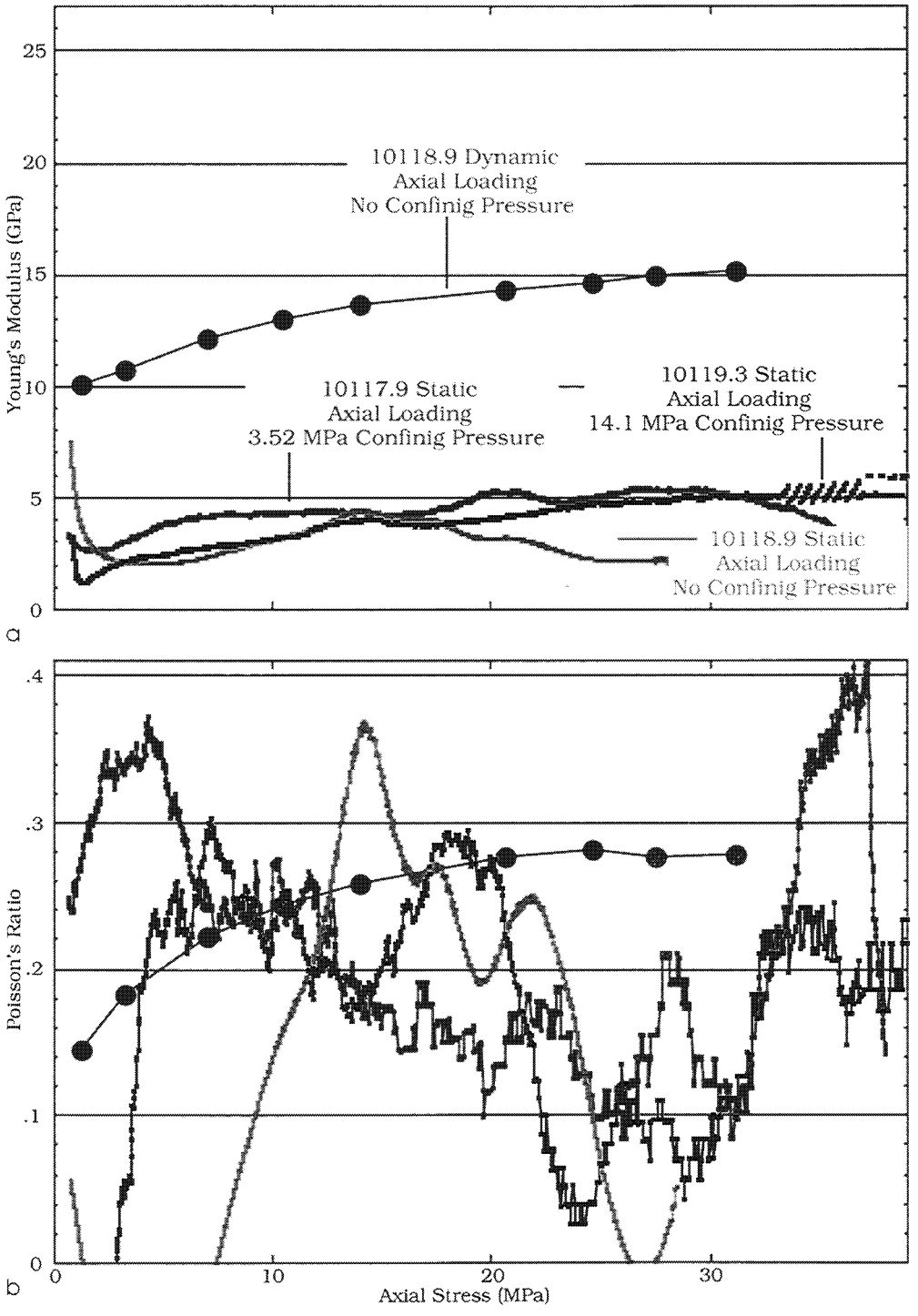

Figure 1.4.24. Young's modulus and Poisson's ratio versus stress for the 10118 group.

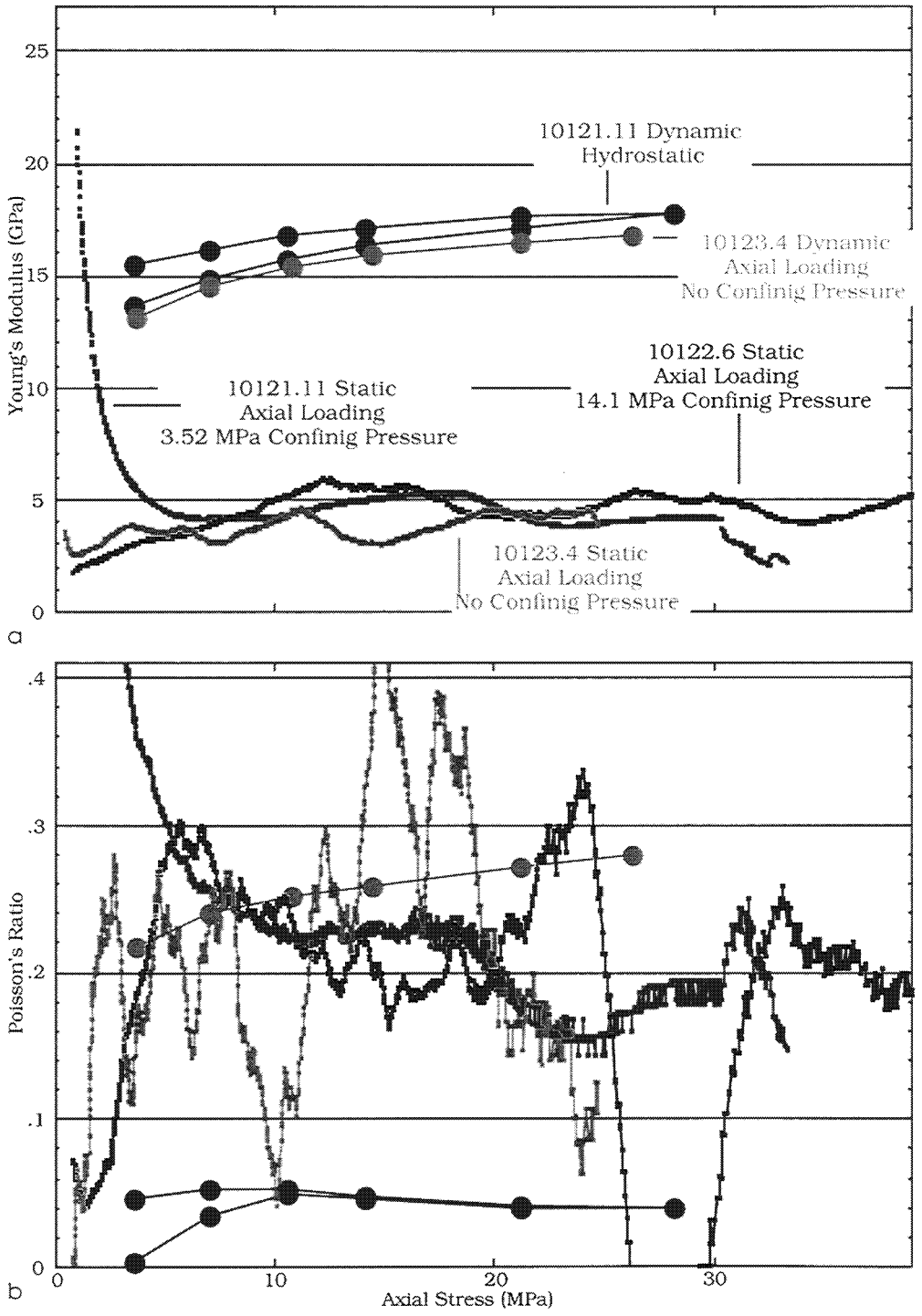

Figure 1.4.25. Young's modulus and Poisson's ratio versus stress for the 10121 group.

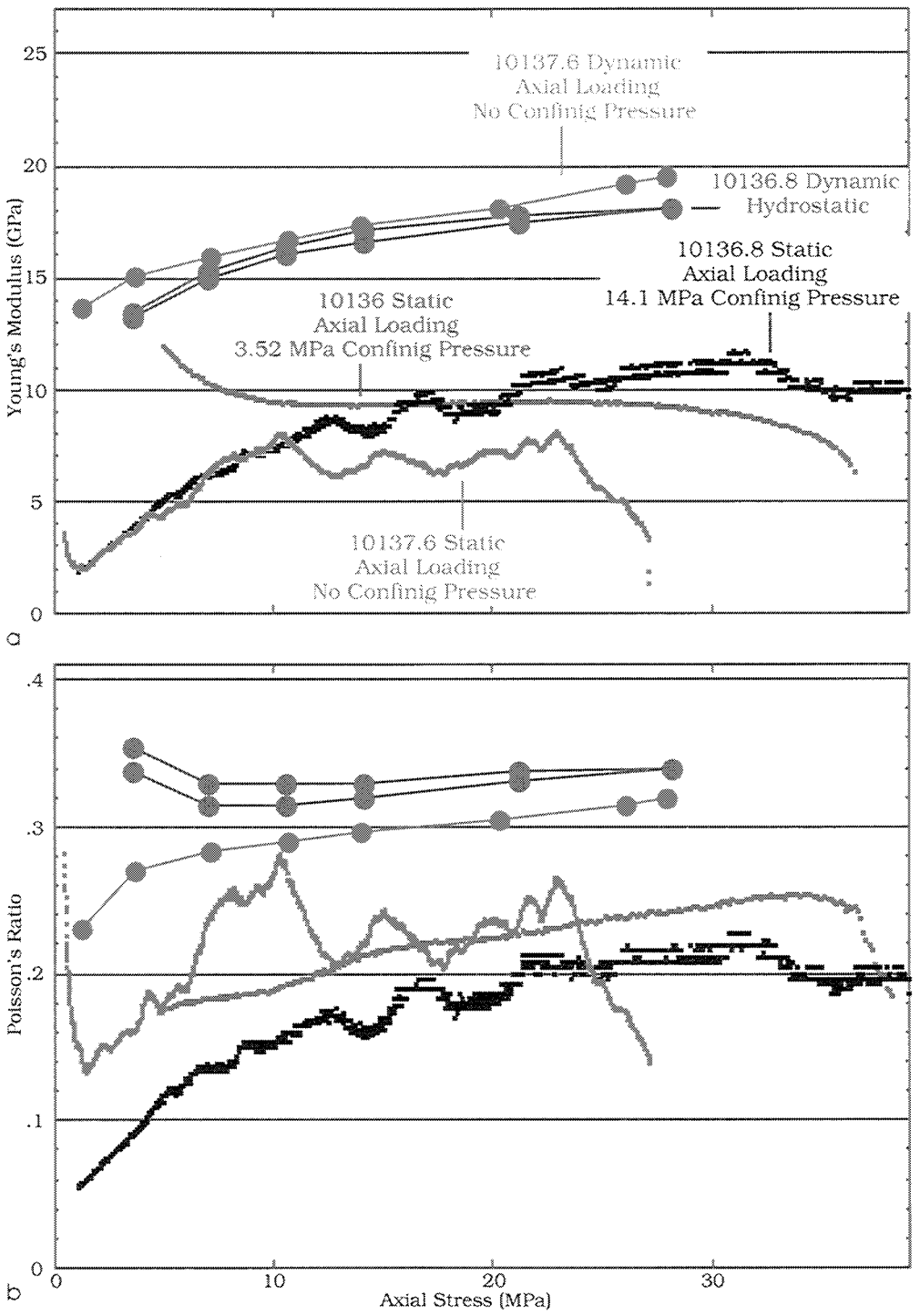

Figure 1.4.26. Young's modulus and Poisson's ratio versus stress for the 10136 group.

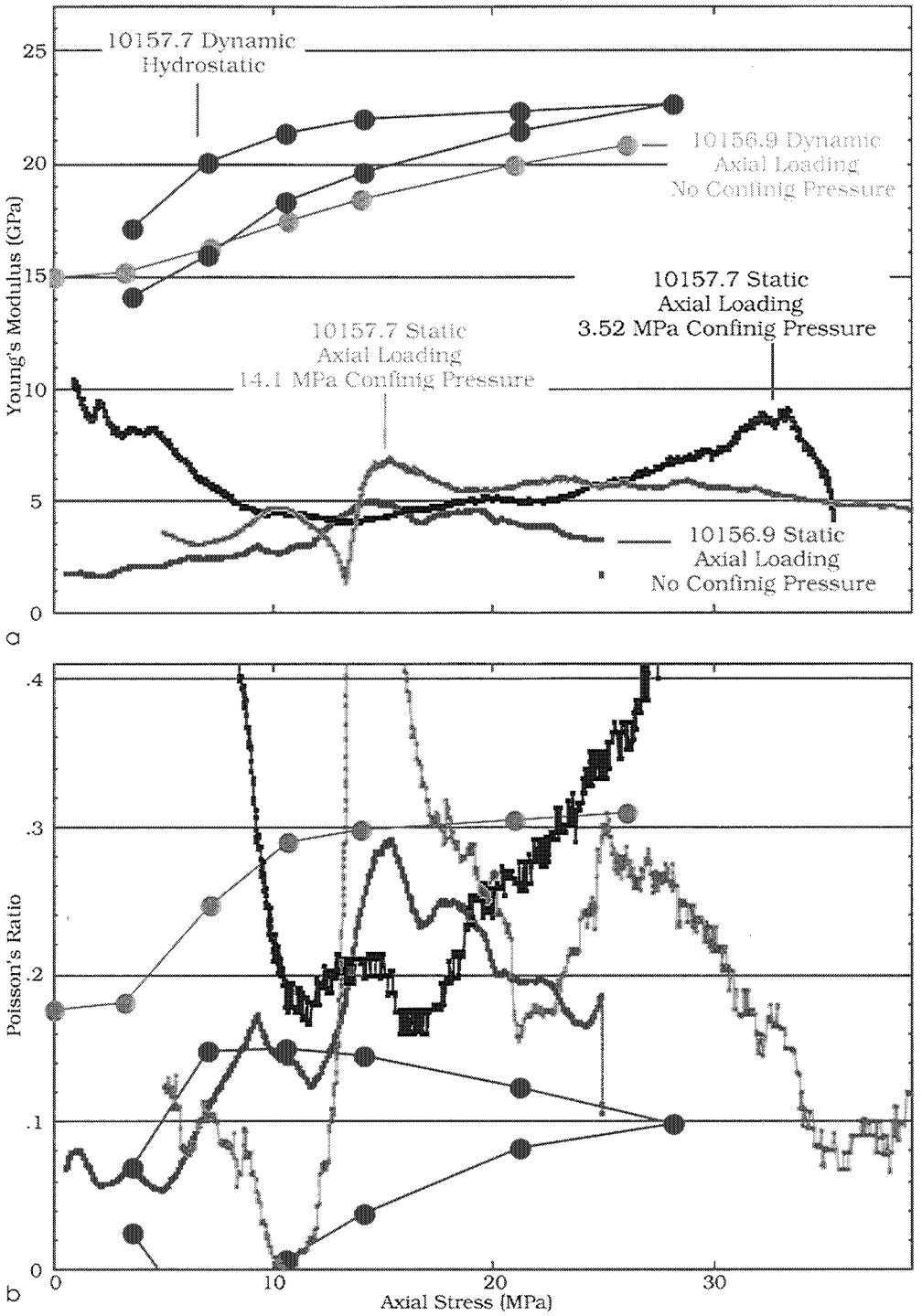

Figure 1.4.27. Young's modulus and Poisson's ratio versus stress for the 10157 group.

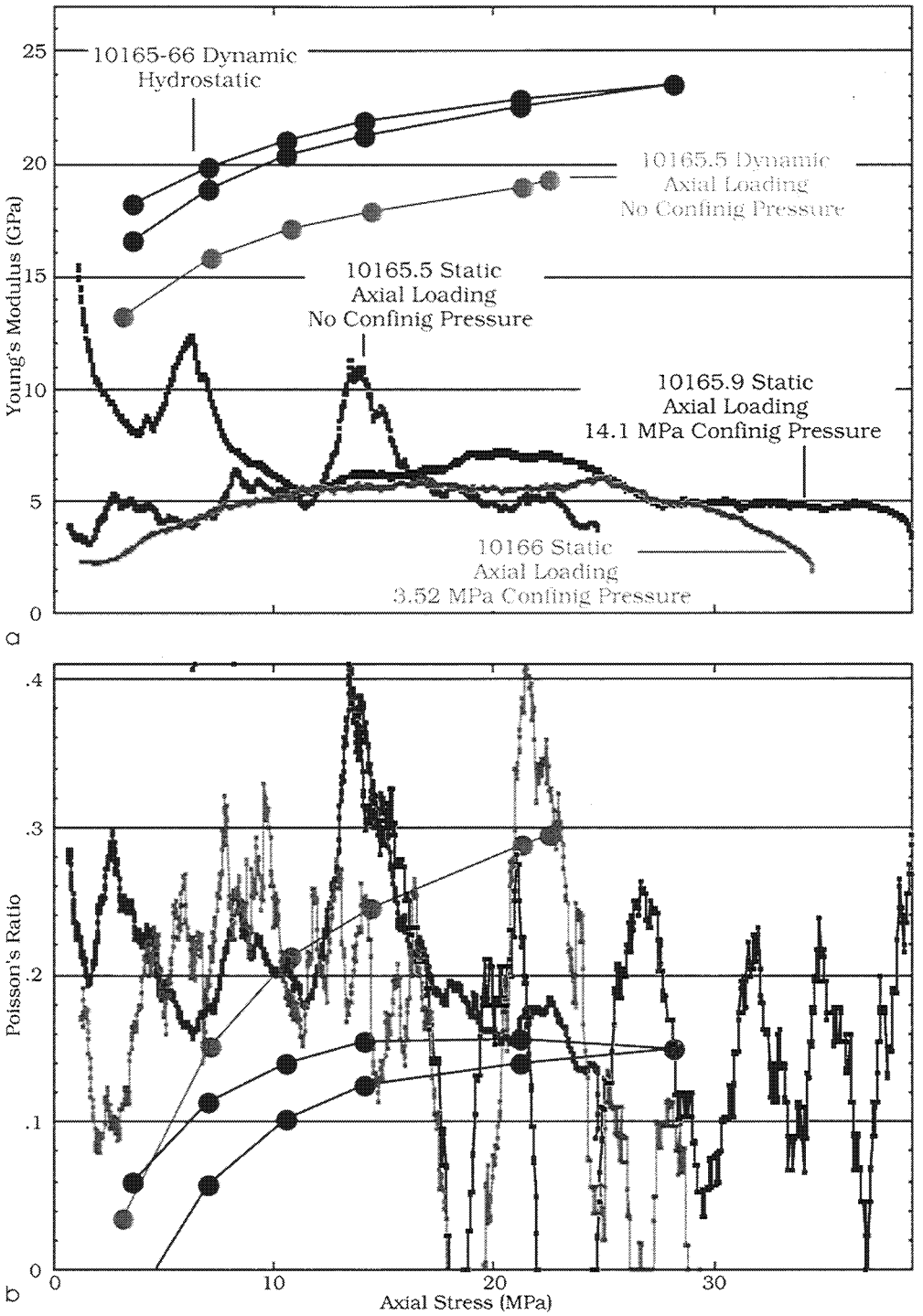

Figure 1.4.28. Young's modulus and Poisson's ratio versus stress for the 10165 group.

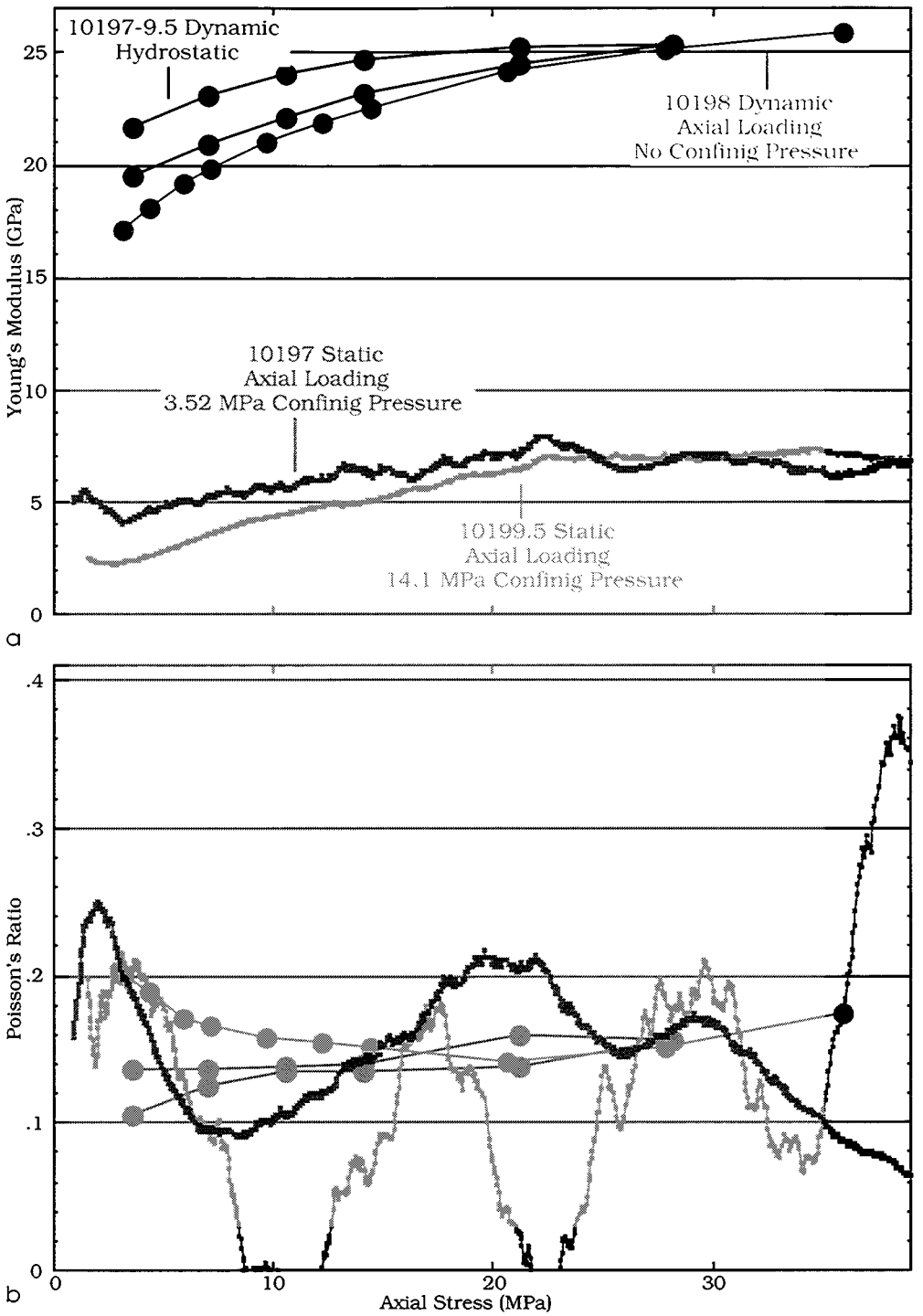

Figure 1.4.29. Young's modulus and Poisson's ratio versus stress for the 10197 group.

1.5. COMPARING STATIC TO DYNAMIC DATA

The static (average tangent) and dynamic (at 25 MPa, loading) elastic moduli are plotted versus porosity, quartz content, clay content, and feldspar content in Figures 1.5.1 – 1.5.4, respectively. Both static Young's modulus and Poisson's ratio show trends when plotted versus quartz content and feldspar content (Figures 1.5.2 and 1.5.4).

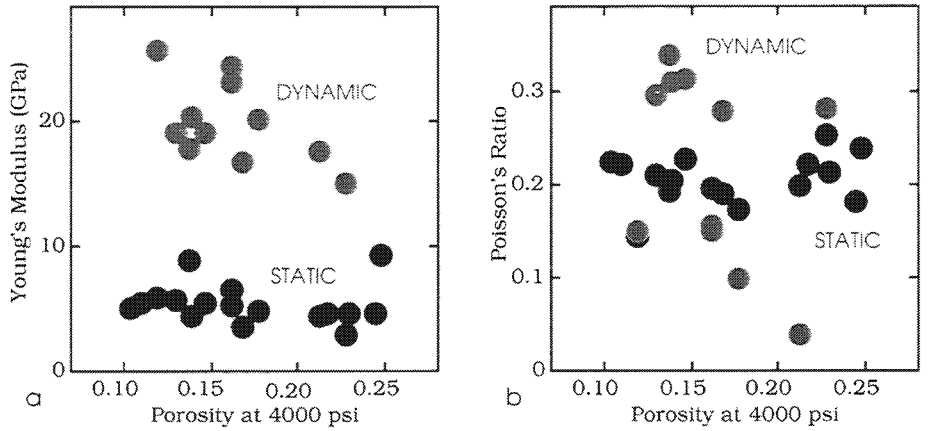

Figure 1.5.1. Young's modulus and Poisson's ratio versus porosity.

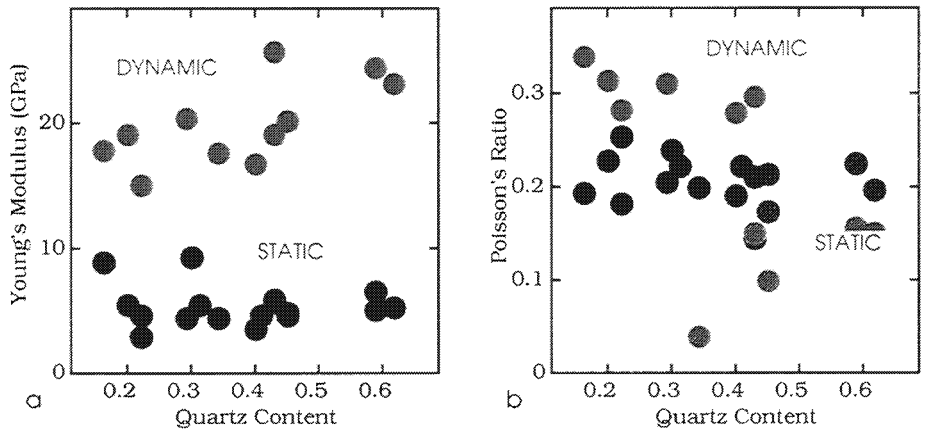

Figure 1.5.2. Young's modulus and Poisson's ratio versus quartz content.

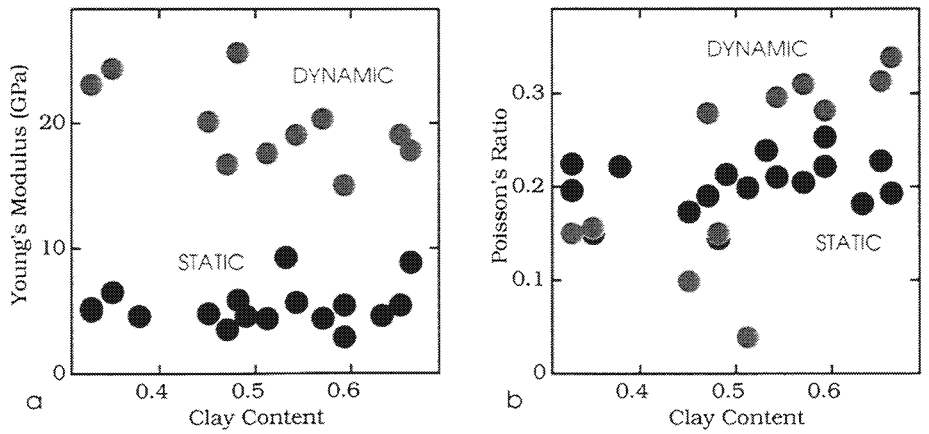

Figure 1.5.3. Young's modulus and Poisson's ratio versus clay content.

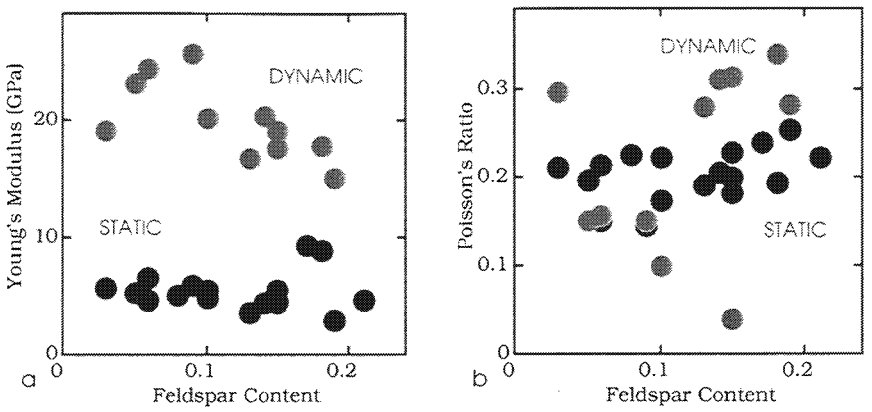

Figure 1.5.4. Young's modulus and Poisson's ratio versus feldspar content.

In Figure 1.5.5a, we plot the static Young's modulus (average tangent) versus the dynamic Young's modulus (at 25 MPa, loading). Except for one out-layer, we see a clear trend. The trend improves if we take out two more samples (Figure 1.5.5b), with linear fit:

E_Static = -1.1 + 0.29 E_Dynamic; R= 0.95,

where the moduli are in GPa. The intercept of this line with the zero-static-modulus line is about 3.8 GPa. This modulus is close to the Young's modulus of dry pure kaolinite (Yin, 1993) at 30 MPa hydrostatic pressure that is 4.2 GPa during loading.

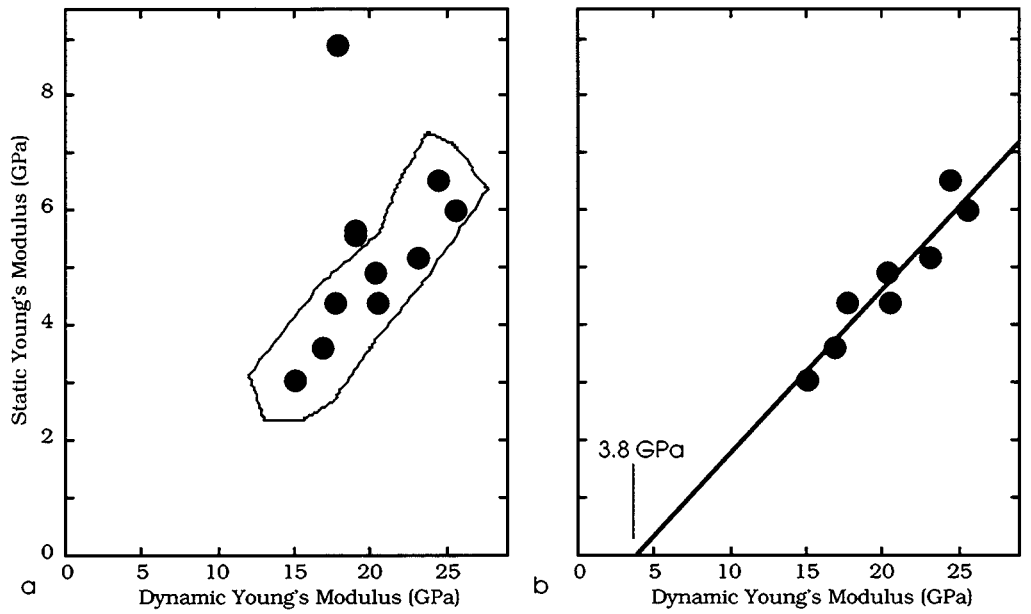

Figure 1.5.5. Static Young's modulus (average tangent) versus dynamic Young's modulus (at 25 MPa, loading) for all (a) and selected (b) samples. The samples selected for the linear fitting are surrounded by a contour in (a).

In Figure 1.5.6, we plot the static Poisson's ratio (average tangent) versus the dynamic Poisson's ratio (at 25 MPa, loading). No clear trend is apparent in this case, unless two datapoints are taken out (see the contour in Figure 1.5.6.

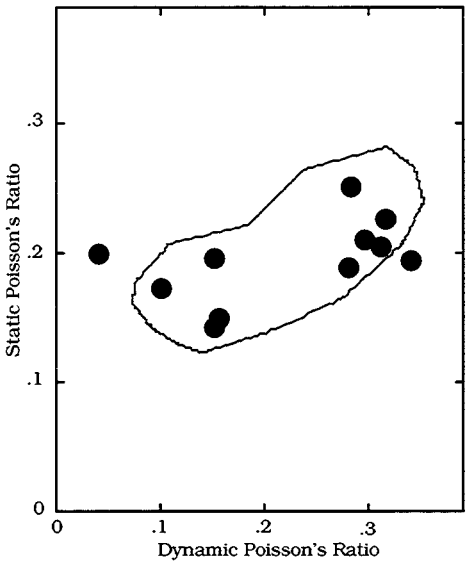

Figure 1.5.6. Static Poisson's ratio (average tangent) versus dynamic Poisson's ratio (at 25 MPa, loading) for all samples. The contour shows a subset that may constitute a trend.

With the goal in mind to be able to predict the static elastic moduli from well log data, let us relate the static moduli to the compressional (bulk density times th P-wave velocity squared) and shear (bulk density times th P-wave velocity squared) moduli.

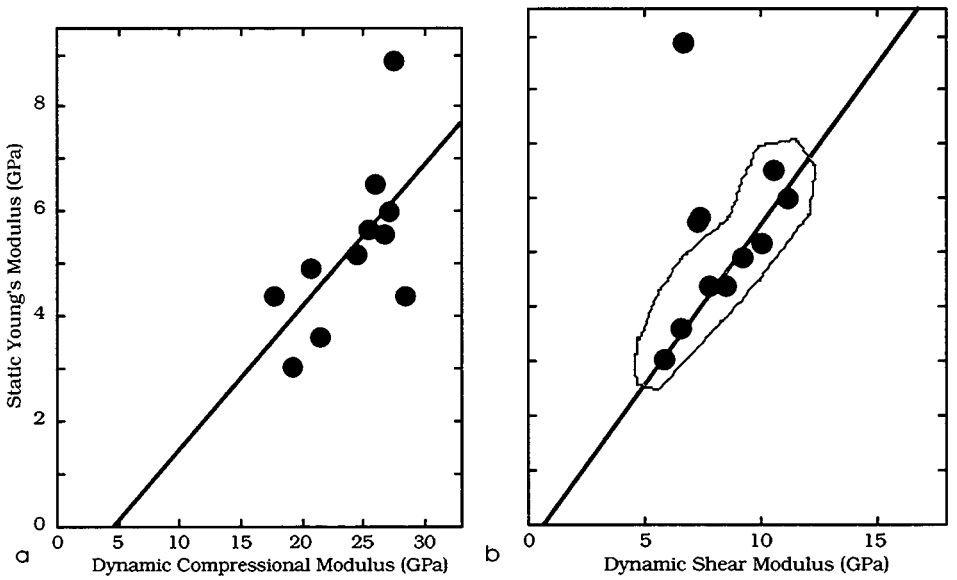

Figure 1.5.7. Static Young's modulus (average tangent) versus dynamic compressional (a) and shear (b) moduli (25 MPa, loading). The contour shows a subset for linear fitting.
The linear-fit trends are (a subset is used in the dynamic shear modulus case):

E_Static = -1.22 + 0.27 M_Dynamic; R= 0.63;
E_Static = -0.34 + 0.59 G_Dynamic; R= 0.96,

where the moduli are in GPa, and "M" stands for the compressional, and "G" for shear modulus, respectively.

The static Poisson's ratio (average tangent) is plotted versus the dynamic compressional and shear moduli (at 25 MPa, loading) in Figure 1.5.8a and 1.5.8b, respectively. No relation is apparent between the static Poisson's ratio and dynamic compressional modulus (Figure 1.5.8a). However, a clear relation exists between the static Poisson's ratio and dynamic shear modulus (Figure 1.5.8b). By using a subset of these data, we obtain the following equation:

PR_Static = 0.37 - 0.0208 G_Dynamic; R= 0.99,

where the moduli are in GPa, and "PR" stands for the static Poisson's ratio.

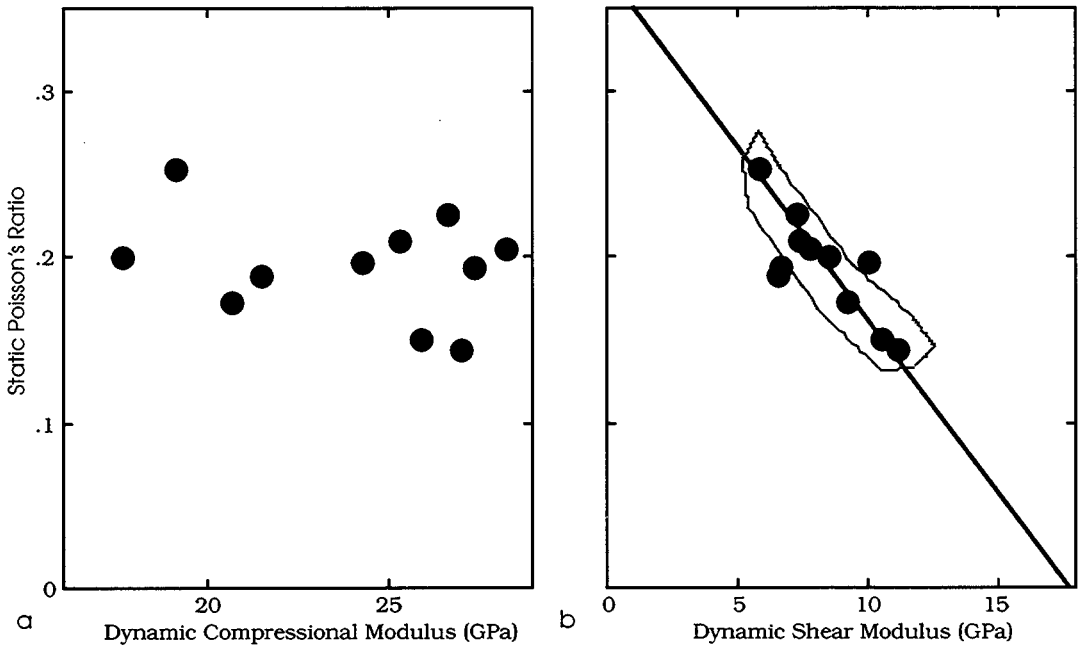

Figure 1.5.8. Static Poisson's ratio (average tangent) versus dynamic compressional (a) and shear (b) moduli (25 MPa, loading). The contour shows a subset for linear fitting.

1.6. The GOM (Gulf of Mexico) Data

Six sandstone plugs have been tested satirically and dynamically. The summary of the static test experiments is given in Figure 1.6.1. The conditions of the experiments are described in Table 1.6.1.

All these plugs are of essentially the same porosity (about 20%). Their permeability appears to be much higher than that of the shaley core from the 10118 ft to 10197 ft interval (Figure 1.6.2). This fact is likely to mean that the GOM plugs have much less clay than the shaley core.

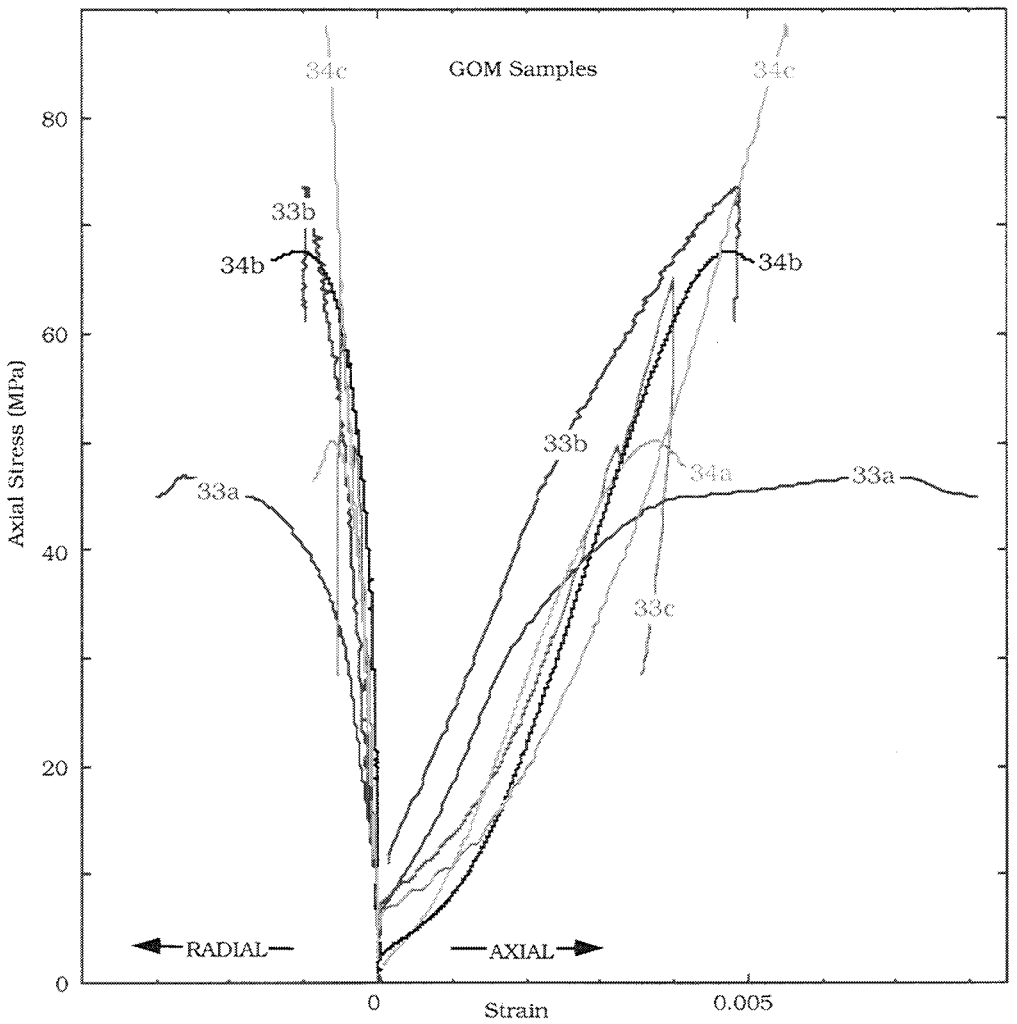

Figure 1.6.1. Axial deformation of the GOM plugs due to axial stress at varying radial stress (see Table 1.6.1).

Table 1.6.1. Properties of the shaley samples tested (10118 - 10197 ft)

Sample	Experiment Conditions
33a	Axial Load, 500 psi Confining Pressure
33b	Axial Load, 2000 psi Confining Pressure
33c	Axial Load, 5000 psi Confining Pressure
34a	Axial Load, 500 psi Confining Pressure
34b	Axial Load, 1000 psi Confining Pressure
34c	Axial Load, 5000 psi Confining Pressure

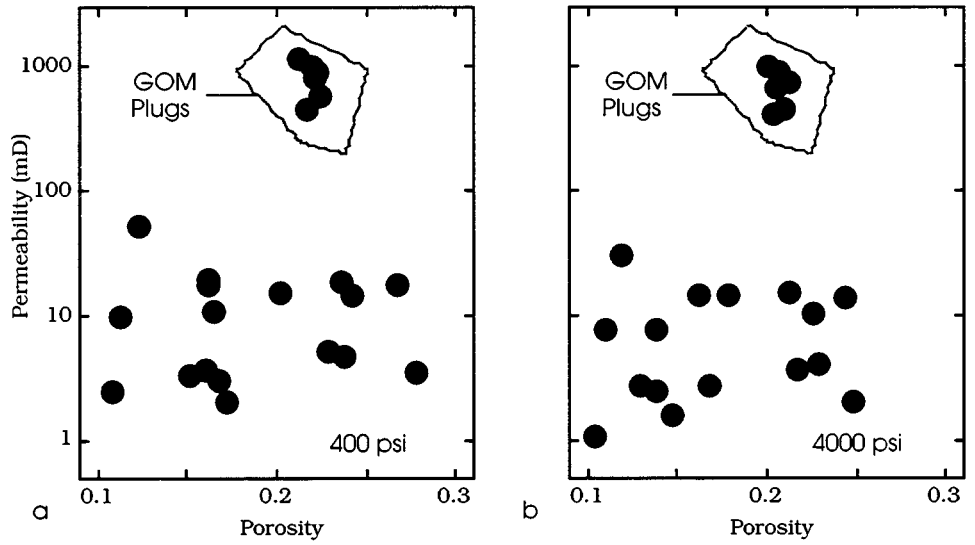

Figure 1.6.2. Permeability versus porosity for the GOM plugs and the shaley core plugs at 400 psi (a) and 4000 psi (b).

The porosity, permeability, and mineralogy of the GOM plugs are summarized in Table 1.6.2. The clay content indicated in Table 1.6.2 seems to be on the order of that indicated in Table 1.2.1 for the shaley core. It is likely that the major part of this "clay" is mica, which explains the high permeability of the GOM samples.

Table 1.6.2. Properties of the GOM plugs

Sample Depth	Grain Density	Porosity @ 400 psi	Porosity @ 4000 psi	Permeability @ 400 psi	Permeability @ 4000 psi	Quartz	F-Spar	Clay
33a	2.606	0.2210	0.2050	853	678	0.54	0.060	0.40
33b	2.631	0.2160	0.2033	456	419	0.19	0.010	0.80
33c	2.631	0.2200	0.2059	1001	928	0.60	0.070	0.33
34a	2.624	0.2123	0.2000	1165	1006	0.39	0.050	0.56
34b	2.633	0.2223	0.2121	903	763	0.38	0.040	0.58
34c	2.612	0.2234	0.2089	597	458	0.41	0.080	0.51

The elastic-wave velocity versus the axial stress is given in Figure 1.6.3. The measurements have been conducted on room-dry plugs at zero axial stress and at 5000 psi (about 35 MPa) radial stress.

The velocity-porosity plots for these plugs, together with those for the shaley core and Han's sandstone data are given in Figure 1.6.4. The data selected are for about 25 MPa axial stress. We can see that the P-wave velocity in the GOM plugs plots above the shaley core trend and close to the clean Han's sandstone data points.

This effect is not that obvious in the S-wave velocity plots (Figure 1.6.4b). Nevertheless, the position of the GOM data points in both the permeability and velocity cross-plots indicate that these plugs have much less clay than the shaley sand core.

The loading curves and the corresponding static Young's modulus and Poisson's ratio are plotted versus the axial stress for the GOM plugs in Figures 1.6.5 – 1.6.10. The static Young's modulus is compared to the dynamic Young's modulus in Figure 1.6.11. It appears in this case that the static and dynamic moduli are very close to each other. The same is approximately true for Poisson's ratio (Figure 1.6.12).

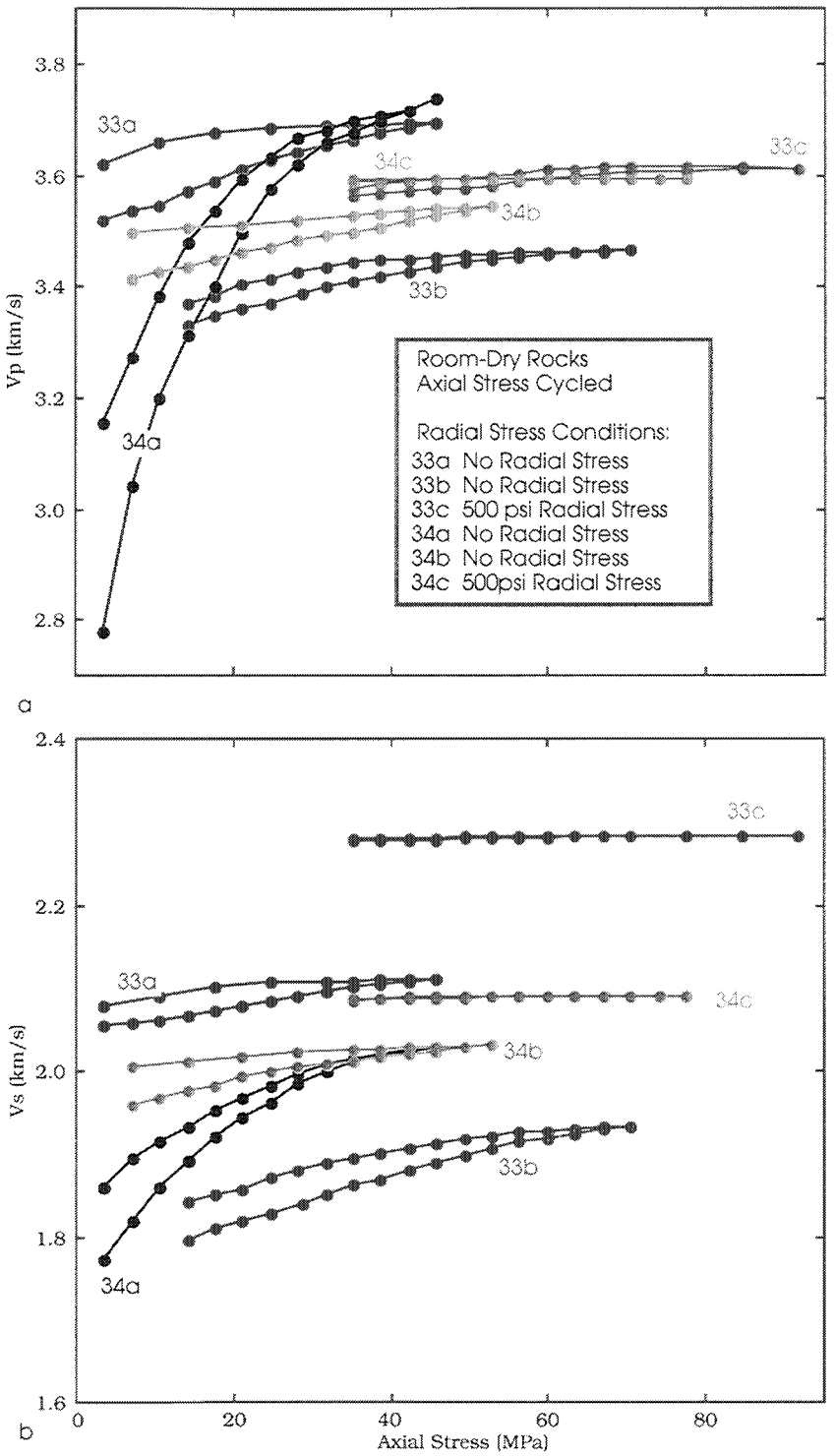

Figure 1.6.3. Elastic-wave velocity Vp (a) and Vs (b) versus axial stress for the GOM plugs. All experiments have been conducted on room-dry plugs. The stress conditions of the experiments are given in the table in (a).

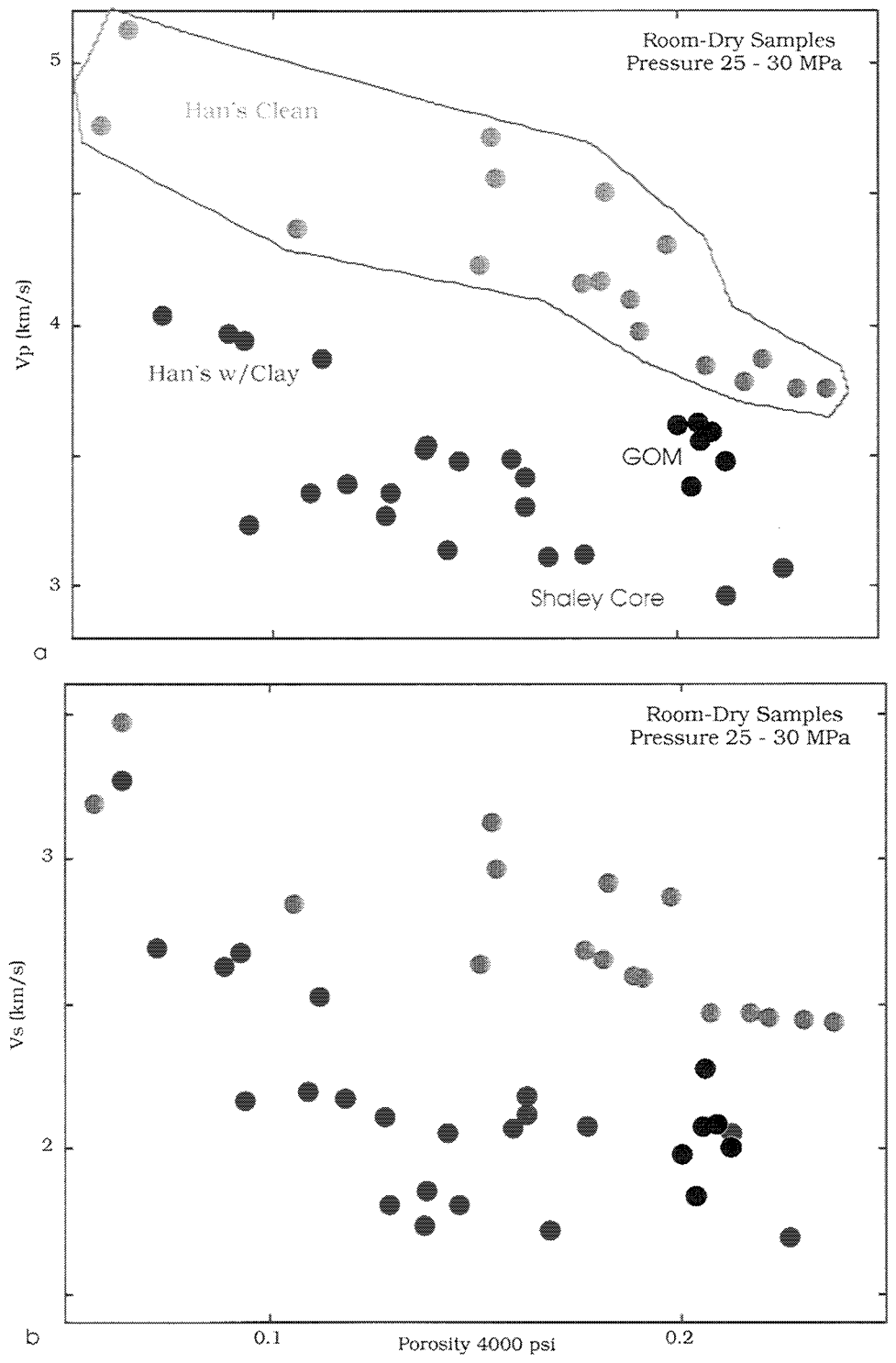

Figure 1.6.4. Elastic-wave velocity Vp (a) and Vs (b) versus porosity (at 4000 psi) for the shaley core plugs, GOM plugs, Han's shaley sandstones, and Han's clean sandstones. All experiments have been conducted on room-dry plugs.

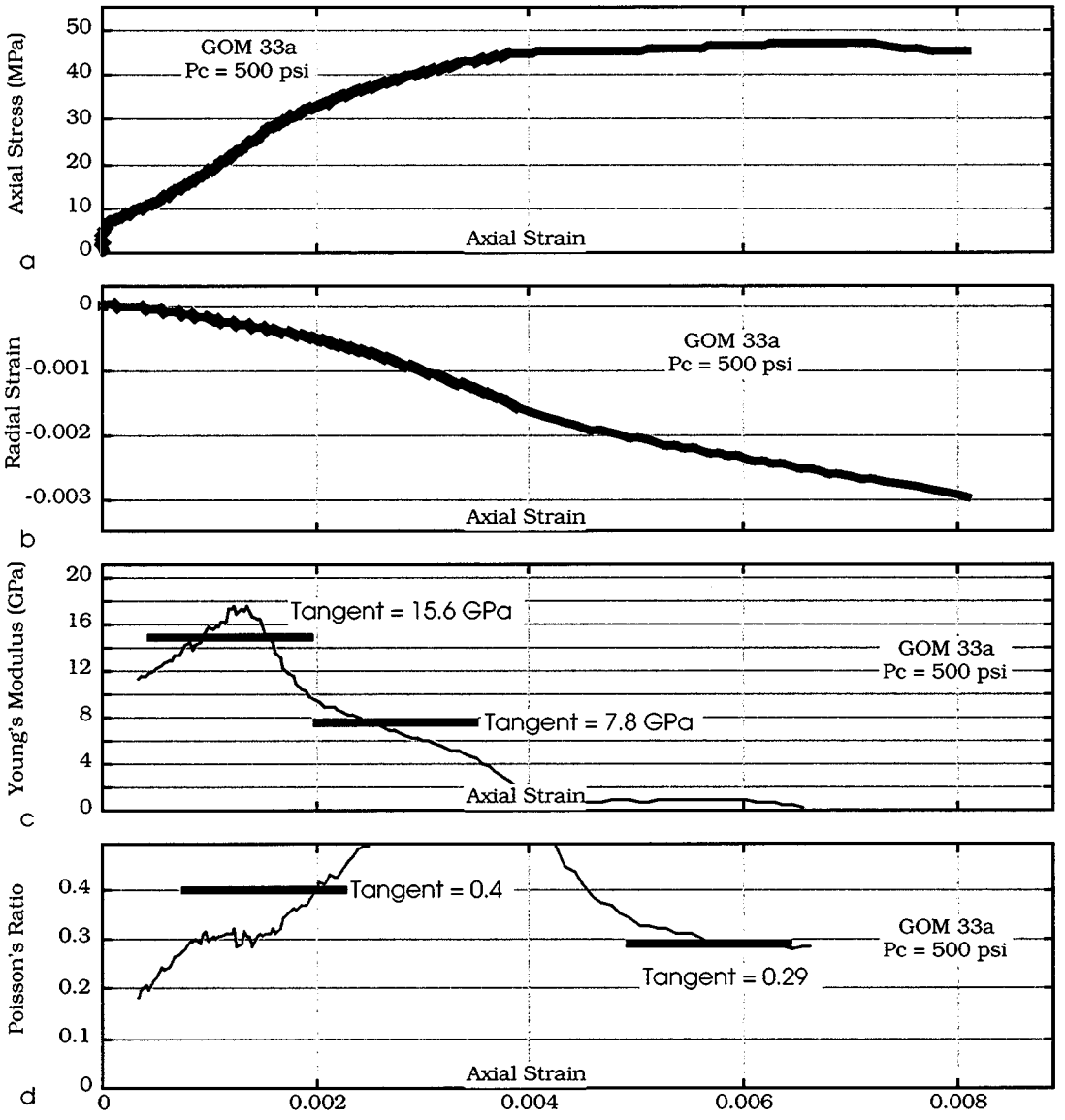

Figure 1.6.5. Loading curves and Young's modulus and Poisson's ratio for plug GOM_33a.

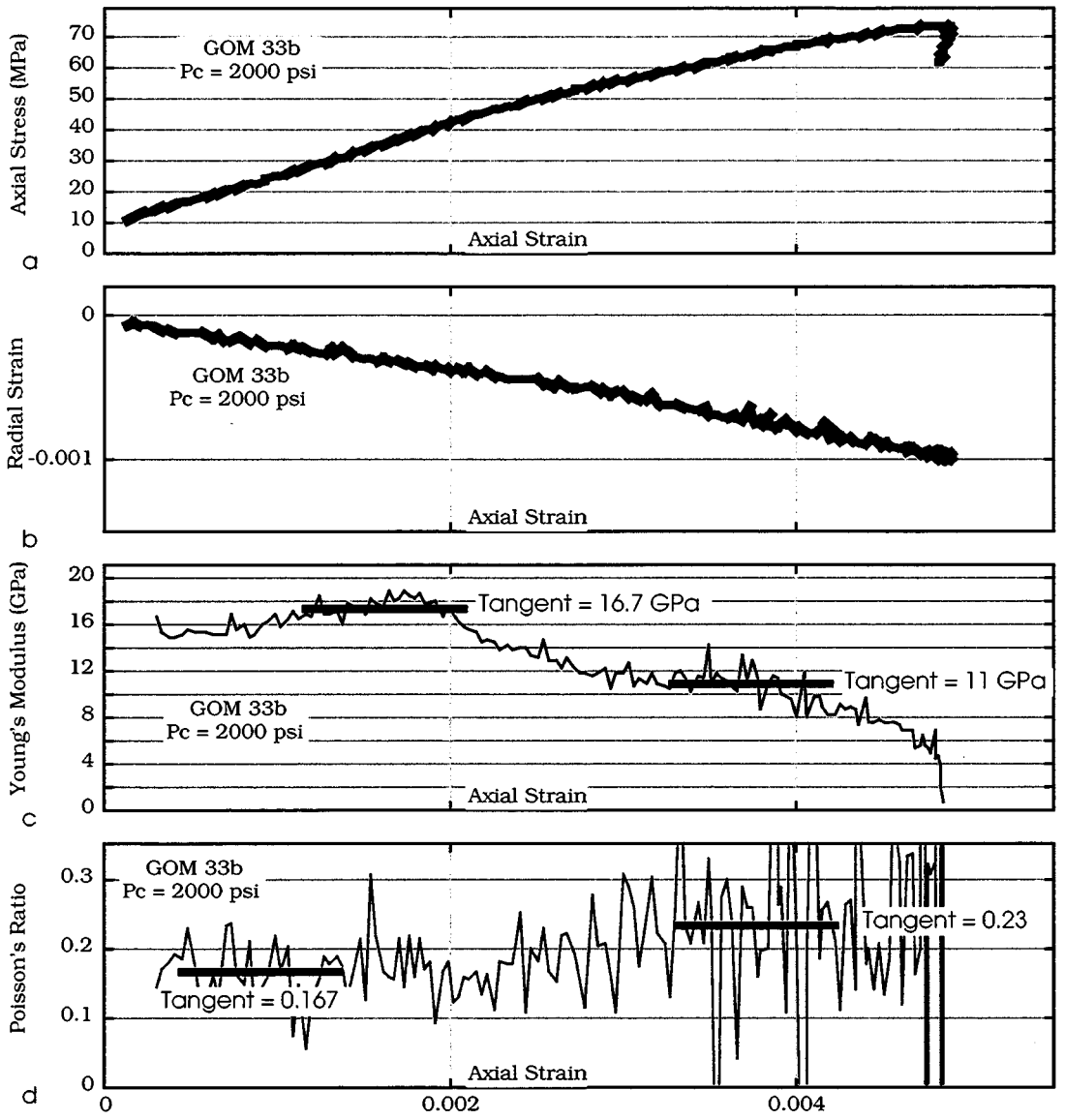

Figure 1.6.6. Loading curves and Young's modulus and Poisson's ratio for plug GOM_33b.

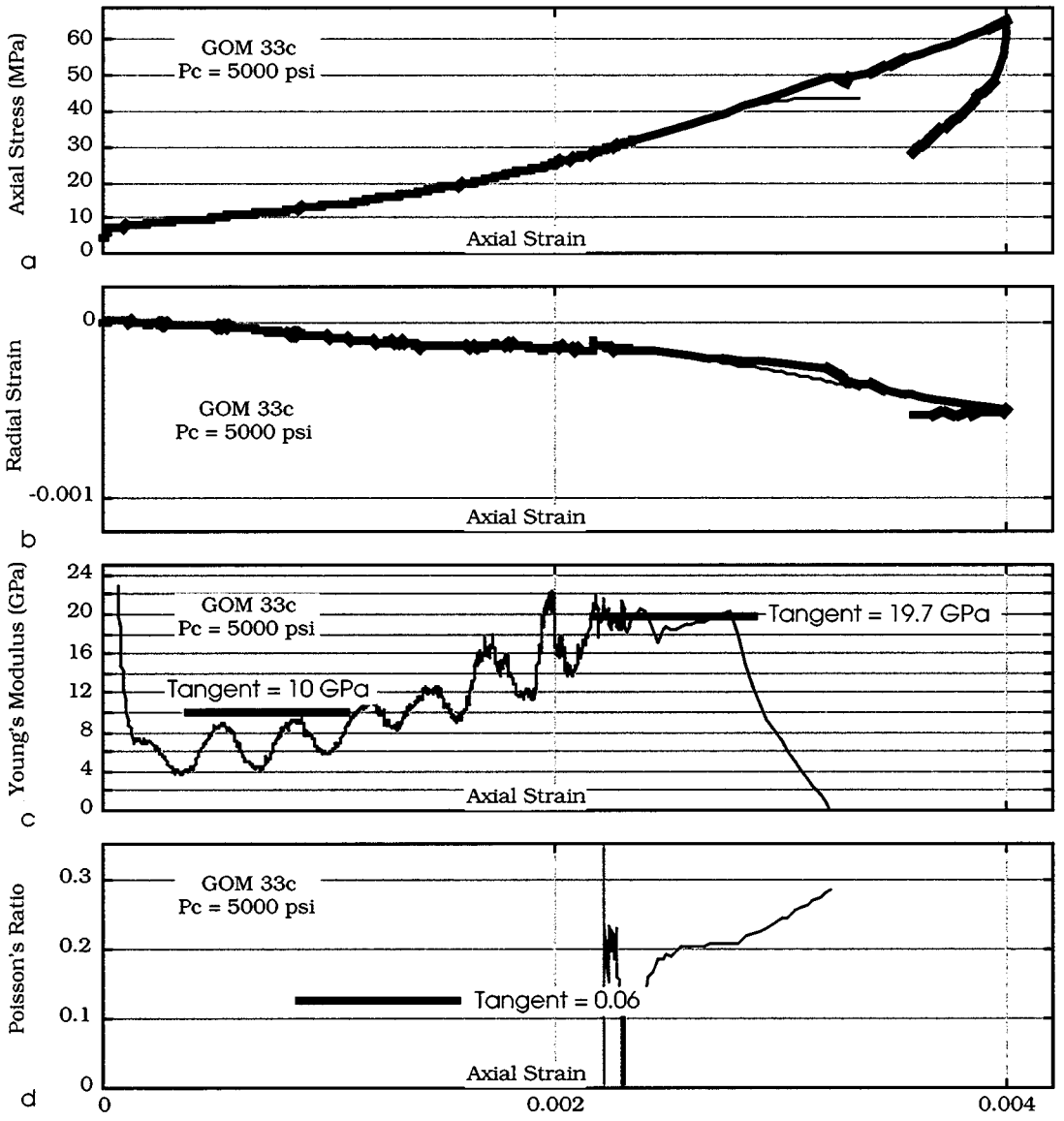

Figure 1.6.7. Loading curves and Young's modulus and Poisson's ratio for plug GOM_33c.

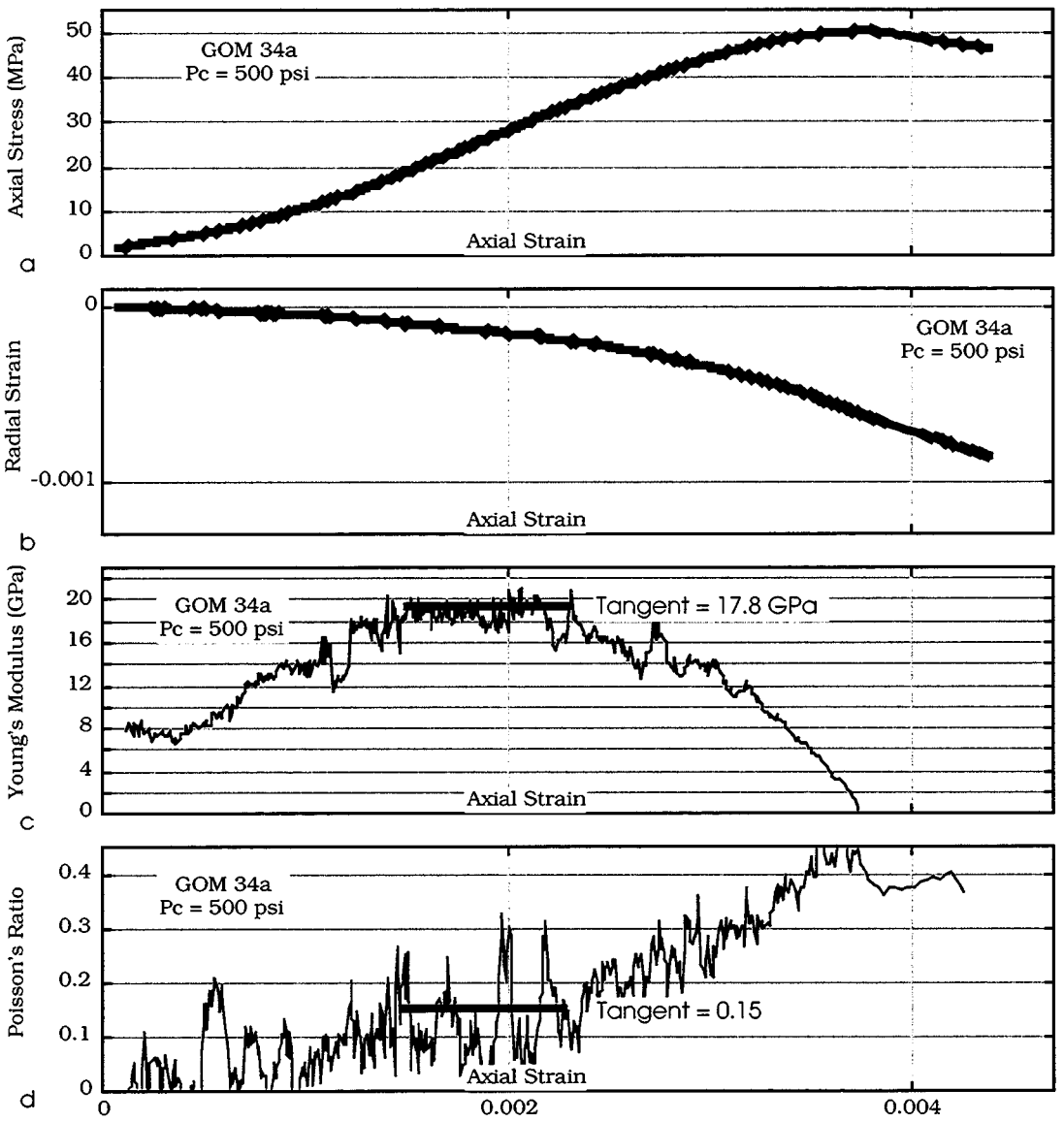

Figure 1.6.8. Loading curves and Young's modulus and Poisson's ratio for plug GOM_34a.

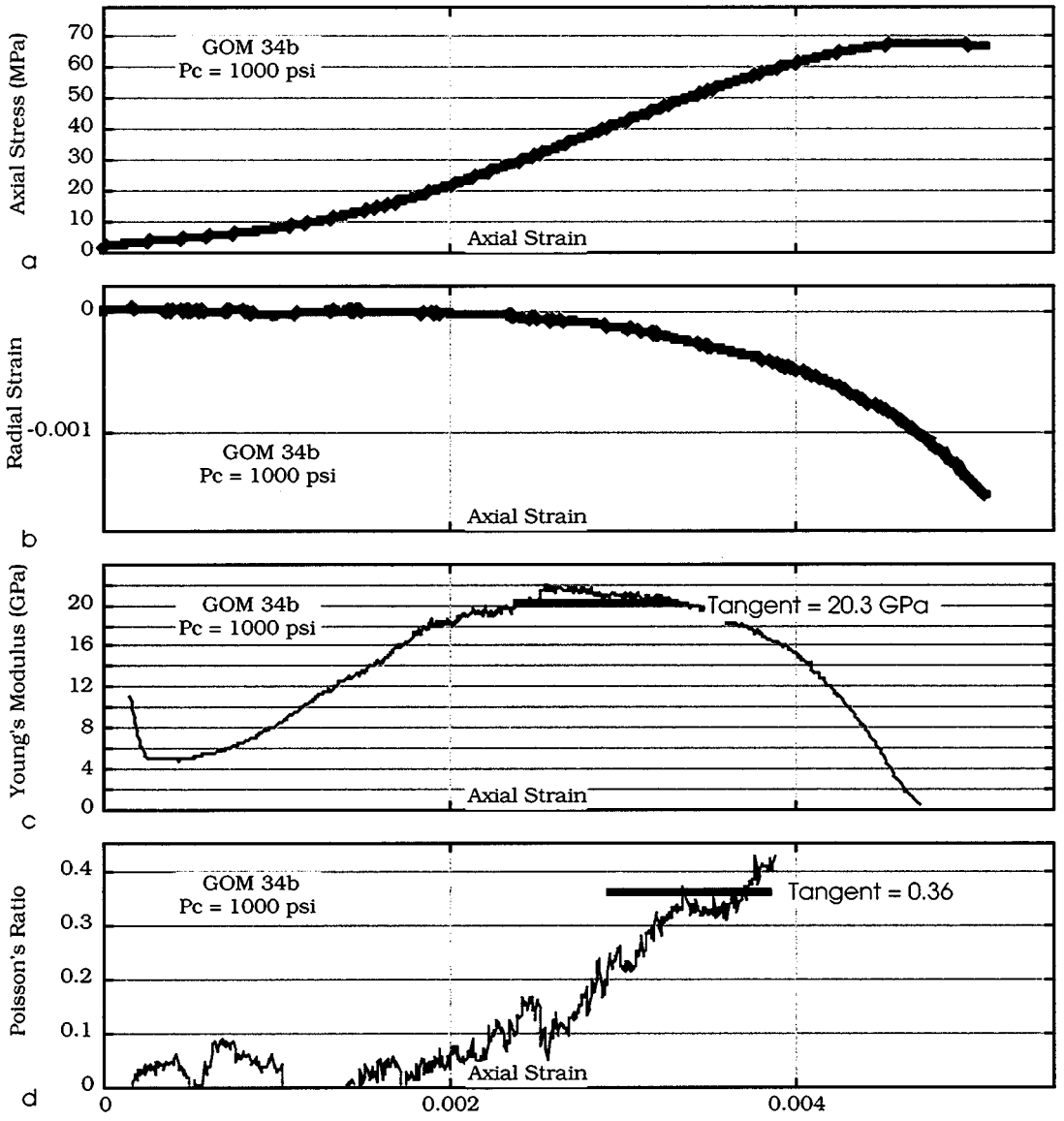

Figure 1.6.9. Loading curves and Young's modulus and Poisson's ratio for plug GOM_34b.

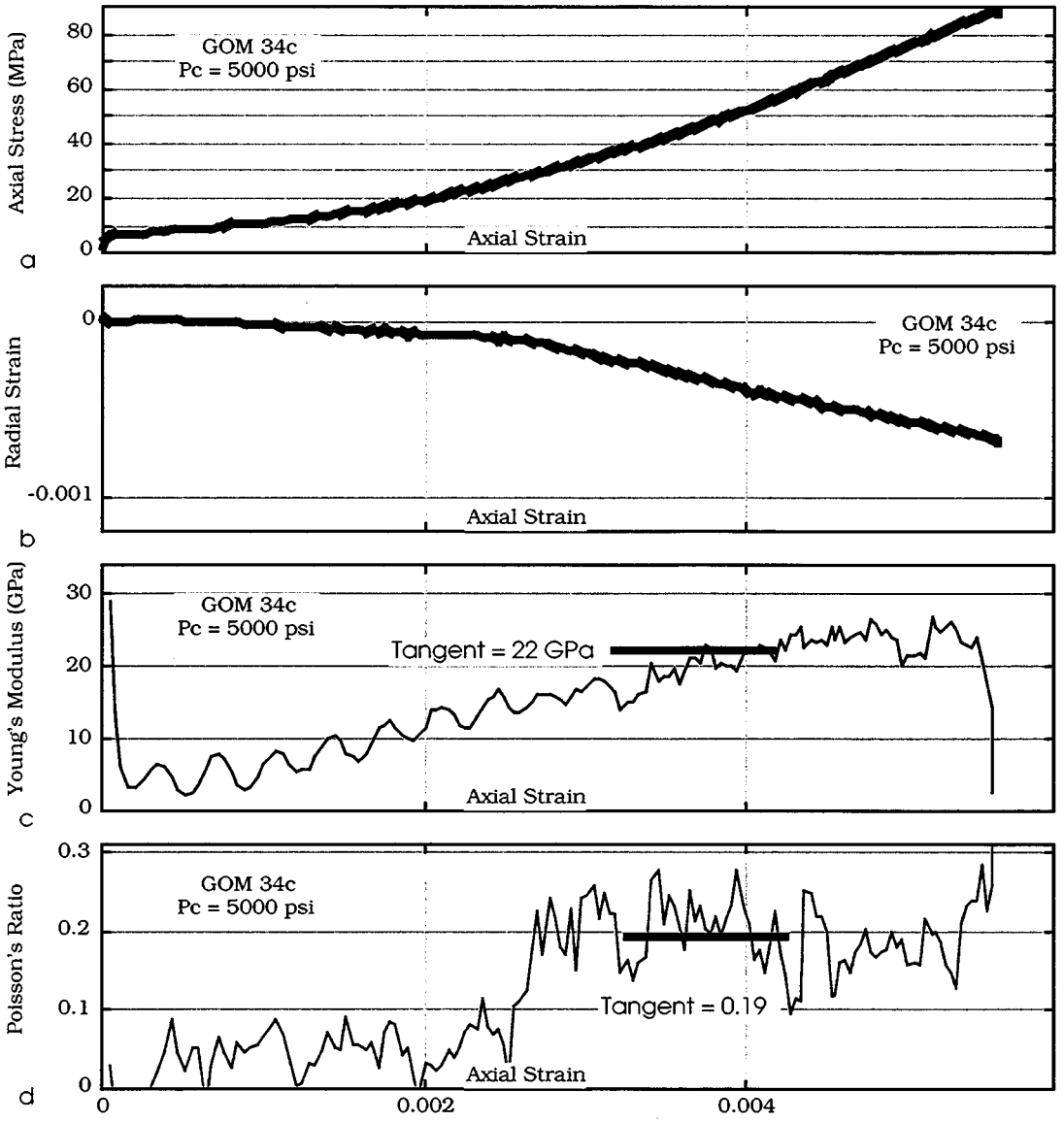

Figure 1.6.10. Loading curves and Young's modulus and Poisson's ratio for plug GOM_34c.

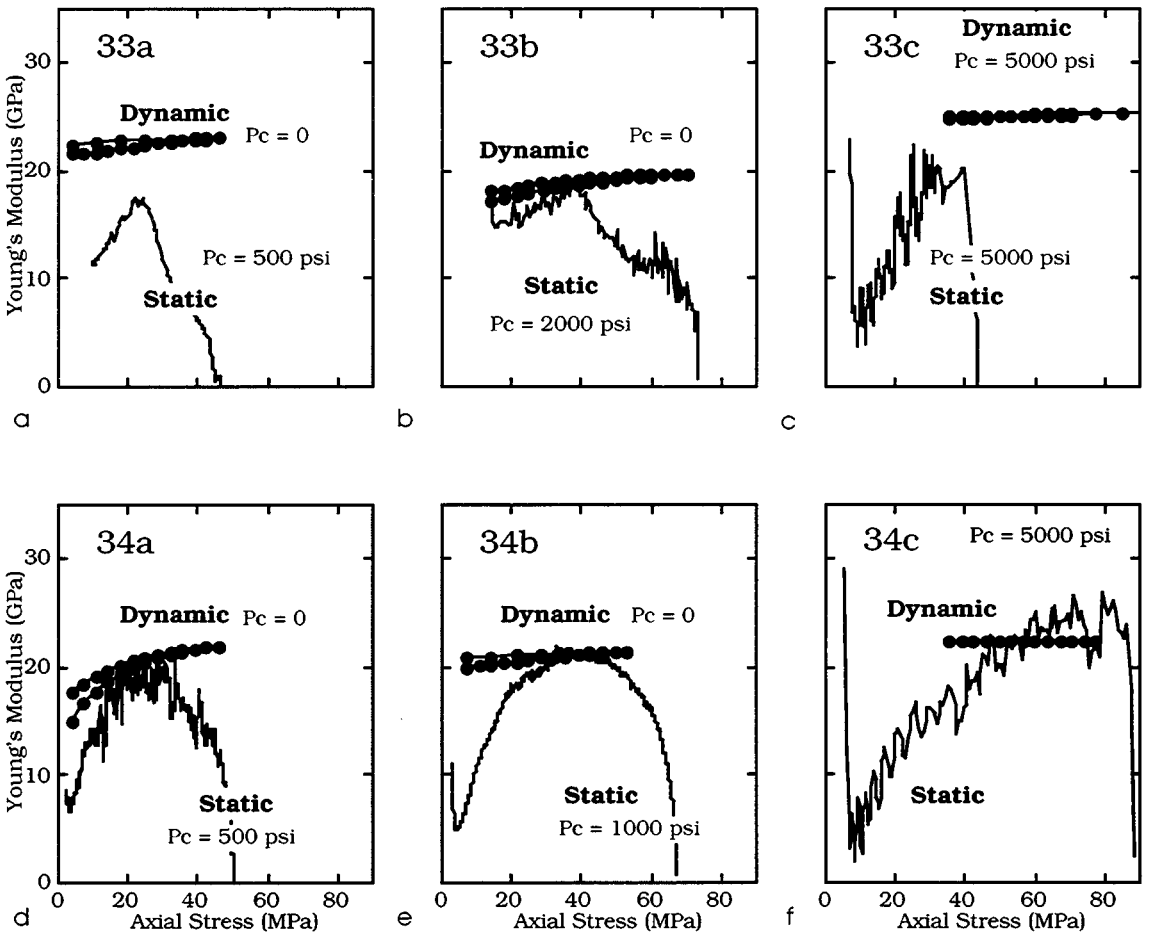

Figure 1.6.11. Dynamic and static Young's moduli versus axial stress for GOM plugs.

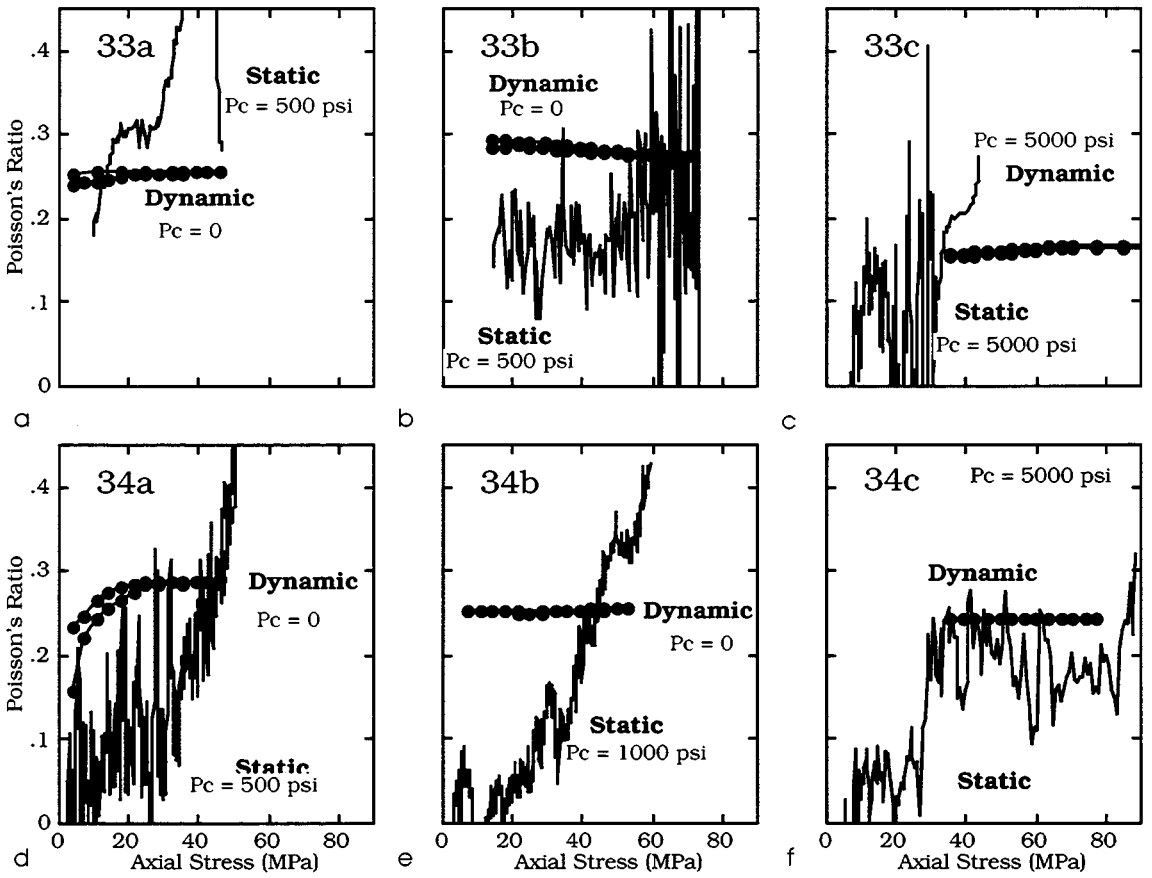

Figure 1.6.12. Dynamic and static Poisson's ratio versus axial stress for GOM plugs.

1.7 Summary of Relations Obtained on the Shaley Core 10118 - 10197 ft

The three useful relations that allow for calculating the static Young's modulus and Poisson's ratio from dynamic data are summarized below in Figures 1.7.1 and 1.7.2.

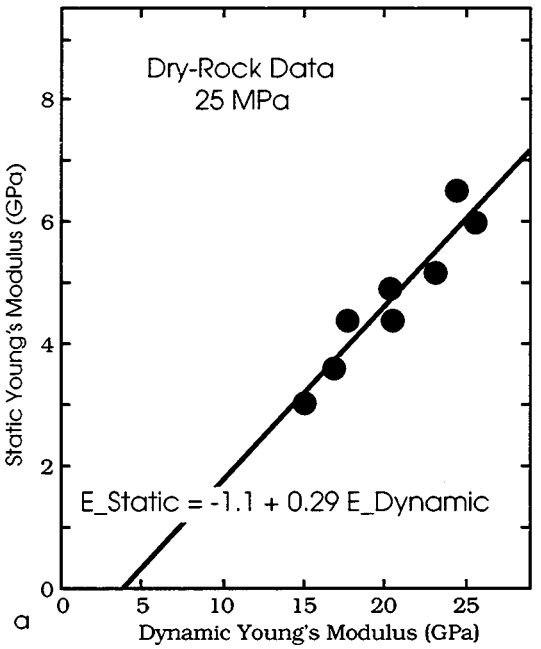

Figure 1.7.1. Static Young's modulus vs. dynamic Young's modulus in 10118 - 10197 ft plugs.

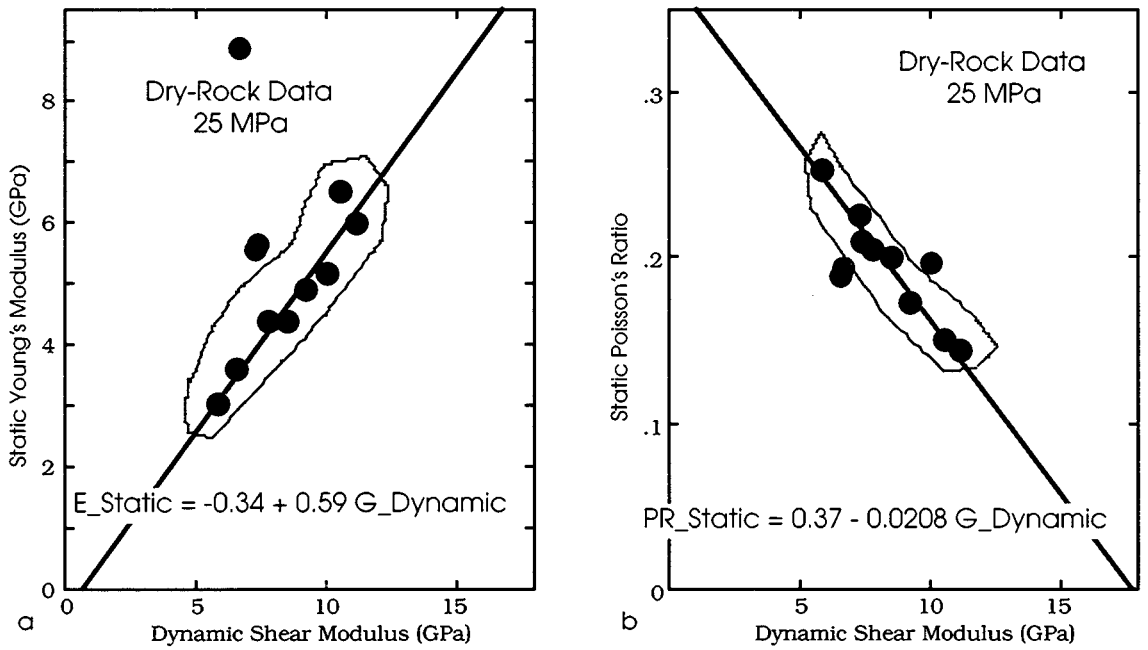

Figure 1.7.2. Static Young's modulus (a) and Poisson's ratio (b) vs. dynamic shear modulus in 10118 - 10197 ft plugs.

1.8 Comparing Shaley Core 10118 - 10197 ft to "GOM" Plugs

Below, we compare the permeability (Figure 1.8.1a), velocity (Figure 1.8.1b), and static moduli (Figure 1.8.2) of the 10118 - 10197 ft plugs to the "GOM" plugs. It appears that the static moduli of the GOM plugs are larger than those of the 10118 - 10197 ft plugs at the same porosity. This observation is consistent with the fact that the permeability and velocity of the "GOM" plugs are larger than those of the 10118 - 10197 ft plugs. The reason may be smaller amount of clay in the "GOM" plugs. This conclusion is in contradiction with Table 1.6.2. One possibility is that the clay content in Table 1.6.2 includes micas as well.

The relations between the static and dynamic moduli for the two data sets are compared in Figure 1.8.3. The relations for the "GOM" samples are very different form those for the 10118 - 10197 ft plugs. Also, these relations for the "GOM" samples have much more scatter.

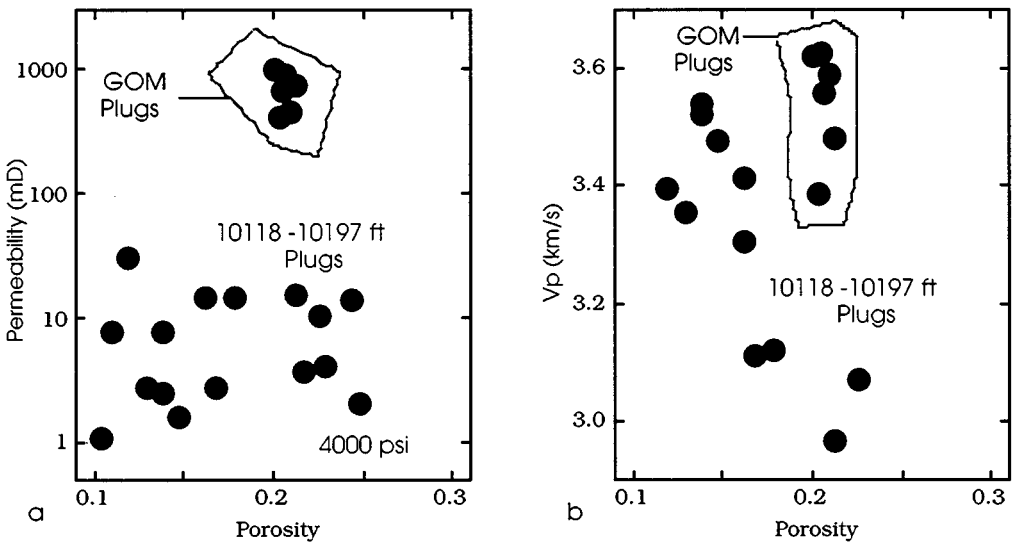

Figure 1.8.1. Permeability (a) and P-wave velocity (b) versus porosity for the 10118 - 10197 ft plugs (blue) and "GOM" plugs (red).

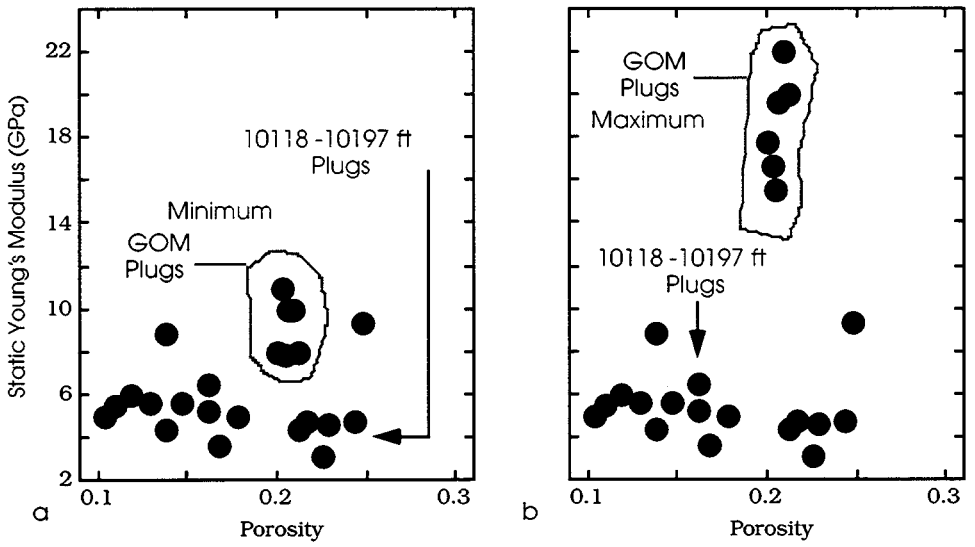

Figure 1.8.2. Static Young's modulus versus porosity for the 10118 - 10197 ft plugs (blue) and "GOM" plugs (red). The moduli for the "GOM" plugs have been calculated from the loading curves at two locations on the curve: minimum modulus and maximum modulus.

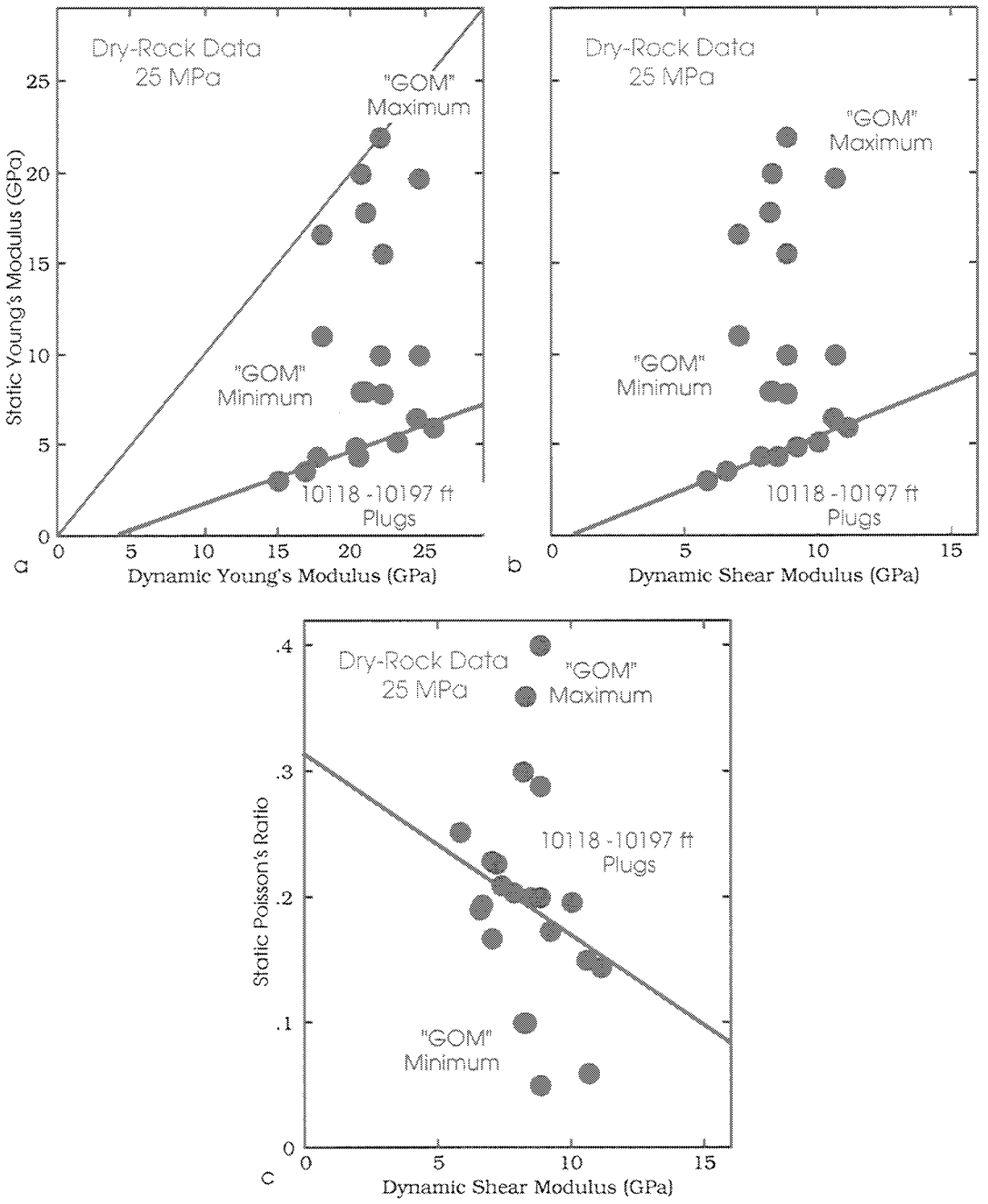

Figure 1.8.3. Static Young's modulus versus dynamic Young's modulus (a) and dynamic shear modulus (b). Static Poisson's ratio versus dynamic shear modulus (c). The data for the 10118 - 10197 ft plugs is blue and for "GOM" plugs is red. The moduli for the "GOM" plugs have been calculated from the loading curves at two locations on the curve: minimum modulus and maximum modulus.

1.9 Failure Data

The Mohr circles based on the ultimate failure axial stress are plotted in Figure 1.9.1 for all the samples under examination.

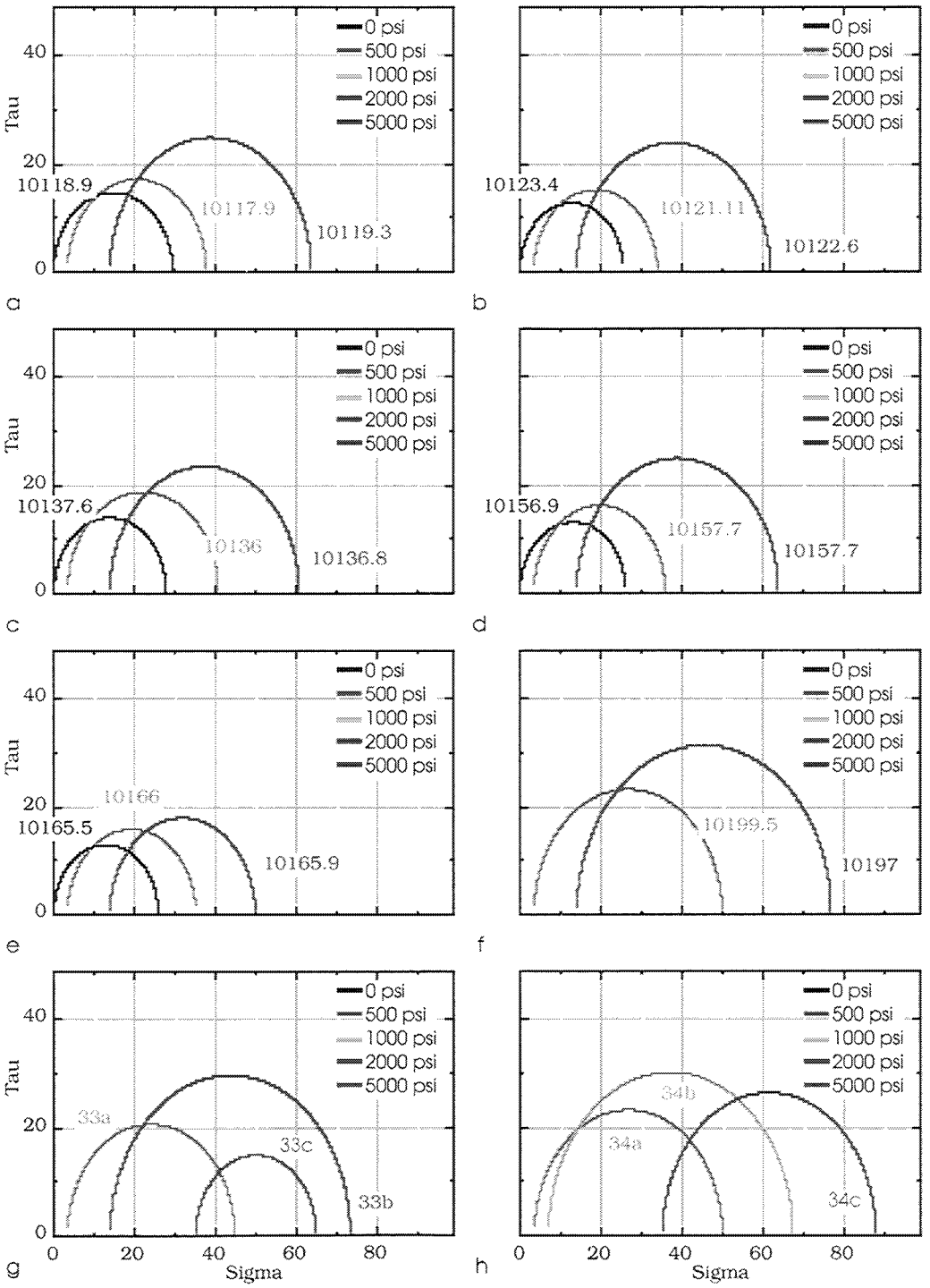

Figure 1.9.1. Mohr circles for the 10118 - 10197 ft plugs (a - f) and for "GOM" plugs (g and h). The radial stress conditions are shown in legend.

1.10. Failure Criteria

The Mohr-Coulomb failure criterion states that on the failure plain, the normal stress σ is related to the shear stress τ as:

$$\tau = c + \sigma \tan \phi, \tag{1.10.1}$$

where c is the cohesion and ϕ is the angle of internal friction. Equation (1.10.1) can be re-written as

$$0.5(\sigma_1 - \sigma_3) = k + 0.5(\sigma_1 + \sigma_3)\tan \phi,\ k = c\cos\phi. \tag{1.10.2}$$

Now we can use the failure data from Section 1.9 to calculate the Mohr-Coulomb failure criterion parameters for the groups of plugs under examination. The coefficients in Equation (1.10.2) are computed from the data shown in Figure 1.10.1.

The *Mohr-Coulomb* failure criterion parameters are very similar for the entire 10117 - 10199 plug suite with the average k = 7.2 MPa and $\tan \phi$ = .47 (Figure 1.10.2a). From these values we calculate the cohesion as c = 8 MPa = 1.14 kpsi and the angle of internal friction as ϕ = 25°.

The 10117 - 10199 plug data are compared to the "GOM" data in Figure 1.10.2b. The two outliers for both plugs, 33 and 34, are the failure data points obtained at 5000 psi radial pressure. If these two data points are eliminated, then the cohesion and angle of internal friction for the "GOM" plugs are close to those in the 10117 - 10199 plug suite.

The *Drucker-Prager* failure criterion operates in the stress invariant space and states that on the failure plain, the first invariant of the stress tensor J_1 and the second invariant of the deviatoric stress tensor J_{2D} are related as

$$\sqrt{J_{2D}} - \alpha J_1 - m = 0, \tag{1.10.3}$$

where α and m are positive material parameters. J_1 and J_{2D} can be computed as:

$$J_1 = \sigma_1 + \sigma_2 + \sigma_3,$$
$$J_{2D} = J_2 - J_1^2 / 6, \qquad (1.10.3)$$
$$J_2 = (\sigma_1^2 + \sigma_2^2 + \sigma_3^2)/ 2,$$

where σ_i are the principal stresses.

For the case under investigation, where

$$\sigma_2 = \sigma_3,$$

we have

$$J_1 = \sigma_1 + 2\sigma_2, \; J_{2D} = J_2 - J_1^2 / 6,$$
$$J_2 = (\sigma_1^2 + 2\sigma_2^2)/ 2,$$

where σ_1 is the axial stress and is the radial stress.

The Drucker-Prager coefficients are shown for the 10117 - 10199 plugs in Figure 1.10.3. All six groups give approximately the same $\alpha \approx 0.2$ and $m = 9 - 15$. The average Drucker-Prager coefficients for these data are $\alpha = 0.22$ and $m = 10$ (Figure 1.10.4a). As in the Mohr-Coulomb case, the "GOM" samples fall approximately on the same failure line except the test data at 5000 psi radial pressure (Figure 1.10.4b).

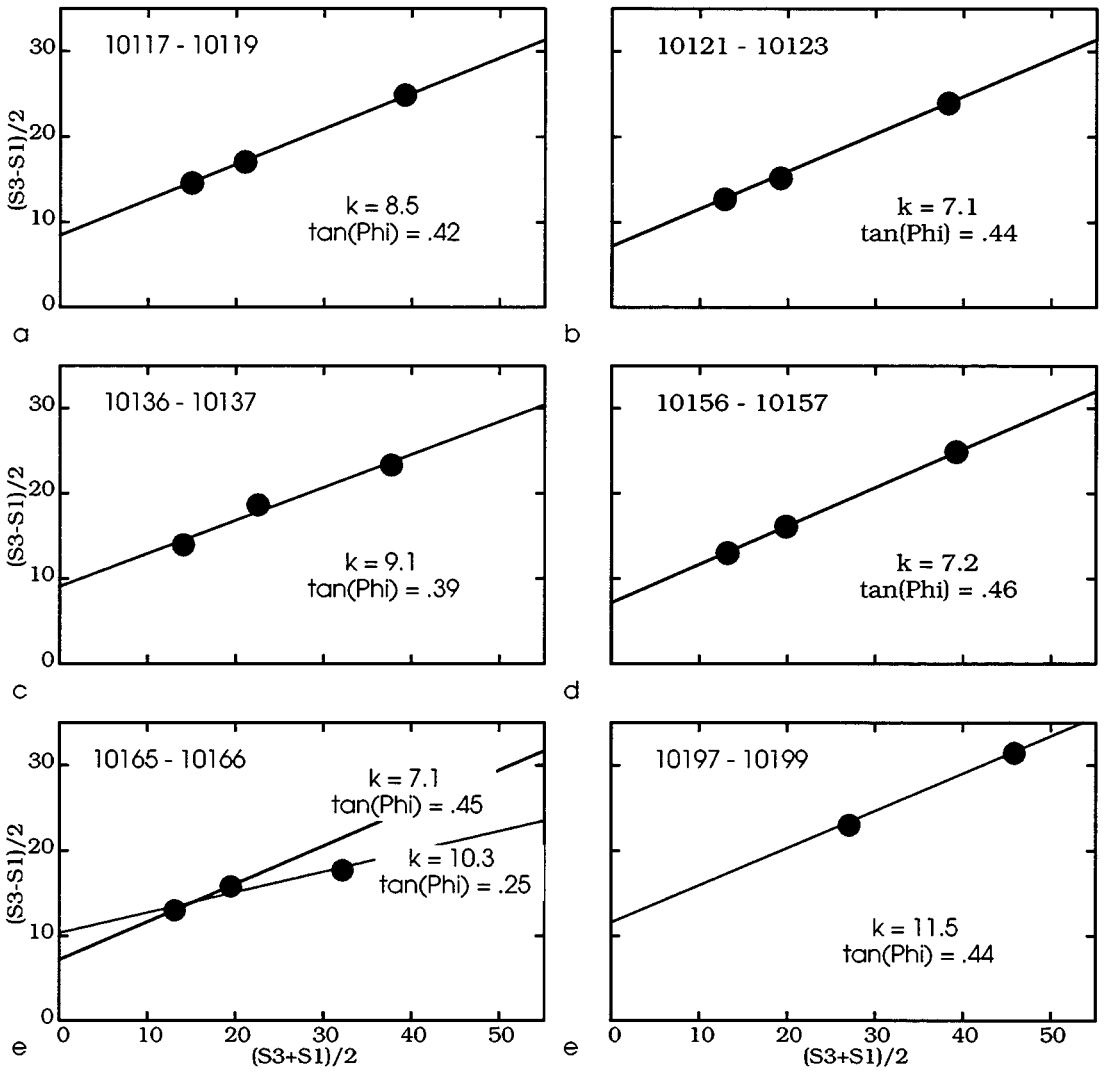

Figure 1.10.1. Determining gradient and intercept for the Mohr-Coulomb failure criterion for the 10118 - 10197 ft plugs. Plug ID is shown on the graphs. For the three 10165 - 10166 plugs, the 2000 psi test data had to be eliminate to achieve the behavior typical for the other plugs. The intercept and gradient are given on the graphs.

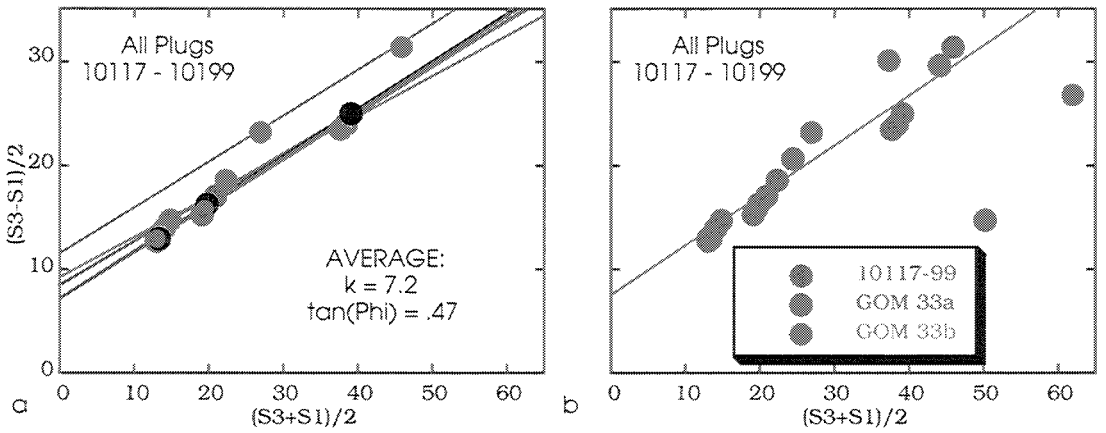

Figure 1.10.2. a. Average gradient and intercept for the Mohr-Coulomb failure criterion for the 10118 - 10197 ft plugs. (b) "GOM" data added. The outliers are the data points at 5000 psi radial pressure.

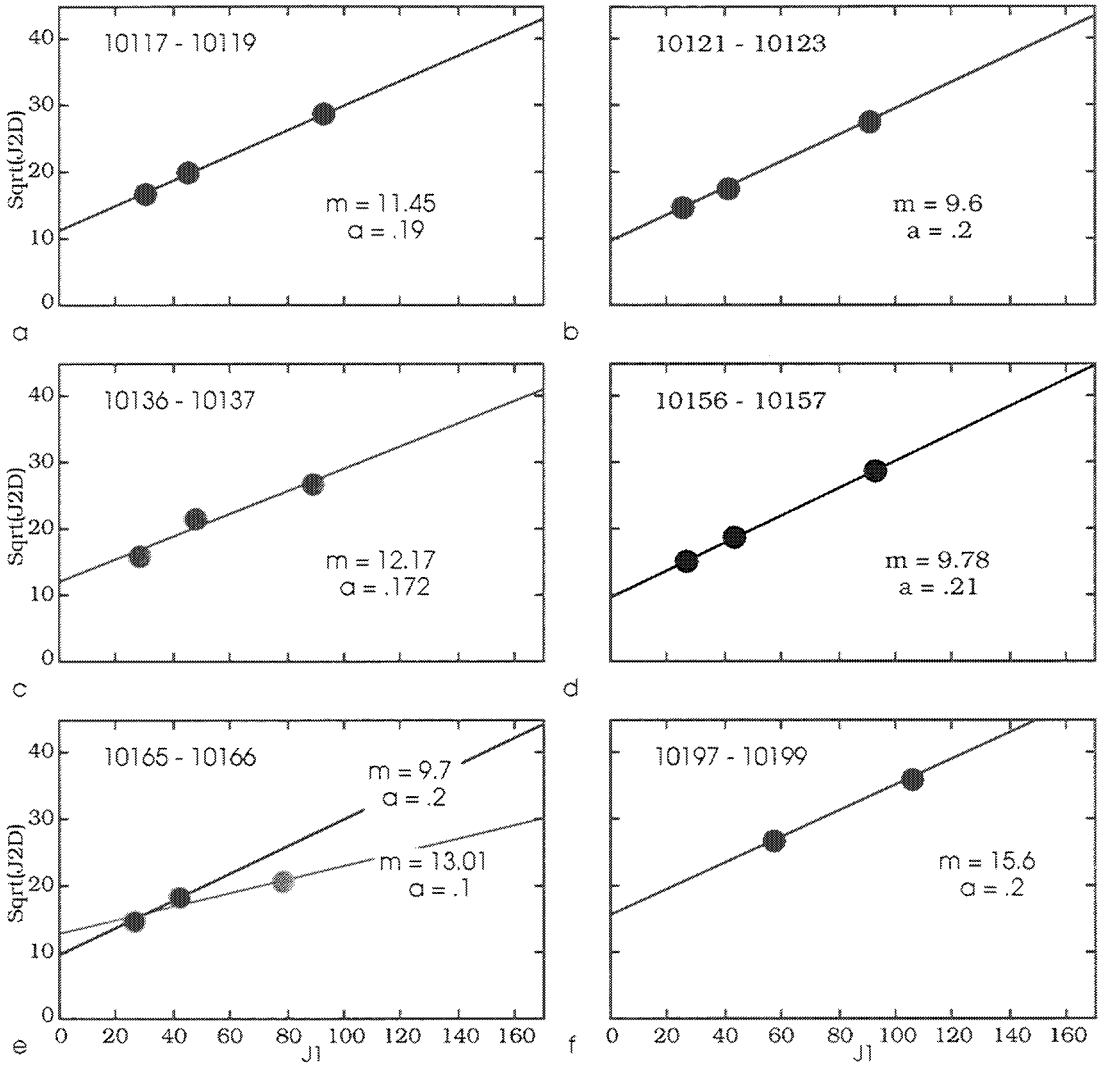

Figure 1.10.3. Drucker-Prager coefficients for the 10118 - 10197 ft plugs.

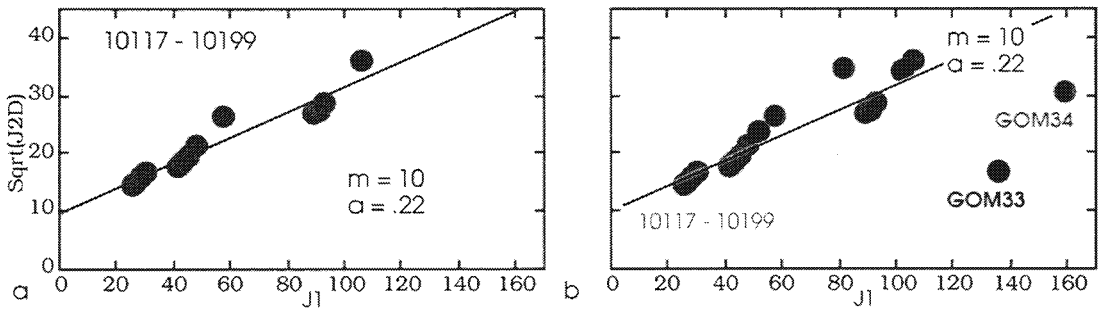

Figure 1.10.4. Average Drucker-Prager coefficients (a) and GOM data (b).

1.11 Volumetric Deformation and CAP Model

In Figure 1.11.1 we plot the hydrostatic stress versus the volumetric deformation for the six groups of the 10118 ft to 10197 ft.

The hydrostatic stress was calculated as the average of the axial stress plus twice the radial stress and the volumetric deformation was the sum of the axial strain plus twice the radial strain (with appropriate signs):

$$P = (\sigma_{Axial} + 2\sigma_{Radial})/\ 3;\ \varepsilon_{Volume} = \varepsilon_{Axial} + 2\varepsilon_{Radial}. \qquad (1.11.1)$$

The failure points and the stress paths in the $(J_1, \sqrt{J_{2D}})$ plane are plotted in Figure 1.11.2.

The cap model uses two yield surfaces: one is the fixed, ultimate failure, surface f_1 and the other is a moving elliptical cap f_2. The equation for f_1 is:

$$f_1 = 0 = \sqrt{J_{2D}} + \gamma e^{-\beta J_1} - \theta J_1 - \alpha, \sqrt{J_{2D}} = -\gamma e^{-\beta J_1} + \theta J_1 + \alpha, \qquad (1.11.2)$$

where γ, β, θ, and α are material constants. The constants in this equation are calculated from the condition that the curve asymptotically approaches the final Drucker-Prager line at $J_1 \to \infty$ and has the same value and tangent as the initial Drucker-Prager line at $J_1 = 0$ (Figure 1.11.3).

Let us assume that the equation for the initial Drucker-Prager line is $y = ax + b$, and for the final Drucker-Prager line is $y = Ax + B$, where $y = \sqrt{J_{2D}}$ and $x = J_1$. At very large J_1, we have

$$\sqrt{J_{2D}} + \gamma e^{-\beta J_1} - \theta J_1 - \alpha \overset{J_1 \to \infty}{\to} \sqrt{J_{2D}} - \theta J_1 - \alpha \equiv \sqrt{J_{2D}} - AJ_1 - B. \qquad (1.11.3)$$

Therefore,

$$\theta = A;\ \alpha = B. \qquad (1.11.4)$$

At $J_1 = 0$, we require that

$$\sqrt{J_{2D}} + \gamma e^{-\beta J_1} - \theta J_1 - \alpha \overset{J_1 = 0}{=} \sqrt{J_{2D}} + \gamma - \alpha \equiv \sqrt{J_{2D}} - b. \qquad (1.11.5)$$

Therefore,

$$\gamma - \alpha = -b,\ \gamma = \alpha - b = B - b. \tag{1.11.6}$$

The tangent of curve given by Equation (1.11.2) is

$$\frac{d\sqrt{J_{2D}}}{dJ_1} = \frac{d(-\gamma e^{-\beta J_1} + \theta J_1 + \alpha)}{dJ_1} = \gamma\beta e^{-\beta J_1} + \theta \overset{J_1=0}{=} \gamma\beta + \theta. \tag{1.11.7}$$

Therefore,

$$\gamma\beta + \theta = a,\ \beta = (a - \theta)/\ \gamma = (a - A)/\ (B - b). \tag{1.11.8}$$

In the example shown in Figure 1.11.3,

$$a = 0.2;\ b = 9.7;\ A = 0.067;\ B = 15.52. \tag{1.11.9}$$

Therefore,

$$\theta = 0.067;\ \alpha = 15.52;\ \gamma = 5.82;\ \beta = 0.0229. \tag{1.11.10}$$

The corresponding curve is shown in red in Figure 1.11.3.

In case where all yield points lay on a straight line (Figure 1.11.2a, b, and d), or only two yield points are available (Figure 1.11.2f), it follows from Equation (1.11.6) that $\gamma = 0$. Therefore, the fixed yield surface becomes a straight line:

$$\sqrt{J_{2D}} = \theta J_1 + \alpha,\ \theta = a = A,\ \alpha = b = B. \tag{1.11.11}$$

Let us now determine the moving elliptical cap. One condition for building a cap is that its center is located on the J_1 axis; the second condition is that the top of the ellipsis is where it intersects the fixed yield surface; and the third condition is that the volumetric plastic deformation is constant on the ellipsis. An equation to describe the cap is:

$$(\sqrt{J_{2D}})^2 + k^2(J_1 - C)^2 - k^2R^2 = 0, \tag{1.11.12}$$

where C is the coordinate of the center; R is the horizontal semi-axis; and $kR = r$ is the vertical semi-axis (Figure 1.11.3).

The distance $Z = C + R$ (Figure 10.3) depends on the volumetric plastic strain ε_v^p as

$$Z = -\frac{1}{D}\ln(1-\frac{\varepsilon_v^p}{W}) + Z_0, \tag{1.11.13}$$

where D, W, and Z_0 are material constants. This is a point on the J_1 axis where a hydrostatic compression condition is realized. Three data points are enough to determine the material constants in Equation (1.11.13). These data can come from triaxial tests from the points where the axial load equals the radial pressure (points where the green loading paths intersect the horizontal axis in Figure 1.11.3).

The plastic volumetric strain ε_v^p is the difference between the total volumetric strain ε_v and the elastic part of the strain ε_v^e:

$$\varepsilon_v^p = \varepsilon_v - \varepsilon_v^e. \tag{1.11.14}$$

The elastic part is proportional to the elastic bulk modulus which is the unloading path modulus in the static tests.

In the case under examination, we do not have unloading data. Therefore, we assume that the plastic deformation ε_v^p equals the total deformation ε_v:

$$\varepsilon_v^p = \varepsilon_v. \tag{1.11.15}$$

Next, we assume that there is no initial yield cap which means the plastic deformation is zero at zero hydrostatic stress (see Figure 1.11.1 where the load paths at zero confining pressure pass through the origin). Then $Z_0 = 0$ in Equation (1.11.13) and

$$Z = -\frac{1}{D}\ln(1-\frac{\varepsilon_v^p}{W}). \tag{1.11.16}$$

This equation can be transformed to

$$\varepsilon_v^p = W(1-e^{-DJ_1}) \equiv W(1-e^{-3DP}), \tag{1.11.17}$$

where $P = J_1 / 3$ is the hydrostatic pressure.

If we know the volumetric strain ε_{v1}^p and ε_{v2}^p at two values of J_1, $J_1 = Z_1$ and $J_1 = Z_2$, respectively, *where the deviatoric stress is zero*, we can calculate the needed constants D and W from equations

$$\frac{\varepsilon_{v1}^p}{\varepsilon_{v2}^p} - \frac{1-e^{-DZ_1}}{1-e^{-DZ_2}} = 0;\ W = \frac{\varepsilon_{v1}^p}{1-e^{-DZ_1}}. \qquad (1.11.18)$$

The key in establishing the hardening equation according to (1.11.15) is to know the true absolute values of the volumetric strain. It is clear from Figure 1.11.1 that the volumetric strain values given in the measurements are relative because the strain appears to be zero at a finite hydrostatic stress. In order to obtain the correct strain values, we assume that all hydrostatic stress-strain curves have to pass through the origin. Furthermore, we will approximate the hydrostatic stress-strain curve by a linear function and then shift it as needed. The corresponding shifted stress-strain curves are shown in Figure 1.11.4. The J_1 (Z) values at $J_{2D} = 0$ and the corresponding ε_v and ε_v^p values are given in Table 1.11.1.

Table 1.11.1. First stress invariant and volumetric deformation at pure volumetric compression points for the shaley samples tested (10118 - 10197 ft).

Plug	Z1 (MPa)	eVP1	Z2 (MPa)	eVP2	Z1/Z2	eVP1/eVP2
10117-19	10.559	0.0014808	42.222	0.0061188	0.25	0.24201
10121-22	10.573	0.0014058	42.221	0.0061757	0.25	0.22763
10136-37	10.551	0.00061362	42.221	0.0023888	0.25	0.25687
10156-57	10.566	0.0013413	42.193	0.0047819	0.25	0.28049
10165-66	10.573	0.0012367	42.221	0.0061486	0.25	0.20114
10197-99	10.566	0.0011768	42.207	0.0047533	0.25	0.24758

Consider Equation (1.11.18) at $D \to 0$. In this limit case $1 - \exp(-DZ) \to DZ$, and $\varepsilon_{v1}^p / \varepsilon_{v2}^p \to Z_1 / Z_2$. The ratio $(1-e^{-DZ_1})/(1-e^{-DZ_2})$ will increase with the increasing D because its derivative with respect to D is positive. Therefore, a solution to Equation (1.11.18) exists only if $\varepsilon_{v1}^p / \varepsilon_{v2}^p > Z_1 / Z_2$.

We can see from Table 1.11.1 that this condition is not satisfied except for plug 10157. This is the only case where both test have been made on the same plug, 10157.7. Therefore, we will use it to resolve Equation (1.11.18) and use the result for all other

cases. We find D = 0.0074 MPa^{-1} and W = 0.018. The volumetric strain is plotted versus the first stress invariant J_1, according to Equation (1.11.17), in Figure 1.11.5.

As we mentioned above, Equation (1.11.17) cannot be fit to the data in Figure 1.11.5, except for plug 10157.7. An alternative solution is to use a linear equation instead of Equation (1.11.17). To find this equation, we fit a straight line to the data points from Table 10.1 (Figure 1.11.5). The corresponding linear equation is:

$$\varepsilon_v^p = W_L + D_L J_1 = -0.000094 + 0.000135 J_1, \qquad (1.11.17a)$$

where W_L and D_L are constants for the linear hardening equation. We suggest that Equation (1.11.17a) may be used alternatively to Equation (1.11.17) when building hardening caps for the experimental data under examination.

In order to build the cap ellipsis, it is enough to have two points with the same volumetric deformation on the $(J_1, \sqrt{J_{2D}})$ plane shown in Figure 1.11.3.

Let us rename the variables as

$$J_1 \equiv x; \sqrt{J_{2D}} \equiv y. \qquad (1.11.19)$$

Then Equation (1.11.12) for the ellipsis becomes

$$y^2 + k^2 (x - C)^2 - k^2 R^2 = 0. \qquad (1.11.20)$$

The condition that its top lies on the fixed yield surface (1.11.2) $\sqrt{J_{2D}} = -\gamma e^{-\beta J_1} + \theta J_1 + \alpha$ gives:

$$y \overset{x=C}{=} kR = -\gamma e^{-\beta J_1} + \theta x + \alpha = -\gamma e^{-\beta C} + \theta C + \alpha. \qquad (1.11.21)$$

Therefore, Equation (1.11.20) becomes

$$y^2 + k^2 (x - C)^2 - (-\gamma e^{-\beta C} + \theta C + \alpha)^2 = 0. \qquad (1.11.22)$$

Now we will use the condition that a cap is a surface of constant volumetric strain. Let us assume that we have two points in the (x, y) plane where the volumetric deformation is the same. These points are (x_1, y_1) and (x_2, y_2). Then we have a system of two equations for determining the constants k and C:

$$y_1^2 + k^2(x_1 - C)^2 - (-\gamma e^{-\beta C} + \theta C + \alpha)^2 = 0,$$
$$y_2^2 + k^2(x_2 - C)^2 - (-\gamma e^{-\beta C} + \theta C + \alpha)^2 = 0. \qquad (1.11.23)$$

From these equations we find:

$$k^2 = -\frac{y_1^2 - y_2^2}{(x_1 - x_2)(x_1 + x_2 - 2C)},$$
$$y_1^2 - \frac{y_1^2 - y_2^2}{(x_1 - x_2)(x_1 + x_2 - 2C)}(x_1 - C)^2 - (-\gamma e^{-\beta C} + \theta C + \alpha)^2 = 0. \qquad (1.11.24)$$

The last of these two equations has to be solved for C. After C is found, it has to be substituted into the first equation of the system (1.11.24) to find k. If the (x_2, y_2) points is located on the J_1 $(y = 0)$ axis, then $y_2 = 0$ and x_2 can be calculated versus the volumetric deformation from equation (1.11.16):

$$Z \equiv J_1 \equiv x_2 = -(1 / D)\ln(1 - \varepsilon_v^p / W). \qquad (1.11.25)$$

Of course now (x_1, y_1) has to be selected such that the volumetric deformation at this point is the same used in Equation (1.11.25). Then the system (1.11.24) simplifies as:

$$k^2 = -\frac{y_1^2}{(x_1 - x_2)(x_1 + x_2 - 2C)},$$
$$y_1^2 - \frac{y_1^2}{(x_1 - x_2)(x_1 + x_2 - 2C)}(x_1 - C)^2 - (-\gamma e^{-\beta C} + \theta C + \alpha)^2 = 0. \qquad (1.11.26)$$

For the group 10117-19, the ultimate surface is a straight line $\sqrt{J_{2D}} = \theta J_1 + \alpha$ with α = 11.45 and θ = 0.19. For the rest of the groups, except group 10165-66, it is reasonable to assume that the ultimate surface is also a straight line. The coefficients α and θ for these groups are given in Table 1.11.2. Coefficient γ for all of them is zero.

Table 1.11.2. Ultimate yield surface constants for plugs 10118 - 10197 ft.

Plug	Alpha	Theta	Gamma	Beta
10117-19	11.45	0.19	0	0
10121-22	9.6	0.2	0	0
10136-37	12.17	0.172	0	0
10156-57	9.78	0.21	0	0
10165-66	15.52	0.067	5.82	0.0229
10197-99	15.581	0.2	0	0

Moving caps for some plugs under examination are plotted in Figure 1.11.6.

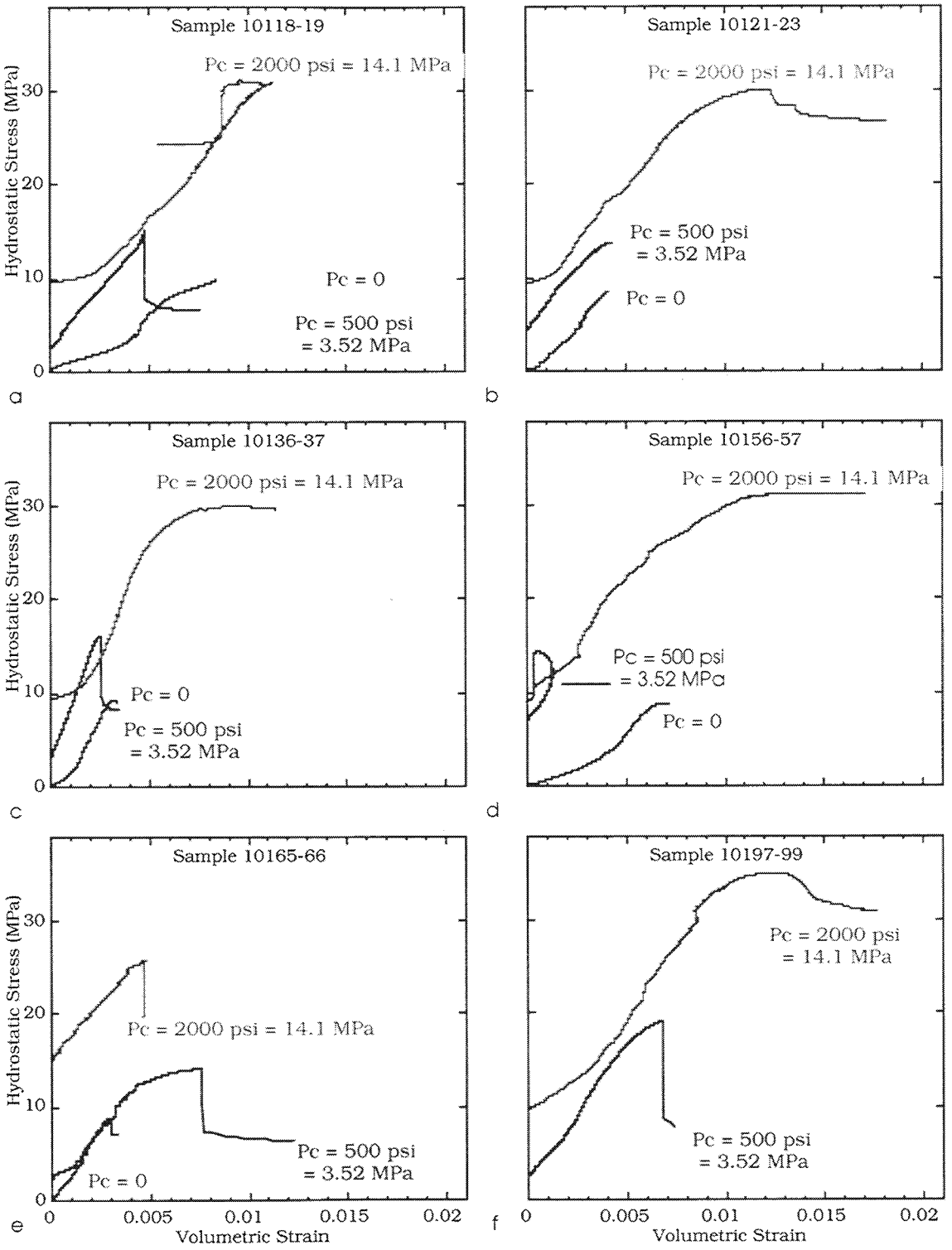

Figure 1.11.1. Average hydrostatic stress versus volumetric deformation for the 10118-97 ft core. Loading is axial.

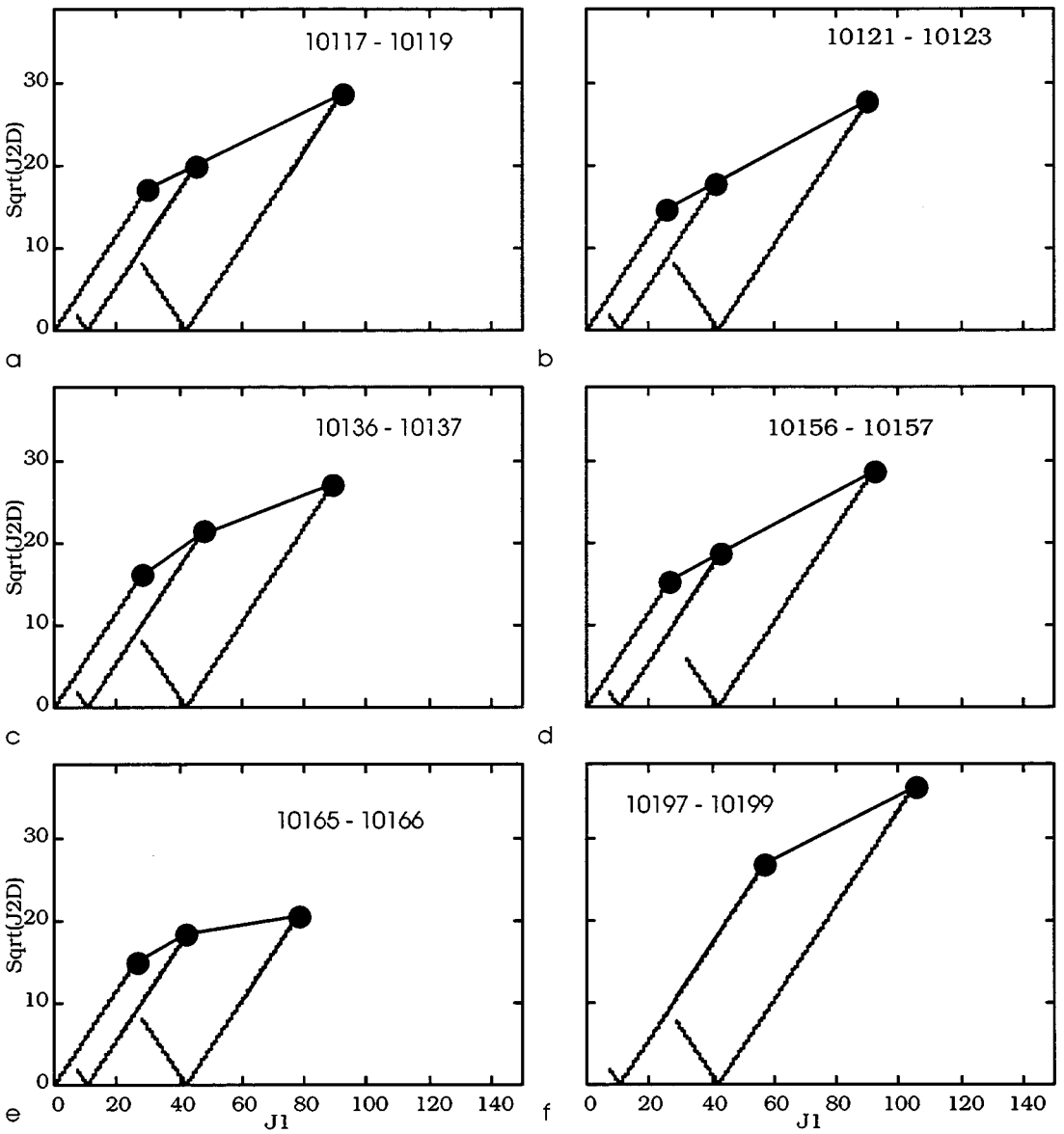

Figure 1.11.2. Failure points and stress paths for the 10118-97 ft core.

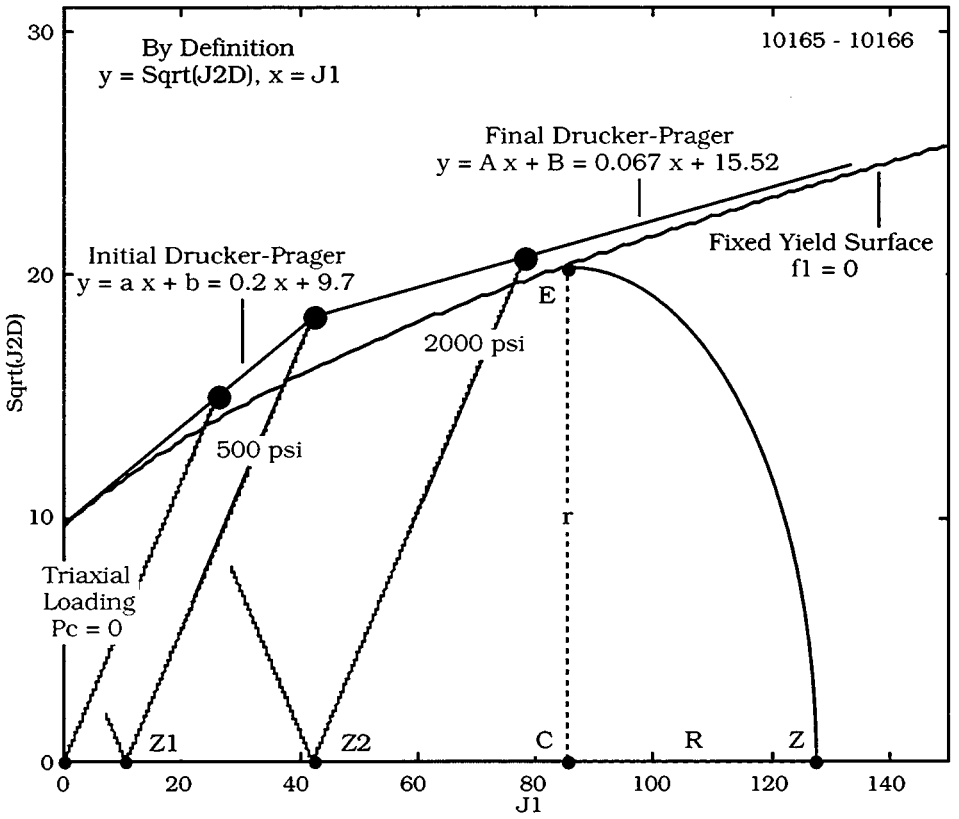

Figure 1.11.3. Building CAP model surfaces. Based on 10165-66 ft data.

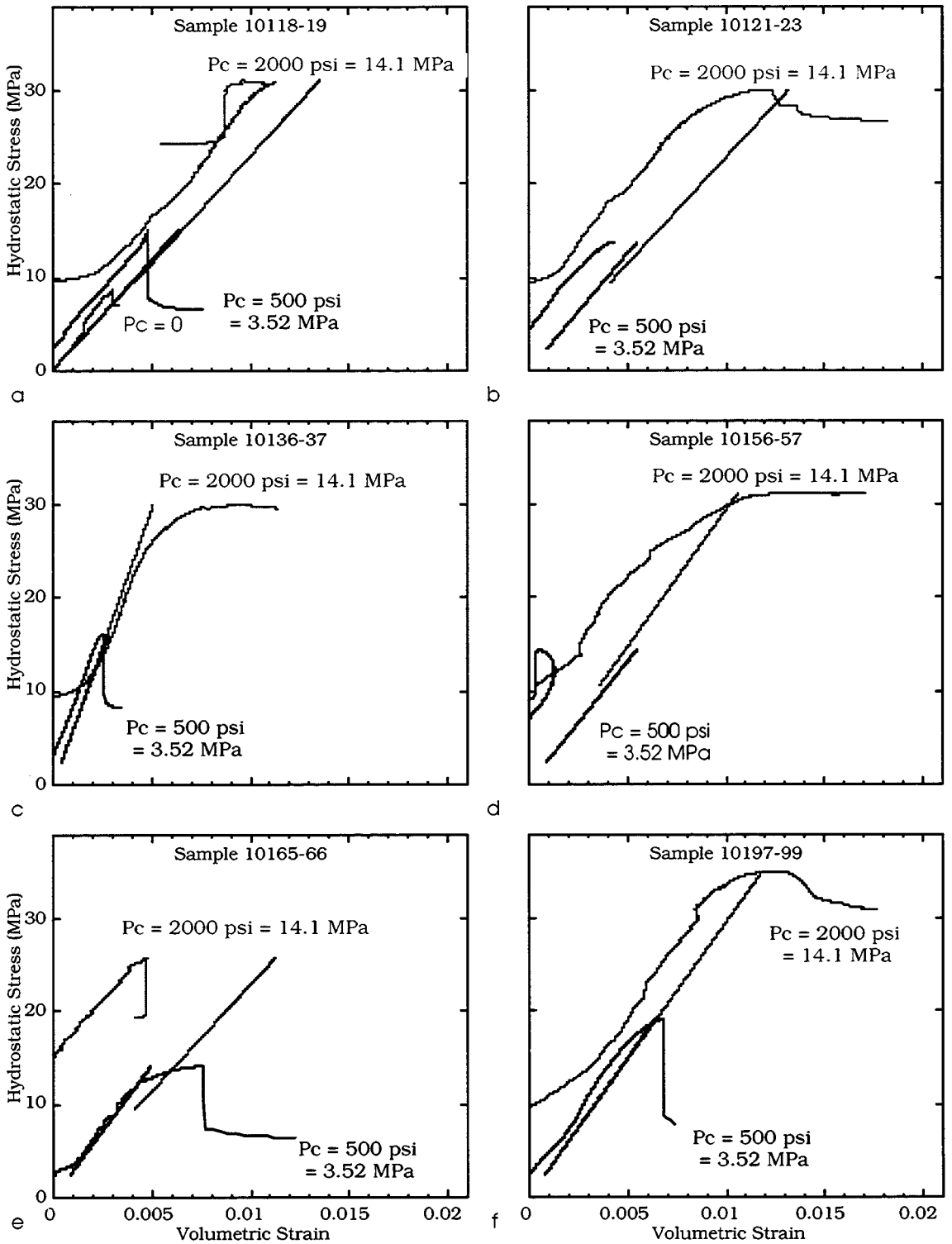

Figure 1.11.4. Average hydrostatic stress versus volumetric deformation for the 10118-97 ft core. Loading is axial. The curves represent the actual data. The straight lines represent the shifted data such that the volumetric deformation is zero at zero hydrostatic stress.

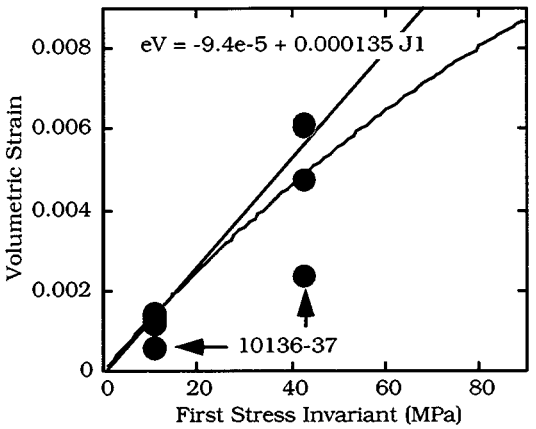

Figure 1.11.5. Average hydrostatic stress versus volumetric deformation for the 10118-97 ft core. Loading is axial. The data points are at pure volumetric deformation where the second deviatoric invariant is zero. The curve follows Equation (1.11.17). The straight line is a linear fit to the points without the outlier 1036-37, according to Equation (1.11.17a).

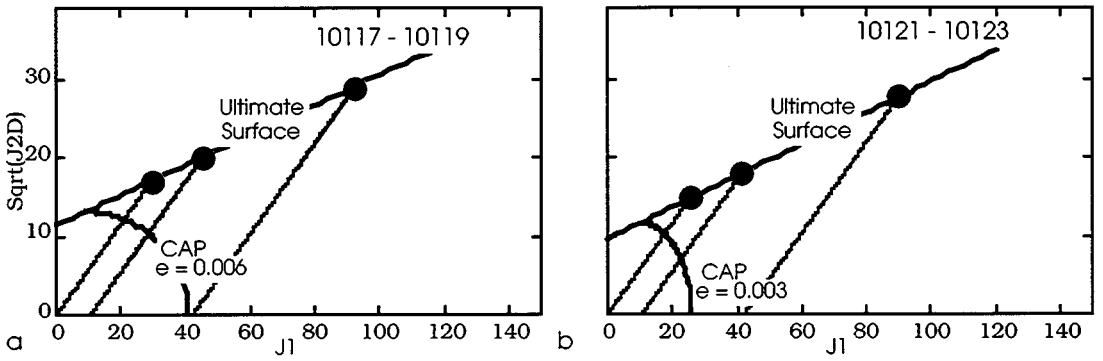

Figure 1.11.6. Yield Surfaces for two plug groups.

2.0 RESULTS OF THE EXPERIMENTAL STUDIES

2.1 Berea Sandstone

Results from the Berea sandstone samples were obtained from pore cycling tests under hydrostatic stress in which two principal stresses are in equal magnitude. The volumetric strains and wave velocities were measured during the tests. Pore pressures in the range from 0 to 9200 psi were employed in the testing program. Static and dynamic measurements were made concurrently on the same sample. It is evident from Table 2.1 and Figure 2.1 that Vp velocities calculated for constant 500 psi effective stresses are decreasing with increasing confining pressures.

Table 2.1 Acoustic properties of the Berea Sandstone tested at variable effective stress

Paxial	Pradial	Ppore	Peff	dX	Tp	Ts	Vp	Vs	Vp/Vs
psi	psi	psi	psi	inch	usec	usec	m/s	m/s	
500	500	0	500	0.0000	13.8460	23.9270	4983	2915	1.7092
1000	1000	500	500	0.0001	13.8460	23.9270	4982	2915	1.7092
1500	1500	1000	500	0.0003	13.8460	23.9068	4982	2917	1.7077
2000	2000	1500	500	0.0004	13.8325	23.9365	4987	2913	1.7118
2500	2500	2000	500	0.0005	13.8319	24.0020	4987	2905	1.7169
3000	3000	2500	500	0.0006	13.8261	24.0180	4989	2902	1.7189
3500	3500	3000	500	0.0007	13.8204	24.0466	4991	2899	1.7219
4000	4000	3500	500	0.0009	13.7940	24.0768	5001	2894	1.7278
5000	5000	4500	500	0.0010	13.7495	24.1430	5018	2886	1.7389
5500	5500	5000	500	0.0011	13.7132	24.2049	5032	2878	1.7487
6000	6000	5500	500	0.0013	13.6948	24.2010	5039	2878	1.7509
6500	6500	6000	500	0.0014	13.6640	24.2348	5051	2873	1.7578
7000	7000	6500	500	0.0014	13.6410	24.2448	5060	2872	1.7618
8000	8000	7500	500	0.0016	13.6327	24.2860	5063	2867	1.7661
8500	8500	8000	500	0.0017	13.6094	24.2849	5072	2867	1.7693
9000	9000	8500	500	0.0020	13.6000	24.2930	5075	2865	1.7713
9000	9000	8000	1000	0.0020	13.3553	23.8893	5175	2918	1.7736
9000	9000	7500	1500	0.0021	13.1900	23.5600	5245	2962	1.7707
9000	9000	7000	2000	0.0022	13.0260	23.1940	5315	3013	1.7645
9000	9000	6500	2500	0.0022	12.8848	22.8693	5378	3059	1.7581
9000	9000	6000	3000	0.0023	12.7790	22.6450	5426	3092	1.7549
9000	9000	5500	3500	0.0023	12.6425	22.4620	5489	3119	1.7597
9000	9000	5000	4000	0.0024	12.5380	22.3700	5538	3133	1.7676
9000	9000	4500	4500	0.0024	12.4180	22.1870	5596	3161	1.7702
9000	9000	5000	4000	0.0024	12.4920	22.2801	5560	3147	1.7669
9000	9000	5500	3500	0.0024	12.5330	22.3700	5540	3133	1.7684
9000	9000	6000	3000	0.0024	12.6292	22.4620	5495	3119	1.7617
9000	9000	6500	2500	0.0024	12.7380	22.5754	5444	3102	1.7551
9000	9000	7000	2000	0.0024	12.8397	22.7360	5398	3078	1.7536
9000	9000	7500	1500	0.0023	12.9921	22.9138	5330	3052	1.7462
9000	9000	8000	1000	0.0023	13.1080	23.1940	5279	3012	1.7526
9000	9000	8500	500	0.0022	13.3130	23.5010	5192	2970	1.7484

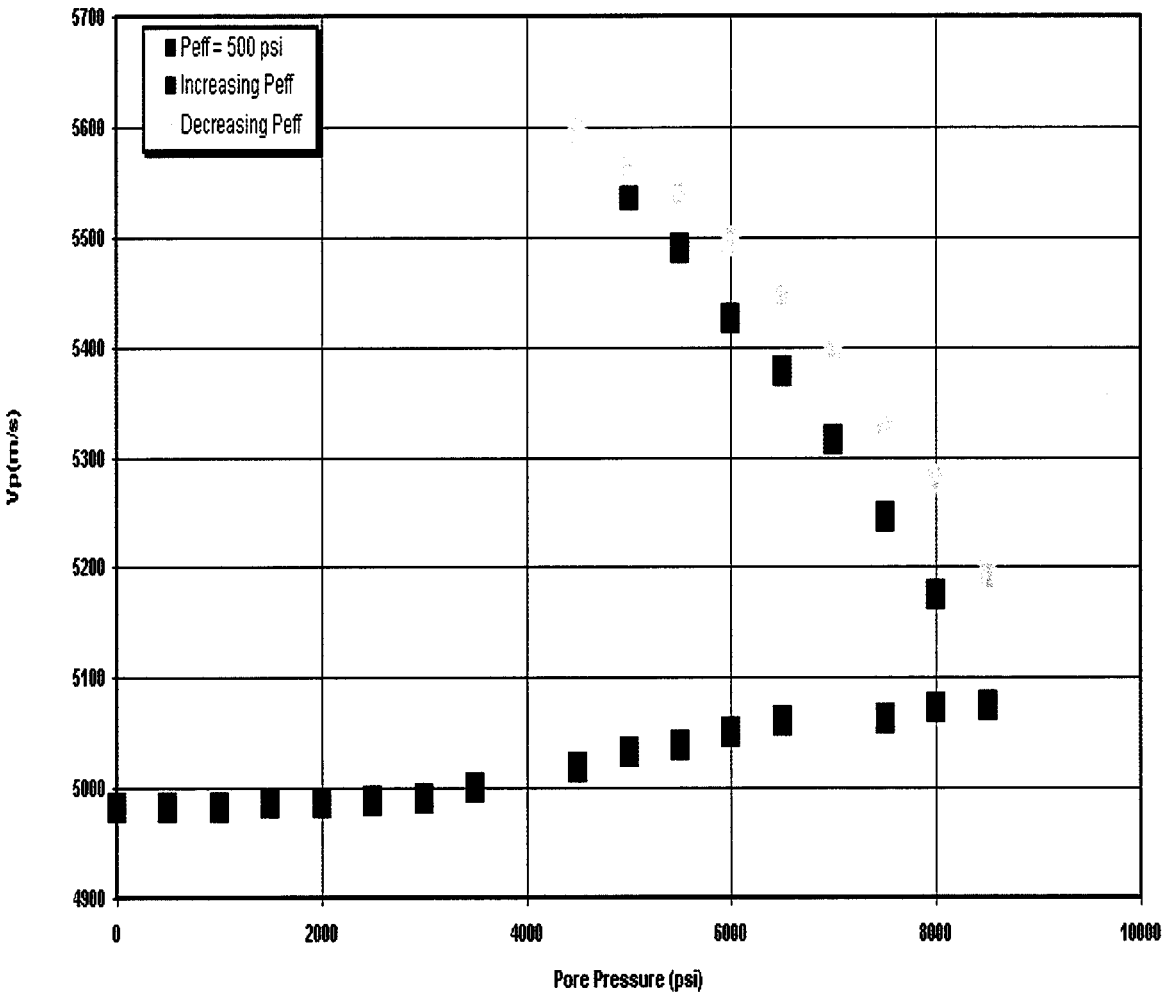

Figure 2.1. P wave velocities of the Berea Sandstone tested at variable effective stress

The initial loading curve for Berea sample (Figure 2.2), generated by keeping the effective stress constant while increasing the pore fluid pressure and confining stress, allows computation of the so-called "unjacketed" compliance of the rock and pore space. Figure 2.3 shows elastic and residual deformations as a function of effective and hydrostatic stresses.

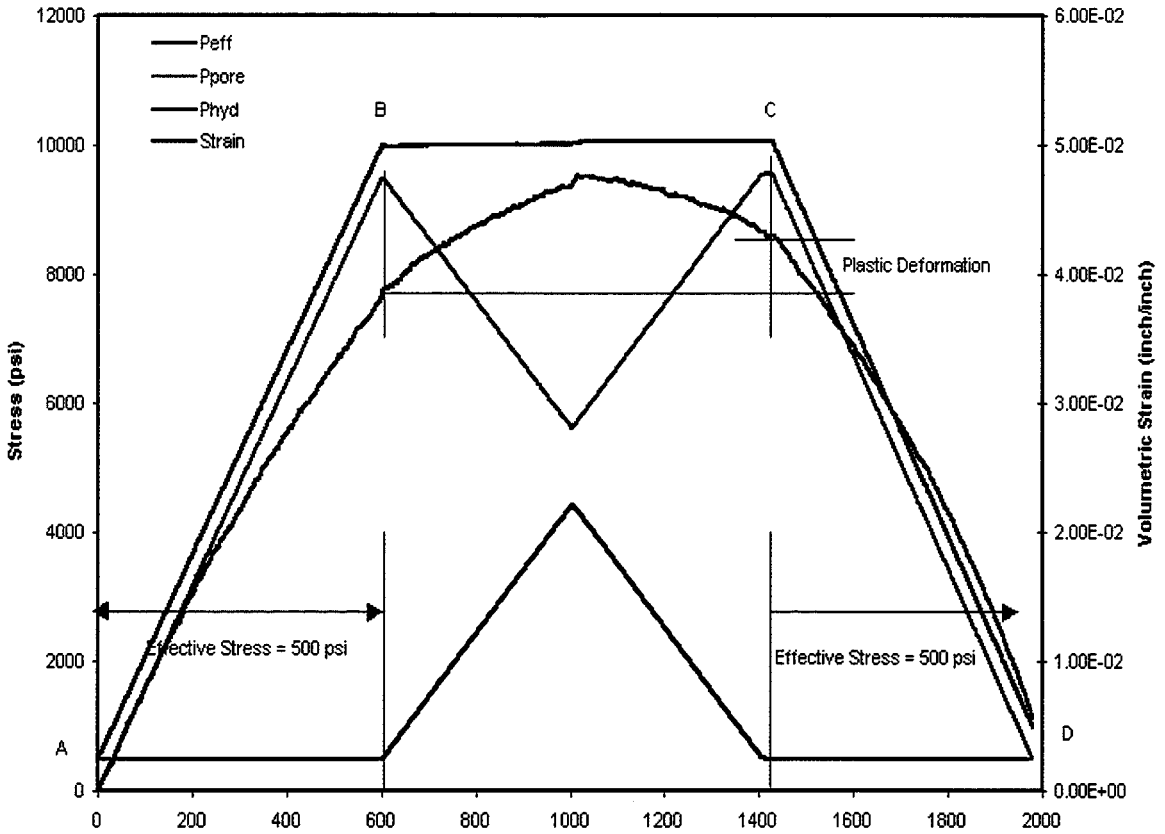

Figure 2.2: Sample loading history showing confining stress, pore pressure and volumetric strain. A-B raise hydrostatic stress at constant effective stress; B-C decrease pore pressure maintaining hydrostatic stress; C-D increase pore pressure to measure plastic deformation; and D to end decrease stresses at constant effective stress.

Loading limbs B-C and C-D reproduce the effects of fluid drawdown and subsequent recharge. The total volume compliance was computed independently for the loading portion (B-C) and then for the unloading portion (C-D) by fitting each portion of the curve to a smooth power law, as shown in Figure 2.3.

$$C_{SB} = \frac{1}{\mathrm{K}_{SB}} = \frac{1}{V}\frac{\partial V}{\partial P_p}\Big|P_c \qquad (7)$$

Inverting the power law relationship allows a computation of the total compressibility due to a change in pore pressure keeping the confining pressure constant which can then be plotted as a function of the sample effective confining stress, Table 2.1.

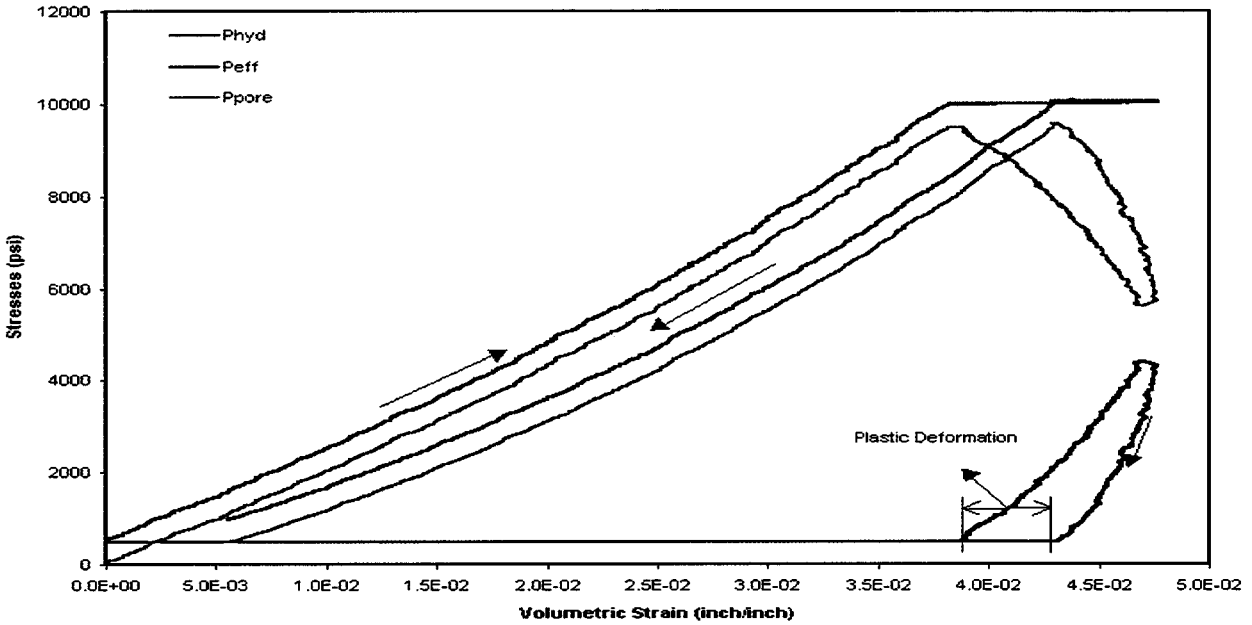

Figure 2.3. Elastic and residual deformations as a function of pore pressure, effective and hydrostatic stresses.

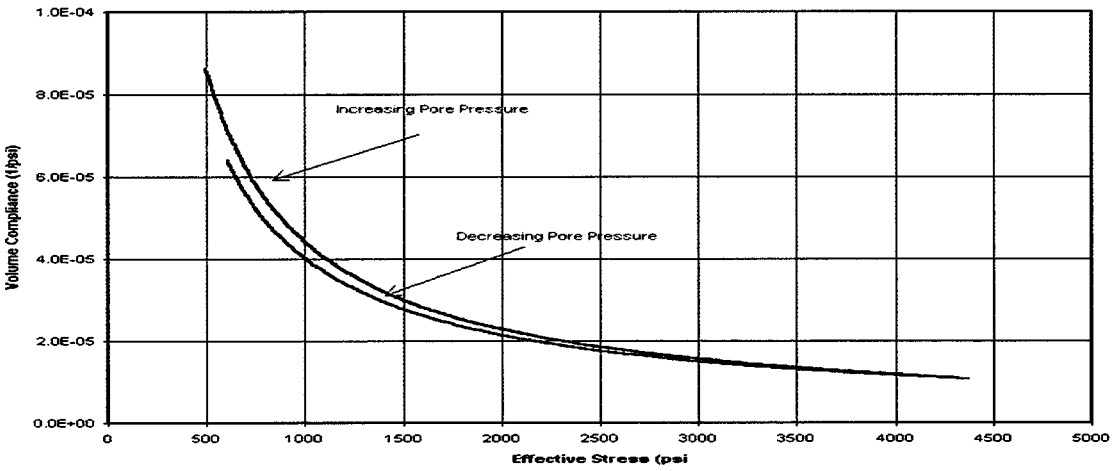

Figure 2.4. Stress-strain curves over the drawdown (B-C) and recharge (C-D) portions of the loading curve. Also shown is the power law fit to each, from which the total compliance due to pore pressure changes can be determined as a function of effective stress at constant confining stress equivalent to the overburden at the depth from which the sample was obtained.

Figure 2.3 indicates that, the compressibility of the Berea sandstone with high permeability (k = 750 mD) is greater during loading (C_{load} = 2.03E-6 psi^{-1}) (that is, during pore pressure reduction accompanying production of hydrocarbons) than during

unloading (C_{unload} = 1.0936E-6 psi^{-1}) (pore pressure increase). From the biaxial test results (Figure 2.6), compressibility of the Berea sandstone with high permeability was calculated to be 2.777E-6 psi^{1}. Figure 2.5 indicates that this is a consequence of the permanent deformation associated with a pore pressure decrease (effective pressure increase), as discussed below. An important implication of this is that the state of the reservoir cannot be recovered by injection once the reservoir fluid pressure has been decreased by production. Neither the total volume change, nor the porosity change, is fully recoverable. Therefore, stresses on casing and surface deformation (subsidence) that occur as a consequence of production cannot be entirely mitigated by re-injection. Experience reveals that in depleted sands only 10% of the volume loss due to production is recoverable.

A consequence of the difference between the loading and unloading compressibilities is that, on increasing the pore fluid pressure (C-D), not all of the volume reduction is recovered. The portion that is not recovered is the anelastic permanent deformation and is approximately $4x10^{-3}$ strain accompanying approximately 4000 psi draw down and recovery.

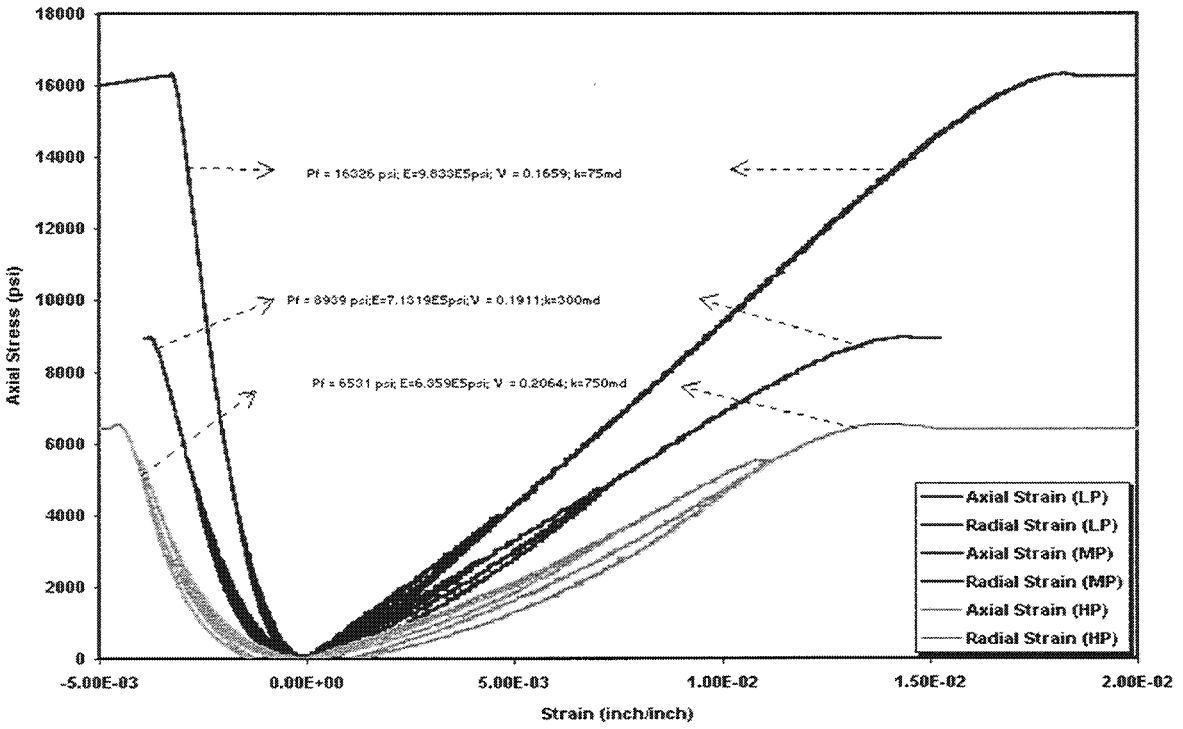

Figure 2.5. Elastic moduli, and failure strength of Berea sandstones with permeabilities of 75 mD, 300 mD and 750 mD.

If the permanent deformation is a linear function of the draw down, this corresponds to a "reservoir non-recoverable compliance" of $8x10^{-7}$ psi^{-1}. Because the rock properties are strongly effective-stress dependent, this is at best only an approximation. The recoverable deformation is approximately 90% of the total volume reduction, indicating that Berea with high permeability has experienced good consolidation and cementation. The values of the compressibilities calculated from two type of the test results obviously indicates that samples should be tested under in situ stress conditions and current testing practices are not representative.

The maintenance of the pore pressure of the formation depends critically on the fluid properties, the porosity, the permeability, the production rate, the pore compliance, and the volume of fluid available to maintain the in situ pressure. The higher the permeability and the lower the production and higher injection rate, the more likely it is that the reservoir pressure can be maintained by recharge. The permeability, pore compliance, and porosity are all measurable in the lab. Once these are known reservoir simulation can be carried out using reasonable reservoir volumes and fluid properties to establish how pore pressure will change as a function of injection or production rate. This allows engineers to choose the injection rate to achieve the desired results.

We address now a method to obtain a measure of the pore compliance associated with the loading path B-C:

$$C_{pore} = \frac{1}{\mathrm{K}_{pore}} = \frac{1}{V_{pore}} \frac{\partial V_{pore}}{\partial P_p} \Big| P_c \qquad (8)$$

This is the portion of the loading path that mimics the behavior of the reservoir during drawdown and thus it is of particular relevance to reservoir performance.

The pore compliance provides a measure of the ability of the reservoir to deliver energy to the system as the fluid is withdrawn. It is not the same as the total compliance presented in Figure 2.8. These results were computed using the strain that was measured over this loading path of the entire volume of the sample (solid plus void). Therefore a correction needs to be applied to this data before a measure of the pore compliance can be obtained. If

(1) The material obeys the Gassmann assumptions, and

(2) The volume change due to a change in pore pressure at constant confining pressure is equal to the volume change due to a change in pore pressure at constant effective pressure minus the volume change due to a change in confining pressure at a constant pore pressure,

then the desired compliance (which describes the pore volume change due to a change in fluid pressure) can be calculated from the measurements as:

$$C_{pore} = \frac{1}{K_{pore}} = \frac{C_{BC}}{\phi} + C_{AB} \qquad (14)$$

The result of this calculation is Cpore = 13.9×10^{-6} psi^{-1} for $\phi = 0.21$ as above.

Compressional and shear velocities of Berea sandstone with various permeabilities were carried out using pulse transmission technique to obtain the corresponding dynamic moduli (Table 2.1, Figures 2.1 and 2.6).

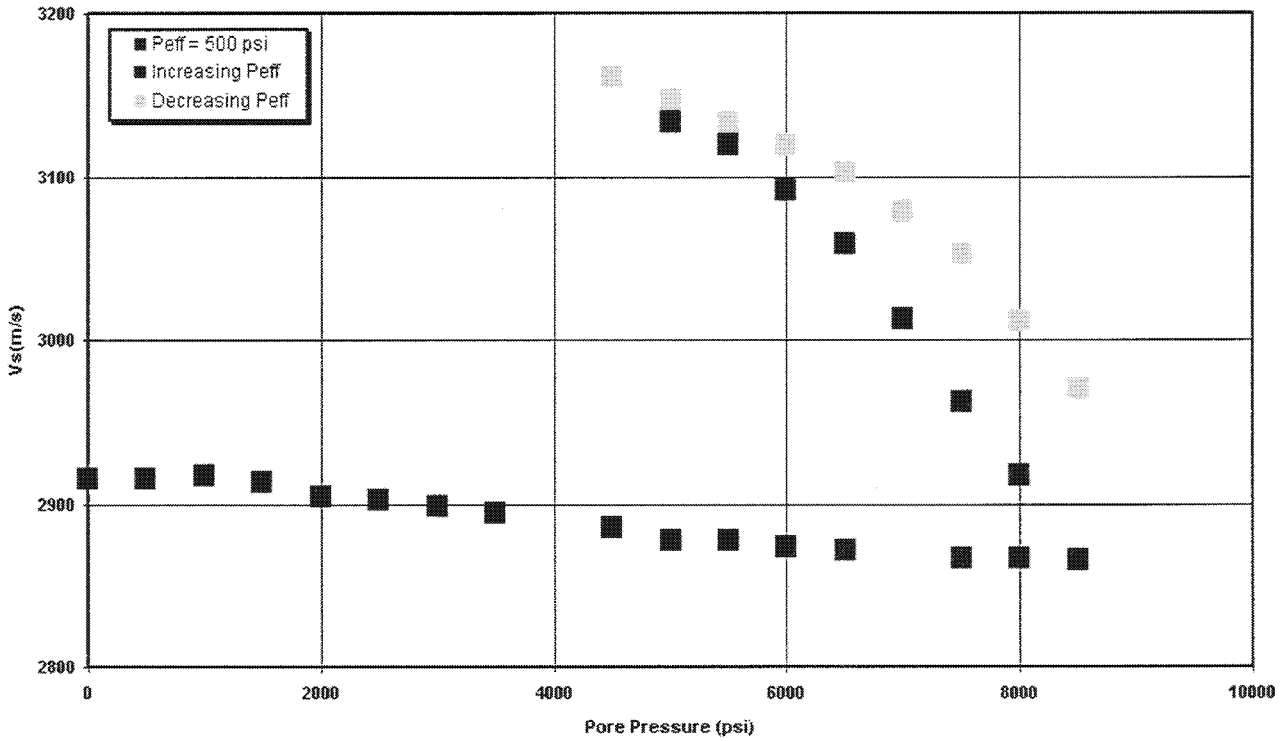

Figure 2.6. S wave velocities of the Berea Sandstone tested at variable effective stress

2.2 Ultrasonic Velocities and Elastic Moduli of GOM Clayey Sandstones

Biaxial compaction test was performed. Pore and confining pressures were held constants as axial pressure was varied, duplicating conventional rock testing procedures. The measured axial and radial strains provided estimated values of Young's modulus and Poisson's ratios for the bulk solid based upon the tangent moduli. The effective stress coefficient of the sample was assumed to be unity. Compressive strength, compressional and shear velocities of the GOM samples were measured. In the testing program confining pressure of 0, 500 and 2000 psi were employed (Figures 2.7 through 2.12 and Tables 2.2 through 2.14).

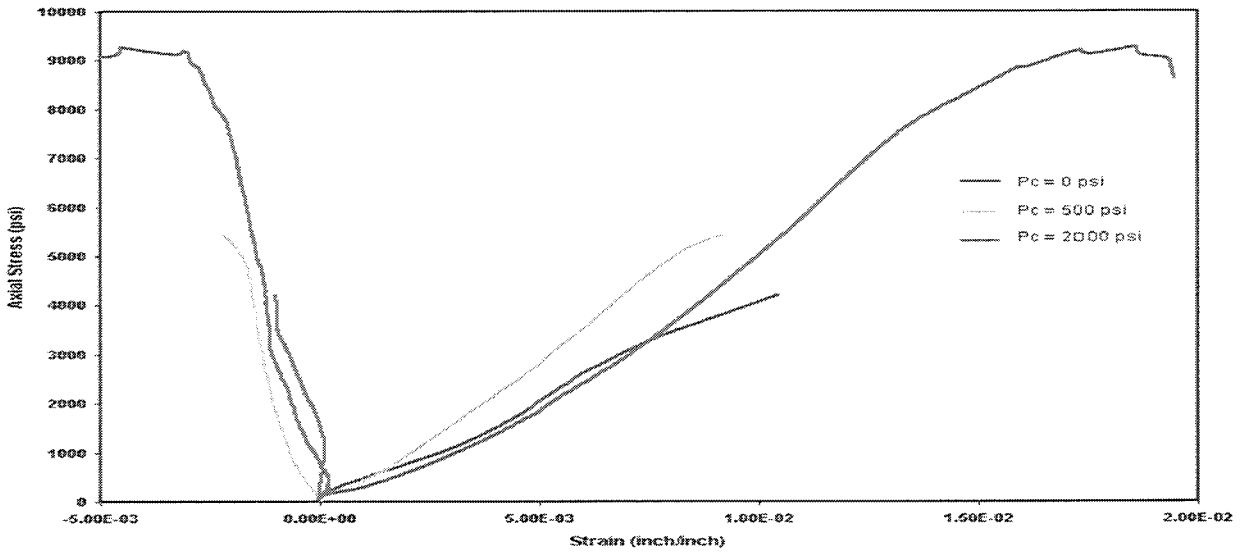

Figure 2.7. Axial, radial strains and failure strength of GOM clayey sandstone (10118') for various confining pressures.

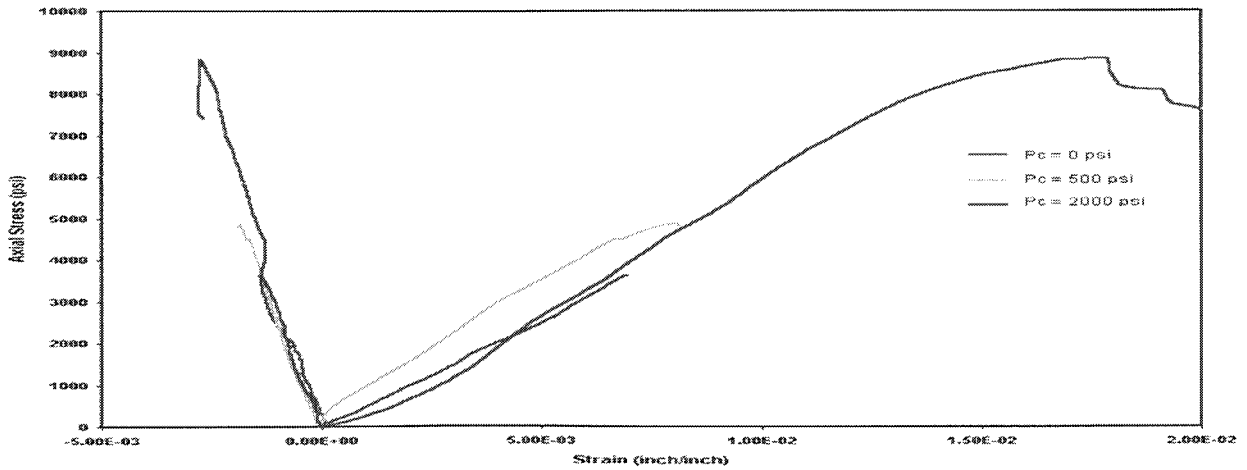

Figure 2.8. Axial, radial strains and failure strength of GOM clayey sandstone (10123') for various confining pressures.

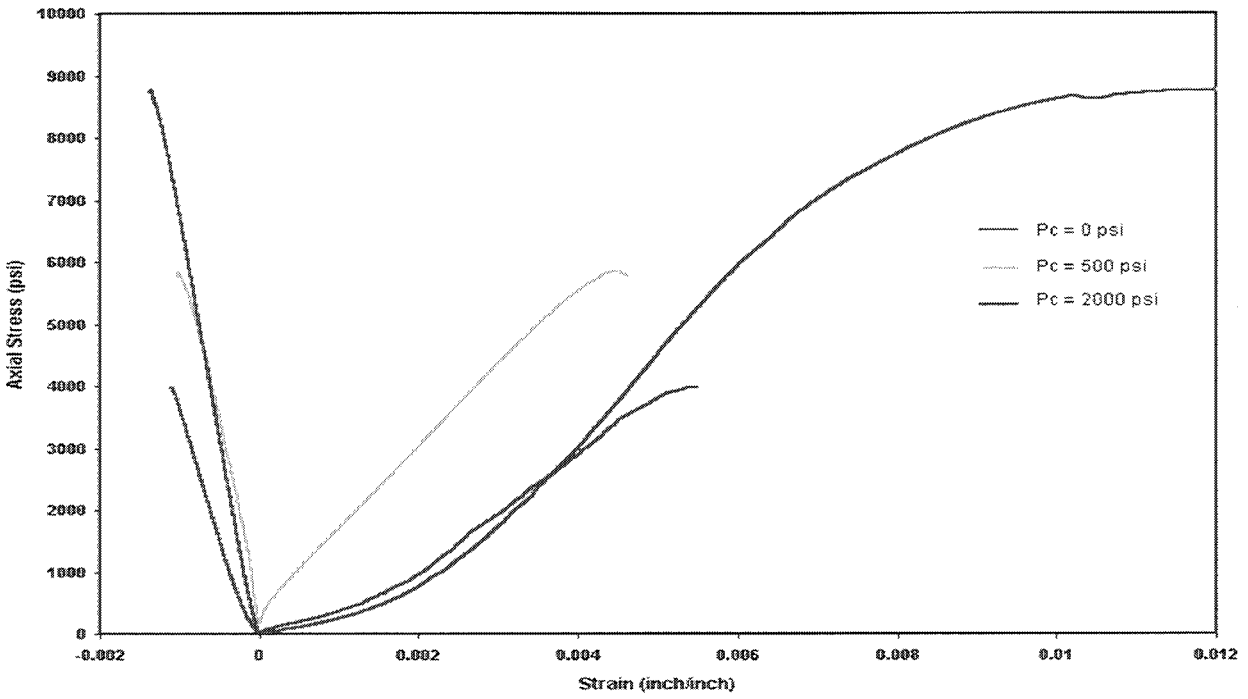

Figure 2.9. Axial, radial strains and failure strength of GOM clayey sandstone (10136') for various confining pressures.

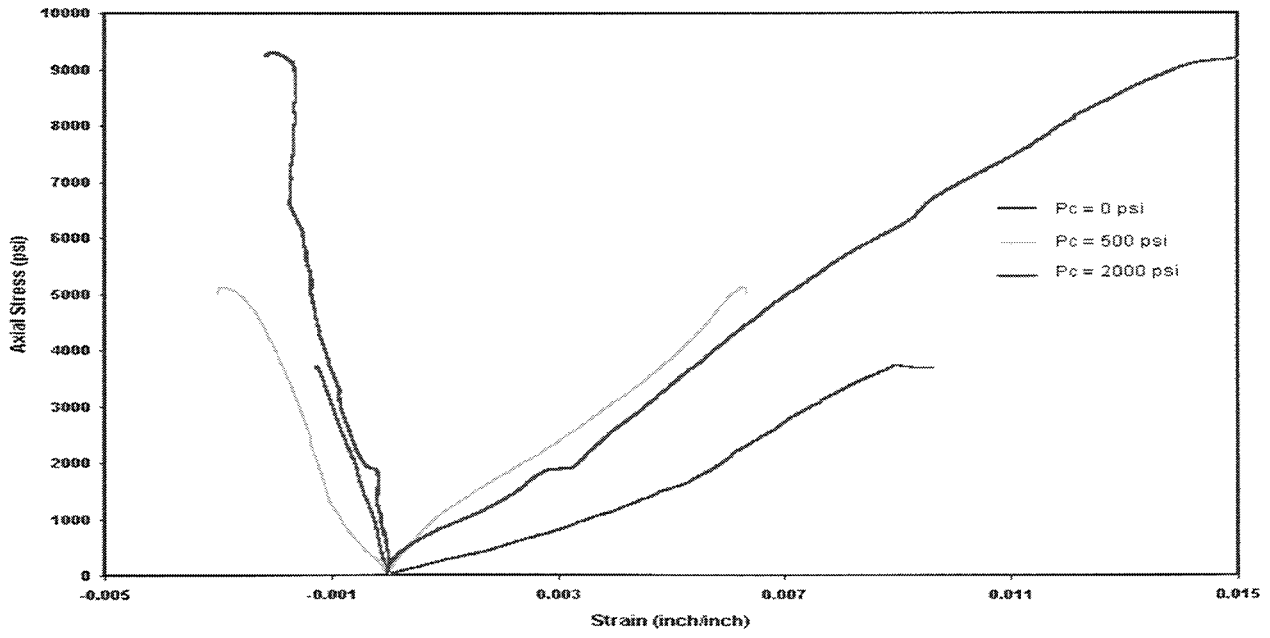

Figure 2.10. Axial, radial strains and failure strength of GOM clayey sandstone (10156') for various confining pressures.

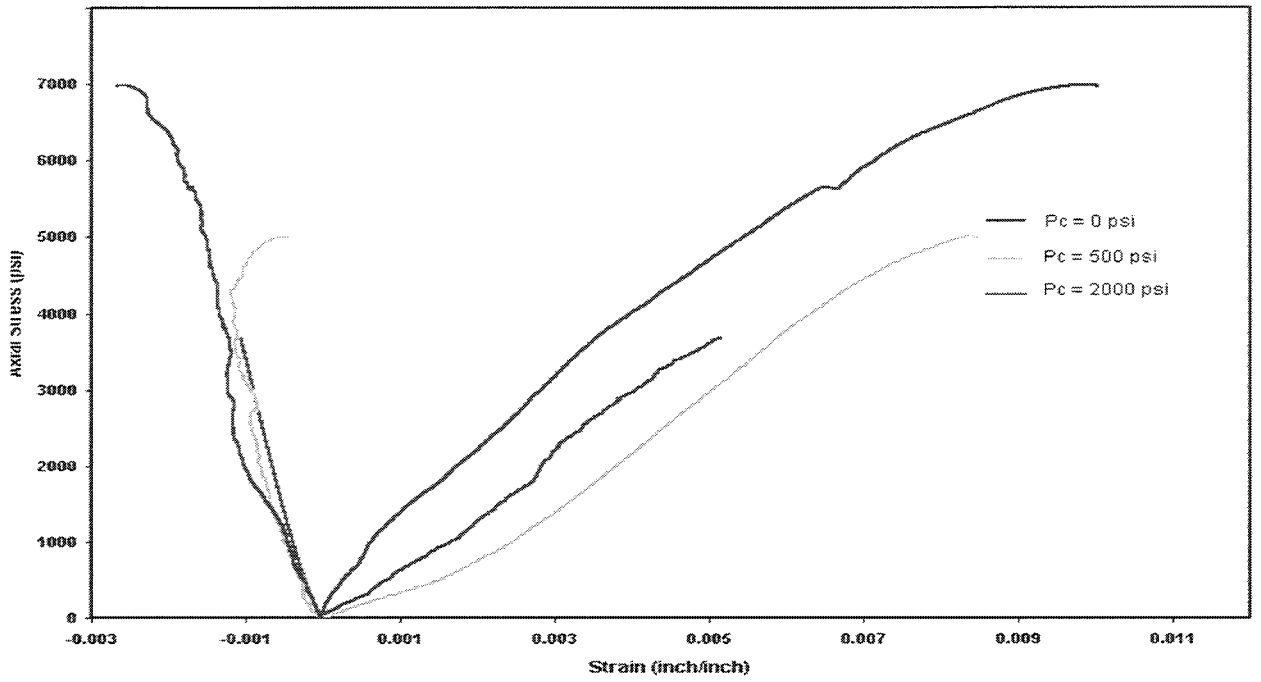

Figure 2.11. Axial, radial strains and failure strength of GOM clayey sandstone (10165') for various confining stresses.

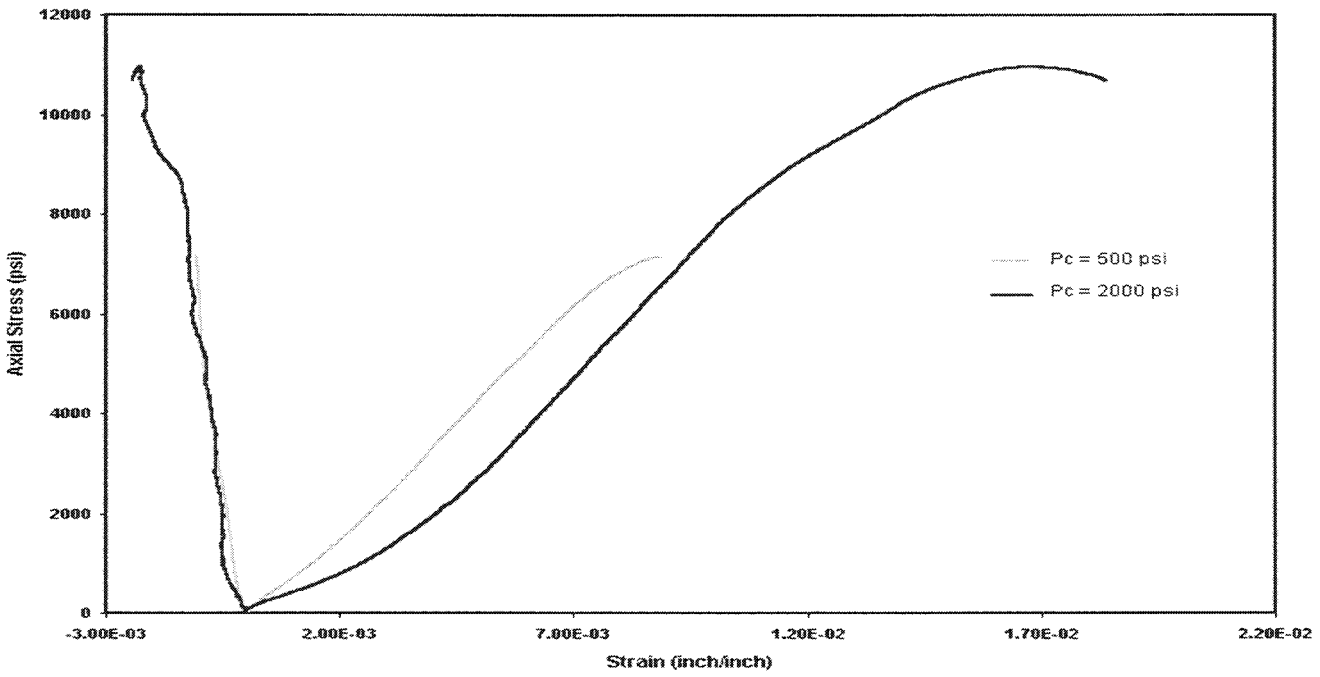

Figure 2.12. Axial, radial strains and failure strength of GOM clayey sandstone (10195') for various confining stresses.

Table 2.2. Compressive strength and elastic moduli of GOM samples tested at various stress conditions.

Depth ft	P_c psi	$P_{failure}$ psi	E psi	ν
10118.90	0	4197	5.44E+05	0.2660
10117.90	500	5915	6.77E+05	0.2434
10119.30	2000	11123	7.01E+05	0.1809
10123.40	0	3627	5.15E+05	0.2296
10121.11	500	5383	6.51E+05	0.2284
10122.60	2000	10849	7.24E+05	0.2200
10137.60	0	3974	9.78E+05	0.2229
10136.00	500	6348	1.33E+06	0.2081
10136.80	2000	10657	1.46E+06	0.2000
10156.90	0	3723	6.03E+05	0.2191
10157.70	500	5613	6.30E+05	0.2026
10157.00	2000	11300	7.02E+05	0.1977
10165.00	0	3673	7.55E+05	0.2096
10166.00	500	5513	7.90E+05	0.1951
10165.90	2000	8989	8.44E+05	0.1889
10199.50	500	7645	8.89E+05	0.1732
10197.00	2000	12961	9.86E+05	0.1711

2.3 Acoustic Moduli of GOM Samples Tested

Compressional and shear velocity measurements have been completed on twelve 1 ½" diameter GOM samples, all samples vertically oriented. The sample depth interval s range from 10118 ft to 10195 ft. An increase in compressional velocity for the all samples designated for hysterisis effect ranged from 10 to 13 percent for the initial increase of net stress from 500 psi to 4000 psi, while shear velocities increased from 12 to 17 percent. When net stress was lowered from maximum to initial stresses, the compressional velocities decreased from 3 to 5.6 percent from maximum velocity and the shear velocities decreased from 3 to 4 percent. The total hysteresis for all samples at around 4000 psi ranges from 2 to 9 percent for compressional velocity and 4 to 12 percent for shear velocities. Poisson's ratio, Vp/Vs, and interval transit times from measurements were calculated.

An initial axial stress of 500 psi was applied to each sample with an atmospheric pressure. The acoustic transmit times were determined via a 100 MHz digital oscillope. Rock transit times corrected for system transit times were then divided by the sample length to obtain velocity. Acoustic velocities were determined for compressional and shear waves. Dynamic elastic moduli are determined from bulk density and compressional and shear wave velocities (Table 2.3 through 2.13).

Table 2.3. Compression, shear wave velocities, and acoustic moduli of sample 10117' tested under various stress conditions.

Paxial	Pconfining	Δx	Tp	Ts	Vp	Vs	Vp/Vs	ν	E
psi	psi	inch	usec	usec	m/s	m/s			psi
500	500	0.0000	11.0110	20.3300	2495	1422	1.7539	0.2592	6.161
1000	1000	0.0007	10.7330	19.1300	2577	1546	1.6673	0.2191	6.364
1500	1500	0.0013	10.5490	18.5300	2634	1615	1.6308	0.1987	6.539
2000	2000	0.0021	10.4180	18.1900	2675	1657	1.6148	0.1890	6.690
3000	3000	0.0038	10.1980	17.9200	2746	1689	1.6259	0.1958	7.089
4000	4000	0.0065	10.0220	17.7800	2801	1703	1.6454	0.2071	7.447
3000	3000	0.0057	10.0440	17.8100	2796	1700	1.6445	0.2067	7.415
2000	2000	0.0049	10.1240	18.0000	2769	1676	1.6522	0.2110	7.300
1500	1500	0.0043	10.2000	18.1400	2744	1659	1.6541	0.2120	7.173
1000	1000	0.0035	10.3300	18.2900	2701	1641	1.6458	0.2074	6.923
500	500	0.0028	10.4620	18.4700	2658	1620	1.6411	0.2047	6.692

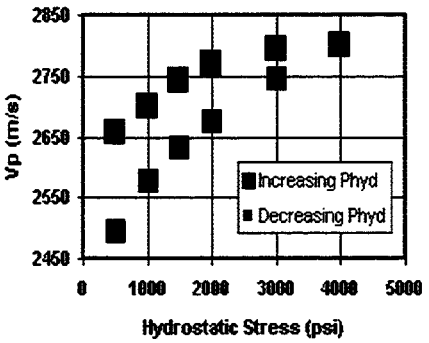

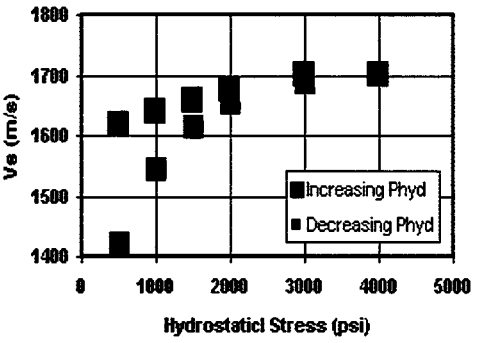

Table 2.4. Unconfined compression, shear wave velocities and acoustic moduli of sample 10118' tested.

Paxial	Δx	Tp	Ts	Vp	Vs	Vp/Vs	ν	E
psi	inch	usec	usec	m/s	m/s			psi
178	0.0000	27.5460	44.2860	2308	1487	1.5524	0.1454	4.7966
462	0.0001	26.3050	43.6260	2428	1512	1.6056	0.1832	5.4848
996	0.0001	24.3460	41.9610	2646	1581	1.6734	0.2223	6.7280
1476	0.0002	23.2420	40.9890	2787	1624	1.7157	0.2427	7.5880
1991	0.0003	22.4370	40.3300	2899	1655	1.7519	0.2584	8.3161
2934	0.0006	21.6480	39.8900	3019	1676	1.8011	0.2772	9.1484
3503	0.0011	21.2970	39.4500	3074	1697	1.8114	0.2808	9.5161
3912	0.0016	21.1640	39.0110	3096	1719	1.8007	0.2771	9.6198
4427	0.0021	21.0000	38.7910	3122	1730	1.8048	0.2785	9.7980

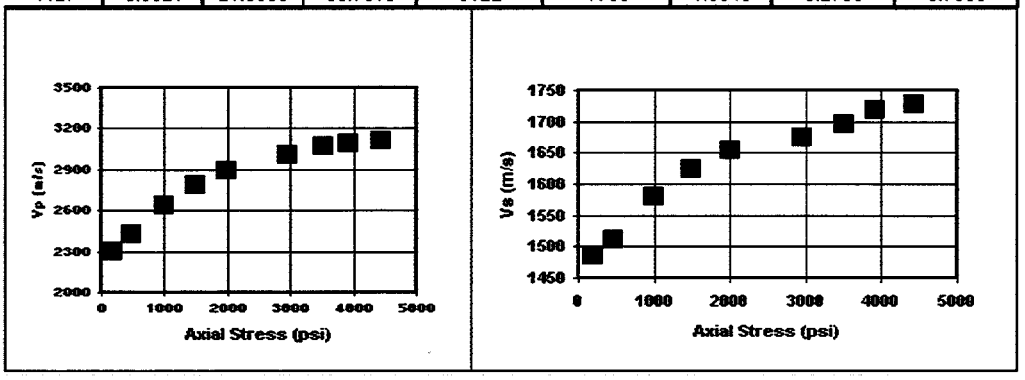

Table 2.5. Compression, shear wave velocities and acoustic moduli of sample 10121' under various stress conditions.

Paxial	Pconfining	Δx	Tp	Ts	Vp	Vs	Vp/Vs	ν	E
psi	psi	inch	usec	usec	m/s	m/s			psi
500	500	0.0000	9.3516	15.1150	2599	1834	1.4171	0.0040	5.331
1000	1000	0.0002	9.0659	14.8660	2711	1882	1.4408	0.0353	5.983
1500	1500	0.0006	8.8560	14.6410	2799	1927	1.4530	0.0501	6.469
2000	2000	0.0012	8.7242	14.4290	2856	1970	1.4497	0.0462	6.711
3000	3000	0.0021	8.5784	14.1850	2921	2022	1.4444	0.0397	6.974
4000	4000	0.0033	8.4725	14.0310	2968	2055	1.4442	0.0395	7.198
3000	3000	0.0026	8.4945	14.0710	2960	2048	1.4456	0.0411	7.171
2000	2000	0.0020	8.5824	14.2340	2920	2012	1.4515	0.0483	7.025
1500	1500	0.0016	8.6484	14.3560	2890	1985	1.4558	0.0533	6.915
1000	1000	0.0012	8.7582	14.5100	2841	1953	1.4548	0.0522	6.675
500	500	0.0008	8.9059	14.6900	2777	1916	1.4494	0.0457	6.338

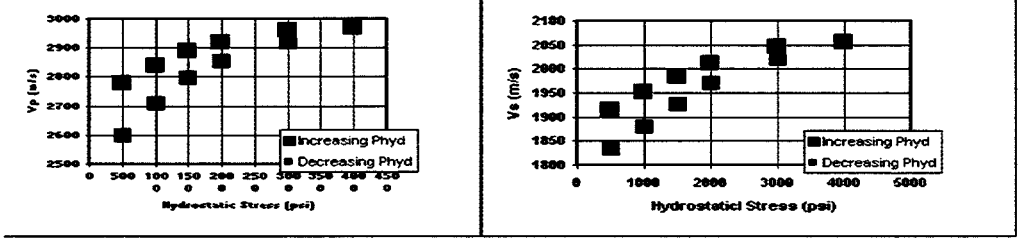

Table 2.6. Compression, shear wave velocities and acoustic moduli of sample 10123' tested at 2000 psi confining pressure.

Paxial	Δx	Tp	Ts	Vp	Vs	Vp/Vs	ν	E
psi	inch	usec	usec	m/s	m/s			psi
516	0.0000	30.1650	51.4290	2593	1558	1.6637	0.2172	6.4324
996	0.0001	28.2420	49.4510	2787	1628	1.7111	0.2407	7.5729
1529	0.0001	27.2340	48.3520	2900	1670	1.7365	0.2519	8.2768
2045	0.0002	26.6850	47.8120	2966	1691	1.7535	0.2590	8.7059
3005	0.0004	25.9520	47.2530	3058	1714	1.7845	0.2711	9.3464
3734	0.0007	25.5310	47.0330	3114	1723	1.8076	0.2795	9.7532

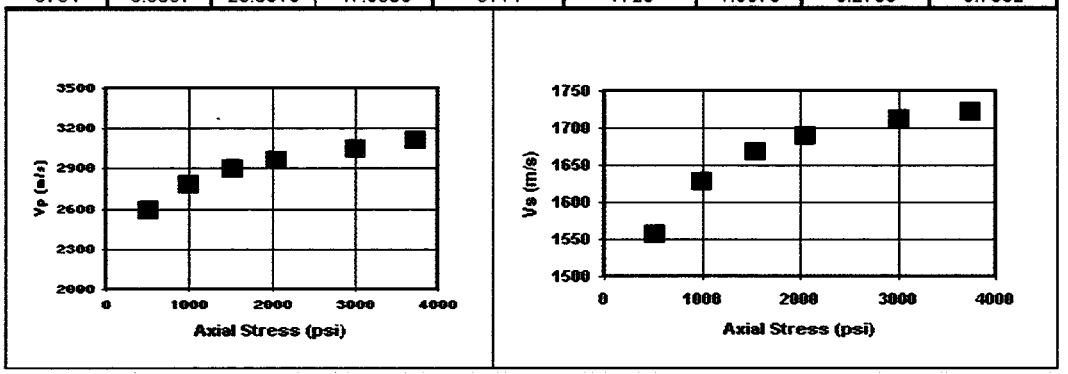

Table 2.7. Compression and shear wave velocities and acoustic moduli of sample 10136' under various stress conditions.

Paxial	Pconfining	Δx	Tp	Ts	Vp	Vs	Vp/Vs	ν	E
psi	psi	inch	usec	usec	m/s	m/s			psi
500	500	0.0000	9.2311	19.0000	3001	1485	2.0205	0.3378	9.469
1000	1000	0.0002	9.0982	18.0700	3061	1594	1.9201	0.3139	9.675
1500	1500	0.0003	8.8766	17.6630	3167	1647	1.9230	0.3147	10.363
2000	2000	0.0005	8.6993	17.4500	3256	1675	1.9437	0.3200	11.004
3000	3000	0.0014	8.4333	17.2000	3399	1709	1.9888	0.3308	12.087
4000	4000	0.0026	8.2117	17.0000	3526	1736	2.0310	0.3400	13.093
3000	3000	0.0023	8.2960	17.1000	3475	1722	2.0187	0.3374	12.699
2000	2000	0.0017	8.4977	17.2900	3361	1695	1.9824	0.3293	11.805
1500	1500	0.0012	8.6393	17.5800	3285	1656	1.9839	0.3297	11.283
1000	1000	0.0007	8.8538	18.0040	3176	1601	1.9837	0.3296	10.545
500	500	0.0003	8.9606	19.0000	3125	1485	2.1052	0.3543	10.399

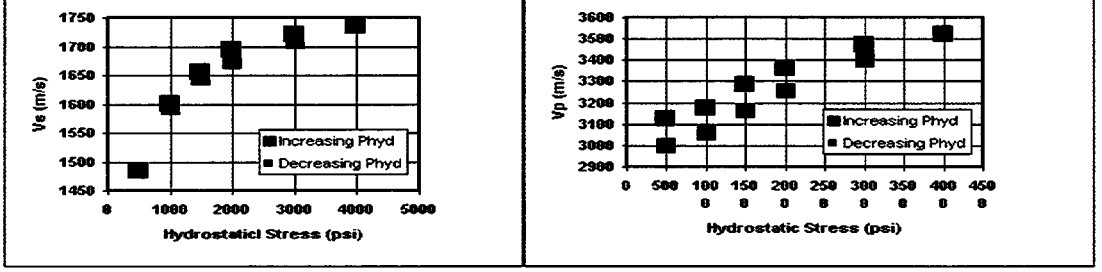

Table 2.8. Unconfined compression, shear wave velocities and acoustic moduli of sample 10137' tested.

Paxial	Δx	Tp	Ts	Vp	Vs	Vp/Vs	ν	E
psi	inch	usec	usec	m/s	m/s			psi
178	0.0000	20.6300	36.0330	2665	1577	1.6895	0.2304	6.8680
516	0.0001	19.1580	35.0550	2900	1629	1.7801	0.2695	8.3939
1013	0.0002	18.4080	34.3150	3037	1671	1.8175	0.2829	9.3015
1511	0.0002	17.9130	33.7360	3134	1705	1.8383	0.2899	9.9620
1991	0.0003	17.5210	33.2970	3216	1732	1.8571	0.2958	10.5366
2880	0.0005	16.9960	32.7470	3332	1766	1.8864	0.3046	11.3886
3698	0.0009	16.3770	32.0880	3480	1810	1.9231	0.3147	12.5191
3974	0.0011	16.1520	31.8900	3538	1823	1.9403	0.3192	12.9771

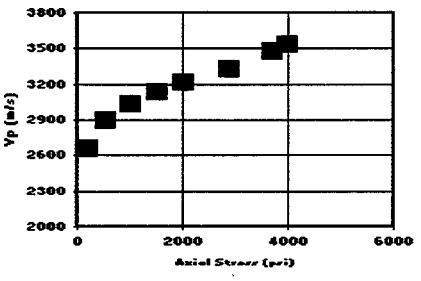

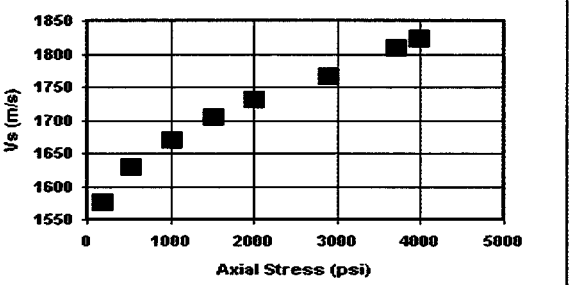

Table 2.9. Unconfined compression, shear velocities and acoustic moduli of sample 10156' tested.

Paxial	Δx	Tp	Ts	Vp	Vs	Vp/Vs	ν	E
psi	inch	usec	usec	m/s	m/s			psi
0	0.0000	24.4080	40.3300	2648	1661	1.5942	0.1756	6.4808
462	0.0001	24.1480	40.1000	2680	1672	1.6027	0.1813	6.6687
1014	0.0001	22.5000	39.8900	2901	1682	1.7244	0.2466	8.2456
1511	0.0002	20.8970	39.2310	3153	1715	1.8389	0.2900	10.0849
1991	0.0002	20.1650	38.3910	3284	1759	1.8675	0.2990	11.0142
2969	0.0003	19.3410	37.2100	3445	1824	1.8888	0.3053	12.1764
3698	0.0006	18.8830	36.5930	3541	1860	1.9039	0.3095	12.9064

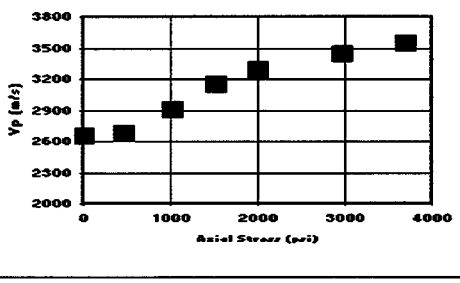

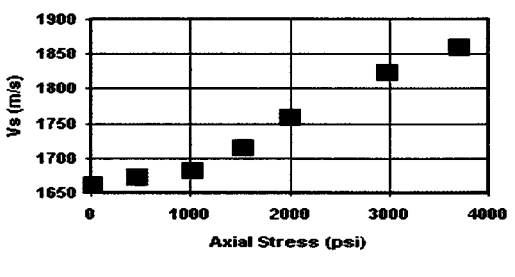

Table 2.10. Compression, shear wave velocities and acoustic moduli of sample 10157' at various stress conditions.

Paxial	Pconfining	Δx	Tp	Ts	Vp	Vs	Vp/Vs	ν	E
psi	psi	inch	usec	usec	m/s	m/s			psi
500	500	0.0000	9.9121	16.0230	2436	1701	1.4324	0.0247	4.781
1000	1000	0.0015	9.4505	15.0470	2593	1869	1.3871	-0.0411	5.068
1500	1500	0.0029	8.9890	14.6130	2772	1954	1.4189	0.0065	6.081
2000	2000	0.0041	8.7473	14.4190	2875	1993	1.4428	0.0377	6.742
3000	3000	0.0069	8.4176	14.1780	3023	2039	1.4825	0.0826	7.778
4000	4000	0.0099	8.2088	13.9660	3120	2081	1.4996	0.0996	8.417
3000	3000	0.0073	8.2308	14.1510	3120	2044	1.5262	0.1238	8.601
2000	2000	0.0048	8.2527	14.3340	3119	2010	1.5522	0.1452	8.760
1500	1500	0.0037	8.3407	14.5070	3077	1974	1.5585	0.1501	8.560
1000	1000	0.0031	8.5385	14.8000	2978	1914	1.5559	0.1481	8.006
500	500	0.0024	9.1648	15.2000	2701	1838	1.4696	0.0689	6.129

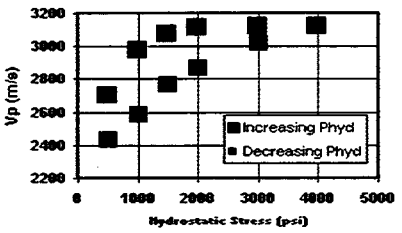

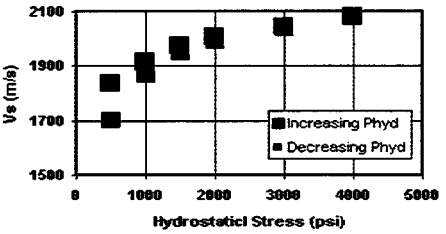

Table 2.11. Unconfined compression, shear velocities and acoustic moduli of sample 10165' tested.

Paxial	Δx	Tp	Ts	Vp	Vs	Vp/Vs	ν	E
psi	inch	usec	usec	m/s	m/s			psi
445	0.0000	24.0000	36.3740	2418	1679	1.4404	0.0348	4.7570
1013	0.0000	21.6330	35.2750	2718	1741	1.5612	0.1521	6.6887
1529	0.0001	20.2740	34.8350	2925	1767	1.6559	0.2130	8.1602
2045	0.0001	19.4600	34.6150	3066	1780	1.7224	0.2458	9.2049
3023	0.0002	18.2330	34.2300	3305	1804	1.8323	0.2879	11.0582
3200	0.0002	17.9860	34.1270	3358	1810	1.8549	0.2951	11.4779

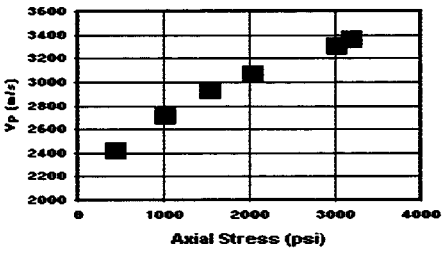

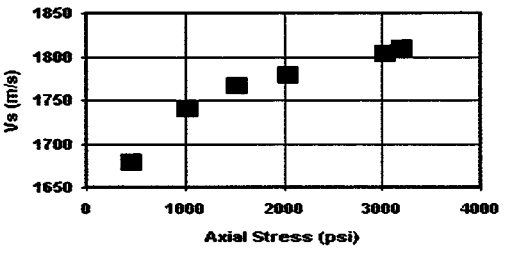

Table 2.12. Compression, shear wave velocities and acoustic moduli of sample 10166' at various stress conditions.

Paxial	Pconfining	Δx	Tp	Ts	Vp	Vs	Vp/Vs	ν	E
psi	psi	inch	usec	usec	m/s	m/s			psi
500	500	0.0000	8.6813	14.0510	2708	1936	1.3986	-0.0230	5.633
1000	1000	0.0001	8.2857	13.8460	2893	1983	1.4589	0.0569	6.954
1500	1500	0.0002	8.0220	13.7000	3031	2018	1.5022	0.1021	7.961
2000	2000	0.0002	7.8681	13.6070	3118	2041	1.5280	0.1254	8.603
3000	3000	0.0002	7.6923	13.4300	3224	2086	1.5456	0.1400	9.315
4000	4000	0.0002	7.5604	13.2910	3308	2123	1.5585	0.1501	9.894
3000	3000	0.0002	7.6224	13.4300	3268	2086	1.5668	0.1563	9.708
2000	2000	0.0002	7.7382	13.5980	3196	2043	1.5642	0.1544	9.268
1500	1500	0.0002	7.8681	13.7030	3118	2017	1.5459	0.1402	8.716
1000	1000	0.0002	8.0719	13.8400	3004	1984	1.5139	0.1129	7.895
500	500	0.0002	8.3835	14.0000	2845	1947	1.4608	0.0591	6.737

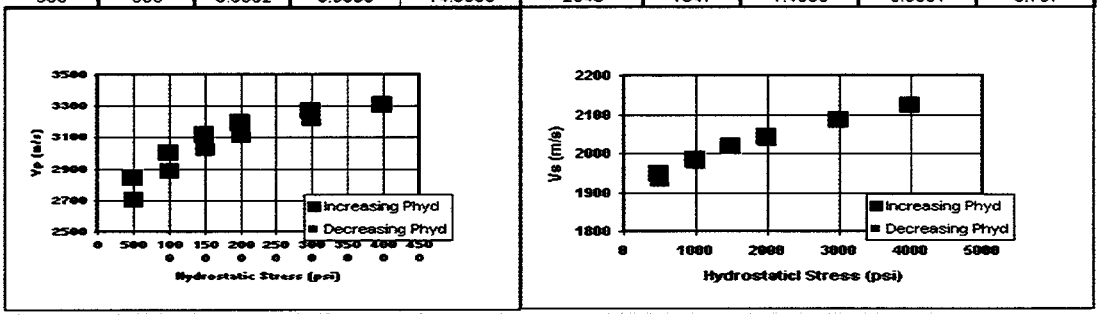

Table 2.13. Compression, shear velocities and acoustic moduli of sample 10197' at various stress conditions.

Paxial	Pconfining	Δx	Tp	Ts	Vp	Vs	Vp/Vs	ν	E
psi	psi	inch	usec	usec	m/s	m/s			psi
500	500	0.0000	11.6570	19.1940	2943	1955	1.5058	0.1055	7.530
1000	1000	0.0000	11.2910	18.8280	3066	2008	1.5269	0.1245	8.311
1500	1500	0.0008	11.0070	18.5050	3166	2056	1.5400	0.1354	8.948
2000	2000	0.0018	10.8030	18.1950	3241	2104	1.5405	0.1358	9.380
3000	3000	0.0035	10.5590	17.8400	3334	2161	1.5430	0.1379	9.944
4000	4000	0.0048	10.3560	17.7070	3416	2181	1.5660	0.1557	10.603
3000	3000	0.0048	10.3560	17.7520	3416	2173	1.5718	0.1600	10.642
2000	2000	0.0040	10.5190	17.7960	3349	2167	1.5453	0.1397	10.050
1500	1500	0.0032	10.6410	17.9730	3301	2138	1.5438	0.1386	9.755
1000	1000	0.0023	10.8220	18.2390	3232	2096	1.5422	0.1373	9.341
500	500	0.0013	11.0880	18.6380	3135	2034	1.5409	0.1362	8.778

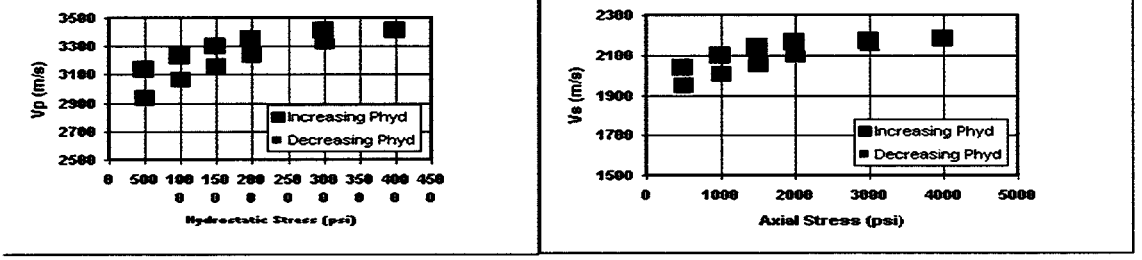

2.4 Ultrasonic Velocities and Elastic moduli of Clearfolk Dolomite

Compressive strength, Elastic moduli, porosity and permeabilities, grain densities, compressional and shear wave velocities of the dry and saturated Clearfolk samples were measured (Table 2.14). In the testing program confining pressure of 4000, 4500, 5000 and 5500 psi were employed (Tables 2.15 through 2.26).

Table 2.14. Dry and saturated elastic moduli, porosity and permeabilities of Clearfolk samples at various stress conditions.

Sample	Pc	E_{load} (psi)*1E+6		ν_{load}		E_{unload} (psi)*1E+6		ν_{unload}		k	ϕ	ρ
No.	(psi)	Dry	Saturated	Dry	Saturated	Dry	Saturated	Dry	Saturated	mD	%	g/cc
1	4000	10.121	11.749	0.1886	0.2451	9.192	15.037	0.1606	0.2482	16.50	14.40	2.84
	4500	8.867	12.580	0.2260	0.1809	7.159	8.965	0.1615	0.2349			
	5000	8.508	12.165	0.1943	0.2015	7.017	8.230	0.1456	___			
	5500	8.676	12.283	0.1883	0.2651	6.179	9.027	0.1096	0.1769			
3	4000	7.356	7.015	0.2043	0.1891	9.088	8.181	0.2325	0.1917	2.45	11.80	2.83
	4500	6.673	9.030	0.2583	0.2094	10.957	7.511	0.1376	0.2113			
	5000	6.666	9.058	0.2186	0.1610	9.790	7.112	0.1751	0.2203			
	5500	6.166	7.371	0.2176	0.1870	10.386	6.188	0.1235	0.2166			
5	4000	9.103	7.839	0.2324	0.2046	10.677	9.742	0.2459	0.2441	0.60	10.30	2.83
	4500	8.903	8.323	0.2619	0.2178	10.319	10.641	0.1992	0.1941			
	5000	7.364	9.456	0.2249	0.2142	9.985	13.170	0.1961	0.1880			
	5500	10.775	8.997	0.2832	0.2470	14.363	9.885	0.2168	0.2632			
9	4000	5.499	7.930	0.1801	0.1847	7.609	9.257	0.2136	0.1807	4.85	11.00	2.84
	4500	5.183	8.002	0.1448	0.1954	6.425	6.506	0.1645	0.1931			
	5000	6.896	6.317	0.1290	0.2062	9.552	9.651	0.1523	0.2154			
	5500	10.479	9.763	0.2255	0.3366	16.656	13.470	0.2667	0.3347			
18	4000	12.308	9.972	0.1626	0.1845	12.008	9.988	0.1766	0.1845	4.76	12.20	2.84
	4500	12.082	9.359	0.1888	0.1737	11.678	9.439	0.1887	___			
	5000	12.270	9.737	0.1839	0.1479	11.216	9.618	0.1805	0.1314			
	5500	12.550	9.214	0.1840	0.1734	11.971	9.802	0.1862	0.1845			
19	4000	9.971	7.792	0.0793	0.1065	11.961	9.439	0.0680	0.1151	0.79	1.00	2.79
	4500	10.344	5.841	0.0748	0.1257	12.607	7.066	0.0776	0.1371			
	5000	12.146	8.491	0.0872	0.0901	15.062	10.830	0.0725	___			
	5500	11.412	8.017	0.1177	0.1209	17.765	11.773	0.0800	0.1331			
20	4000	11.168	9.087	0.1772	0.1970	14.231	10.976	0.2423	0.1539	0.75	5.10	2.81
	4500	___	10.127	___	___	___	12.143	___	0.3443			
	5000	9.748	7.223	0.2026	0.1874	14.338	7.381	0.1161	0.1096			
	5500	11.922	6.605	0.1785	0.2167	10.566	8.870	0.2890	0.1090			
22	4000	5.481	___	0.2146	___	8.040	___	0.3321	___	16.30	10.80	2.83
	4500	6.572	6.561	0.2069	0.2356	8.379	10.457	0.2525	0.3061			
	5500	6.897	6.533	0.2047	0.2391	9.385	11.471	0.2739	0.3991			
	5500	5.798	5.889	0.1927	0.2210	8.865	8.174	0.2841	0.2960			
24	4000	7.871	8.613	0.1254	0.1149	___	10.088	___	0.0998	16.20	11.00	2.83
	4500	11.999	8.127	0.0984	0.2160	14.621	7.931	0.0679	0.2185			
	5000	12.709	6.784	0.1183	0.1767	15.559	7.972	0.0552	0.0788			
	5500	11.875	8.142	0.1094	0.1752	16.056	10.705	0.0386	0.0805			
27	4000	8.527	8.843	0.2638	0.2072	14.875	10.114	0.2835	0.1895	0.36	2.70	2.84
	4500	9.611	8.170	0.1052	0.2104	14.454	11.883	0.1514	0.2094			
	5000	10.290	7.795	0.1665	0.2008	17.314	11.693	___	0.2512			
	5500	11.559	10.600	0.1663	0.1513	16.587	12.213	0.0954	0.1673			
30	4000	9.043	10.890	0.1541	0.1536	___	___	0.1919	___	8.45	11.30	2.82
	4500	11.303	7.955	0.1733	0.2157	___	10.856	0.2454	0.3600			
	5000	11.638	11.063	0.2702	0.1836	___	16.527	___	0.2122			
	5500	11.437	9.917	0.1539	0.2632	___	8.174	___	___			
34	4000	___	5.713	___	___	___	7.345	___	___	13.10	10.10	2.83
	4500	8.487	7.432	0.2572	0.3830	9.496	7.371	0.1173	0.2907			
	5000	8.858	6.500	0.2194	0.2993	12.653	7.065	0.1311	0.2106			
	5500	7.615	6.815	0.3311	___	10.228	9.920	0.1782	___			
36	4000	7.772	5.712	0.1582	0.2156	12.520	10.259	0.2210	___	1.34	6.00	2.71
	4500	8.625	6.754	0.2007	0.2561	17.017	12.804	0.2951	___			
	5000	6.279	6.802	0.1700	0.2599	13.313	12.879	___	___			
	5500	6.922	6.207	0.2006	0.1613	11.151	11.399	0.3479	0.3140			
41	4000	5.696	8.788	0.1739	0.1648	12.634	9.670	0.2995	0.2041	9.85	12.85	2.83
	4500	6.941	6.649	0.1870	0.1608	20.073	16.613	0.3228	0.2880			
	5000	8.125	10.876	0.1675	0.2190	25.248	23.965	___	___			
	5500	8.640	10.567	0.1647	0.2120	31.304	30.154	___	___			

Table 2.15. Compressional and shear wave velocities, acoustic moduli, strain response for various confining pressures of dry and saturated Clearfolk sample No. 1

Axial	Net Axial	Vp (m/sec)		Vs (m/sec)		Vp/Vs		E (psi*1E6)		ν	
Stress (psi)	Stress (psi)	Dry	Saturated	Dry	Saturated	Dry	Saturated	Dry	Saturated	Dry	Saturated
4000	0	4890	5118	2856	2764	1.7125	1.8514	7.7580	7.5780	0.2413	0.2940
5250	1250	4970	5150	2899	2764	1.7145	1.8632	7.9996	7.5994	0.2422	0.2977
6500	2500	5032	5206	2937	2764	1.7134	1.8833	8.2074	7.6345	0.2417	0.3037
4500	500	4985	5150	2911	2714	1.7123	1.8981	8.0625	7.3806	0.2412	0.3079
4500	0	4996	5167	2920	2714	1.7110	1.9042	8.1054	7.3903	0.2406	0.3096
5750	1250	5021	5178	2933	2714	1.7122	1.9082	8.1800	7.3965	0.2412	0.3107
7000	2500	5069	5223	2954	2727	1.7159	1.9150	8.3114	7.4817	0.2428	0.3125
5000	500	5027	5178	2933	2710	1.7142	1.9107	8.1858	7.3813	0.2420	0.3114
5000	0	5032	5167	2941	2714	1.7109	1.9041	8.2238	7.3910	0.2406	0.3096
6250	1250	5053	5200	2954	2727	1.7104	1.9067	8.2947	7.4688	0.2403	0.3103
7500	2500	5090	5234	2971	2741	1.7131	1.9094	8.4010	7.5489	0.2416	0.3110
5500	500	5063	5194	2954	2726	1.7141	1.9053	8.3061	7.4620	0.2420	0.3099
5500	0	5063	5189	2958	2727	1.7116	1.9031	8.3227	7.4596	0.2409	0.3093
6750	1250	5084	5200	2967	2728	1.7136	1.9059	8.3780	7.4740	0.2418	0.3101
8000	2500	5111	5274	2989	2751	1.7100	1.9174	8.4913	7.6149	0.2402	0.3132
6000	500	5079	5228	2971	2734	1.7093	1.9123	8.3894	7.5145	0.2398	0.3118

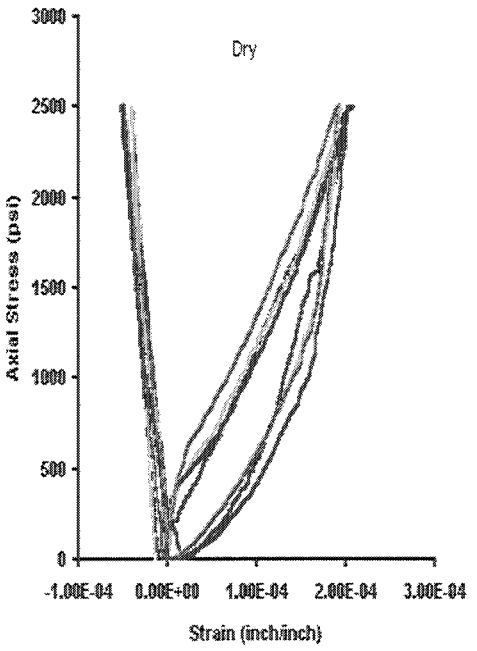

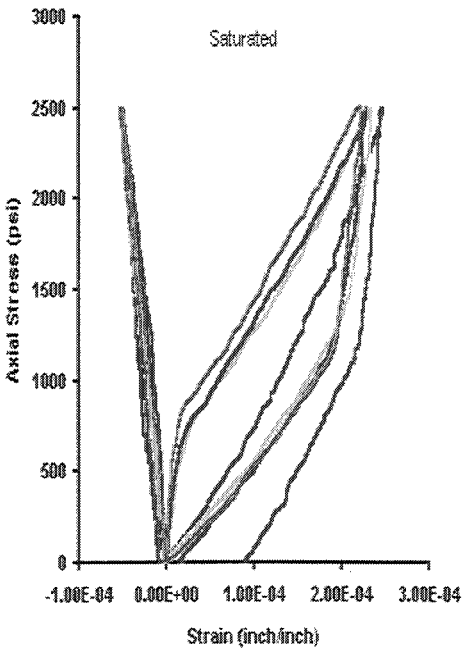

Table 2.16. Compressional and shear wave velocities, acoustic moduli, strain response for various confining pressures of dry and saturated Clearfolk sample No. 3

Axial	Net Axial	Vp (m/sec)		Vs (m/sec)		Vp/Vs		E (psi*1E6)		ν	
Stress (psi)	Stress (psi)	Dry	Saturated	Dry	Saturated	Dry	Saturated	Dry	Saturated	Dry	Saturated
4000	0	5597	5495	3668	3583	1.5260	1.5336	11.5771	11.1129	0.1302	0.3152
5250	1250	5604	5533	3671	3615	1.5264	1.5305	11.6012	11.2858	0.1275	0.3100
6500	2500	5623	5565	3681	3635	1.5274	1.5310	11.6741	11.4128	0.1280	0.3035
4500	500	5604	5552	3675	3635	1.5250	1.5274	11.6099	11.3814	0.1249	0.3129
4500	0	5623	5561	3681	3635	1.5274	1.5299	11.6741	11.4029	0.1270	0.3110
5750	1250	5636	5559	3681	3635	1.5309	1.5293	11.7050	11.3980	0.1265	0.3054
7000	2500	5623	5571	3681	3641	1.5274	1.5300	11.6741	11.4451	0.1271	0.3032
5000	500	5604	5565	3681	3641	1.5222	1.5282	11.6272	11.4302	0.1256	0.3090
5000	0	5610	5571	3681	3641	1.5239	1.5300	11.6429	11.4451	0.1271	0.3136
6250	1250	5610	5584	3681	3641	1.5239	1.5334	11.6429	11.4748	0.1300	0.3049
7500	2500	5636	5584	3688	3648	1.5281	1.5307	11.7230	11.4925	0.1277	0.2983
5500	500	5610	5578	3688	3648	1.5211	1.5289	11.6601	11.4775	0.1262	0.3064
5500	0	5604	5580	3681	3648	1.5222	1.5297	11.6272	11.4842	0.1269	0.3037
6750	1250	5616	5584	3681	3648	1.5257	1.5307	11.6585	11.4925	0.1277	0.3003
8000	2500	5656	5597	3688	3655	1.5335	1.5316	11.7711	11.5419	0.1284	0.2968
6000	500	5623	5590	3688	3655	1.5246	1.5296	11.6917	11.5252	0.1268	0.3016

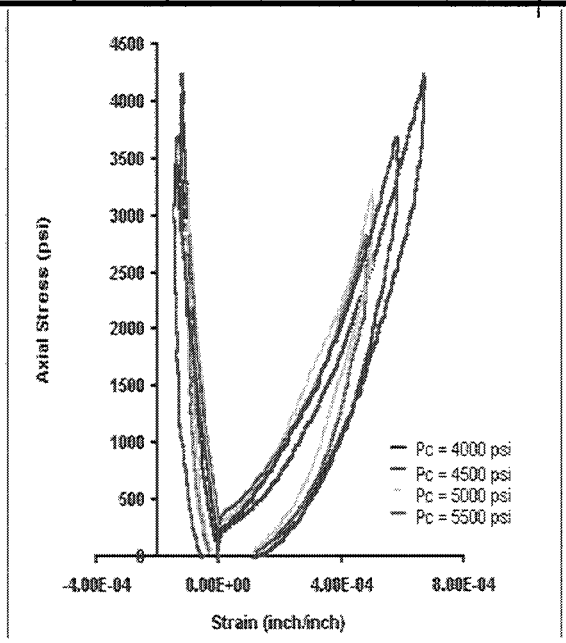

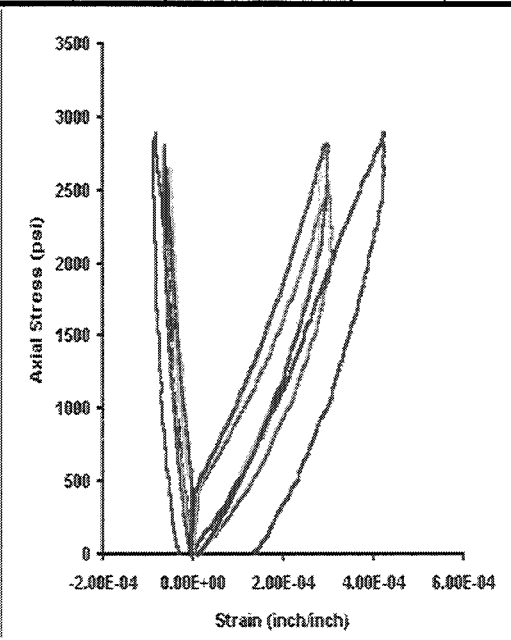

Table 2.17. Compressional and shear wave velocities, acoustic moduli, strain response for various confining pressures of dry and saturated Clearfolk sample No. 5

Axial	Net Axial	Vp (m/sec)		Vs (m/sec)		Vp/Vs		E (psi*1E6)		ν	
Stress (psi)	Stress (psi)	Dry	Saturated	Dry	Saturated	Dry	Saturated	Dry	Saturated	Dry	Saturated
4000	0	4659	4722	2834	2630	1.6441	1.7952	6.7598	9.6753	0.2064	0.2751
5250	1250	4707	4736	2859	2796	1.6461	1.6938	7.3860	9.6500	0.2076	0.2325
6500	2500	4761	4796	2930	2823	1.6249	1.6987	7.5439	9.7183	0.1952	0.2348
4500	500	4702	4766	2868	2801	1.6395	1.7019	7.4311	9.6792	0.2038	0.2363
4500	0	4717	4746	2879	2813	1.6384	1.6873	7.4545	9.8840	0.2031	0.2293
5750	1250	4736	4756	2910	2831	1.6278	1.6800	7.5283	9.6889	0.1969	0.2256
7000	2500	4766	4776	2932	2845	1.6254	1.6791	7.5972	9.7082	0.1955	0.2252
5000	500	4731	4756	2881	2822	1.6421	1.6851	7.4984	9.6772	0.2053	0.2282
5000	0	4659	4761	2834	2819	1.6441	1.6888	7.4923	9.4136	0.2064	0.2300
6250	1250	4659	4771	2834	2830	1.6441	1.6861	7.5399	9.4244	0.2064	0.2287
7500	2500	4659	4781	2834	2845	1.6441	1.6808	7.6027	9.4351	0.2064	0.2260
5500	500	4659	4761	2834	2828	1.6441	1.6838	7.5218	9.4280	0.2064	0.2276
5500	0	4659	4761	2834	2833	1.6441	1.6804	7.5418	9.4280	0.2064	0.2258
6750	1250	4659	4776	2834	2845	1.6441	1.6791	7.5972	9.4498	0.2064	0.2252
8000	2500	4659	4781	2834	2845	1.6441	1.6808	7.6027	9.4737	0.2064	0.2260
6000	500	4659	4761	2834	2836	1.6441	1.6788	7.5512	9.4560	0.2064	0.2250

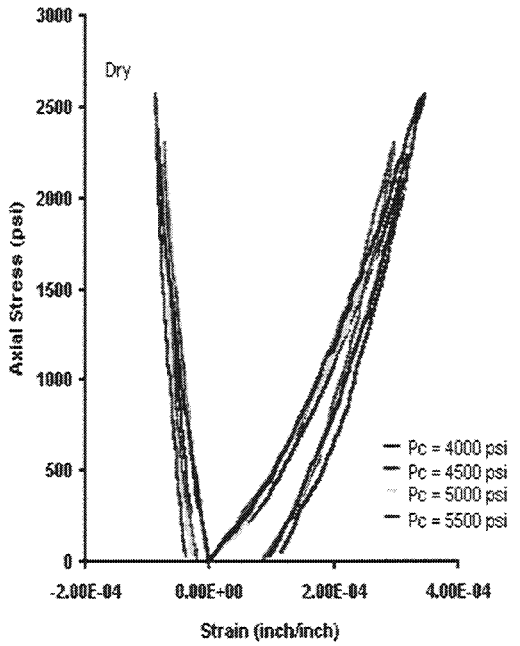

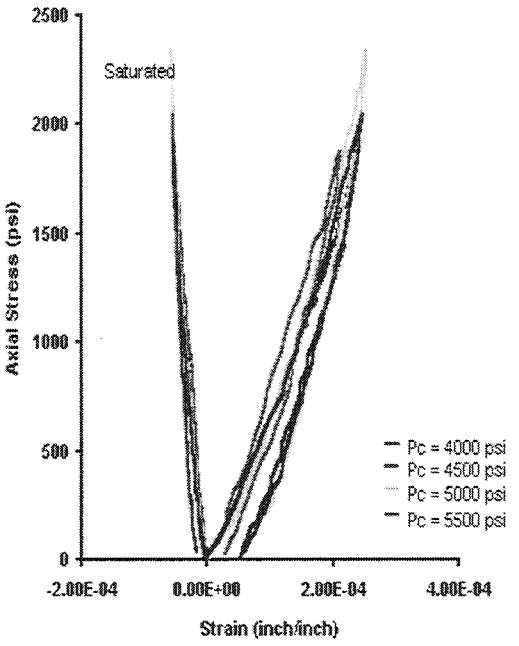

Table 2.18. Compressional and shear wave velocities, acoustic moduli, strain response for various confining pressures of dry and saturated Clearfolk sample No. 18

Axial	Net Axial	Vp (m/sec)		Vs (m/sec)		Vp/Vs		E (psi*1E6)		ν	
Stress (psi)	Stress (psi)	Dry	Saturated	Dry	Saturated	Dry	Saturated	Dry	Saturated	Dry	Saturated
4000	0	4758	5265	3121	3271	1.5243	1.6094	8.3785	9.7233	0.1222	0.1856
5250	1250	5100	5328	3196	3306	1.5958	1.6115	9.2114	9.9420	0.1767	0.1869
6500	2500	5183	5385	3240	3330	1.5995	1.6173	9.4870	10.1150	0.1792	0.1905
4500	500	5088	5315	3188	3283	1.5961	1.6191	9.1660	9.8420	0.1769	0.1917
4500	0	5123	5315	3193	3289	1.6044	1.6163	9.2395	9.8621	0.1823	0.1899
5750	1250	5183	5366	3234	3321	1.6023	1.6159	9.4688	10.0539	0.1810	0.1897
7000	2500	5219	5372	3268	3345	1.5967	1.6063	9.6386	10.1463	0.1773	0.1836
5000	500	5147	5334	3223	3303	1.5968	1.6148	9.3745	9.9418	0.1773	0.1890
5000	0	5164	5346	3229	3288	1.5994	1.6258	9.4210	9.9096	0.1791	0.1957
6250	1250	5213	5398	3263	3336	1.5977	1.6184	9.6102	10.1573	0.1780	0.1912
7500	2500	5261	5444	3291	3360	1.5985	1.6205	9.7850	10.3147	0.1785	0.1925
5500	500	5183	5379	3251	3321	1.5940	1.6197	9.5233	10.0738	0.1755	0.1920
5500	0	5188	5366	3251	3327	1.5958	1.6130	9.5331	10.0745	0.1767	0.1879
6750	1250	5225	5392	3286	3351	1.5901	1.6093	9.7041	10.1993	0.1729	0.1855
8000	2500	5274	5431	3309	3375	1.5937	1.6094	9.8626	10.3477	0.1753	0.1855
6000	500	5231	5385	3274	3339	1.5976	1.6130	9.6771	10.1463	0.1779	0.1878

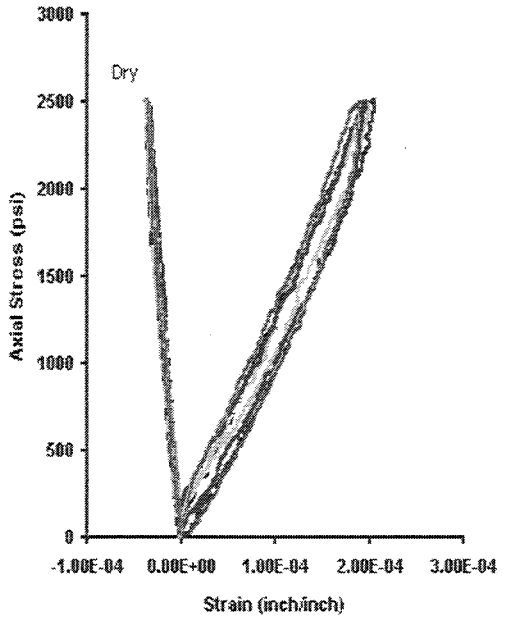

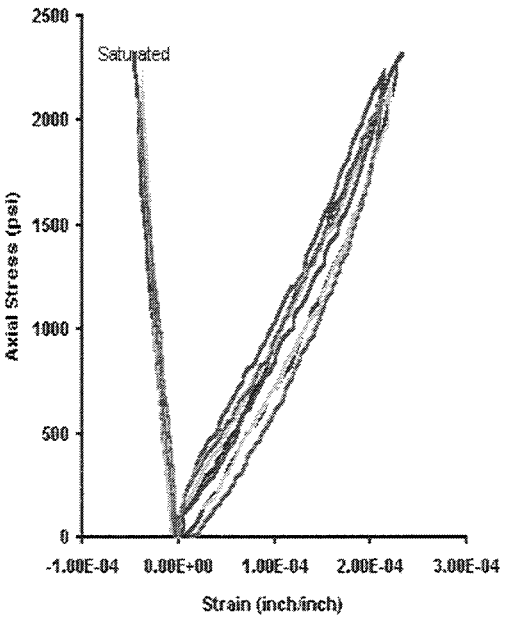

Table 2.19. Compressional and shear wave velocities, acoustic moduli, strain response for various confining pressures of dry and saturated Clearfolk sample No. 19

Axial	Net Axial	Vp (m/sec)		Vs (m/sec)		Vp/Vs		E (psi*1E6)		ν	
Stress (psi)	Stress (psi)	Dry	Saturated	Dry	Saturated	Dry	Saturated	Dry	Saturated	Dry	Saturated
4000	0	6922	6864	4035	3728	1.7155	1.8415	15.4806	13.7253	0.2427	0.2909
5250	1250	6919	6867	4054	3744	1.7068	1.8343	15.5755	13.8189	0.2387	0.2886
6500	2500	6922	6872	4073	3772	1.6996	1.8219	15.6784	13.9850	0.2352	0.2844
4500	500	6913	6864	4063	3764	1.7015	1.8237	15.6168	13.9309	0.2362	0.2850
4500	0	6911	6864	4073	3764	1.6968	1.8237	15.6620	13.9309	0.2339	0.2850
5750	1250	6913	6864	4082	3764	1.6935	1.8237	15.7154	13.9309	0.2323	0.2850
7000	2500	6930	6864	4082	3764	1.6976	1.8237	15.7404	13.9309	0.2343	0.2850
5000	500	6913	6864	4073	3764	1.6975	1.8237	15.6661	13.9309	0.2343	0.2850
5000	0	6918	6864	4082	3764	1.6947	1.8237	15.7226	13.9309	0.2329	0.2850
6250	1250	6922	6864	4092	3764	1.6916	1.8237	15.7774	13.9309	0.2314	0.2850
7500	2500	6927	6864	4092	3764	1.6929	1.8237	15.7858	13.9309	0.2320	0.2850
5500	500	6925	6864	4082	3764	1.6962	1.8237	15.7321	13.9309	0.2336	0.2850
5500	0	6941	6864	4082	3764	1.7003	1.8237	15.7569	13.9309	0.2356	0.2850
6750	1250	6947	6864	4092	3764	1.6976	1.8237	15.8149	13.9309	0.2343	0.2850
8000	2500	6960	6864	4102	3764	1.6970	1.8237	15.8860	13.9309	0.2340	0.2850
6000	500	6947	6864	4092	3764	1.6976	1.8237	15.8149	13.9309	0.2343	0.2850

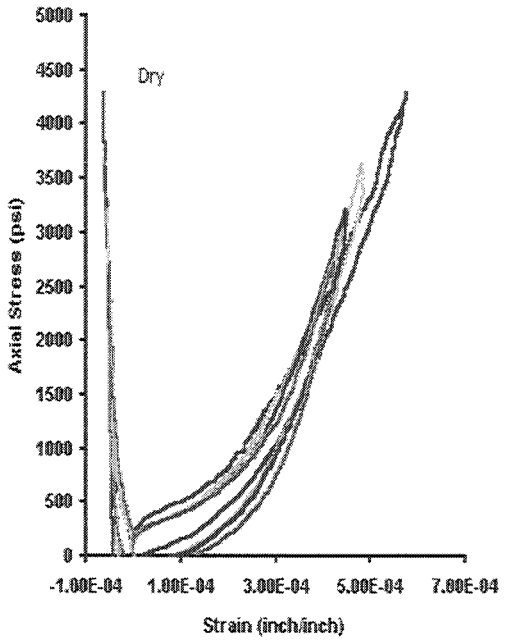

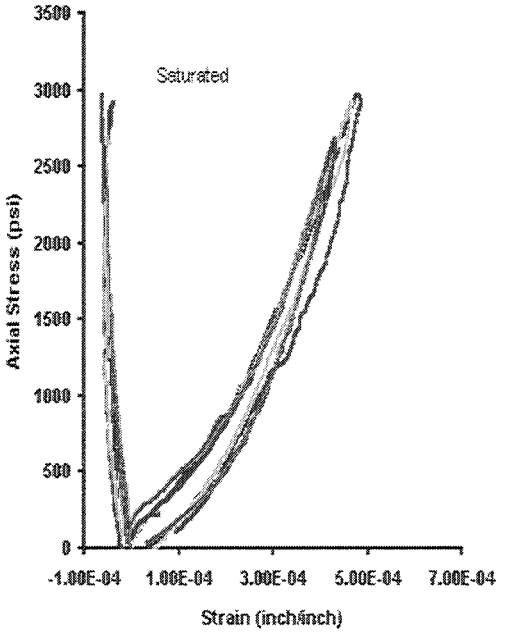

Table 2.20. Compressional and shear wave velocities, acoustic moduli, strain response for various confining pressures of dry and saturated Clearfolk sample No. 20

Axial	Net Axial	Vp (m/sec)		Vs (m/sec)		Vp/Vs		E (psi*1E6)		ν	
Stress (psi)	Stress (psi)	Dry	Saturated	Dry	Saturated	Dry	Saturated	Dry	Saturated	Dry	Saturated
4000	0	6371	6401	3555	3551	1.7921	1.8027	12.3329	12.3419	0.2739	0.2778
5250	1250	6403	6428	3579	3567	1.7889	1.8019	12.4923	12.4525	0.2728	0.2775
6500	2500	6414	6449	3585	3592	1.7890	1.7954	12.5346	12.6026	0.2728	0.2751
4500	500	6392	6401	3561	3575	1.7952	1.7904	12.3851	12.4689	0.2751	0.2733
4500	0	6403	6414	3579	3575	1.7889	1.7941	12.4923	12.4821	0.2728	0.2746
5750	1250	6425	6414	3651	3592	1.7600	1.7858	12.8820	12.5676	0.2616	0.2716
7000	2500	6425	6436	3659	3617	1.7558	1.7793	12.9256	12.7191	0.2600	0.2692
5000	500	6414	6409	3642	3584	1.7611	1.7885	12.8263	12.5195	0.2621	0.2726
5000	0	6414	6414	3642	3642	1.7611	1.7611	12.8263	12.8263	0.2621	0.2621
6250	1250	6425	6425	3651	3651	1.7600	1.7600	12.8820	12.8820	0.2616	0.2616
7500	2500	6425	6425	3668	3668	1.7517	1.7517	12.9693	12.9693	0.2583	0.2583
5500	500	6414	6414	3651	3651	1.7570	1.7570	12.8697	12.8697	0.2604	0.2604
5500	0	6425	6425	3651	3600	1.7600	1.7846	12.8820	12.6215	0.2616	0.2712
6750	1250	6425	6425	3659	3625	1.7558	1.7722	12.9256	12.7512	0.2600	0.2664
8000	2500	6436	6430	3668	3633	1.7547	1.7698	12.9821	12.7984	0.2595	0.2655
6000	500	6425	6430	3651	3617	1.7600	1.7778	12.8820	12.7135	0.2616	0.2686

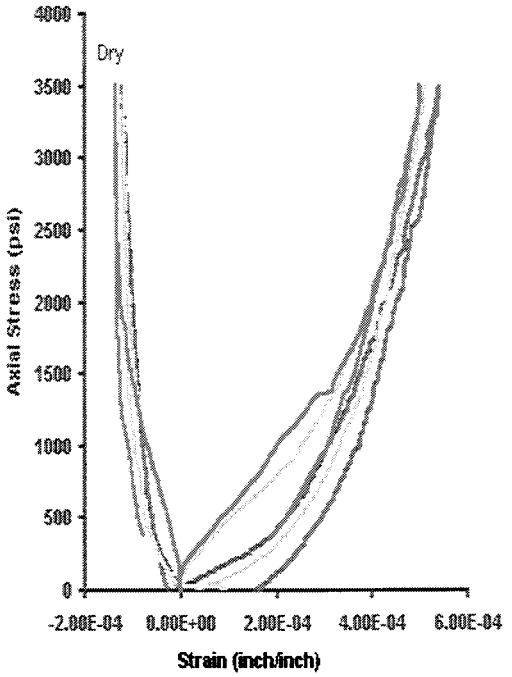

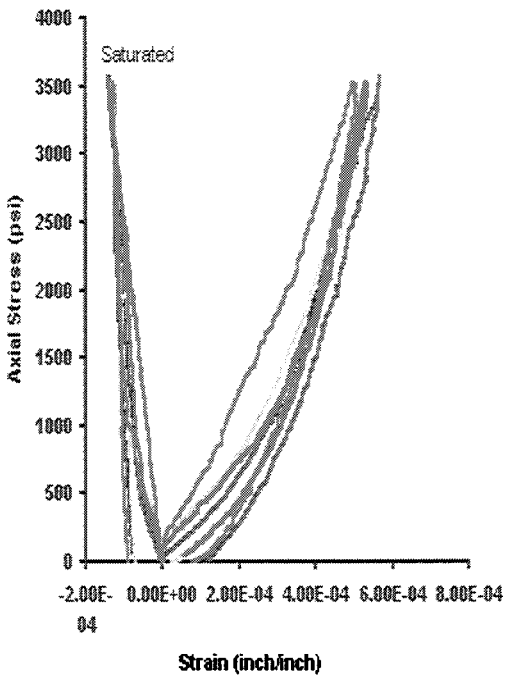

Table 2.21. Compressional and shear wave velocities, acoustic moduli, strain response for various confining pressures of dry and saturated Clearfolk sample No. 22

Axial	Net Axial	Vp (m/sec)		Vs (m/sec)		Vp/Vs		E (psi*1E6)		ν	
Stress (psi)	Stress (psi)	Dry	Saturated	Dry	Saturated	Dry	Saturated	Dry	Saturated	Dry	Saturated
4000	0	5720	6027	3279	3167	1.7443	1.9031	10.3459	10.0645	0.2552	0.3093
5250	1250	5834	6047	3330	3169	1.7520	1.9079	10.6949	10.0888	0.2584	0.3106
6500	2500	5920	6059	3377	3170	1.7532	1.9112	11.0009	10.1013	0.2589	0.3115
4500	500	5894	6036	3357	3168	1.7555	1.9053	10.8831	10.0761	0.2598	0.3099
4500	0	5920	6043	3374	3169	1.7545	1.9072	10.9891	10.0830	0.2594	0.3104
5750	1250	5940	6059	3380	3171	1.7572	1.9108	11.0380	10.1047	0.2605	0.3114
7000	2500	5948	6066	3383	3172	1.7584	1.9123	11.0589	10.1165	0.2610	0.3118
5000	500	5931	6051	3378	3169	1.7555	1.9092	11.0207	10.0926	0.2598	0.3110
5000	0	5941	6066	3391	3170	1.7518	1.9133	11.0921	10.1072	0.2583	0.3121
6250	1250	5956	6080	3398	3173	1.7530	1.9165	11.1366	10.1281	0.2588	0.3130
7500	2500	5962	6086	3400	3174	1.7536	1.9174	11.1554	10.1384	0.2590	0.3132
5500	500	5950	6074	3395	3171	1.7525	1.9152	11.1180	10.1165	0.2586	0.3126
5500	0	5979	6081	3410	3174	1.7532	1.9158	11.2217	10.1366	0.2589	0.3128
6750	1250	5990	6089	3413	3176	1.7552	1.9173	11.2424	10.1490	0.2597	0.3132
8000	2500	5992	6096	3413	3176	1.7556	1.9192	11.2489	10.1578	0.2598	0.3137
6000	500	5955	6085	3402	3175	1.7506	1.9166	11.1547	10.1433	0.2578	0.3130

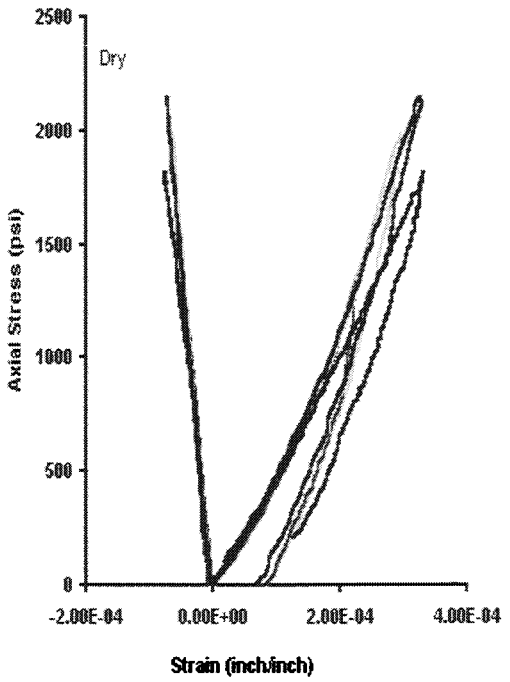

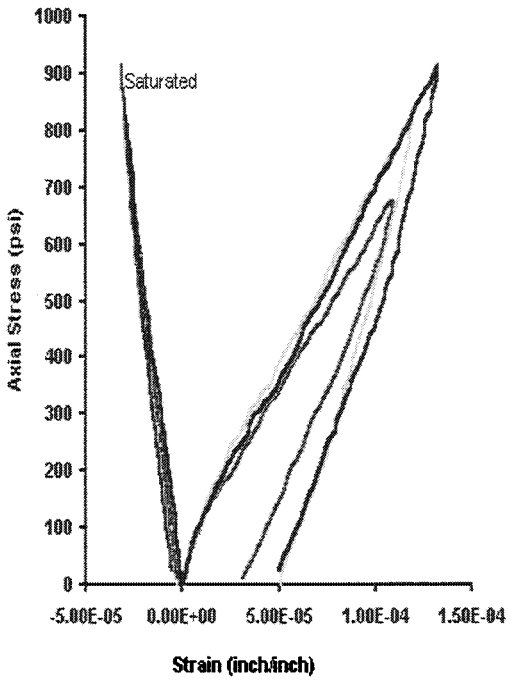

Table 2.22. Compressional and shear wave velocities, acoustic moduli, strain response for various confining pressures of dry and saturated Clearfolk sample No. 24

Axial	Net Axial	Vp (m/sec)		Vs (m/sec)		Vp/Vs		E (psi*1E6)		ν	
Stress (psi)	Stress (psi)	Dry	Saturated	Dry	Saturated	Dry	Saturated	Dry	Saturated	Dry	Saturated
4000	0	5523	5612	3021	3014	1.8284	1.8620	8.9794	9.0150	0.2866	0.2973
5250	1250	5555	5615	3048	3019	1.8225	1.8601	9.1299	9.0380	0.2846	0.2968
6500	2500	5579	5624	3057	3019	1.8248	1.8632	9.1907	9.0446	0.2854	0.2977
4500	500	5584	5612	2960	3014	1.8867	1.8620	8.7417	9.0150	0.3046	0.2973
4500	0	5587	5621	3067	3023	1.8217	1.8595	9.2393	9.0637	0.2844	0.2965
5750	1250	5593	5621	3067	3023	1.8238	1.8595	9.2443	9.0637	0.2851	0.2965
7000	2500	5599	5628	3076	3028	1.8203	1.8588	9.2922	9.0894	0.2839	0.2963
5000	500	5608	5568	3076	3019	1.8233	1.8447	9.2995	9.0044	0.2849	0.2919
5000	0	5624	5624	3078	3023	1.8270	1.8604	9.3226	9.0657	0.2861	0.2968
6250	1250	5628	5630	3078	3028	1.8282	1.8595	9.3254	9.0909	0.2865	0.2966
7500	2500	5633	5639	3083	3032	1.8272	1.8598	9.3516	9.1188	0.2862	0.2966
5500	500	5631	5628	3078	3028	1.8291	1.8588	9.3277	9.0894	0.2868	0.2963
5500	0	5631	5640	3083	3032	1.8263	1.8600	9.3494	9.1194	0.2859	0.2967
6750	1250	5643	5646	3083	3037	1.8305	1.8593	9.3595	9.1453	0.2873	0.2965
8000	2500	5649	5649	3088	3041	1.8295	1.8575	9.3859	9.1688	0.2870	0.2959
6000	500	5648	5643	3083	3032	1.8321	1.8612	9.3634	9.1219	0.2878	0.2971

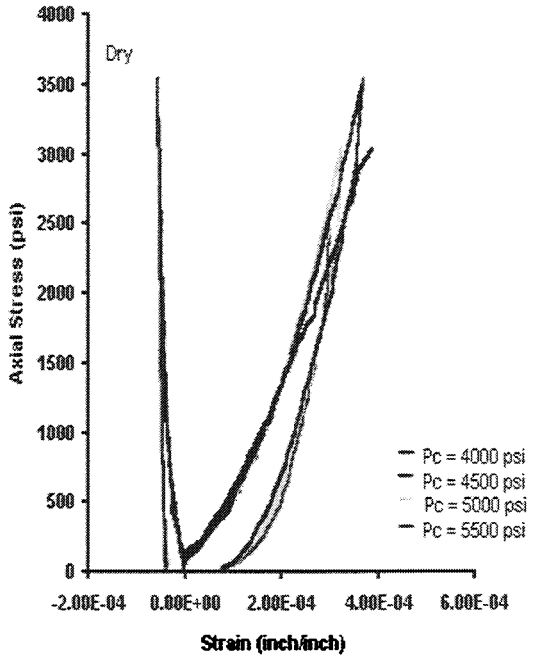

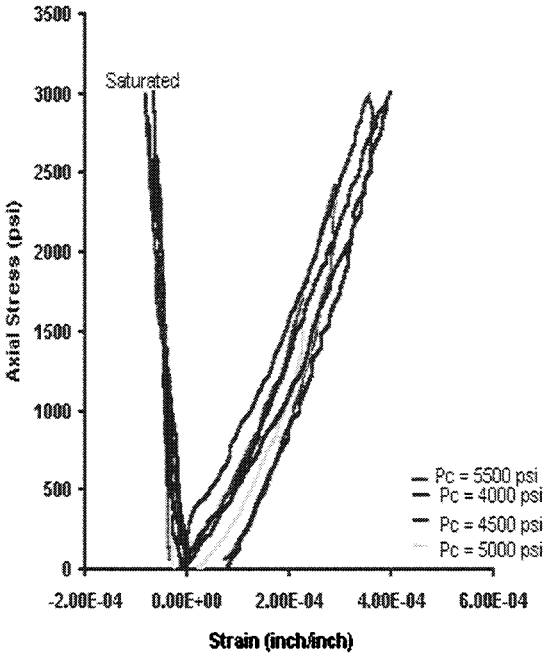

Table 2.23. Compressional and shear wave velocities, acoustic moduli, strain response for various confining pressures of dry and saturated Clearfolk sample No. 27

Axial	Net Axial	Vp (m/sec)		Vs (m/sec)		Vp/Vs		E (psi*1E6)		ν	
Stress (psi)	Stress (psi)	Dry	Saturated	Dry	Saturated	Dry	Saturated	Dry	Saturated	Dry	Saturated
4000	0	6664	6790	3480	3527	1.9152	1.9251	12.1747	12.5332	0.3126	0.3152
5250	1250	6689	6807	3491	3572	1.9159	1.9058	12.2588	12.8025	0.3128	0.3100
6500	2500	6731	6815	3502	3620	1.9218	1.8826	12.3501	13.0871	0.3144	0.3035
4500	500	6689	6807	3494	3552	1.9144	1.9164	12.2741	12.6892	0.3124	0.3129
4500	0	6697	6833	3495	3578	1.9162	1.9094	12.2856	12.8604	0.3129	0.3110
5750	1250	6722	6833	3506	3616	1.9174	1.8894	12.3652	13.0781	0.3132	0.3054
7000	2500	6747	6858	3516	3645	1.9191	1.8818	12.4399	13.2624	0.3136	0.3032
5000	500	6714	6807	3499	3579	1.9185	1.9021	12.3227	12.8424	0.3135	0.3090
5000	0	6714	6824	3508	3556	1.9141	1.9191	12.3691	12.7238	0.3123	0.3136
6250	1250	6731	6858	3519	3633	1.9129	1.8876	12.4434	13.1979	0.3120	0.3049
7500	2500	6756	6867	3541	3682	1.9080	1.8653	12.5878	13.4811	0.3106	0.2983
5500	500	6731	6841	3513	3614	1.9158	1.8928	12.4122	13.0743	0.3128	0.3064
5500	0	6722	6833	3513	3628	1.9135	1.8832	12.4061	13.1465	0.3121	0.3037
6750	1250	6739	6858	3524	3664	1.9122	1.8720	12.4808	13.3723	0.3118	0.3003
8000	2500	6773	6876	3609	3696	1.8768	1.8602	12.9864	13.5736	0.3018	0.2968
6000	500	6747	6841	3519	3647	1.9176	1.8761	12.4556	13.2590	0.3132	0.3016

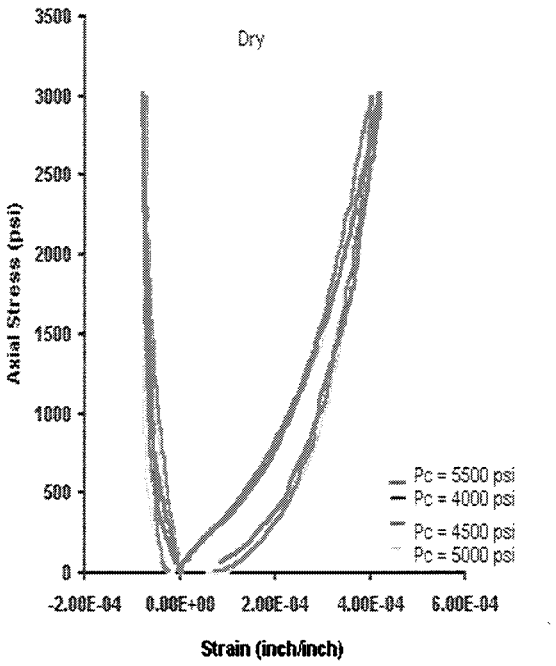

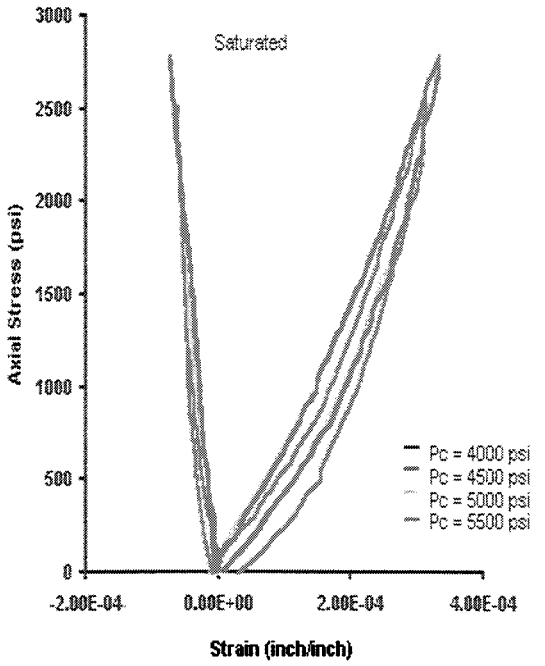

Table 2.24. Compressional and shear wave velocities, acoustic moduli, strain response for various confining pressures of dry and saturated Clearfolk sample No. 30

Axial	Net Axial	Vp (m/sec)		Vs (m/sec)		Vp/Vs		E (psi*1E6)		ν	
Stress (psi)	Stress (psi)	Dry	Saturated	Dry	Saturated	Dry	Saturated	Dry	Saturated	Dry	Saturated
4000	0	5254	5530	2974	2986	1.7665	1.8517	8.5630	8.8388	0.2642	0.2941
5250	1250	5318	5558	2989	3040	1.7794	1.8284	8.6828	9.1056	0.2692	0.2866
6500	2500	5371	5609	3009	3063	1.7852	1.8313	8.8147	9.2500	0.2714	0.2876
4500	500	5325	5566	2989	3003	1.7816	1.8536	8.6885	8.9387	0.2700	0.2947
4500	0	5338	5558	2989	3006	1.7860	1.8489	8.6998	8.9514	0.2717	0.2932
5750	1250	5371	5573	3004	3032	1.7881	1.8381	8.7929	9.0791	0.2725	0.2898
7000	2500	5405	5587	3029	3068	1.7843	1.8211	8.9319	9.2569	0.2710	0.2841
5000	500	5365	5544	2999	3027	1.7889	1.8317	8.7655	9.0339	0.2728	0.2877
5000	0	5371	5573	3004	3029	1.7881	1.8397	8.7929	9.0673	0.2725	0.2903
6250	1250	5405	5573	3024	3055	1.7873	1.8241	8.9097	9.1857	0.2722	0.2852
7500	2500	5432	5602	3045	3071	1.7842	1.8242	9.0229	9.2805	0.2710	0.2852
5500	500	5405	5573	3019	3050	1.7903	1.8272	8.8875	9.1619	0.2733	0.2862
5500	0	5412	5580	3024	3050	1.7896	1.8296	8.9155	9.1675	0.2730	0.2870
6750	1250	5432	5587	3045	3071	1.7842	1.8195	9.0229	9.2689	0.2710	0.2836
8000	2500	5460	5616	3060	3071	1.7841	1.8290	9.1152	9.2920	0.2710	0.2868
6000	500	5419	5602	3040	3065	1.7827	1.8274	8.9884	9.2563	0.2704	0.2863

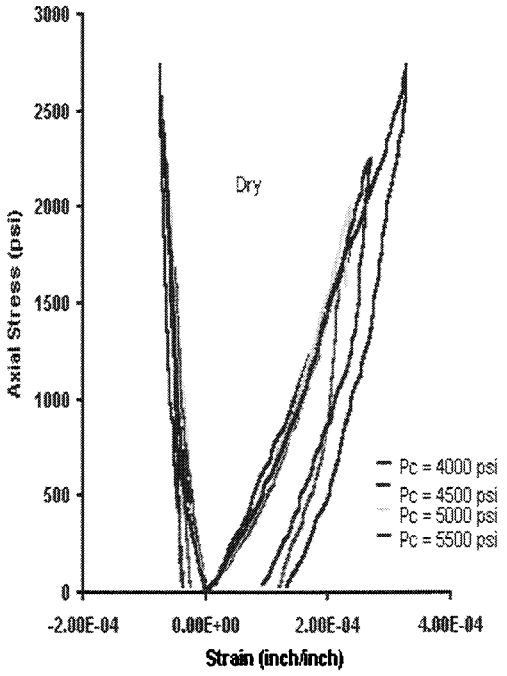

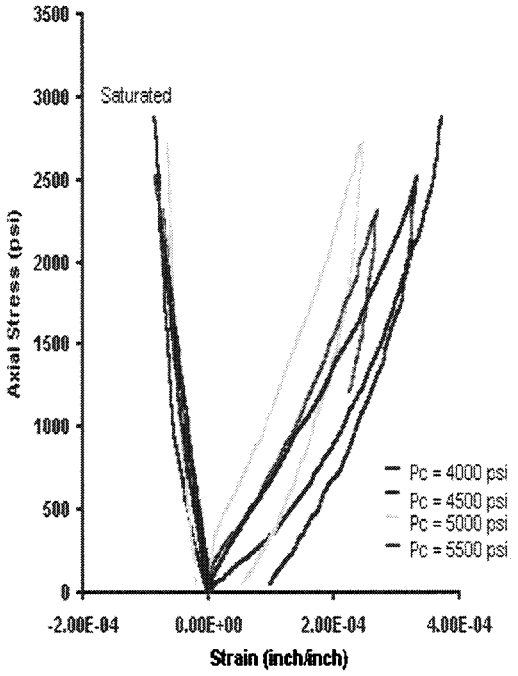

Table 2.25. Compressional and shear wave velocities, acoustic moduli, strain response for various confining pressures of dry and saturated Clearfolk sample No. 34

Axial	Net Axial	Vp (m/sec)		Vs (m/sec)		Vp/Vs		E (psi*1E6)		ν	
Stress (psi)	Stress (psi)	Dry	Saturated	Dry	Saturated	Dry	Saturated	Dry	Saturated	Dry	Saturated
4000	0	6042	6131	3336	3322	1.8113	1.8453	10.9151	10.9217	0.2808	0.2921
5250	1250	6095	6177	3352	3172	1.8182	1.9477	11.0441	10.1766	0.2832	0.3210
6500	2500	6142	6217	3369	3311	1.8228	1.8774	11.1683	10.9329	0.2847	0.3020
4500	500	6080	6138	3352	3137	1.8136	1.9566	11.0306	9.9738	0.2816	0.3232
4500	0	6088	6633	3352	3142	1.8159	2.1109	11.0374	10.2475	0.2824	0.3553
5750	1250	6126	6177	3369	3157	1.8183	1.9568	11.1548	10.0989	0.2832	0.3233
7000	2500	6149	6217	3380	3149	1.8191	1.9739	11.2318	10.0830	0.2835	0.3274
5000	500	6111	6154	3364	3149	1.8167	1.9540	11.1132	10.0466	0.2826	0.3226
5000	0	6118	6146	3364	3149	1.8190	1.9515	11.1199	10.0419	0.2834	0.3220
6250	1250	6142	6170	3375	3164	1.8198	1.9498	11.1966	10.1330	0.2837	0.3215
7500	2500	6165	6193	3386	3170	1.8206	1.9536	11.2741	10.1777	0.2840	0.3225
5500	500	6142	6177	3369	3154	1.8228	1.9583	11.1683	10.0860	0.2847	0.3236
5500	0	6142	6177	3375	3162	1.8198	1.9538	11.1966	10.1247	0.2837	0.3225
6750	1250	6165	6209	3380	3167	1.8237	1.9607	11.2455	10.1694	0.2850	0.3242
8000	2500	6181	6209	3392	3168	1.8222	1.9598	11.3165	10.1765	0.2845	0.3240
6000	500	6157	6170	3380	3154	1.8214	1.9561	11.2386	10.0818	0.2842	0.3231

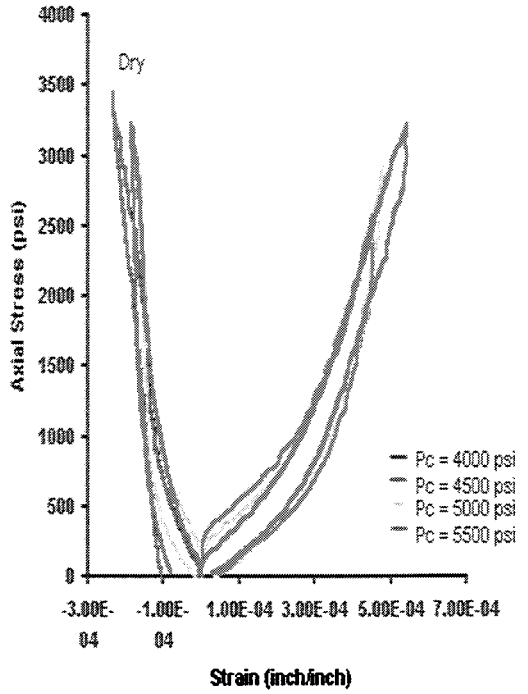

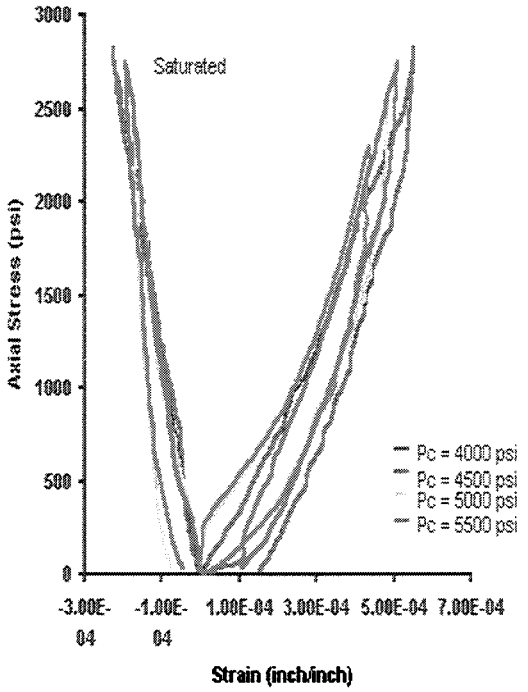

Table 2.26. Compressional and shear wave velocities, acoustic moduli, strain response for various confining pressures of dry and saturated Clearfolk sample No. 36

Axial	Net Axial	Vp (m/sec)		Vs (m/sec)		Vp/Vs		E (psi*1E6)		ν	
Stress (psi)	Stress (psi)	Dry	Saturated	Dry	Saturated	Dry	Saturated	Dry	Saturated	Dry	Saturated
4000	0	5328	6189	2970	3076	1.7943	2.0118	8.6023	9.6753	0.2747	0.3359
5250	1250	5387	6236	2970	3067	1.8141	2.0332	8.6496	9.6500	0.2817	0.3404
6500	2500	5441	6276	2983	3076	1.8241	2.0400	8.7487	9.7183	0.2851	0.3419
4500	500	5435	6197	2974	3076	1.8274	2.0143	8.7055	9.6792	0.2863	0.3365
4500	0	5453	6696	3109	3075	1.7537	2.1778	9.3154	9.8840	0.2591	0.3664
5750	1250	5453	6236	3119	3075	1.7484	2.0283	9.3560	9.6889	0.2569	0.3394
7000	2500	5459	6276	3124	3075	1.7476	2.0413	9.3822	9.7082	0.2566	0.3421
5000	500	5447	6213	3119	3075	1.7465	2.0206	9.3501	9.6772	0.2561	0.3378
5000	0	5465	6205	3124	3025	1.7496	2.0509	9.3881	9.4136	0.2574	0.3440
6250	1250	5447	6228	3128	3025	1.7412	2.0587	9.3907	9.4244	0.2539	0.3456
7500	2500	5465	6252	3133	3025	1.7442	2.0665	9.4291	9.4351	0.2552	0.3471
5500	500	5453	6236	3128	3025	1.7431	2.0613	9.3967	9.4280	0.2547	0.3461
5500	0	5459	6236	3076	3025	1.7745	2.0613	9.1783	9.4280	0.2673	0.3461
6750	1250	5465	6268	3067	3027	1.7817	2.0709	9.1433	9.4498	0.2701	0.3480
8000	2500	5471	6268	3076	3031	1.7783	2.0678	9.1891	9.4737	0.2688	0.3474
6000	500	5465	6229	3076	3031	1.7764	2.0549	9.1837	9.4560	0.2680	0.3448

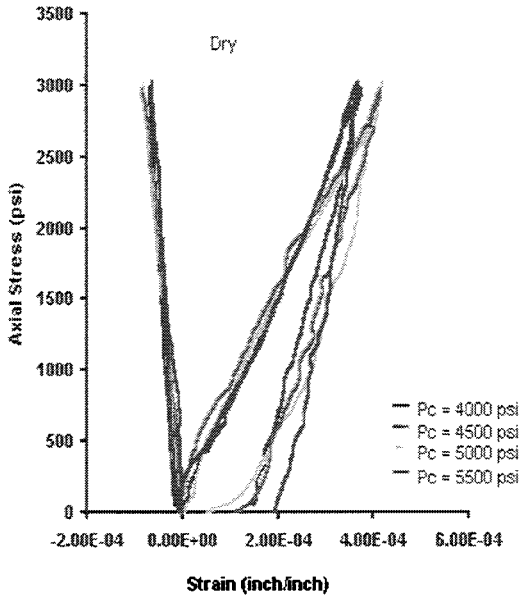

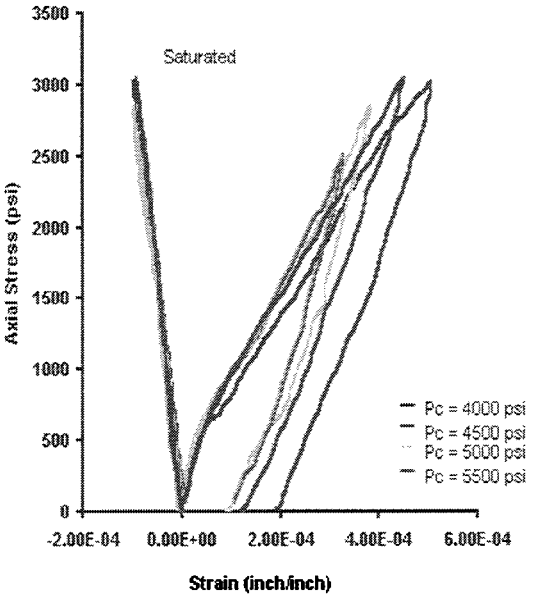

2.5 ULTRASONIC VELOCITIES IN NORTH SEA FRIABLE SANDS

Measurements were performed in the following order.

- CT scans
- Compressional and shear velocity vs. Stress of dry samples
- Grain density
- Porosity and permeability vs. Stress
- Particle Size Distribution

CT density scans of the horizontal cross section were taken of each sample prior to testing. Each sample was then cleaned and trimmed to achieve parallelism between opposite faces. Porosity and permeability were measured under hydrostatic stress state at controlled room temperature. Dry and saturated wave velocities were measured after first cycle of loading and unloading completed between 725 and 3625 psi in 725 psi increments along both the loading and unloading cycle. The change in length was measured as a function of stress and used to correct the sample length in the velocity calculations.

Wave velocities were measured using the ultrasonic pulsed through-transmission technique. The central frequency of the compressional and shear transducers was 0.8 MHz. Compressional wave velocity calculations were based on signal first arrivals, while shear wave velocity calculations were based on the shear signal first negative peak. Calibration of the apparatus included measuring the intrinsic delay times of both the compressional and shear wave signals as a function of stress. These delay times were subtracted from the corresponding signal arrival times in the wave velocity calculations. Signal waveforms of dry and saturated samples were captured and stored in electronic files.

During the measurement of the acoustic properties simultaneous measurements are carried out for the pore volume and air permeability at three different hydrostatic stress levels - 725 psi, 2175 psi, and 3625 psi. These three stress levels were chosen so that correlation between velocity and porosity/permeability could be adjusted for stress. The grain density was measured using Boyle's Law helium porosimetry and was performed at the conclusion of the porosity/permeability measurements. Particle size distributions of each sample were then determined.

Table 2.27. Change of porosity and permeability as a function of hydrostatic stress.

Sample : 12

Grain Density (gm/cc) = 2.6400 Grain Volume (cc) = 9.0030

Hydrostatic Stress psi	Pore Volume cc	Porosity cc/cc	Permeability mD
0.5	3.1031	24.6157	13.1900
1.5	3.0176	23.9375	12.3204
7.5	2.9750	23.5995	12.2226
15	2.9505	23.4052	11.9538
20	2.9274	23.2219	11.7604
25	2.9072	23.0617	11.5359
20	2.9288	23.2330	11.5669

Table 2.28: Acoustic properties of Sample # 12, Depth = 4041.55 m. 34/11-3

Paxial	Tpi	Tsi	dX	Tp	Ts	Vp	Vs	Vp/Vs
Mpa	usec	usec	inch	usec	usec	m/s	m/s	
2.5	2.7216	5.4029	0.0000	12.0879	19.0109	2693	1853	1.4529
5.0	2.7216	5.4029	0.0036	11.5164	18.3699	2857	1938	1.4744
7.5	2.7124	5.4029	0.0079	10.9010	17.7289	3056	2030	1.5053
10.0	2.7033	5.4029	0.0115	10.4615	17.1794	3214	2117	1.5179
15.0	2.7033	5.4029	0.0176	10.0769	16.7216	3360	2189	1.5350
20.0	2.7033	5.4029	0.0228	9.8791	16.4468	3434	2231	1.5390
24.9	2.7033	5.4029	0.0264	9.7912	16.2383	3464	2266	1.5287
20.0	2.7033	5.4029	0.0261	9.7912	16.2637	3465	2261	1.5323
15.0	2.7033	5.4029	0.0244	9.8348	16.3553	3450	2246	1.5358
10.0	2.7033	5.4029	0.0205	9.9923	16.5384	3389	2218	1.5277
7.5	2.7124	5.4029	0.0178	10.1208	16.7216	3344	2188	1.5278
5.0	2.7124	5.4029	0.0138	10.3846	16.9963	3242	2145	1.5111
2.5	2.7124	5.4029	0.0085	10.6881	17.3673	3135	2090	1.5001

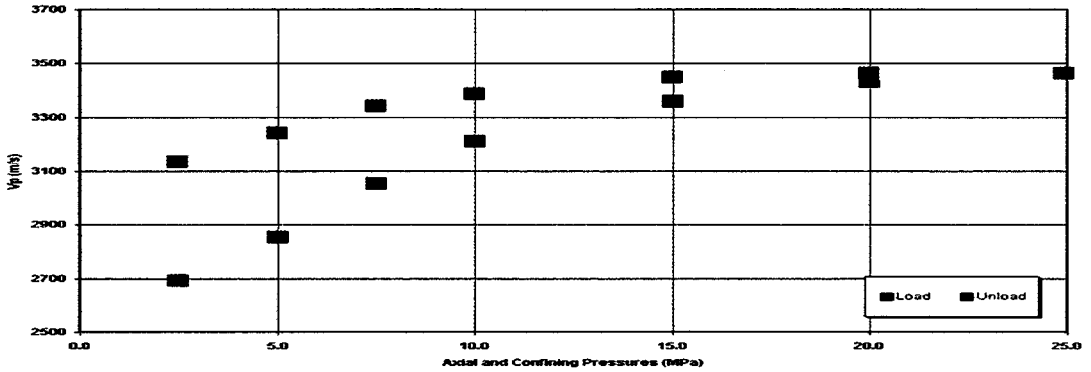

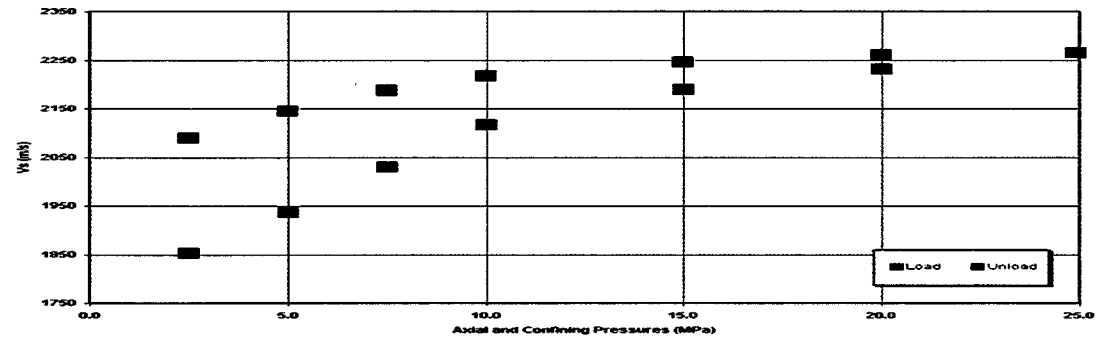

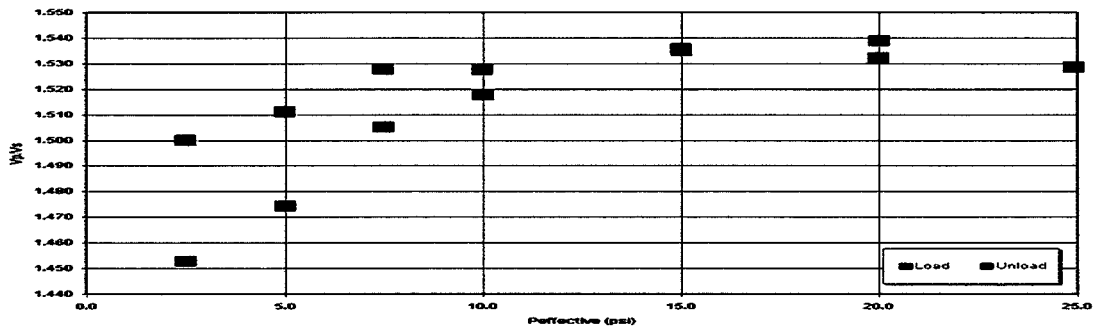

Figure 2. 13: Acoustic properties of Sample # 12, Depth = 4041.55 m. 34/11-3

Table 2.29. Change of porosity and permeability as a function of hydrostatic stress.

Sample : 14

Grain Density (gm/cc) = 2.6500 Grain Volume (cc) = 9.3480

Hydrostatic Stress psi	Pore Volume cc	Porosity cc/cc	Permeability mD
0.5	2.8584	22.6749	9.9876
1.5	2.7953	22.1741	9.4675
7.5	2.7767	22.0266	9.2192
15	2.7525	21.8346	8.6556
20	2.7543	21.8489	8.2176
25	2.7312	21.6657	7.8156
20	2.7506	21.8196	7.9038

Table 2.30. Acoustic properties of Sample # 14, Depth = 4042.00 m. 34/11-3

Paxial Mpa	Tpi usec	Tsi usec	dX inch	Tp usec	Ts usec	Vp m/s	Vs m/s	Vp/Vs
2.5	2.7216	5.4029	0.0000	11.4285	17.1881	2911	2151	1.3535
5.0	2.7216	5.4029	0.0002	10.5699	16.7112	3229	2241	1.4409
7.5	2.7124	5.4029	0.0004	10.1738	16.3738	3396	2310	1.4704
10.0	2.7033	5.4029	0.0005	9.9123	16.2024	3515	2346	1.4981
15.0	2.7033	5.4029	0.0007	9.6923	16.0128	3624	2388	1.5181
20.0	2.7033	5.4029	0.0009	9.6263	15.8974	3658	2413	1.5159
24.9	2.7033	5.4029	0.0012	9.5164	15.8341	3716	2427	1.5311
20.0	2.7033	5.4029	0.0012	9.5164	15.8448	3716	2425	1.5326
15.0	2.7033	5.4029	0.0011	9.5384	15.9318	3705	2405	1.5404
10.0	2.7033	5.4029	0.0010	9.5604	16.0453	3693	2379	1.5520
7.5	2.7124	5.4029	0.0010	9.6263	16.1954	3663	2346	1.5610
5.0	2.7124	5.4029	0.0010	9.8021	16.4468	3572	2293	1.5577
2.5	2.7124	5.4029	0.0009	10.2197	16.8131	3373	2220	1.5199

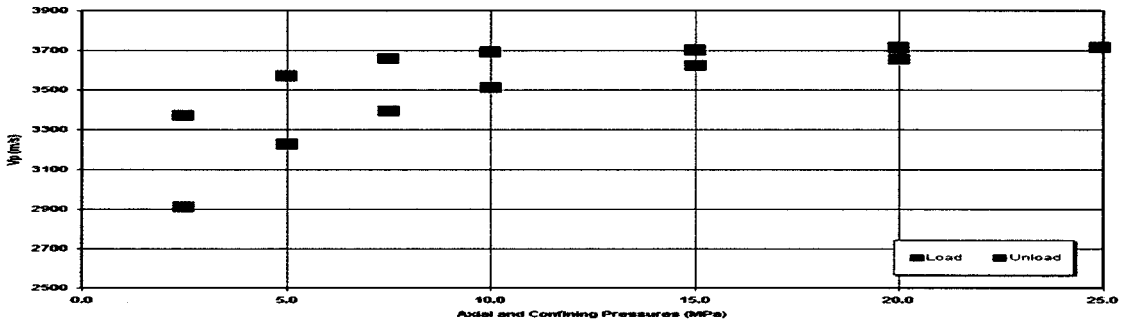

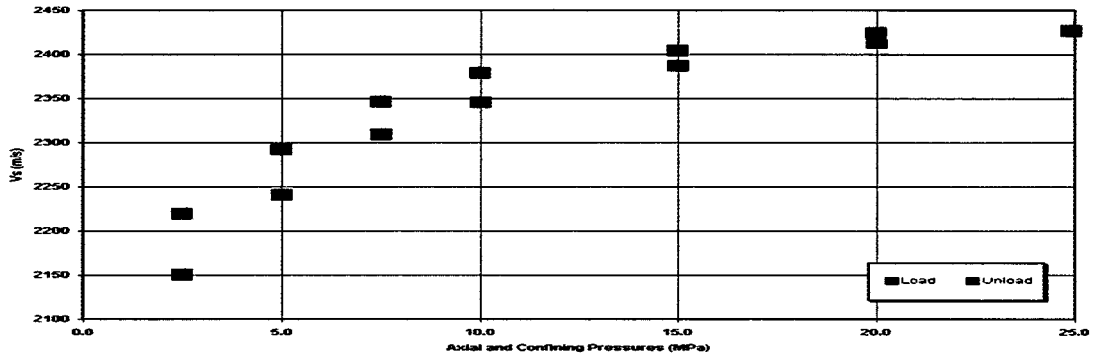

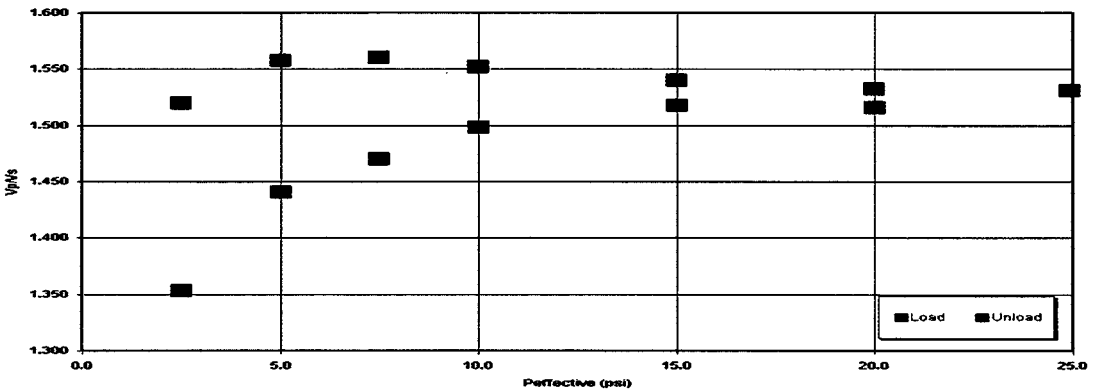

Figure 2. 14: Acoustic properties of Sample # 14, Depth = 4042.00 m. 34/11-3

Table 2.31. Change of porosity and permeability as a function of hydrostatic stress.

Sample : 18

Grain Density (gm/cc) = 2.6920 **Grain Volume (cc) = 9.7520**

Hydrostatic Stress psi	Pore Volume cc	Porosity cc/cc	Permeability mD
0.5	2.7543	21.8487	2.0920
1.5	2.5827	20.4875	1.9742
7.5	2.5261	20.0385	1.8812
15	2.4676	19.5745	1.7818
20	2.4470	19.4111	1.7356
25	2.4291	19.2691	1.6600
20	2.4474	19.4142	1.7096

Table 2.32: Acoustic properties of sample 18.

Paxial Mpa	Tpi usec	Tsi usec	dX inch	Tp usec	Ts usec	Vp m/s	Vs m/s	Vp/Vs
2.5	2.7216	5.4029	0.0000	10.3406	16.7216	3324	2237	1.4856
5.0	2.7216	5.4029	0.0019	10.0270	16.4186	3460	2295	1.5079
7.5	2.7124	5.4029	0.0036	9.8045	16.2393	3558	2329	1.5280
10.0	2.7033	5.4029	0.0046	9.6344	16.0970	3637	2357	1.5429
15.0	2.7033	5.4029	0.0060	9.4625	15.9296	3724	2391	1.5574
20.0	2.7033	5.4029	0.0067	9.3956	15.8488	3759	2408	1.5609
24.9	2.7033	5.4029	0.0071	9.3296	15.8058	3795	2417	1.5699
20.0	2.7033	5.4029	0.0071	9.3296	15.8058	3795	2417	1.5699
15.0	2.7033	5.4029	0.0068	9.3797	15.8751	3767	2402	1.5685
10.0	2.7033	5.4029	0.0063	9.4711	15.9890	3718	2377	1.5642
7.5	2.7124	5.4029	0.0059	9.5867	16.0805	3662	2358	1.5533
5.0	2.7124	5.4029	0.0051	9.7105	16.2637	3600	2320	1.5520
2.5	2.7124	5.4029	0.0039	9.9154	16.4727	3502	2279	1.5368

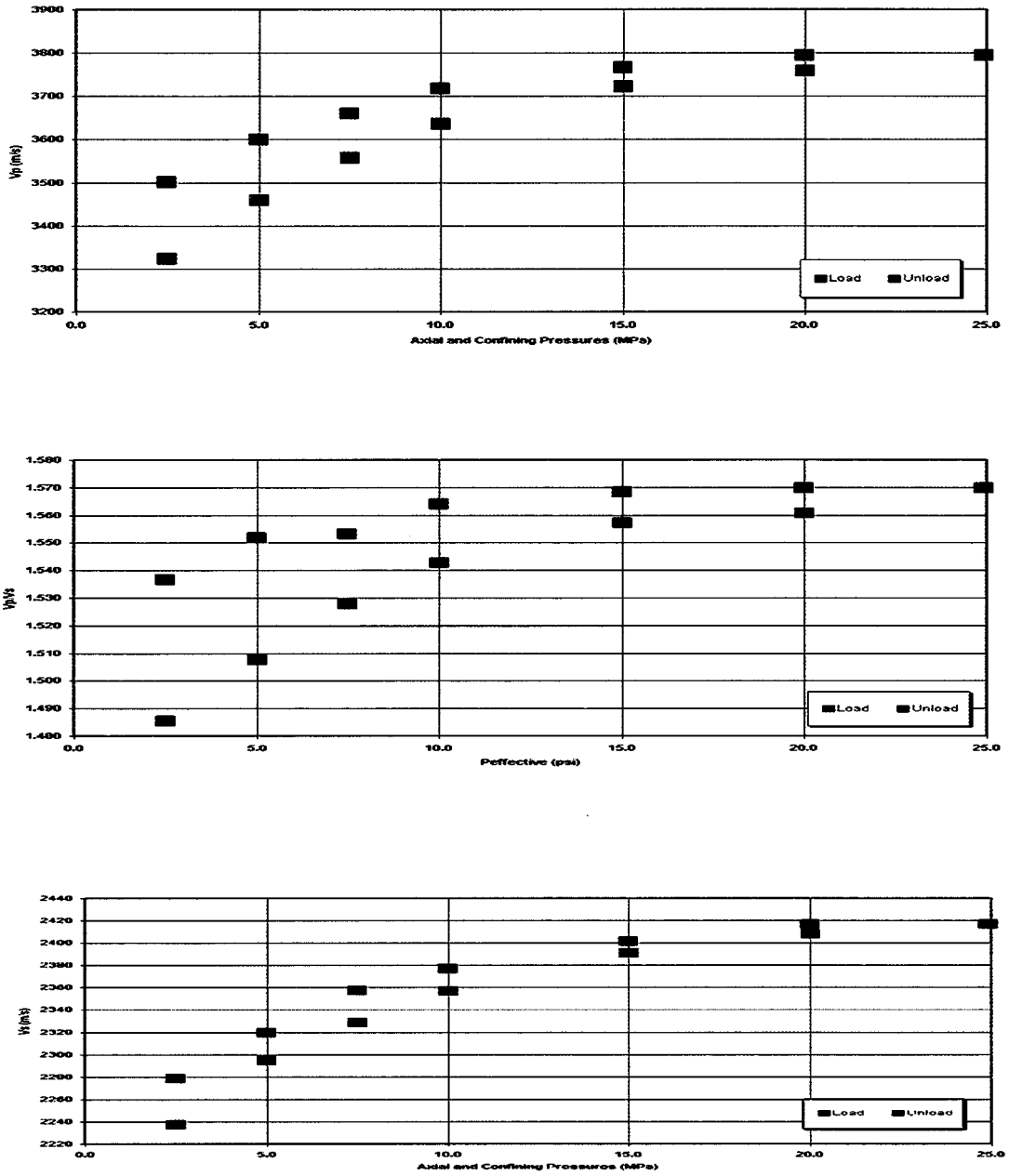

Figure 2. 15: Acoustic properties of Sample # 18

Table 2.33. Change of porosity and permeability as a function of hydrostatic stress.

Sample : 26

Grain Density (gm/cc) = 2.6500 Grain Volume (cc) = 10.3610

Hydrostatic Stress psi	Pore Volume cc	Porosity cc/cc	Permeability mD
0.5	1.9245	15.2659	0.4960
1.5	1.8694	14.8288	0.3636
7.5	1.8530	14.6987	0.3473
15	1.8428	14.6178	0.3194
20	1.8232	14.4623	0.3042
25	1.8218	14.4512	0.2820
20	1.8290	14.5084	0.2912

Table 2.34: Acoustic properties of sample 26.

Paxial Mpa	Tpi usec	Tsi usec	dX inch	Tp usec	Ts usec	Vp m/s	Vs m/s	Vp/Vs
2.5	2.7216	5.4029	0.0000	10.4395	16.8131	3288	2224	1.4784
5.0	2.7216	5.4029	0.0017	10.2229	16.6151	3377	2259	1.4947
7.5	2.7124	5.4029	0.0026	10.0476	16.4336	3450	2294	1.5038
10.0	2.7033	5.4029	0.0034	9.9367	16.2892	3496	2323	1.5050
15.0	2.7033	5.4029	0.0044	9.7435	16.0941	3588	2363	1.5186
20.0	2.7033	5.4029	0.0052	9.6549	15.9910	3631	2384	1.5231
25.0	2.7033	5.4029	0.0058	9.5604	15.8974	3679	2404	1.5305
20.0	2.7033	5.4029	0.0057	9.5972	15.9237	3660	2398	1.5261
15.0	2.7033	5.4029	0.0055	9.6754	16.0143	3619	2378	1.5220
10.0	2.7033	5.4029	0.0052	9.8174	16.1721	3548	2344	1.5138
7.5	2.7124	5.4029	0.0051	9.9076	16.2780	3509	2321	1.5114
5.0	2.7124	5.4029	0.0049	10.0400	16.4193	3446	2292	1.5034
2.5	2.7124	5.4029	0.0047	10.1894	16.5747	3378	2261	1.4942

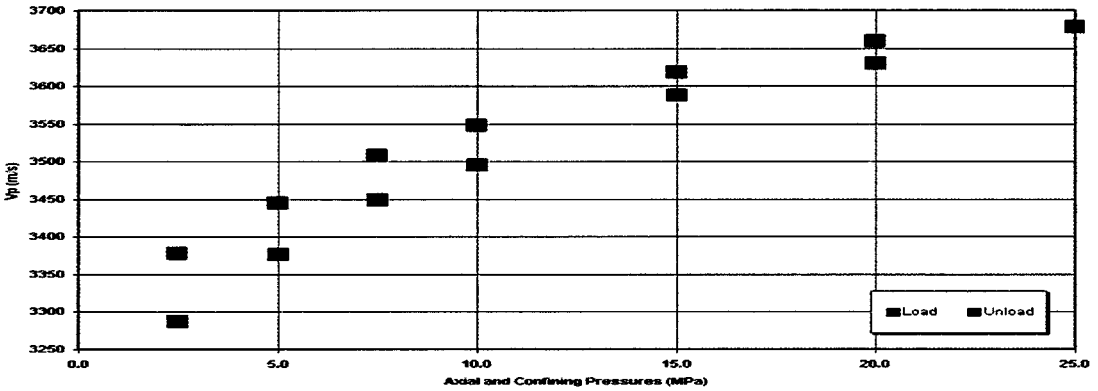

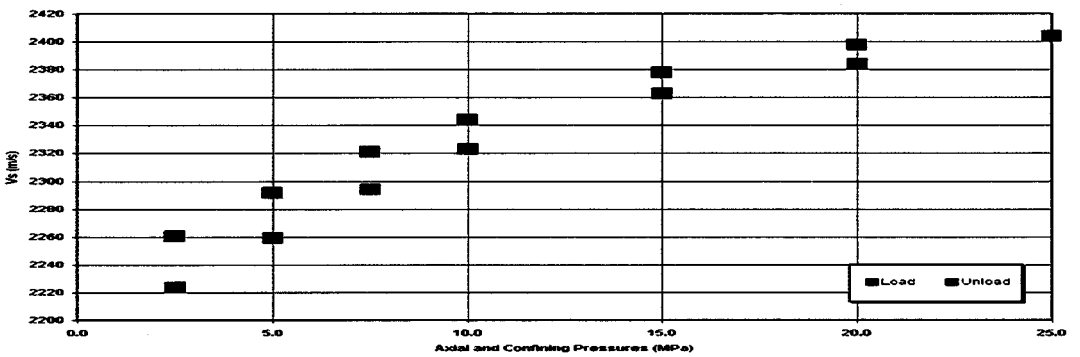

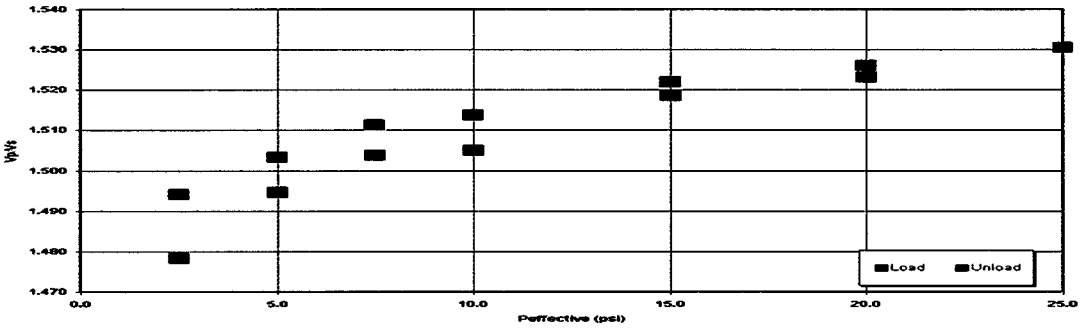

Figure 2. 16: Acoustic properties of Sample # 26

Table 2.35. Change of porosity and permeability as a function of hydrostatic stress.

Sample : 37

Grain Density (gm/cc) = 2.6510 **Grain Volume (cc) = 9.6200**

Hydrostatic Stress psi	Pore Volume cc	Porosity cc/cc	Permeability mD
0.5	2.9859	24.3070	8.8395
1.5	2.9642	24.1306	8.8455
7.5	2.6166	21.3009	7.6567
15	2.5622	20.8580	6.8933
20	2.5400	20.6773	5.8455
25	2.5256	20.5601	5.2688
20	2.5363	20.6472	5.6256

Table 2.36: Acoustic properties of Sample # 37, Depth = 4049.05 m. 34/11-3

Phyd Mpa	Tpl usec	Tsl usec	dX inch	Tp usec	Ts usec	Vp m/s	Vs m/s	Vp/Vs
1.4	2.7216	5.4029	0.0000	11.8681	17.3626	2774	2122	1.3076
3.4	2.7216	5.4029	0.0029	10.9909	15.7638	3060	2442	1.2529
6.9	2.7124	5.4029	0.0046	10.2967	14.8575	3330	2671	1.2466
10.3	2.7033	5.4029	0.0056	9.9450	14.2475	3484	2853	1.2213
13.8	2.7033	5.4029	0.0064	9.7728	13.8241	3566	2994	1.1912
17.2	2.7033	5.4029	0.0070	9.6263	13.6043	3640	3072	1.1847
20.7	2.7033	5.4029	0.0077	9.5229	13.4725	3692	3120	1.1833
24.1	2.7033	5.4029	0.0085	9.4432	13.3406	3733	3170	1.1777
27.6	2.7033	5.4029	0.0094	9.3699	13.2527	3770	3202	1.1775
31.0	2.7033	5.4029	0.0105	9.3315	13.1648	3788	3235	1.1710
34.5	2.7033	5.4029	0.0113	9.2673	13.0329	3822	3288	1.1624
31.0	2.7033	5.4029	0.0110	9.2673	13.0329	3823	3289	1.1624
27.6	2.7033	5.4029	0.0106	9.2967	13.0769	3808	3271	1.1639
24.1	2.7033	5.4029	0.0103	9.3058	13.0769	3804	3273	1.1623
20.7	2.7033	5.4029	0.0100	9.3791	13.1648	3763	3236	1.1627
17.2	2.7033	5.4029	0.0098	9.4149	13.2967	3744	3183	1.1761
13.8	2.7033	5.4029	0.0095	9.489	13.4285	3704	3132	1.1827
10.3	2.7033	5.4029	0.0091	9.6721	13.6923	3608	3033	1.1895
6.9	2.7124	5.4029	0.0088	9.901	13.956	3499	2941	1.1898
3.4	2.7124	5.4029	0.0083	10.4395	14.5274	3257	2758	1.1808
1.4	2.7124	5.4029	0.0080	11.0989	15.4945	3001	2494	1.2033

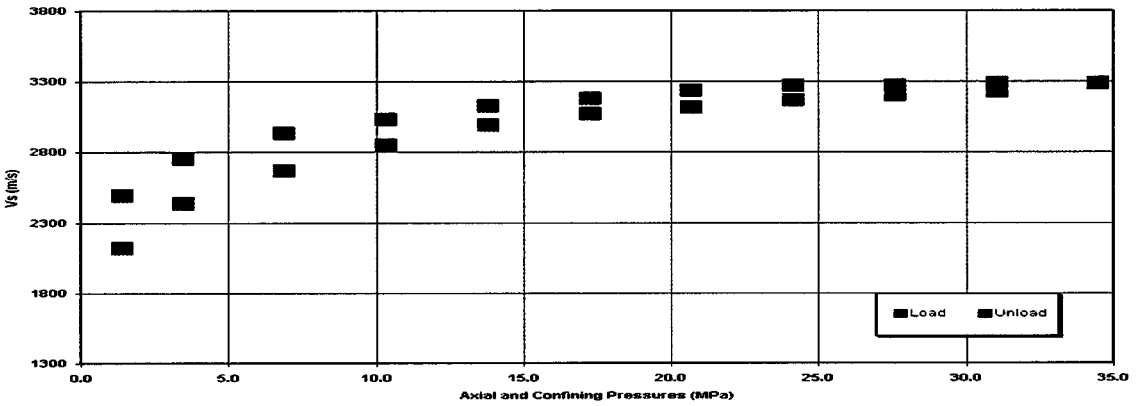

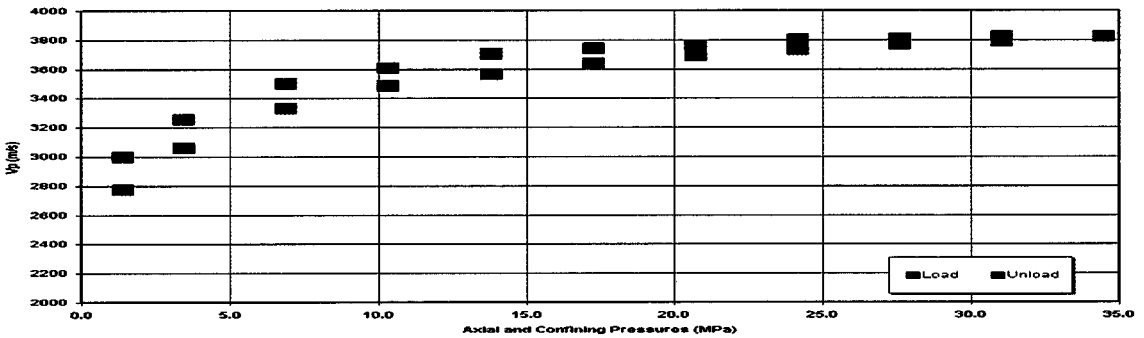

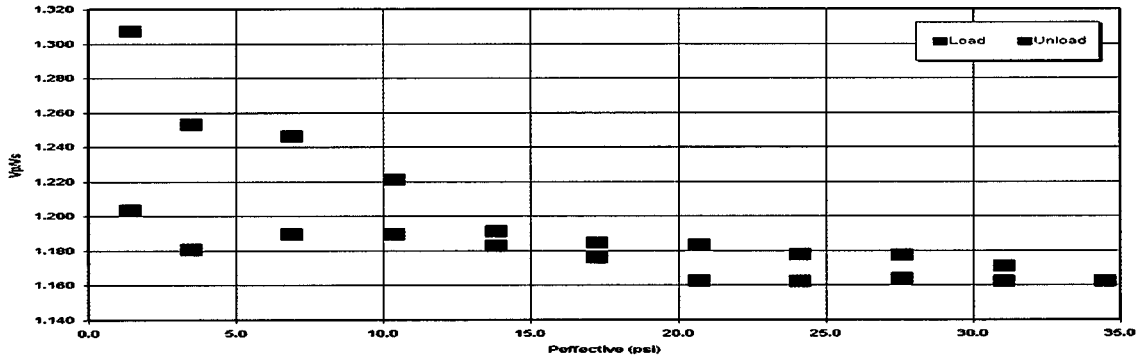

Figure 2. 17: Acoustic properties of Sample # 37

Table 2.37. Change of porosity and permeability as a function of hydrostatic stress.

Sample : 60

Grain Density (gm/cc) = 2.6410 Grain Volume (cc) = 9.5080

Hydrostatic Stress psi	Pore Volume cc	Porosity cc/cc	Permeability mD
0.5	2.7982	20.2363	10.4390
1.5	2.6292	19.0140	10.2652
7.5	2.6138	18.9026	10.0462
15	2.6008	18.8086	9.8078
20	2.5887	18.7211	9.4084
25	2.5803	18.6603	8.9743
20	2.6041	18.8324	9.2112

Table 2.38. Acoustic properties of Sample # 60, Depth = 4095.00 m. 34/11-3

Phyd	Tpi	Tsi	dX	Tp	Ts	Vp	Vs	Vp/Vs
Mpa	usec	usec	inch	usec	usec	m/s	m/s	
1.4	2.7216	5.4029	0.0000	11.9010	19.0109	2759	1861	1.4824
3.4	2.7216	5.4029	0.0001	11.2571	18.6042	2967	1918	1.5466
6.9	2.7124	5.4029	0.0002	10.5120	18.1868	3246	1981	1.6390
10.3	2.7033	5.4029	0.0003	10.0842	17.7308	3430	2054	1.6702
13.8	2.7033	5.4029	0.0004	9.8736	17.4774	3530	2097	1.6840
17.2	2.7033	5.4029	0.0004	9.6758	17.3376	3630	2121	1.7117
20.7	2.7033	5.4029	0.0005	9.5934	17.1945	3674	2147	1.7114
24.1	2.7033	5.4029	0.0005	9.5109	17.0288	3718	2177	1.7078
27.6	2.7033	5.4029	0.0005	9.4285	16.9010	3764	2201	1.7097
31.0	2.7033	5.4029	0.0005	9.4010	16.8020	3779	2220	1.7019
34.5	2.7033	5.4029	0.0006	9.3967	16.7614	3781	2228	1.6970
31.0	2.7033	5.4029	0.0005	9.3967	16.8261	3781	2216	1.7066
27.6	2.7033	5.4029	0.0005	9.4461	16.8947	3754	2202	1.7043
24.1	2.7033	5.4029	0.0005	9.5164	16.96389364	3715	2189	1.6969
20.7	2.7033	5.4029	0.0005	9.5208	17.0879	3713	2166	1.7140
17.2	2.7033	5.4029	0.0005	9.5868	17.1434901	3677	2156	1.7056
13.8	2.7033	5.4029	0.0005	9.686568959	17.271	3625	2133	1.6995
10.3	2.7033	5.4029	0.0005	9.8021	17.4542	3566	2100	1.6977
6.9	2.7124	5.4029	0.0005	10.0835	17.7044572	3434	2058	1.6689
3.4	2.7124	5.4029	0.0004	10.4725	18.13226375	3262	1989	1.6404
1.4	2.7124	5.4029	0.0004	10.9362	18.40407494	3078	1947	1.5809

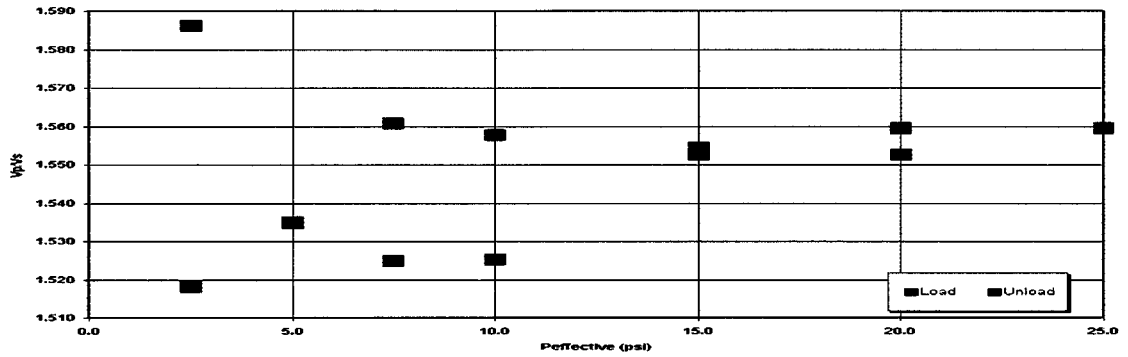

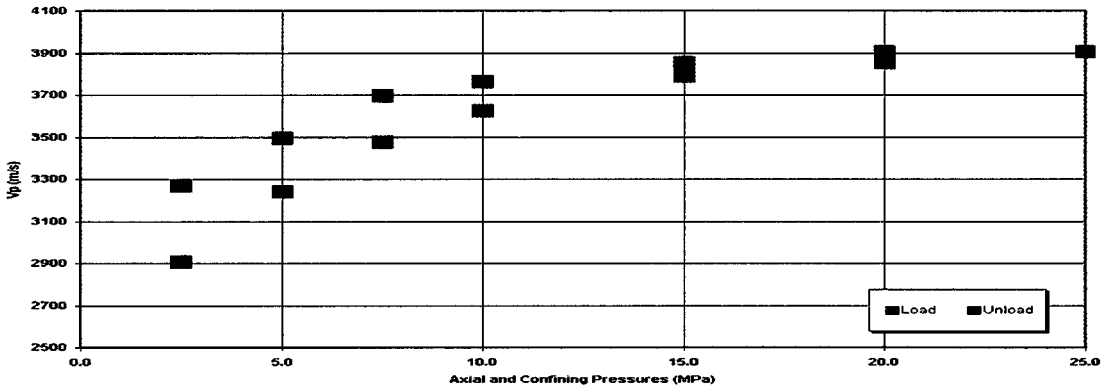

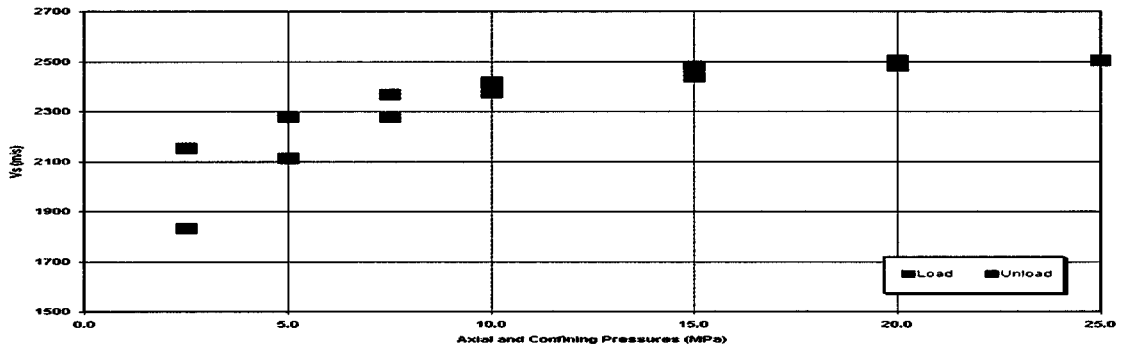

Figure 2. 18: Acoustic properties of Sample # 60

Table 2.39. Change of porosity and permeability as a function of hydrostatic stress.

Sample : 76

Grain Density (gm/cc) = 2.6380 Grain Volume (cc) = 9.3920

Hydrostatic Stress psi	Pore Volume cc	Porosity cc/cc	Permeability mD
0.5	3.2186	25.4960	6.8810
1.5	3.2181	25.4924	6.0310
7.5	2.9175	23.1111	4.7564
15	2.8861	22.8624	4.3043
20	2.8559	22.6232	3.6734
25	2.8091	22.2524	3.2850
20	2.8191	22.3317	3.3948

Table 2.40: Acoustic properties of Sample # 76, Depth = 4099.00 m. 34/11-3

Phyd	Tpi	Tsi	dX	Tp	Ts	Vp	Vs	Vp/Vs
Mpa	usec	usec	inch	usec	usec	m/s	m/s	
1.4	2.7216	5.4029	0.0000	11.9010	19.0109	2759	1861	1.4824
3.4	2.7216	5.4029	0.0001	11.2571	18.6042	2867	1918	1.5456
6.9	2.7124	5.4029	0.0002	10.5120	10.1060	3246	1901	1.6090
10.3	2.7033	5.4029	0.0003	10.0842	17.7308	3430	2054	1.6702
13.8	2.7033	5.4029	0.0004	9.8736	17.4774	3530	2097	1.6840
17.2	2.7033	5.4029	0.0004	9.6758	17.3376	3630	2121	1.7117
20.7	2.7033	5.4029	0.0005	9.5934	17.1945	3674	2147	1.7114
24.1	2.7033	5.4029	0.0005	9.5109	17.0288	3718	2177	1.7078
27.6	2.7033	5.4029	0.0005	9.4285	16.9010	3764	2201	1.7097
31.0	2.7033	5.4029	0.0005	9.4010	16.8020	3779	2220	1.7019
34.5	2.7033	5.4029	0.0006	9.3967	16.7614	3781	2228	1.6970
31.0	2.7033	5.4029	0.0005	9.3967	16.8261	3781	2216	1.7066
27.6	2.7033	5.4029	0.0005	9.4461	16.8947	3754	2202	1.7043
24.1	2.7033	5.4029	0.0005	9.5164	16.96389364	3715	2189	1.6969
20.7	2.7033	5.4029	0.0005	9.5208	17.0879	3713	2166	1.7140
17.2	2.7033	5.4029	0.0005	9.5868	17.1434901	3677	2156	1.7056
13.8	2.7033	5.4029	0.0005	9.686568959	17.271	3625	2133	1.6995
10.3	2.7033	5.4029	0.0005	9.8021	17.4542	3566	2100	1.6977
6.9	2.7124	5.4029	0.0005	10.0835	17.7044572	3434	2058	1.6689
3.4	2.7124	5.4029	0.0004	10.4725	18.13226375	3262	1989	1.6404
1.4	2.7124	5.4029	0.0004	10.9362	18.40407494	3078	1947	1.5809

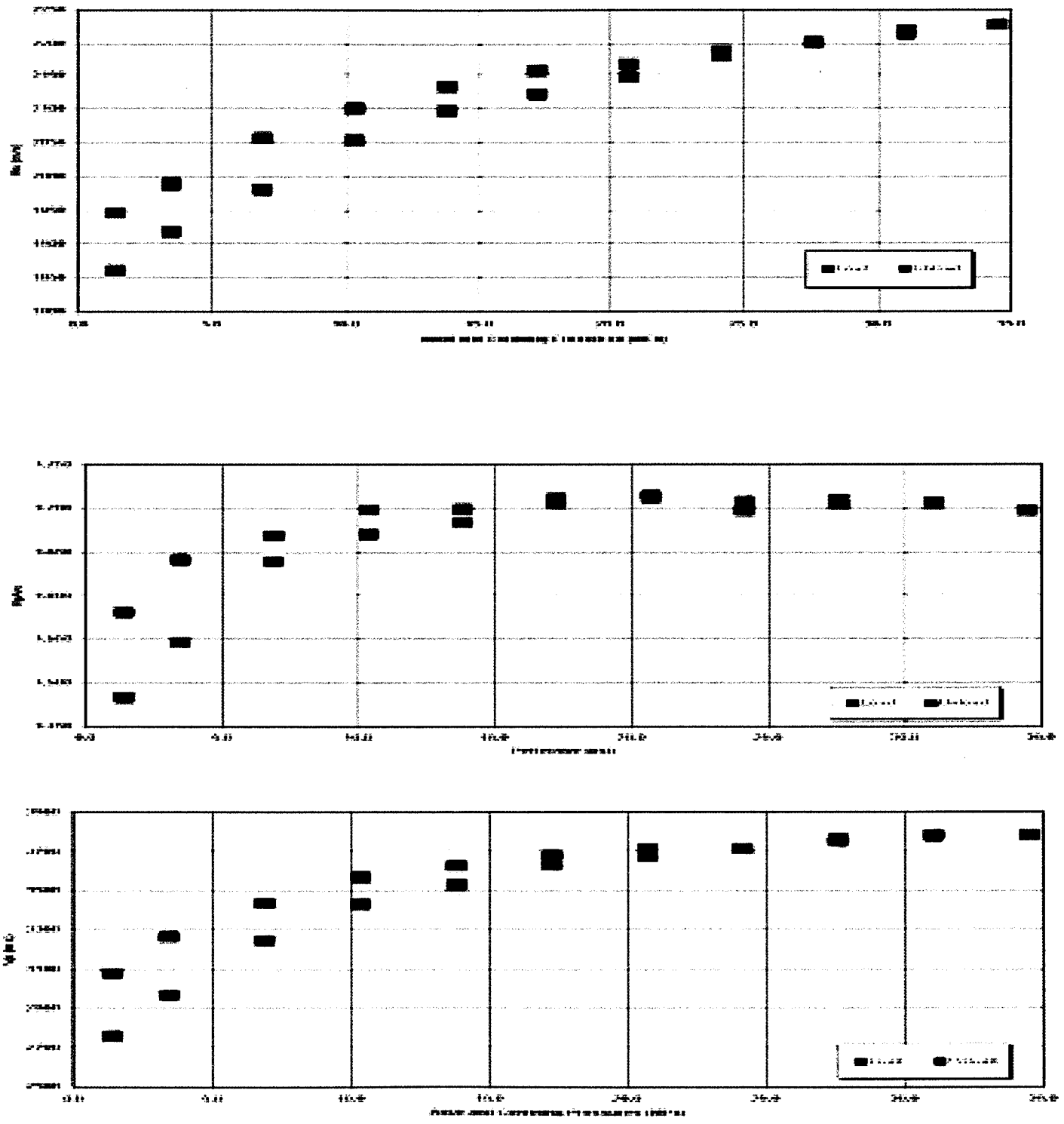

Figure 2. 19: Acoustic properties of Sample # 76

Table 2.41. Change of porosity and permeability as a function of hydrostatic stress.

Sample : 92

Grain Density (gm/cc) = 2.6360 Grain Volume (cc) = 9.4170

Hydrostatic Stress psi	Pore Volume cc	Porosity cc/cc	Permeability mD
0.5	3.1892	25.2990	4.4480
1.5	3.1220	24.7658	4.4412
7.5	2.8440	22.5606	4.0405
15	2.7941	22.1647	3.5424
20	2.7890	22.1243	3.3563
25	2.7800	22.0529	3.0584
20	2.7900	22.1322	3.0905

Table 2.42: Acoustic properties of Sample # 92, Depth = 4103.00 m. 34/11-3

Phyd Mpa	Tpi usec	Tsi usec	dX inch	Tp usec	Ts usec	Vp m/s	Vs m/s	Vp/Vs
1.4	2.7216	5.4029	0.0000	11.6630	21.9047	2838	1538	1.8455
3.4	2.7216	5.4029	0.0004	10.7545	19.5238	3158	1796	1.7579
6.9	2.7124	5.4029	0.0010	10.2700	10.7912	3051	1093	1.7696
10.3	2.7033	5.4029	0.0014	9.8864	18.2417	3527	1974	1.7874
13.8	2.7033	5.4029	0.0019	9.4941	17.9670	3729	2016	1.8502
17.2	2.7033	5.4029	0.0025	9.5293	17.6823	3708	2080	1.8004
20.7	2.7033	5.4029	0.0031	9.4285	17.5091	3762	2090	1.8001
24.1	2.7033	5.4029	0.0036	9.3736	17.4175	3790	2104	1.8012
27.6	2.7033	5.4029	0.0042	9.3095	17.3260	3825	2119	1.8048
31.0	2.7033	5.4029	0.0049	9.2545	17.2344	3854	2134	1.8060
34.5	2.7033	5.4029	0.0057	9.2282	17.1428	3867	2149	1.7993
31.0	2.7033	5.4029	0.0056	9.2395	17.1428	3860	2149	1.7961
27.6	2.7033	5.4029	0.0055	9.2461	17.1428	3857	2150	1.7943
24.1	2.7033	5.4029	0.0054	9.2505	17.2344	3855	2133	1.8071
20.7	2.7033	5.4029	0.0053	9.2901	17.2344	3832	2133	1.7962
17.2	2.7033	5.4029	0.0051	9.3296	17.326	3810	2117	1.7994
13.8	2.7033	5.4029	0.0048	9.3868	17.4175	3779	2102	1.7977
10.3	2.7033	5.4029	0.0043	9.4615	17.6007	3738	2071	1.8049
6.9	2.7124	5.4029	0.0038	9.6395	17.8754	3649	2027	1.8005
3.4	2.7124	5.4029	0.0033	9.9956	18.4249	3473	1942	1.7890
1.4	2.7124	5.4029	0.0029	10.589	19.3406	3212	1815	1.7695

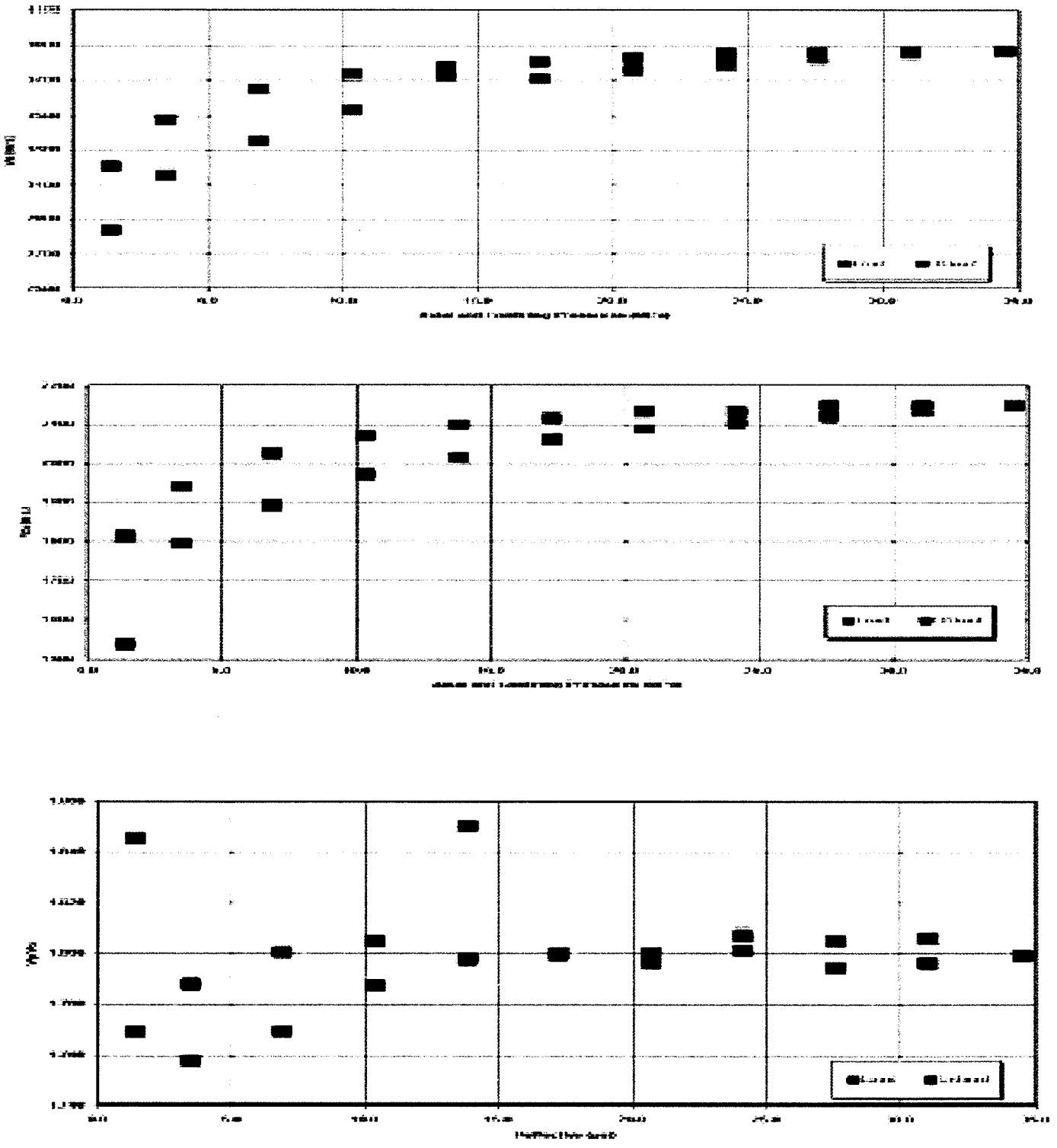

Figure 2. 20: Acoustic properties of Sample # 92

Table 2.43. Change of porosity and permeability as a function of hydrostatic stress.

Sample : 104

Grain Density (gm/cc) = 2.6590 Grain Volume (cc) = 9.6990

Hydrostatic Stress psi	Pore Volume cc	Porosity cc/cc	Permeability mD
0.5	2.7070	21.4733	16.5500
1.5	2.6404	20.9449	15.3869
7.5	2.5627	20.3285	14.9122
15	2.5479	20.2111	14.5920
20	2.5252	20.0311	14.1001
25	2.5219	20.0049	13.7320
20	2.5312	20.0787	13.7750

Table 2.44. Acoustic properties of Sample # 104, Depth = 4106.00 m. 34/11-3

Paxial	Tpi	Tsi	dX	Tp	Ts	Vp	Vs	Vp/Vs
Mpa	usec	usec	inch	usec	usec	m/s	m/s	
2.5	2.7216	5.4029	0.0000	10.9560	17.5457	3072	2083	1.4746
5.0	2.7216	5.4029	0.0043	10.6483	17.0998	3178	2154	1.4756
7.5	2.7124	5.4029	0.0087	10.4505	16.8095	3241	2198	1.4741
10.0	2.7033	5.4029	0.0127	10.2080	16.5863	3328	2233	1.4902
15.0	2.7033	5.4029	0.0208	9.8791	16.2637	3452	2281	1.5135
20.0	2.7033	5.4029	0.0272	9.6813	15.9890	3526	2325	1.5171
25.0	2.7033	5.4029	0.0328	9.4615	15.8058	3620	2352	1.5393
20.0	2.7033	5.4029	0.0300	9.4947	15.8700	3613	2344	1.5412
15.0	2.7033	5.4029	0.0265	9.5273	15.9372	3608	2338	1.5437
10.0	2.7033	5.4029	0.0233	9.6037	16.0168	3580	2328	1.5382
7.5	2.7124	5.4029	0.0209	9.6851	16.0935	3552	2317	1.5332
5.0	2.7124	5.4029	0.0178	9.7912	16.2229	3510	2296	1.5285
2.5	2.7124	5.4029	0.0125	10.1776	16.4468	3346	2262	1.4794

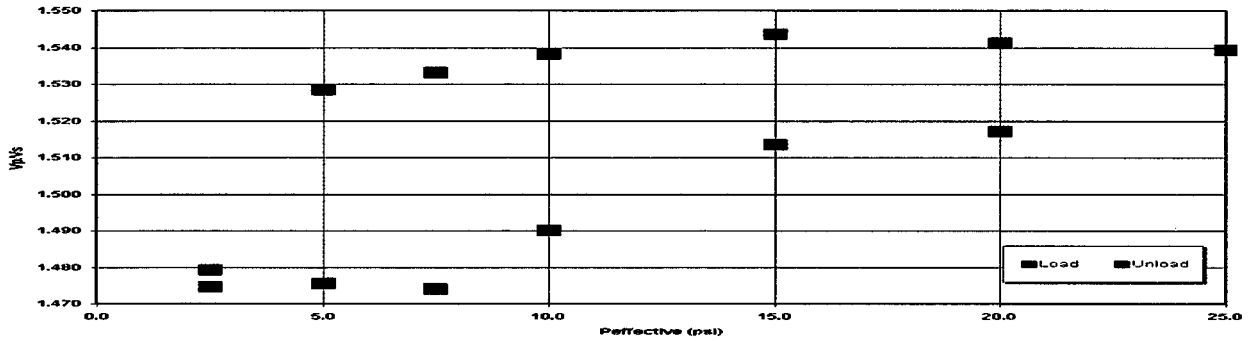

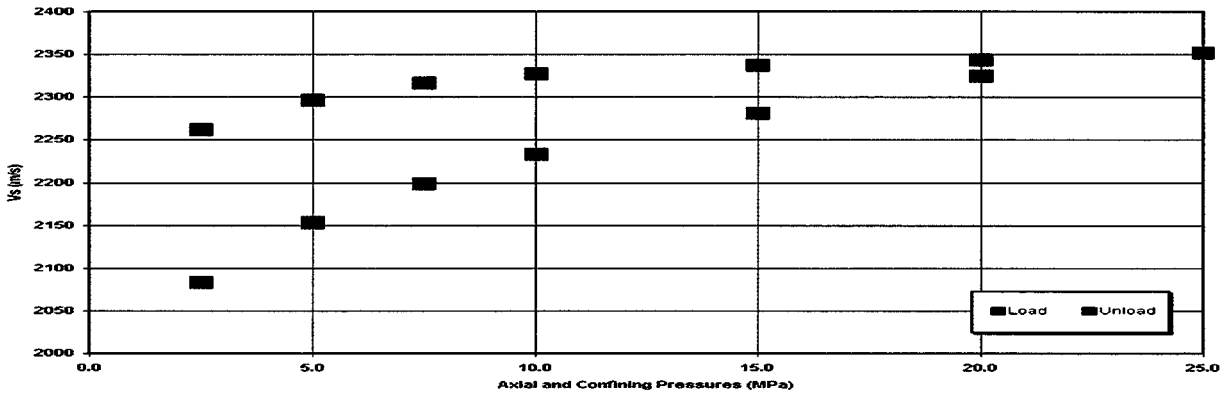

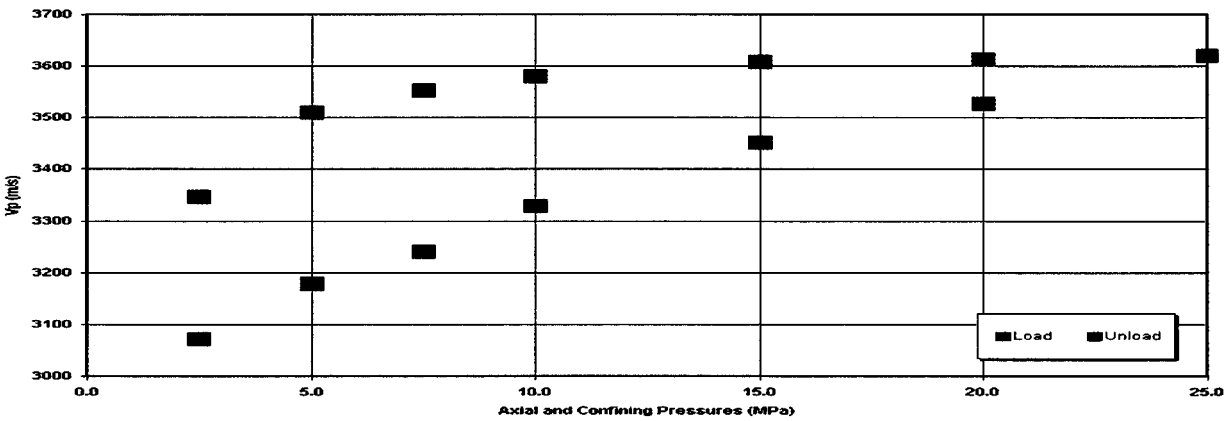

Figure 2. 21: Acoustic properties of Sample # 104

Table 2.45. Change of porosity and permeability as a function of hydrostatic stress.

Sample : 116

Grain Density (gm/cc) = 2.6640 Grain Volume (cc) = 9.5420

Hydrostatic Stress psi	Pore Volume cc	Porosity cc/cc	Permeability mD
0.5	3.0642	24.3070	5.6140
1.5	3.0574	24.2529	4.9110
7.5	2.6770	21.2354	4.2511
15	2.6494	21.0164	3.9932
20	2.5929	20.5682	3.5836
25	2.5748	20.4247	3.3438
20	2.5975	20.6047	3.5011

Table 2.46: Acoustic properties of Sample # 116, Depth = 4109.00 m. 34/11-3

Phyd Mpa	Tpi usec	Tsi usec	dX inch	Tp usec	Ts usec	Vp m/s	Vs m/s	Vp/Vs
1.4	2.7216	5.4029	0.0000	10.6721	19.7510	3188	1767	1.8047
3.4	2.7216	5.4029	0.0010	10.3223	19.4229	3332	1806	1.8446
6.9	2.7124	5.4029	0.0014	9.9835	18.9727	3481	1865	1.8663
10.3	2.7033	5.4029	0.0018	9.6904	18.7362	3621	1898	1.9083
13.8	2.7033	5.4029	0.0023	9.5295	18.4615	3705	1937	1.9130
17.2	2.7033	5.4029	0.0027	9.3956	18.1868	3777	1977	1.9102
20.7	2.7033	5.4029	0.0032	9.3315	18.0034	3812	2005	1.9010
24.1	2.7033	5.4029	0.0036	9.2857	17.8205	3837	2034	1.8865
27.6	2.7033	5.4029	0.0043	9.2582	17.6676	3851	2058	1.8711
31.0	2.7033	5.4029	0.0049	9.2195	17.5457	3871	2077	1.8635
34.5	2.7033	5.4029	0.0058	9.1848	17.4542	3888	2091	1.8593
31.0	2.7033	5.4029	0.0055	9.2109	17.4676	3874	2089	1.8539
27.6	2.7033	5.4029	0.0053	9.2307	17.5259	3863	2080	1.8572
24.1	2.7033	5.4029	0.0050	9.2615	17.59839281	3846	2068	1.8596
20.7	2.7033	5.4029	0.0048	9.295615165	17.66036142	3827	2058	1.8594
17.2	2.7033	5.4029	0.0045	9.3494	17.77782298	3797	2039	1.8620
13.8	2.7033	5.4029	0.0042	9.4065	17.91592713	3766	2017	1.8667
10.3	2.7033	5.4029	0.0040	9.5208	18.09013621	3703	1990	1.8610
6.9	2.7124	5.4029	0.0039	9.7296	18.29601003	3598	1958	1.8374
3.4	2.7124	5.4029	0.0035	10.0417	18.53481624	3447	1924	1.7917
1.4	2.7124	5.4029	0.0031	10.3714	18.71294969	3299	1899	1.7378

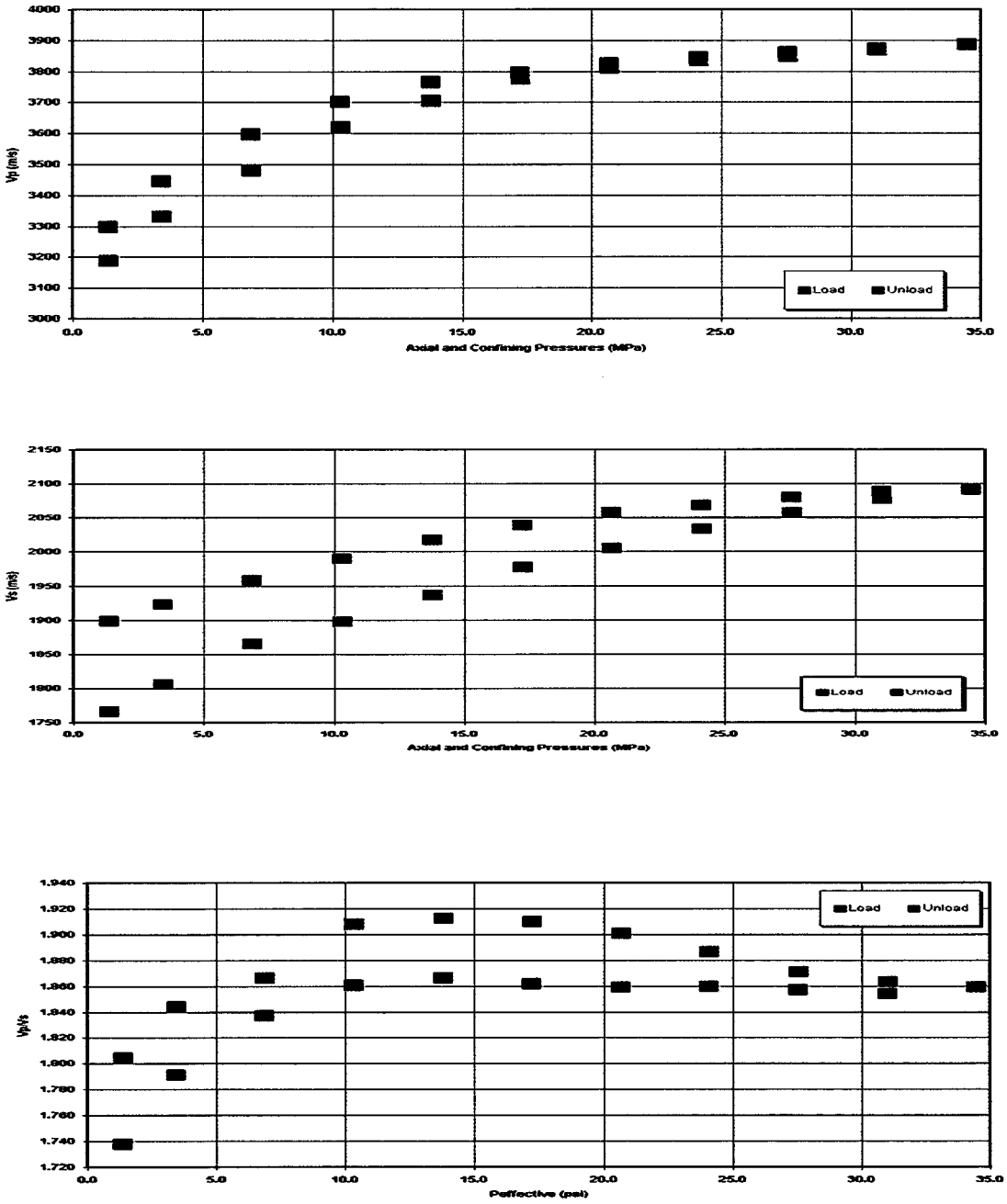

Figure 2.22: Acoustic properties of Sample # 116

Table 2.47 Change of porosity and permeability as a function of hydrostatic stress.

Sample : 120

Grain Density (gm/cc) = 2.6420 Grain Volume (cc) = 9.3370

Hydrostatic Stress psi	Pore Volume cc	Porosity cc/cc	Permeability mD
0.5	3.0696	24.3504	45.3920
1.5	2.8922	22.9432	43.0527
7.5	2.8426	22.5497	41.0569
15	2.8156	22.3355	38.7717
20	2.8079	22.2744	36.4348
25	2.7928	22.1547	35.0362
20	2.8123	22.3093	35.9004

Table 2.48: Acoustic properties of Sample # 120, Depth = 4110.00 m. 34/11-3

Paxial Mpa	Tpi usec	Tsi usec	dX inch	Tp usec	Ts usec	Vp m/s	Vs m/s	Vp/Vs
2.5	2.7216	5.4029	0.0000	11.3516	19.4688	2934	1800	1.6299
5.0	2.7216	5.4029	0.0009	10.8740	18.2384	3104	1971	1.5745
7.5	2.7124	5.4029	0.0016	10.5144	17.5457	3241	2082	1.5564
10.0	2.7033	5.4029	0.0021	10.2706	17.1749	3340	2147	1.5556
15.0	2.7033	5.4029	0.0028	9.9638	16.7216	3478	2231	1.5589
20.0	2.7033	5.4029	0.0035	9.8131	16.3553	3549	2304	1.5405
25.0	2.7033	5.4029	0.0042	9.7032	16.1721	3603	2342	1.5385
20.0	2.7033	5.4029	0.0039	9.7032	16.1721	3604	2342	1.5385
15.0	2.7033	5.4029	0.0036	9.7252	16.2637	3593	2323	1.5467
10.0	2.7033	5.4029	0.0032	9.7692	16.3553	3572	2305	1.5500
7.5	2.7124	5.4029	0.0030	9.8571	16.4468	3534	2286	1.5457
5.0	2.7124	5.4029	0.0027	9.9450	16.6300	3492	2249	1.5523
2.5	2.7124	5.4029	0.0024	10.4945	17.1911	3246	2143	1.5148

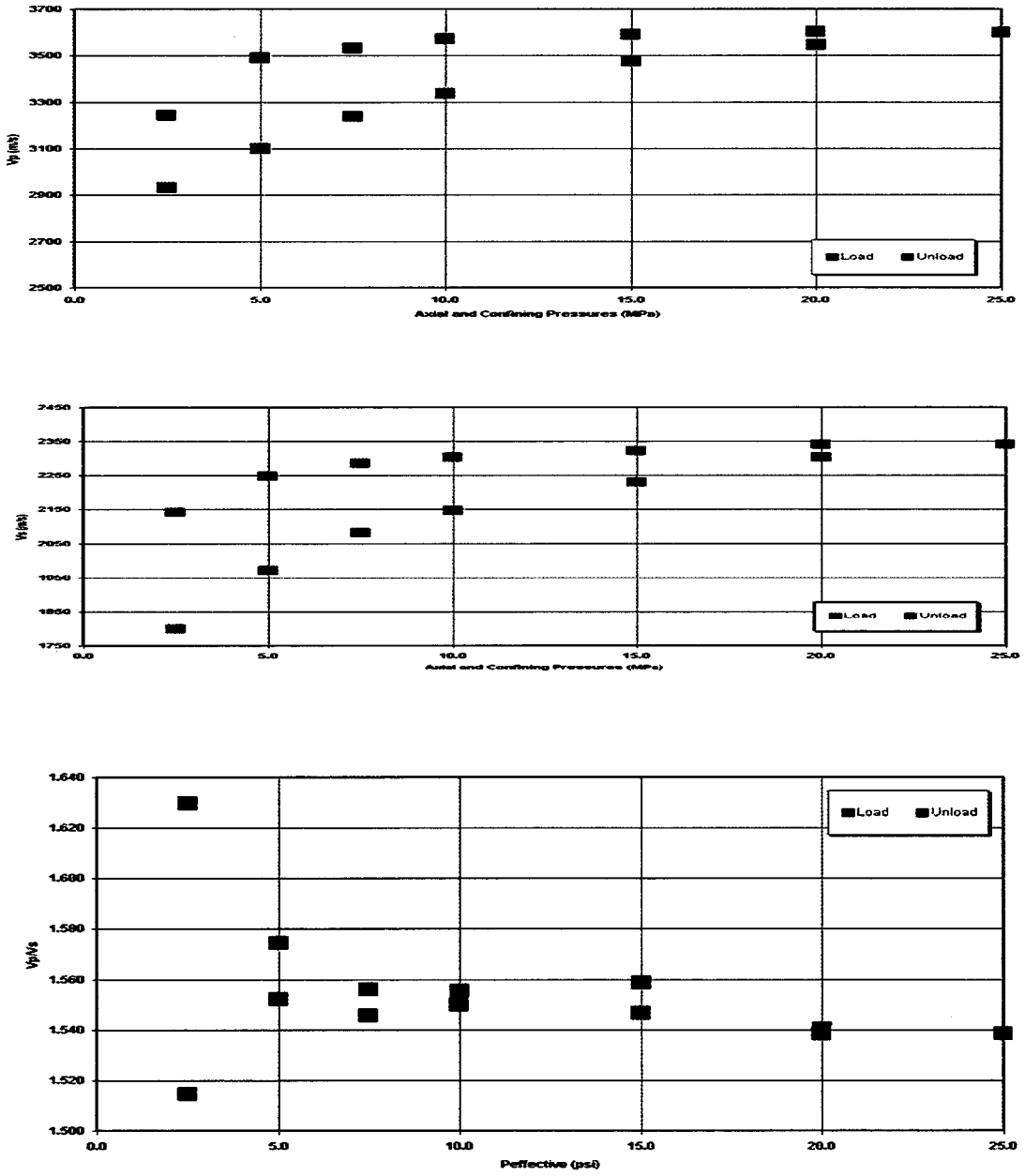

Figure 2.23: Acoustic properties of Sample # 120

Table 2.49. Change of porosity and permeability as a function of hydrostatic stress.

Sample : 127

Grain Density (gm/cc) = 2.6370 Grain Volume (cc) = 10.6910

Hydrostatic Stress psi	Pore Volume cc	Porosity cc/cc	Permeability mD
0.5	1.9150	15.1910	0.3453
1.5	1.6393	13.0042	0.2811
7.5	1.5691	12.4473	0.2886
15	1.5149	12.0173	0.2657
20	1.5067	11.9523	0.2542
25	1.4918	11.8341	0.2428
20	1.5100	11.9785	0.2657

Table 2.50: Acoustic properties of Sample # 127, Depth = 4142.00 m. 34/11-3

Paxial	Tpi	Tsi	dX	Tp	Ts	Vp	Vs	Vp/Vs
Mpa	usec	usec	inch	usec	usec	m/s	m/s	
2.5	2.7216	5.4029	0.0000	10.5274	16.6300	3247	2258	1.4383
5.0	2.7216	5.4029	0.0025	9.9412	15.8862	3502	2412	1.4521
7.5	2.7124	5.4029	0.0060	9.6710	15.5413	3621	2485	1.4570
10.0	2.7033	5.4029	0.0094	9.4789	15.3102	3706	2535	1.4622
15.0	2.7033	5.4029	0.0162	9.2081	14.9816	3834	2603	1.4725
20.0	2.7033	5.4029	0.0215	9.0769	14.7985	3892	2640	1.4741
25.0	2.7033	5.4029	0.0262	8.9670	14.7069	3941	2653	1.4854
20.0	2.7033	5.4029	0.0248	8.9948	14.7069	3929	2657	1.4788
15.0	2.7033	5.4029	0.0229	9.0493	14.7759	3903	2642	1.4770
10.0	2.7033	5.4029	0.0209	9.1009	14.8800	3879	2619	1.4814
7.5	2.7124	5.4029	0.0191	9.1753	14.9871	3847	2594	1.4829
5.0	2.7124	5.4029	0.0165	9.2956	15.1620	3787	2555	1.4824
2.5	2.7124	5.4029	0.0136	9.4562	15.4957	3708	2477	1.4966

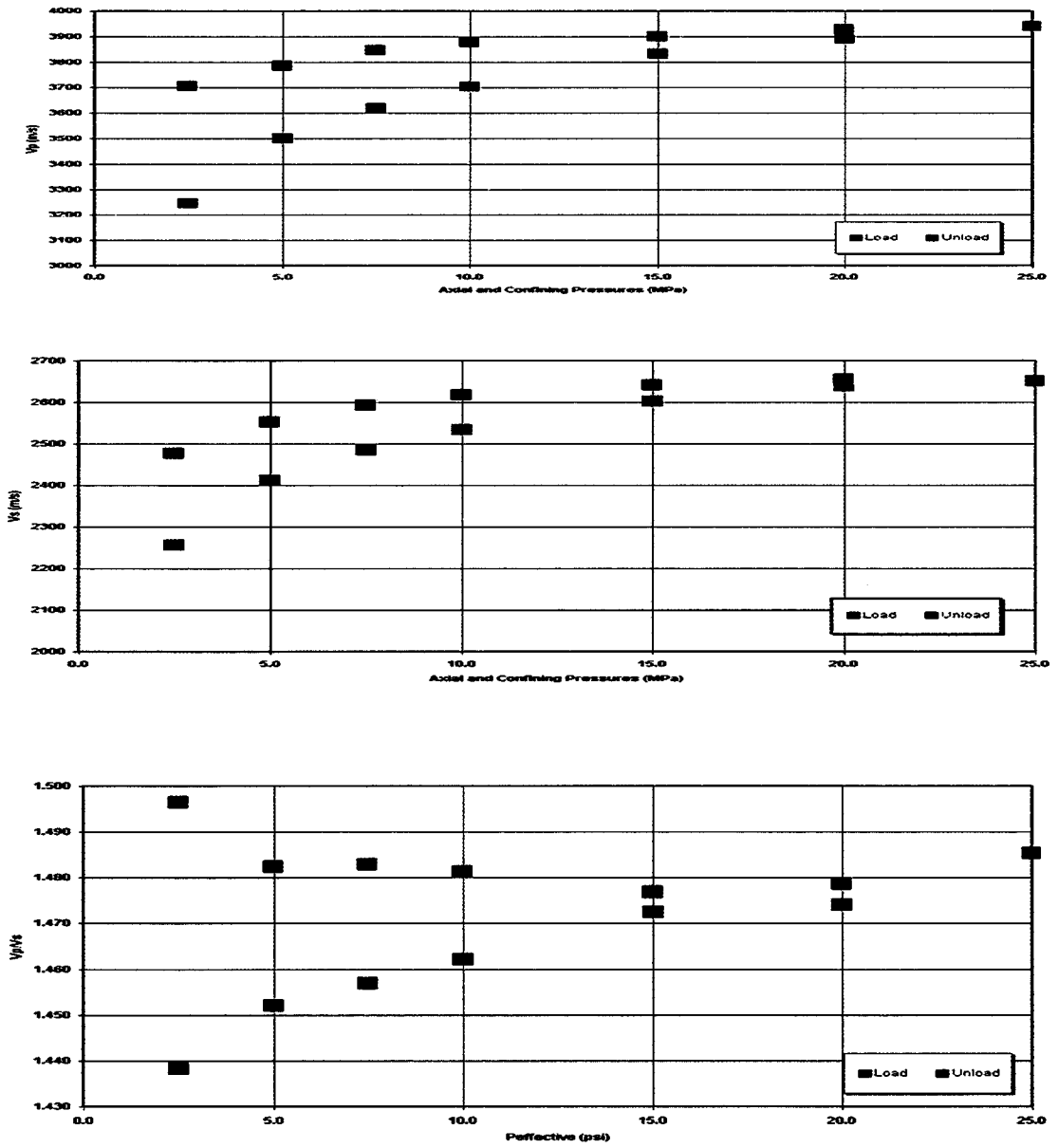

Figure 2.24: Acoustic properties of Sample # 127

Table 2.51. Change of porosity and permeability as a function of hydrostatic stress.

Sample : 143

Grain Density (gm/cc) = 2.6640 Grain Volume (cc) = 9.7820

Hydrostatic Stress psi	Pore Volume cc	Porosity cc/cc	Permeability mD
0.5	2.5246	20.0265	8.8395
1.5	2.4045	19.0741	3.3353
7.5	2.3903	18.9615	3.0409
15	2.3386	18.5514	2.5703
20	2.3286	18.4721	2.1771
25	2.3060	18.2928	1.9293
20	2.3182	18.3896	2.0054

Table 2.52: Acoustic properties of Sample # 143, Depth = 4146.00 m. 34/11-3

Paxial	Tpi	Tsi	dX	Tp	Ts	Vp	Vs	Vp/Vs
Mpa	usec	usec	inch	usec	usec	m/s	m/s	
2.5	2.7216	5.4029	0.0000	10.8131	17.4756	3158	2117	1.4920
5.0	2.7216	5.4029	0.0003	10.3591	16.7216	3345	2257	1.4820
7.5	2.7124	5.4029	0.0005	10.0681	16.1329	3472	2380	1.4587
10.0	2.7033	5.4029	0.0007	9.8139	15.8852	3591	2436	1.4742
15.0	2.7033	5.4029	0.0009	9.5073	15.6463	3752	2492	1.5055
20.0	2.7033	5.4029	0.0011	9.3112	15.5289	3863	2521	1.5324
25.0	2.7033	5.4029	0.0014	9.1868	15.4395	3936	2542	1.5480
20.0	2.7033	5.4029	0.0014	9.2455	15.4585	3900	2538	1.5370
15.0	2.7033	5.4029	0.0014	9.2951	15.4962	3871	2528	1.5312
10.0	2.7033	5.4029	0.0013	9.3991	15.5311	3811	2520	1.5126
7.5	2.7124	5.4029	0.0013	9.5256	15.6227	3746	2497	1.5000
5.0	2.7124	5.4029	0.0013	9.6850	15.8441	3660	2444	1.4975
2.5	2.7124	5.4029	0.0012	9.8881	16.2637	3557	2350	1.5135

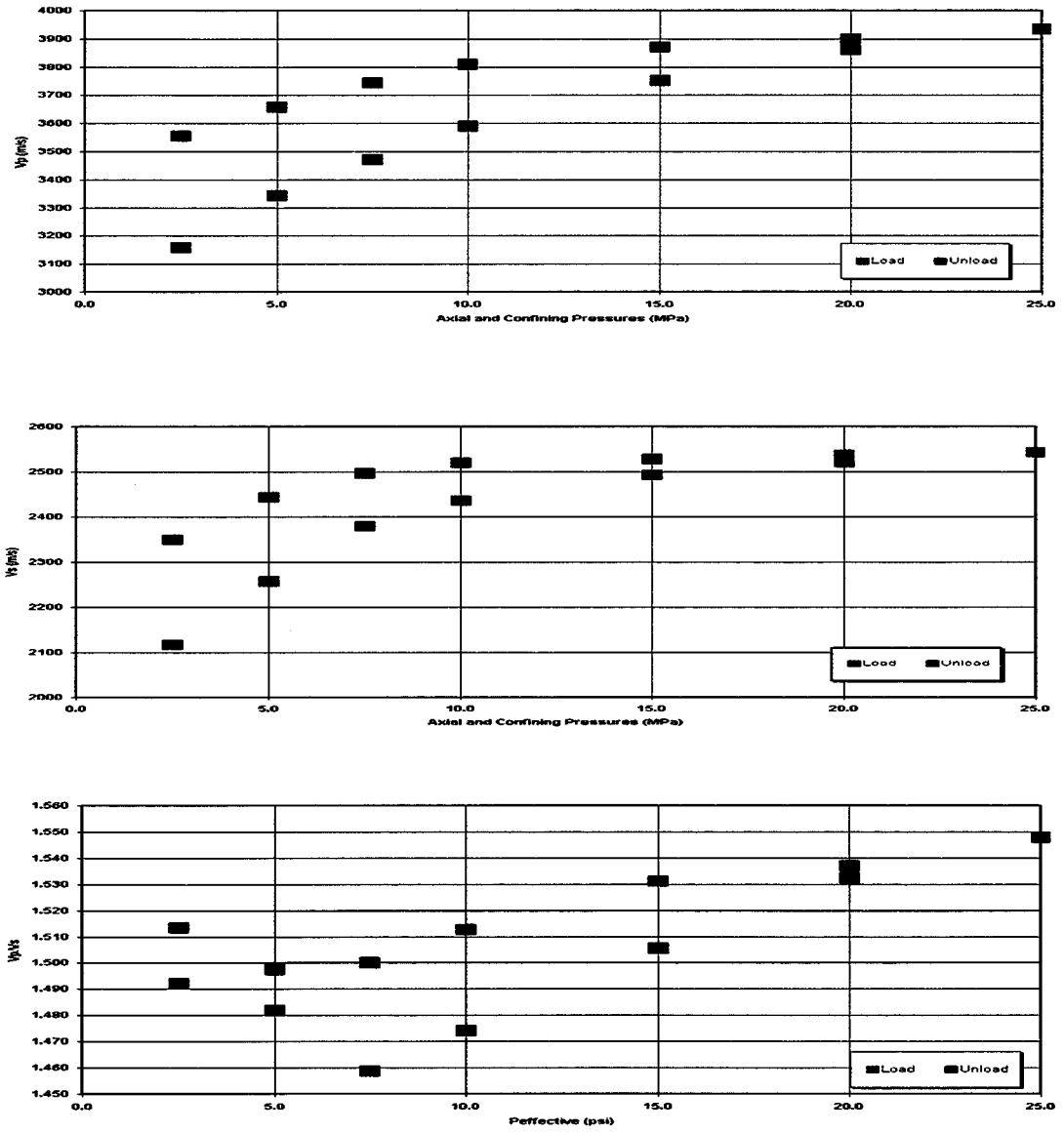

Figure 2.25: Acoustic properties of Sample # 143

Table 2.53. Change of porosity and permeability as a function of hydrostatic stress.

Sample : 147

Grain Density (gm/cc) = 2.6420 Grain Volume (cc) = 9.6500

Hydrostatic Stress psi	Pore Volume cc	Porosity cc/cc	Permeability mD
0.5	2.5558	21.0671	14.5140
1.5	2.4227	19.9698	13.4198
7.5	2.4122	19.8833	13.1240
15	2.3994	19.7778	12.4090
20	2.3839	19.6500	11.9852
25	2.3717	19.5494	11.5944
20	2.3858	19.6657	11.8490

Table 2.54: Acoustic properties of Sample # 147, Depth = 4147.00 m. 34/11-3

Paxial	Tpi	Tsi	dX	Tp	Ts	Vp	Vs	Vp/Vs
Mpa	usec	usec	inch	usec	usec	m/s	m/s	
2.5	2.7216	5.4029	0.0000	10.6153	16.4363	3227	2309	1.3977
5.0	2.7216	5.4029	0.0012	10.0932	16.0942	3452	2380	1.4503
7.5	2.7124	5.4029	0.0023	9.8219	15.8968	3575	2422	1.4760
10.0	2.7033	5.4029	0.0033	9.5934	15.7142	3685	2463	1.4965
15.0	2.7033	5.4029	0.0050	9.3166	15.5362	3833	2502	1.5323
20.0	2.7033	5.4029	0.0065	9.1504	15.4395	3926	2522	1.5568
25.0	2.7033	5.4029	0.0080	9.0109	15.3479	4007	2541	1.5767
20.0	2.7033	5.4029	0.0078	9.0378	15.3652	3991	2537	1.5727
15.0	2.7033	5.4029	0.0076	9.1009	15.4161	3952	2525	1.5651
10.0	2.7033	5.4029	0.0073	9.2307	15.4725	3874	2512	1.5427
7.5	2.7124	5.4029	0.0072	9.3626	15.5311	3803	2497	1.5230
5.0	2.7124	5.4029	0.0071	9.5389	15.7142	3706	2453	1.5105
2.5	2.7124	5.4029	0.0069	9.8104	15.9105	3565	2408	1.4804

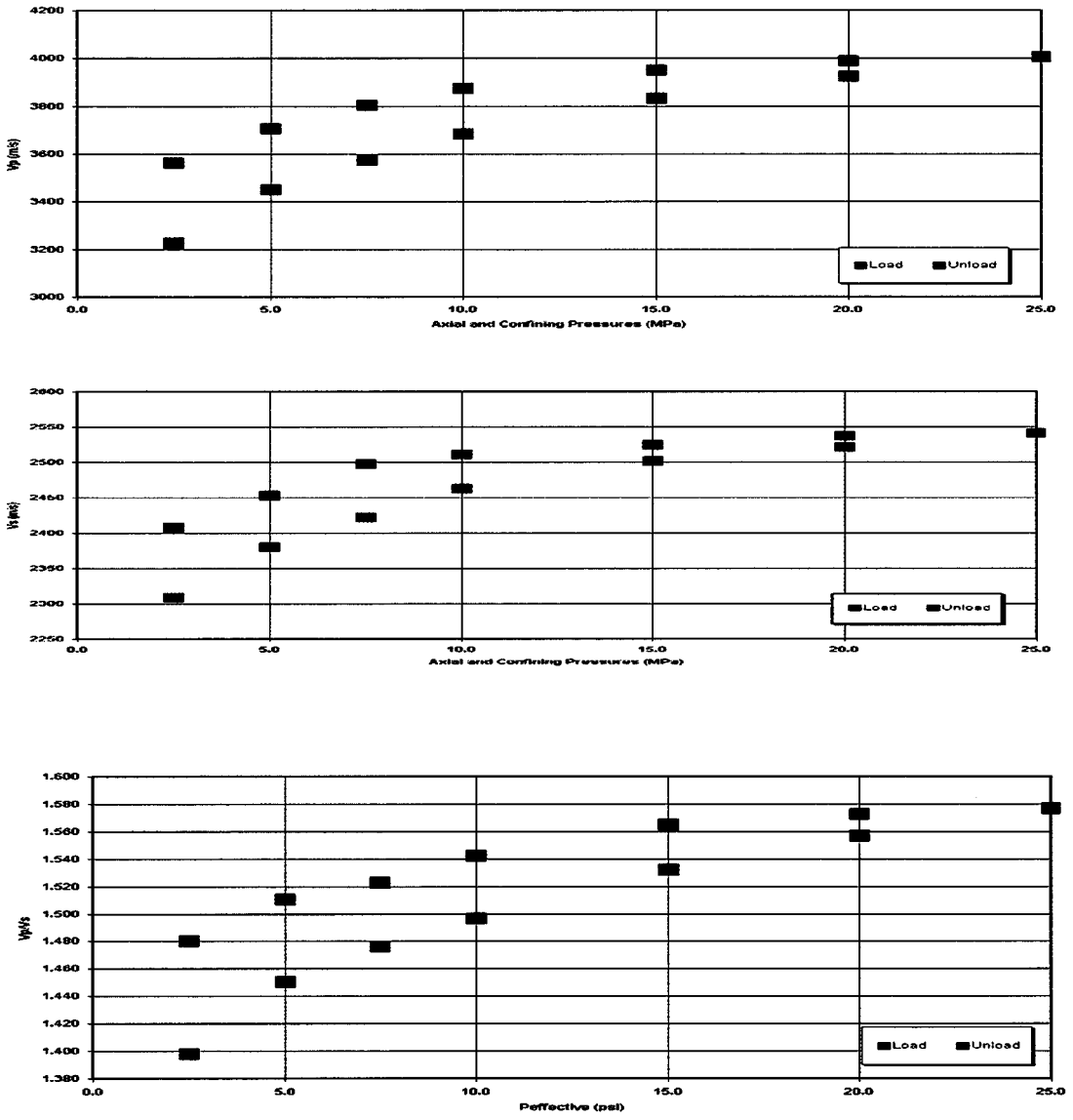

Figure 2.26: Acoustic properties of Sample # 147

Table 2.55. Change of porosity and permeability as a function of hydrostatic stress.

Sample : 155

Grain Density (gm/cc) = 2.6420 Grain Volume (cc) = 9.6570

Hydrostatic Stress psi	Pore Volume cc	Porosity cc/cc	Permeability mD
0.5	2.7020	20.8101	12.5500
1.5	2.6504	20.4127	11.2588
7.5	2.6027	20.0453	11.0739
15	2.5312	19.4946	10.5029
20	2.5118	19.3452	10.3485
25	2.5049	19.2921	9.8001
20	2.5114	19.3421	9.8629

Table 2.56: Acoustic properties of Sample # 155, Depth = 4149.00 m. 34/11-3

Paxial	Tpi	Tsi	dX	Tp	Ts	Vp	Vs	Vp/Vs
Mpa	usec	usec	inch	usec	usec	m/s	m/s	
2.5	2.7216	5.4029	0.0000	10.7142	17.3626	3184	2128	1.4963
5.0	2.7216	5.4029	0.0009	10.1436	16.8131	3426	2229	1.5373
7.5	2.7124	5.4029	0.0018	9.8028	16.3553	3583	2320	1.5447
10.0	2.7033	5.4029	0.0040	9.5253	15.9890	3716	2395	1.5518
15.0	2.7033	5.4029	0.0085	9.1821	15.6227	3895	2469	1.5774
19.9	2.7033	5.4029	0.0129	8.9780	15.3479	4004	2526	1.5849
25.0	2.7033	5.4029	0.0166	8.7791	15.1648	4119	2564	1.6067
20.0	2.7033	5.4029	0.0157	8.8241	15.1648	4093	2566	1.5949
15.0	2.7033	5.4029	0.0137	8.9120	15.2698	4043	2544	1.5892
10.0	2.7033	5.4029	0.0113	9.0879	15.4395	3941	2507	1.5720
7.5	2.7124	5.4029	0.0090	9.2128	15.6227	3880	2468	1.5722
5.0	2.7124	5.4029	0.0066	9.4013	15.8974	3780	2409	1.5689
2.5	2.7124	5.4029	0.0044	9.6699	16.3553	3642	2314	1.5742

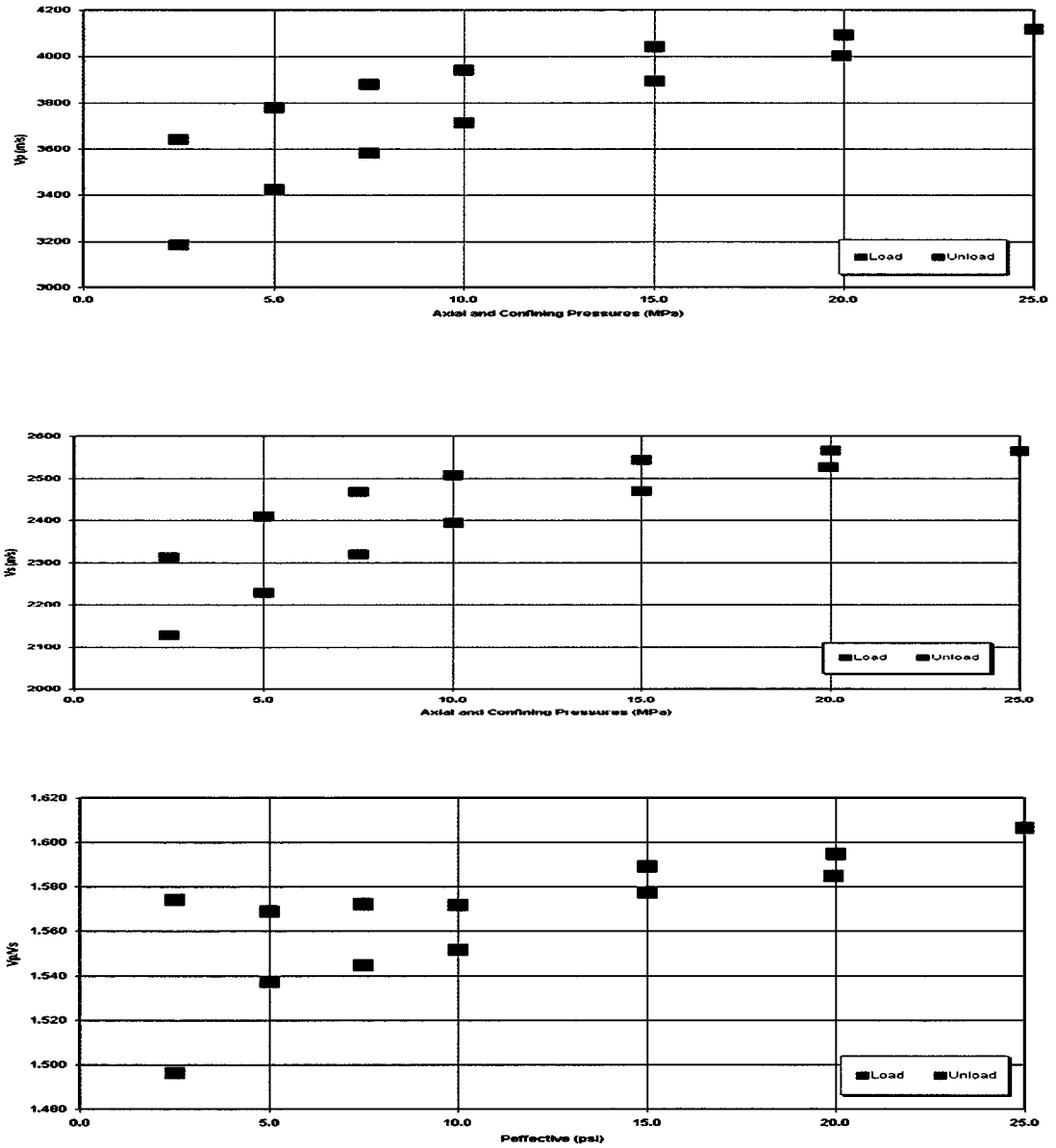

Figure 2.27: Acoustic properties of Sample # 155

Table 2.57. Change of porosity and permeability as a function of hydrostatic stress.

Sample# 187

Hydrostatic Stress Mpa	Pore Volume cc	Porosity cc/cc	Permeability mD
0.5	2.0795	16.4960	1.3345
1.5	2.0350	16.1432	1.2298
3.5	1.9880	15.7703	1.0063
7.5	1.9410	15.3975	0.9529
10	1.9110	15.1595	0.9373
15	1.8690	14.8263	0.8723
20	1.8370	14.5725	0.7993
25	1.7980	14.2631	0.7979
20	1.8240	14.4693	0.8016

Table 2.58: Acoustic properties of Sample # 187, Depth = 4157.00 m. 34/11-3

Phyd Mpa	Tpi usec	Tsi usec	dX inch	Tp usec	Ts usec	Vp m/s	Vs m/s	Vp/Vs
1.4	2.7216	5.4029	0.0000	11.5312	18.6998	2889	1914	1.5094
3.4	2.7216	5.4029	0.0091	10.7472	18.0586	3142	1993	1.5769
6.9	2.7124	5.4029	0.0153	10.1538	17.4175	3368	2086	1.6146
10.3	2.7033	5.4029	0.0188	9.7243	17.1428	3557	2127	1.6721
13.8	2.7033	5.4029	0.0212	9.3846	16.9449	3729	2158	1.7276
17.2	2.7033	5.4029	0.0229	9.1868	16.8108	3836	2180	1.7595
20.7	2.7033	5.4029	0.0242	9.0651	16.7495	3904	2189	1.7835
24.1	2.7033	5.4029	0.0252	8.9981	16.6849	3941	2199	1.7923
27.6	2.7033	5.4029	0.0260	8.9249	16.6564	3985	2203	1.8088
31.0	2.7033	5.4029	0.0272	8.8791	16.6293	4009	2205	1.8178
34.5	2.7033	5.4029	0.0287	8.8469	16.6075	4024	2206	1.8238
31.0	2.7033	5.4029	0.0282	8.8638	16.6178	4015	2205	1.8204
27.6	2.7033	5.4029	0.0276	8.9109	16.6293	3987	2205	1.8085
24.1	2.7033	5.4029	0.0270	8.9335	16.6541	3975	2201	1.8059
20.7	2.7033	5.4029	0.0264	8.9873	16.6831	3956	2197	1.8008
17.2	2.7033	5.4029	0.0258	9.0046	16.7250	3935	2190	1.7968
13.8	2.7033	5.4029	0.0245	9.0942	16.8230	3885	2174	1.7869
10.3	2.7033	5.4029	0.0234	9.1763	16.9335	3840	2156	1.7813
6.9	2.7124	5.4029	0.0219	9.3955	17.0500	3725	2137	1.7428
3.4	2.7124	5.4029	0.0197	9.9560	17.2344	3444	2108	1.6334
1.4	2.7124	5.4029	0.0181	10.6263	17.5723	3158	2054	1.5377

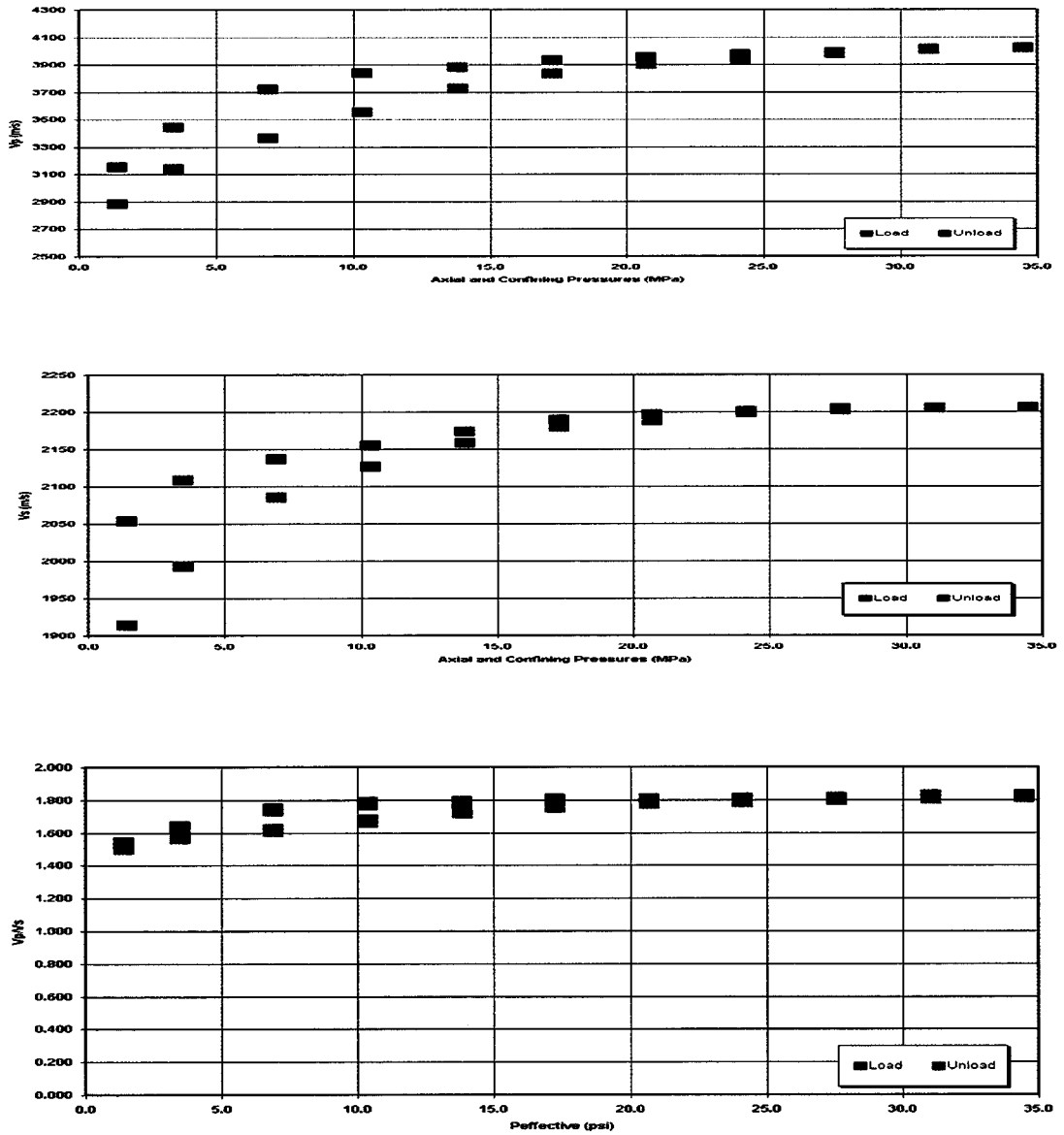

Figure 2.28: Acoustic properties of Sample # 187

Table 2.59. Change of porosity and permeability as a function of hydrostatic stress.

Sample : 215

Grain Density (gm/cc) = 2.6660 Grain Volume (cc) = 10.2060

Hydrostatic Stress psi	Pore Volume cc	Porosity cc/cc	Permeability mD
0.5	2.3001	18.2458	2.6840
1.5	2.2261	17.6589	2.6446
7.5	2.1491	17.0481	2.4917
15	2.1128	16.7601	2.4492
20	2.0978	16.6411	2.4015
25	2.0859	16.5467	2.3643
20	2.1027	16.6800	2.4300

Table 2.60: Acoustic properties of Sample # 215, Depth = 4164.00 m. 34/11-3

Paxial	Tpi	Tsi	dX	Tp	Ts	Vp	Vs	Vp/Vs
Mpa	usec	usec	inch	usec	usec	m/s	m/s	
2.5	2.7216	5.4029	0.0000	11.9560	20.0025	2748	1738	1.5810
5.0	2.7216	5.4029	0.0063	11.3406	18.8827	2926	1871	1.5640
7.5	2.7124	5.4029	0.0113	10.9010	17.9670	3064	1997	1.5343
10.0	2.7033	5.4029	0.0157	10.5494	17.4175	3183	2079	1.5313
15.0	2.7033	5.4029	0.0243	10.2471	16.8131	3282	2170	1.5125
20.0	2.7033	5.4029	0.0312	9.9780	16.2637	3379	2263	1.4930
25.0	2.7033	5.4029	0.0370	9.7582	15.8974	3464	2328	1.4875
20.0	2.7033	5.4029	0.0369	9.8021	15.9918	3443	2308	1.4916
15.0	2.7033	5.4029	0.0359	9.8204	16.0805	3437	2291	1.5003
10.0	2.7033	5.4029	0.0347	9.8461	16.2599	3429	2256	1.5200
7.5	2.7124	5.4029	0.0333	9.8901	16.4616	3417	2218	1.5407
5.0	2.7124	5.4029	0.0302	9.9780	16.7381	3387	2171	1.5601
2.5	2.7124	5.4029	0.0241	10.2585	17.1222	3282	2113	1.5530

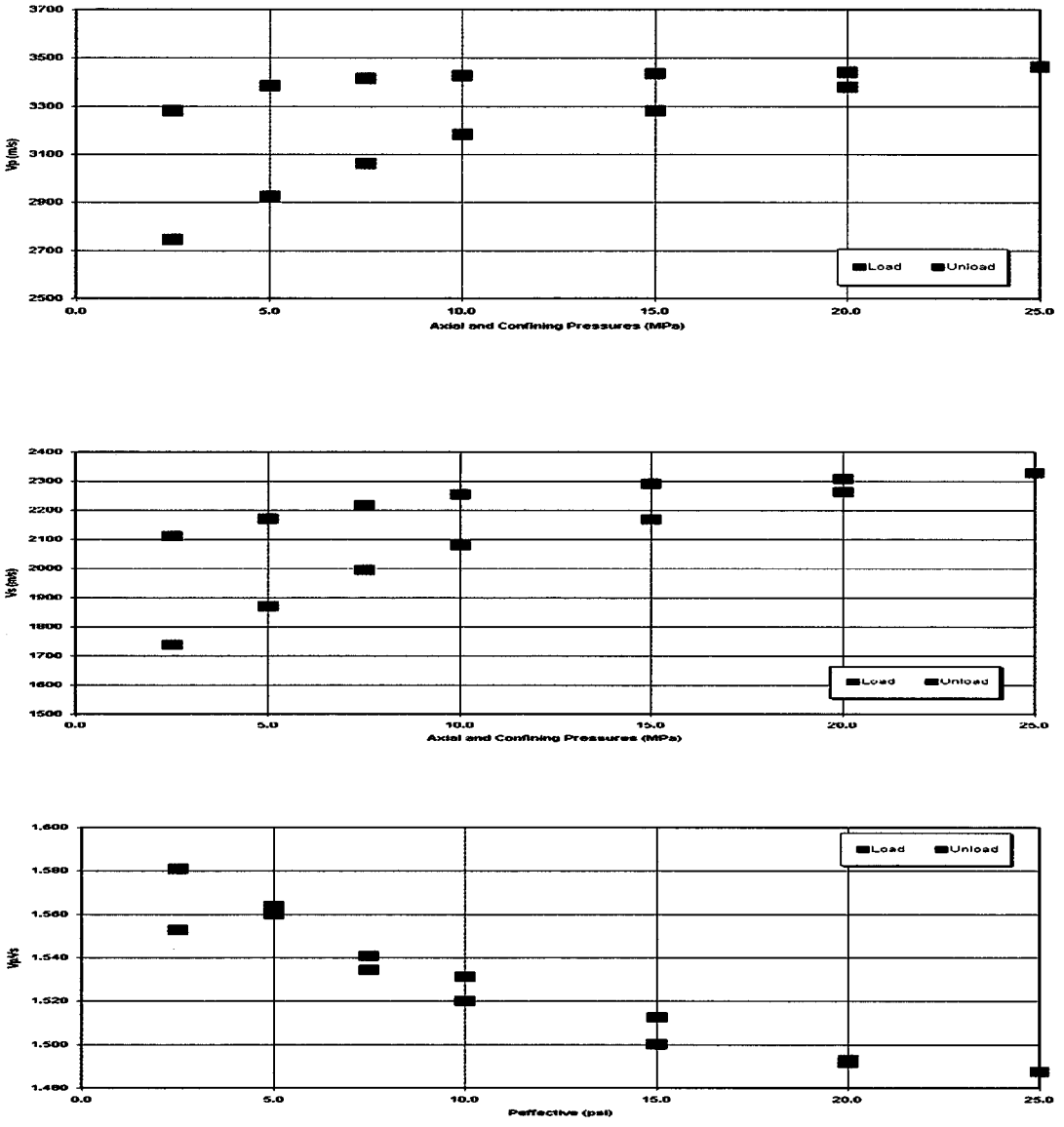

Figure 2.29: Acoustic properties of Sample # 215

Table 2.61. Change of porosity and permeability as a function of hydrostatic stress.

Sample : 4058.25

Grain Density (gm/cc) = 2.5420 Grain Volume (cc) = 9.4210

Hydrostatic Stress psi	Pore Volume cc	Porosity cc/cc	Permeability mD
0.5	2.7857	22.0982	5.1286
1.5	2.6188	20.7744	5.0820
7.5	2.3608	18.7275	3.8789
15	2.2997	18.2428	3.4801
20	2.2386	17.7581	2.7381
25	2.2230	17.6344	2.3075
20	2.2248	17.6486	2.2320

Table 2.62: Acoustic properties of Sample # 4085.25, Depth = 4058.25 m. 34/11-1

Phyd Mpa	Tpi usec	Tsi usec	dX inch	Tp usec	Ts usec	Vp m/s	Vs m/s	Vp/Vs
1.4	2.7216	5.4029	0.0000	10.1318	19.8351	3373	1732	1.9476
3.4	2.7216	5.4029	0.0018	9.8131	18.8452	3518	1856	1.8955
6.9	2.7124	5.4029	0.0062	9.3278	18.0952	3754	1957	1.9186
10.3	2.7033	5.4029	0.0092	9.0164	17.6373	3922	2024	1.9379
13.8	2.7033	5.4029	0.0111	8.7362	17.2710	4096	2082	1.9672
17.2	2.7033	5.4029	0.0127	8.6355	17.0879	4159	2111	1.9698
20.7	2.7033	5.4029	0.0134	8.5572	16.9047	4211	2143	1.9648
24.1	2.7033	5.4029	0.0142	8.5033	16.7216	4247	2176	1.9515
27.6	2.7033	5.4029	0.0148	8.4523	16.5384	4282	2211	1.9369
31.0	2.7033	5.4029	0.0153	8.4157	16.4468	4307	2228	1.9333
34.5	2.7033	5.4029	0.0158	8.3699	16.3949	4340	2237	1.9398
31.0	2.7033	5.4029	0.0159	8.3882	16.4003	4326	2236	1.9345
27.6	2.7033	5.4029	0.0158	8.3882	16.4296	4326	2231	1.9395
24.1	2.7033	5.4029	0.0157	8.4065	16.4468	4312	2227	1.9364
20.7	2.7033	5.4029	0.0155	8.4249	16.48871752	4300	2219	1.9375
17.2	2.7033	5.4029	0.0152	8.4432	16.5384	4287	2210	1.9400
13.8	2.7033	5.4029	0.0149	8.4432	16.63	4288	2192	1.9560
10.3	2.7033	5.4029	0.0146	8.4523	16.7216	4283	2175	1.9688
6.9	2.7124	5.4029	0.0139	8.4981	16.9047	4259	2142	1.9880
3.4	2.7124	5.4029	0.0128	8.6703	17.4542	4141	2047	2.0227
1.4	2.7124	5.4029	0.0114	8.934	17.912	3971	1975	2.0106

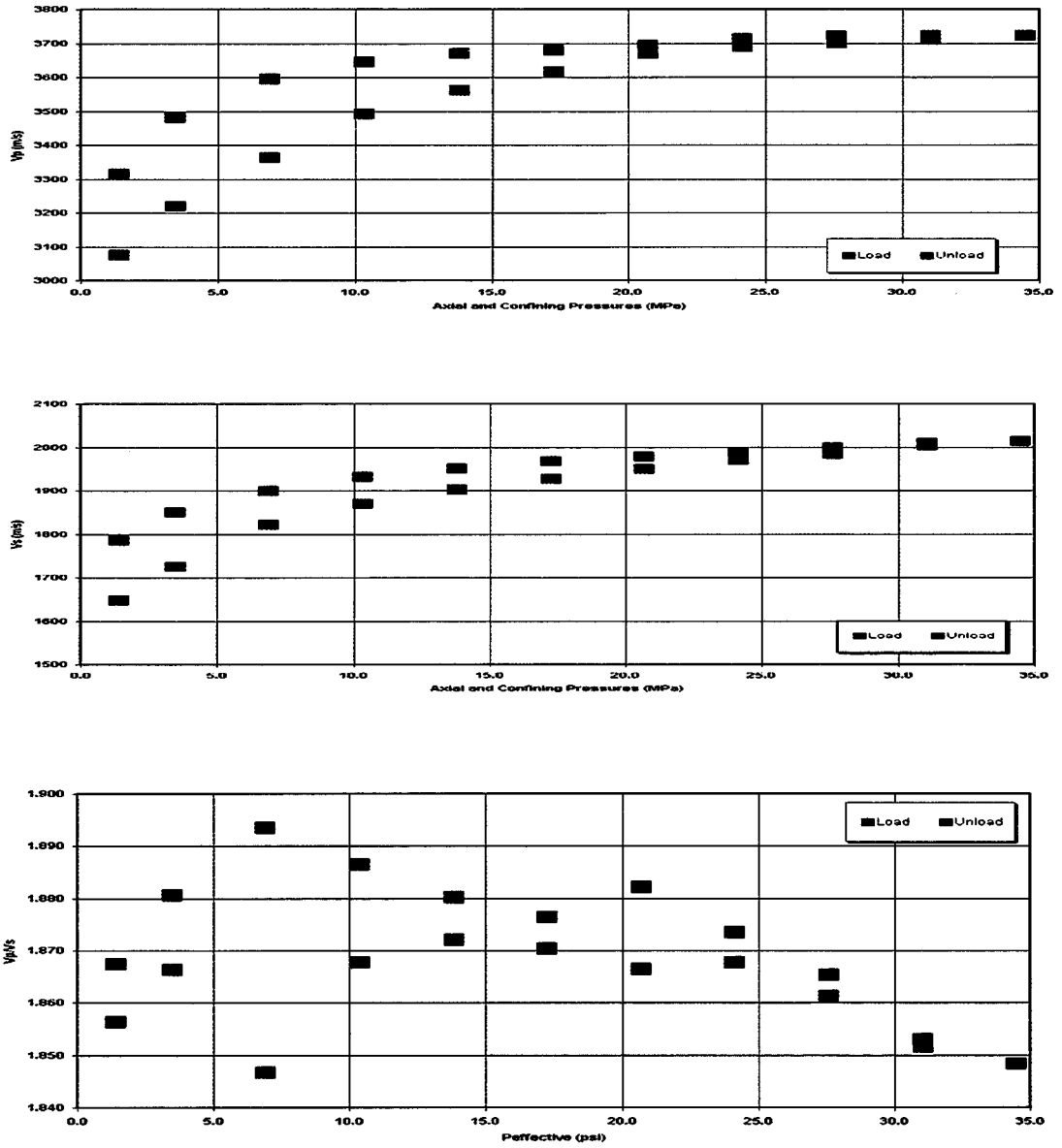

Figure 2.30: Acoustic properties of Sample # ***, Depth = 4058.25 m. 34/11-3

Table 2.63. Change of porosity and permeability as a function of hydrostatic stress.

Sample : 158

Grain Density (gm/cc) = 2.6480 Grain Volume (cc) = 10.6900

Hydrostatic Stress psi	Pore Volume cc	Porosity cc/cc	Permeability mD
0.5	1.9166	15.2040	0.5462
1.5	1.8197	14.9994	0.5400
7.5	1.7610	14.5156	0.5328
15	1.6736	13.7951	0.5024
20	1.6631	13.7086	0.4810
25	1.6430	13.5429	0.4596
20	1.6518	13.6154	0.4795

Table 2.64: Acoustic properties of Sample # 158, Depth = 4143.77 m. 34/11-1.

Paxial	Tpi	Tsi	dX	Tp	Ts	Vp	Vs	Vp/Vs
Mpa	usec	usec	inch	usec	usec	m/s	m/s	
2.5	2.7216	5.4029	0.0000	11.1758	17.7289	3046	2090	1.4580
5.0	2.7216	5.4029	0.0000	10.6043	16.8093	3267	2258	1.4470
7.5	2.7124	5.4029	0.0002	10.1648	16.2366	3456	2377	1.4537
10.0	2.7033	5.4029	0.0003	9.7921	15.7142	3632	2497	1.4546
15.0	2.7033	5.4029	0.0009	9.3296	15.1648	3884	2636	1.4732
20.0	2.7033	5.4029	0.0016	8.9780	14.7069	4098	2764	1.4828
25.0	2.7033	5.4029	0.0024	8.8681	14.4322	4168	2846	1.4647
20.0	2.7033	5.4029	0.0024	8.9120	14.4730	4139	2833	1.4609
15.0	2.7033	5.4029	0.0022	8.9535	14.5238	4112	2818	1.4593
10.0	2.7033	5.4029	0.0016	8.9780	14.6153	4098	2791	1.4682
7.5	2.7124	5.4029	0.0012	9.0219	14.7985	4077	2738	1.4891
5.0	2.7124	5.4029	0.0008	9.1978	15.1648	3968	2636	1.5052
2.5	2.7124	5.4029	0.0004	9.5714	15.6196	3754	2520	1.4895

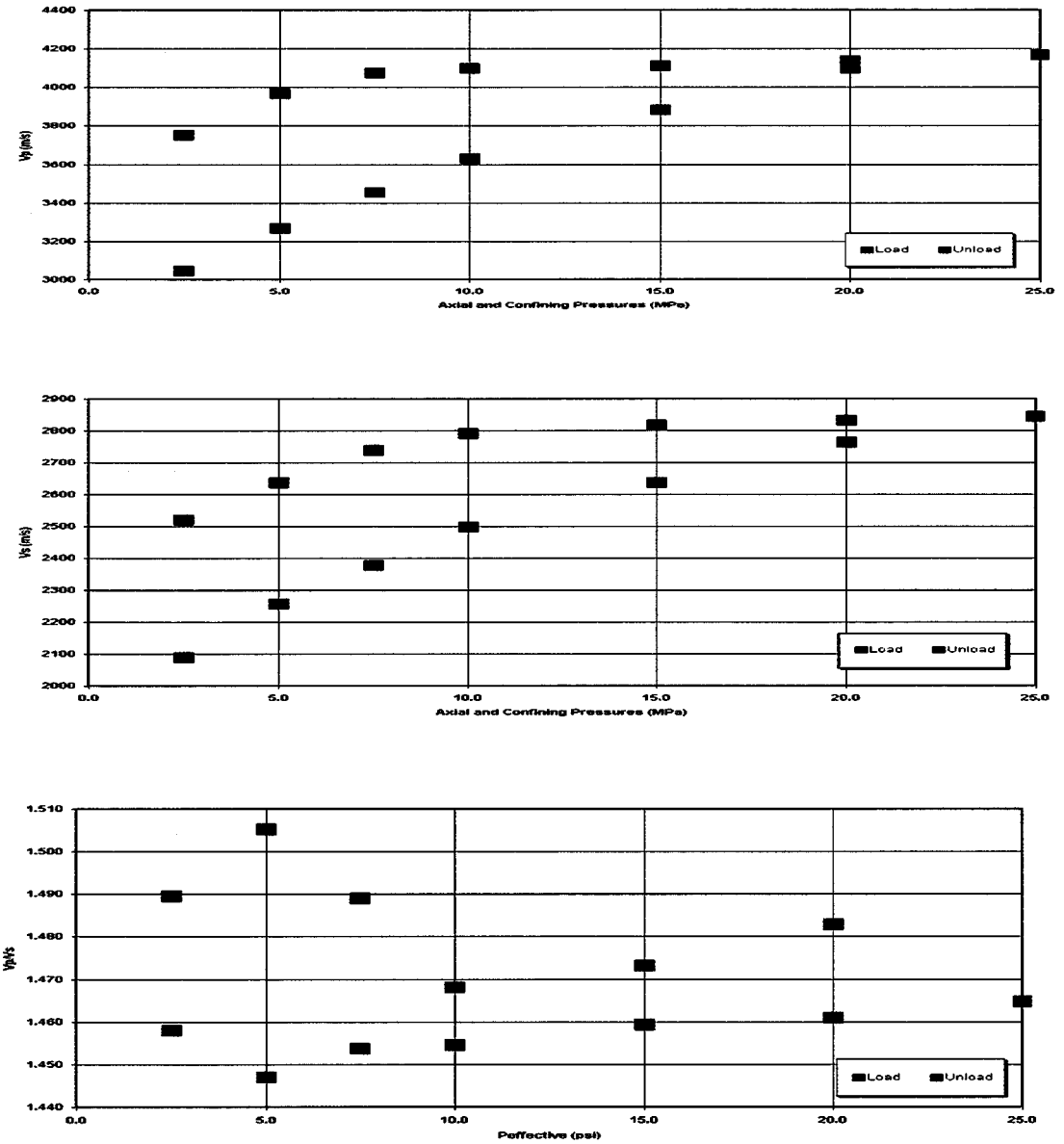

Figure 2.31: Acoustic properties of Sample # 158

CONCLUSIONS

As a result of the studies, relations were established between the *static Young's modulus* and *Poisson's ratio* on the one hand and the dynamic shear modulus on the other hand (the dynamic properties are those that are calculated from the elastic-wave velocity measurements). From these relations, we prepared theoretical models that will allow one to predict the static moduli from velocity well log data for elastic systems, and provide an order of magnitude estimate for systems exhibiting both elastic and plastic deformation.

We also determined that the *failure* envelope for the samples can be adequately modeled by the Drucker-Prager and CAP model. The hardening law can be approximated by either CAP algorithms or linear equation that are fairly close to each other in the case under examination. As a part of the experimental part of the project, the static-dynamic moduli transforms and the CAP model were programmed as Matlab applets.

The theoretical models developed include:

1. **Elastic moduli/porosity/texture relations**. These relations to can be used diagnose rock, i.e., derive its texture type, and, eventually, strength and permeability, from well log data. A step-by-step manual for application of these relations is given in Appendix 1.
2. **Static-to-dynamic moduli relations**. These relations allow one to predict the static Young's modulus and Poisson's ratio (required for cutting injection design) from shear-wave velocity well log data.
3. **Strength and failure relations**. These relations are given in subsections 1.10 and 1.11 of the Experimental Section of this report.

The magnitude of residual plastic deformation of Berea sandstones, GOM clayey sandstones and Clearfolk dolomite discovered during the experimental was unexpected. The results indicate that the problem is more complex than originally estimated. A missing parameter not included in the scope of the study is the stress distribution around the well bore, i.e., tangential stress as a function of overburden, S_{hmin} and S_{hmax} (minimum and maximum horizontal stresses), hydrostatic stress, and deviation.

It is recommended that additional work be undertaken to simulate and measure the tangential stresses around the well bores, using selected samples from downhole formations. The data developed can then be used to calibrate or modify the theoretical models to consider both elastic and plastic deformation. (Special attention should be paid to the properties of depleted sands, as these remain the primary targets for drill cutting injection.) Based on these results, we should be able to provide the needed input for designing the cutting injection process.

REFERENCES

Avseth, P., Dvorkin, J., Mavko, G., and Rykkje, J., 1998, Diagnosing high-porosity sands for reservoir characterization using sonic and seismic, SEG 66 Annual Meeting, Expanded Abstracts, 1024-1025.

Batzle, M., and Wang, Z., 1992, Seismic properties of pore fluids: Geophysics, **57**, 1396-1408.

Bjørlykke, K., and Egeberg, P.K., 1993, Quartz cementation in sedimentary basins: AAPG Bulletin, v. 77, 1538-1548.

Blangy, J.P., 1992, Integrated seismic lithologic interpretation: The petrophysical basis: Ph.D. thesis, Stanford University.

Bourbie, T., Coussy, O., and Zinszner, B., 1987, Acoustics of porous media, Gulf Publishing Company.

Carmichael, R.S., 1990, Practical handbook of physical properties of rocks and minerals: CRC Press.

Castagna, J.P., 1993, AVO analysis – tutorial and review, in: Offset Dependent Reflectivity – Theory and Practice of AVO Analysis, Castagna, J.P., and Backus, M., eds., Investigations in Geophysics, no. 8, Society of Exploration Geophysicists, Tulsa, 348 pp.

Castagna, J.P., Batzle, M.L., and Eastwood, R.L., 1985, Relationships between compressional-wave and shear-wave velocities in clastic silicate rocks, Geophysics, 50, 571-581.

Castagna, J.P., Batzle, M.L., and Kan, T.K., 1993, Rock physics—The link between rock properties and AVO response: in Castagna, J.P. and Backus, eds., Offset-Dependent Reflectivity-Theory and Practice of AVO Analysis, 134-171.

Dvorkin, J., Nur, A., and Yin, H., 1994, Effective Properties of Cemented Granular Materials, Mechanics of Materials, 18, 351-366.

Dvorkin, J., and Nur, A., 1996, Elasticity of High-Porosity Sandstones: Theory for Two North Sea Datasets, Geophysics, 61, 1363-1370.

Dvorkin, J., Moos, D., Packwood, J., and Nur, A., 1999, Identifying patchy saturation from well logs: Geophysics, 64 1-5.

Dvorkin, J., Prasad, M., Sakai, A., and Lavoie, D., 1999, Elasticity of marine sediments, GRL, 26, 1781-1784.

Eberhart-Phillips, D.M., 1989, Investigation of Crustal Structure and Active Tectonic Processes in the Coast Ranges, Central California, Ph.D. dissertation, Stanford University.

Gassmann, F., 1951, Uber die elastizitat poroser medien, Vier. der Natur Gesellschaft, 96, 1-23.

Gardner, G.H.F., Gardner, L.W., and Gregory, A.R., 1974, Formation velocity and density -- The diagnostic basis for stratigraphic traps, Geophysics, 39, 770-780.

Greenberg, M.L. and Castagna, J.P., 1992, Shear-wave velocity estimation in porous rocks: theoretical formulation, preliminary verification and applications, Geophysical Prospecting, 40, 195-209.

Gutierrez, M., 1998, personal communication.

Han, D.-H., 1986, Effects of Porosity and Clay Content on Acoustic Properties of Sandstones and Unconsolidated Sediments, Ph.D. dissertation, Stanford University.

Hashin, Z. and Shtrikman, S., 1962, A variational approach to the theory of effective magnetic permeability of multiphase materials, Journal of Applied Physics, 33, 3125-3131.

Hashin, Z., and Shtrikman, S., 1963, A variational approach to the elastic behavior of multiphase materials: J. Mech. Phys. Solids, 11, 127-140.

Hill, R., 1952, The elastic behavior of crystalline aggregate, Proceedings of the Physical Society, London, A65, 349-354.

Hill, R., 1963, Elastic properties of reinforced solids: some theoretical principles, Journal of the Mechanics and Physics of Solids, 11, 357-372.

Krief, M., Garat, J., Stellingwerff, J., and Ventre, J., 1990, A petrophysical interpretation using the velocities of P and S waves (full-waveform sonic), The Log Analyst, November.

Marion, D., 1990, Acoustical, mechanical, and transport properties of sediments and granular materials: Ph.D. thesis, Stanford University.

Mavko, G., Chan, C., and Mukerji, T., 1995, Fluid substitution: estimating changes in Vp without knowing Vs, Geophysics, 60, 1750-1755.

Mavko, G., Mukerji, T., and Dvorkin, J., 1998, The rock physics handbook, Cambridge University Press.

Mindlin, R.D., 1949, Compliance of elastic bodies in contact, J. Appl. Mech., 16, 259-268.

Moos, D., Dvorkin, J., and Hooks, A.J., 1997, Application of theoretically derived rock physics relationships for clastic rocks to log data from Wilmington field, CA: Geophysical Research Letters, **24**, 329-332.

Nadeau, P.H., 1998, The Sleipner effect: A possible relationship between hydrocarbon charge and the distribution of sandstone reservoir cements: in Mineral diagenesis and reservoir quality -- the way forward, Conference abstracts, University of Cambridge, UK, March 1998, 162.

Nur, A., Mavko, G., Dvorkin, J., and Galmudi, D., 1998, Critical Porosity: A Key to Relating Physical Properties to Porosity in Rocks, The Leading Edge, 17, 357-362.

Raymer, L.L., Hunt, E.R., and Gardner, J.S., 1980, An improved sonic transit time-to-porosity transform, Society of Professional Well Log Analysts, 21st Annual Logging Symposium, July 1980.

Reuss, A., 1929, Berechnung der fliessgrense von mischkristallen auf grund der plastizitatsbedinggung fur einkristalle, Zeitschrift fur Angewandte Mathematik and Mechanik, 9, 49-58.

Strandenes, S., 1991, Rock physics analysis of the Brent Group reservoir in the Oseberg Field: Unpublished Data.

Strandenes, S., 1995, Personal communication.

Tosaya, C. and Nur, A., 1982, Effects of diagenesis and clays on compressional velocities in rocks, Geophysical Research Letters, 9, 5-8.

Wang, Z. and Nur, A., 1992, Seismic and acoustic velocities in reservoir rocks, v. 2, theoretical and model studies, Society of Engineering Geology, Geophysics Reprint Series.

Wood, A.W., 1955, A Textbook of Sound, The MacMillan Co., New York, 360 pp.

Wyllie, M.R.J., Gardner, G.H.F., and Gregory, A.R., 1963, Studies of elastic wave attenuation in porous media, Geophysics, 27, 569-589.

Wyllie, M.R.J. and Gregory, A.R., 1953, Formation factors of unconsolidated porous media: Influence of particle shape and effect of cementation, Transactions of the American Institute of Mechanical Engineers, 198, 103-110.

Wyllie, M.R.J., Gregory, A.R., and Gardner, L.W., 1956, Elastic wave velocities in heterogeneous and porous media, Geophysics, 21, 41-70.

Wyllie, M.R.J., Gregory, A.R., and Gardner, G.H.F., 1958, An experimental investigation of factors affecting elastic wave velocities in porous media, Geophysics, 23, 459-493.

Yin, H., 1993, Acoustic velocity and attenuation of rocks: isotropy, intrinsic anisotropy, and stress-induced anisotropy, Ph.D dissertation, Stanford University.

APPENDIX A
GUIDE TO VELOCITY-POROSITY MODELS

For detailed assumptions, limitations and applicability of the models see Mavko, Mukerji, and Dvorkin, 1998, "The Rock Physics Handbook."

Below, velocity is in km/s; porosity is in volumetric fraction (pu); clay content is in volumetric fraction; density is in g/cm^3; and modulus is in GPa.

1. Wyllie et al. (1956) Time Average (Empirical)

$$\frac{1}{V_p} = \frac{\phi}{V_{p-fl}} + \frac{1-\phi}{V_{p-mineral}},$$

where ϕ is total porosity; and V_{p-fl} and $V_{p-mineral}$ are the compressional-wave velocity in the common pore fluid and mineral phase, respectively. V_{p-fl} should be calculated from the bulk modulus $\overline{K}_{fluid}$ and fluid density $\overline{\rho}_{fluid}$ as

$$V_{p-fl} = \sqrt{\overline{K}_{fluid} / \overline{\rho}_{fluid}}.$$

$V_{p-mineral}$ should be calculated from $K_{mineral}$, $\mu_{mineral}$, and mineral density $\rho_{mineral}$ as

$$V_{p-mineral} = \sqrt{(K_{mineral} + 4\mu_{mineral}/3)/\rho_{mineral}}.$$

For calculating $\overline{K}_{fluid}$, $\overline{\rho}_{fluid}$, $K_{mineral}$, $\mu_{mineral}$, and $\rho_{mineral}$, see below

To calculate the compressional modulus from Wyllie's equation, use

$$M_{common}^{Wyllie} = \rho_b V_p^{\,2},$$

where ρ_b is bulk density of the rock saturated with common fluid.

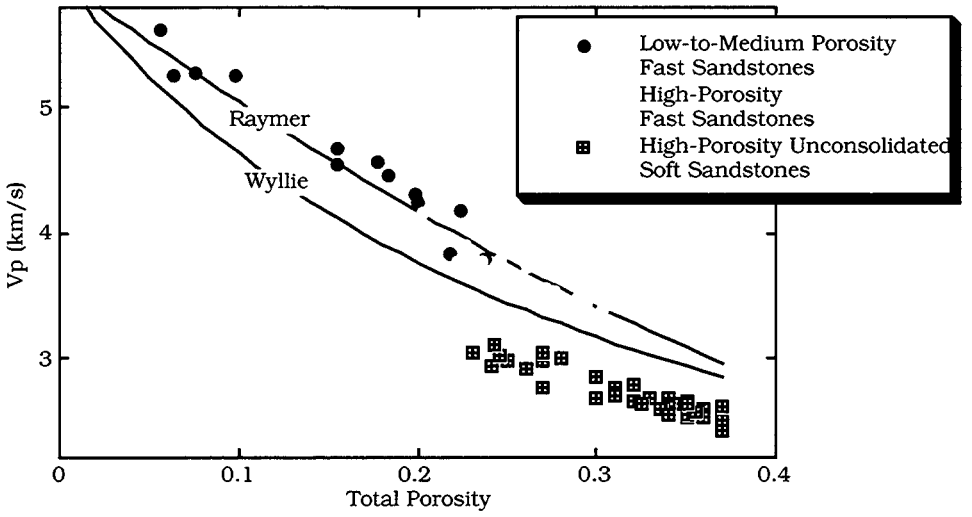

Figure A1.1. Applicability of Wyllie's and Raymer's models to sandstones.

Adjustable parameters in Wyllie's equation are the elastic moduli of the mineral components that make up the mineral phase. For example, for quartz, the bulk modulus may be chosen between 34 GPa and 38 GPa; for clay these moduli may span quite a wide interval (see Mavko et al., 1998).

Wyllie et al. recommend the following ranges for $V_{p-mineral}$:

Rock Type	Mineral Velocity (km/s)
Sandstone	5.480 to 5.950
Limestone	6.400 to 7.000
Dolomite	7.000 to 7.925

This model has a very simple analytical expression but is strictly empirical. It can be applied only to fully-saturated rocks and should not be applied to soft unconsolidated rocks (Figure A1.1).

2. Raymer-Hunt-Gardner (1980) Relations (Empirical)

$$V_p = (1-\phi)^2 V_{p-mineral} + \phi V_{p-fl} \quad \text{for} \quad \phi < 37\%;$$

$$M_{common}^{Raymer} = \phi / \overline{K}_{fluid} + (1-\phi)/(K_{mineral} + 4\mu_{mineral}/3) \quad \text{for} \quad \phi > 47\%;$$

$$1/V_p = 10[(0.47-\phi)/V_{37} + (\phi - 0.37)/V_{47}].$$

where V_{37} and V_{47} are calculated from the first-line equation at $\phi = .37$ and second-line equation at $\phi = .47$, respectively. As in the Wyllie model, the compressional modulus at common saturation is $M_{common}^{Raymer} = \rho_b V_p^{\,2}$. This model is strictly empirical and mimics real data much better than Wyllie's model does (Figure A1.1 and A1.2). It should not be applied to soft unconsolidated rocks.

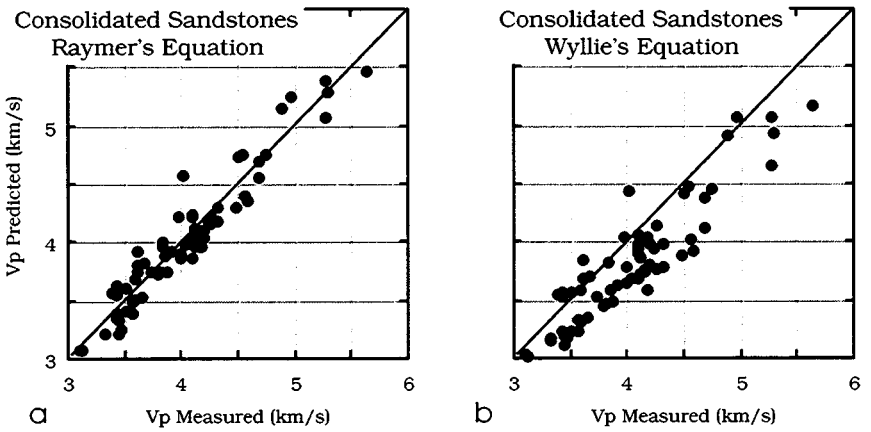

Figure A1.2. Raymer's equation (a) mimics data better than Wyllie's equation (b).

3. Han's (1986) Relations (Empirical)

Clean Water-Saturated Sandstones Effective Pressure 40 MPa:

$$V_p = 6.08 - 8.06\phi, \quad V_s = 4.06 - 6.28\phi.$$

Shaley Water-Saturated Sandstones
Effective Pressure:

40 MPa: $V_p = 5.59 - 6.93\phi - 2.18C, \quad V_s = 3.52 - 4.91\phi - 1.89C;$

30 MPa: $V_p = 5.55 - 6.96\phi - 2.18C, \quad V_s = 3.47 - 4.84\phi - 1.87C;$

20 MPa: $V_p = 5.49 - 6.94\phi - 2.17C, \quad V_s = 3.39 - 4.73\phi - 1.81C;$

10 MPa: $V_p = 5.39 - 7.08\phi - 2.13C, \quad V_s = 3.29 - 4.73\phi - 1.74C;$

5 MPa: $V_p = 5.26 - 7.08\phi - 2.02C, \quad V_s = 3.16 - 4.77\phi - 1.64C.$

Shaley Room-Dry Sandstones Effective Pressure 40 MPa:

$$V_p = 5.41 - 6.35\phi - 2.87C, \quad V_s = 3.57 - 4.57\phi - 1.83C.$$

In these equations, C is the volumetric clay content in rock. These equations have been obtained from lab ultrasonic measurements on sandstones saturated with pure water (density 1 g/cm^3 and bulk modulus 2.25 GPa). They cannot be used for any other pore fluid. Be cautious when using these equation at small (below 30 MPa) effective pressure. The ultrasonic velocity dispersion effect may bias the results. The compressional modulus can be calculated from Vp and bulk density as $M_{common}^{Han} = \rho_b V_p^{\,2}$.

4. Tosaya and Nur (1982) Relations (Empirical)

Shaley Water-Saturated Sandstones Effective Pressure 40 MPa:

$$V_p = 5.8 - 8.6\phi - 2.4C, \quad V_s = 3.7 - 6.3\phi - 2.1C,$$

where C is the volumetric clay content in rock. These equations have been obtained from laboratory ultrasonic measurements on high-shale-content sandstones saturated with pure water. When using them to diagnose rock, use pure water (density 1 g/cm^3 and bulk modulus 2.25 GPa) as common fluid. See velocity dispersion effect warning for Han's equations. The compressional modulus is $M_{common}^{Tosaya} = \rho_b V_p^{\,2}$.

5. Eberhart-Phillips (1989) Relations (Empirical)

Shaley Water-Saturated Sandstones

$$V_p = 5.77 - 6.94\phi - 1.73\sqrt{C} + 0.446(P - e^{-16.7P}),$$

$$V_s = 3.70 - 4.94\phi - 1.57\sqrt{C} + 0.361(P - e^{-16.7P}).$$

This equations are very approximate and should be used for rough estimates only. In these equations, C is the volumetric clay content in rock and P is the effective pressure (overburden minus pore pressure) in kilobars. These equations have been obtained from laboratory ultrasonic measurements on high-shale-content sandstones saturated with pure water. When using them to diagnose rock, use pure water (density 1 g/cm^3 and bulk modulus 2.25 GPa) as common fluid. See velocity dispersion effect warning for Han's equations below. The compressional modulus is $M_{common}^{Tosaya} = \rho_b V_p^{\,2}$.

6. Critical Porosity (Nur et al., 1998) -- Modified Voigt Average (heuristic)

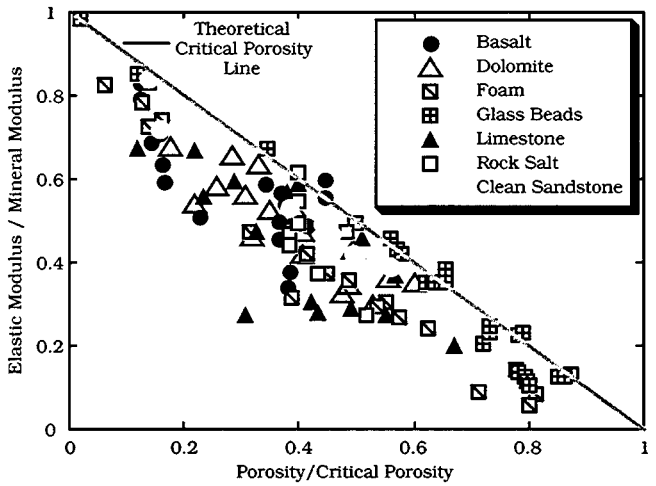

Figure A1.3. Critical porosity model and data for various rocks. The model overestimates the data.

$$K_{dry} = K_{mineral}(1 - \phi / \phi_c), \quad \mu_{dry} = \mu_{mineral}(1 - \phi / \phi_c),$$

where ϕ_c is the critical porosity. See details in Mavko et al., 1998. To calculate the saturated-rock moduli, use Gassmann's fluid substitution equation. Below is a table for critical porosity values in different

rocks. This model tends to over-estimate the elastic moduli (Figure A1.3). Adjustable parameters in the Critical Porosity model are: critical porosity, and the bulk and shear moduli of the mineral phase.

7. Contact Cement Model of Dvorkin and Nur, 1996 (Theoretical)

This model assumes that sandstone starts as a pack of identical spherical grains at critical porosity and porosity reduces due to the uniform deposition of cement on the surface of every grain (Figure A1.4).

Inputs: critical porosity in fraction (ϕ_c);

bulk modulus of grain in GPa (K_s);

shear modulus of grain in GPa (G_s);

bulk modulus of cement in GPa (K_c);

shear modulus of cement in GPa (G_c);

bulk modulus of common fluid in GPa (K_{cf});

coordination number (n) (number of contacts per grain: 6-9);

total porosity ϕ (varies between 0.15 and ϕ_c).

The effective bulk (K_{dry}) and shear (G_{dry}) moduli of dry rock are:

$$K_{dry} = n(1-\phi_c)M_c S_n / 6,\ G_{dry} = 3K_{dry} / 5 + 3n(1-\phi_c)G_c S_\tau / 20,$$

where $M_c = K_c + 4G_c / 3$ is the compressional modulus of the cement. S_n and S_τ are:

$$S_n = A_n(\Lambda_n)\alpha^2 + B_n(\Lambda_n)\alpha + C_n(\Lambda_n),\ A_n(\Lambda_n) = -0.024153 \cdot \Lambda_n^{-1.3646},$$

$$B_n(\Lambda_n) = 0.20405 \cdot \Lambda_n^{-0.89008},\ C_n(\Lambda_n) = 0.00024649 \cdot \Lambda_n^{-1.9864};$$

$$S_\tau = A_\tau(\Lambda_\tau, \nu_s)\alpha^2 + B_\tau(\Lambda_\tau, \nu_s)\alpha + C_\tau(\Lambda_\tau, \nu_s),$$

$$A_\tau(\Lambda_\tau, \nu_s) = -10^{-2} \cdot (2.26\nu_s^2 + 2.07\nu_s + 2.3) \cdot \Lambda_\tau^{0.079\nu_s^2 + 0.1754\nu_s - 1.342},$$

$$B_\tau(\Lambda_\tau, \nu_s) = (0.0573\nu_s^2 + 0.0937\nu_s + 0.202) \cdot \Lambda_\tau^{0.0274\nu_s^2 + 0.0529\nu_s - 0.8765},$$

$$C_\tau(\Lambda_\tau, \nu_s) = 10^{-4} \cdot (9.654\nu_s^2 + 4.945\nu_s + 3.1) \cdot \Lambda_\tau^{0.01867\nu_s^2 + 0.4011\nu_s - 1.8186};$$

$$\Lambda_n = 2G_c(1-\nu_s)(1-\nu_c) / [\pi G_s(1-2\nu_c)],\ \Lambda_\tau = G_c / (\pi G_s);$$

$$\alpha = [(2/3)(\phi_c - \phi) / (1-\phi_c)]^{0.5};$$

$$\nu_c = 0.5(K_c / G_c - 2/3) / (K_c / G_c + 1/3);\ \nu_s = 0.5(K_s / G_s - 2/3) / (K_s / G_s + 1/3).$$

The bulk modulus K_{sat} of the rock saturated with common fluid is calculated from K_{dry} using Gassmann's equation. The bulk modulus of the solid phase K_{so} to for Gassmann's equation is Hill's average of those of the grains and cement:

$$K_{so} = 0.5[(f_{gs}K_s + f_{cs}K_c) + 1 / (f_{gs} / K_s + f_{cs} / K_c)],$$

$f_{gs} = (1-\phi_c)/(1-\phi)$, $f_{cs} = (\phi_c - \phi)/(1-\phi)$.

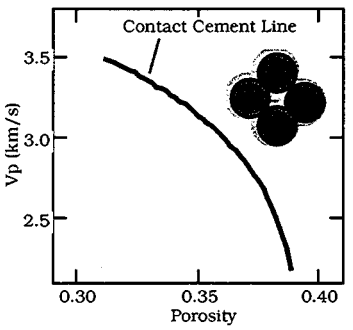

Figure A1.4. Cementation model.

The desired theoretical compressional modulus is: $M^{cem}_{common} = K_{sat} + 4G_{dry}/3$.

Adjustable parameters in this model are: n (between 6 and 9), ϕ_c (between 0.35 and 0.42 for sandstones); as well as the elastic moduli of the mineral components that make up the grains and cement. An example is given below in Figure A1.5.

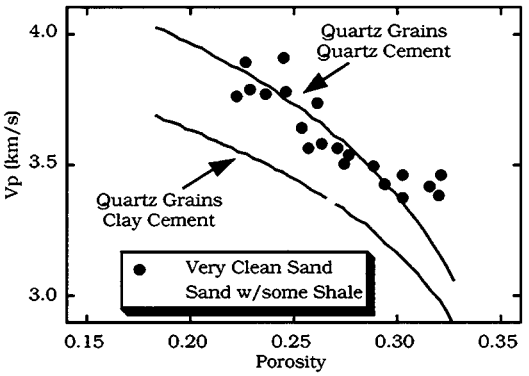

Figure A1.5. Example of adjusting cementation model to a lab data set. By changing the properties of cement, we can match the very clean sandstone data and the data from sandstones with more shale.

8. Constant Cement Model of Avseth et al. (Theoretical)

This model assumes that sandstone starts as a pack of identical spherical grains at critical porosity, then porosity reduces to some "cemented porosity" due to the uniform deposition of cement on the surface of every grain. After that porosity reduces due to the deposition of cement away from grain contacts.

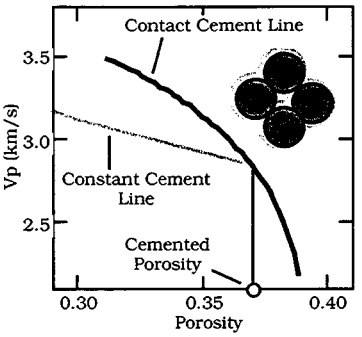

Figure A1.6. Constant cement model.

At cemented porosity, the dry-rock moduli are calculated from the contact-cement theory. For smaller porosities, we connect the cemented porosity point with the solid-phase modulus at zero porosity. This solid-phase modulus is that of the mixture of $1-\phi_c$ fractions of grains and ϕ_c fraction of cement. We connect these two points in the lower Hashin-Shtrikman fashion (Figure A1.6).

Inputs: critical porosity in fraction (ϕ_c);

cemented porosity in fraction (ϕ_b);

bulk modulus of grain in GPa (K_s);

shear modulus of grain in GPa (G_s);

bulk modulus of cement in GPa (K_c);

shear modulus of cement in GPa (G_c);

bulk modulus of common fluid in GPa (K_{cf});

coordination number (n) (number of contacts per grain: 6-9);

total porosity ϕ (varies between 0.1 and ϕ_c).

The effective bulk (K_{dry}) and shear (G_{dry}) moduli of dry rock are:

$$K_{dry} = \left(\frac{\phi/\phi_b}{K_b + 4G_b/3} + \frac{1-\phi/\phi_b}{K_{fs} + 4G_b/3}\right)^{-1} - 4G_b/3,$$

$$G_{dry} = \left(\frac{\phi/\phi_b}{G_b + z} + \frac{1-\phi/\phi_b}{G_{fs} + z}\right)^{-1} - z, \quad z = \frac{G_b}{6}\frac{9K_b + 8G_b}{K_b + 2G_b};$$

$$K_{fs} = \frac{1}{2}\left((1-\phi_c)K_s + \phi_c K_c + \frac{1}{(1-\phi_c)/K_s + \phi_c/K_c}\right),$$

$$G_{fs} = \frac{1}{2}\left((1-\phi_c)G_s + \phi_c G_c + \frac{1}{(1-\phi_c)/G_s + \phi_c/G_c}\right)$$

where K_b and G_b are the dry-rock bulk and shear moduli, respectively, calculated from the cementation

model at $\phi = \phi_b$ (see previous model).

The bulk modulus K_{sat} of the rock saturated with common fluid is calculated from K_{dry} using Gassmann's equation. The bulk modulus of the solid phase K_{so} to be used in Gassmann's equation is calculated as Hill's average of those of the grains and cement:

$$K_{so} = 0.5[(f_{gs}K_s + f_{cs}K_c) + 1/(f_{gs}/K_s + f_{cs}/K_c)],$$
$$f_{gs} = (1-\phi_c)/(1-\phi), \quad f_{cs} = (\phi_c - \phi)/(1-\phi).$$

The desired theoretical compressional modulus is: $M_{common}^{const\ cem} = K_{sat} + 4G_{dry}/3.$

Adjustable parameters in this model are: ϕ_b (choose it to match the data); n (between 6 and 9), ϕ_c (between 0.35 and 0.42 for sandstones); as well as the elastic moduli of the mineral components that make up the grains and cement. An example is given in Figure A1.7.

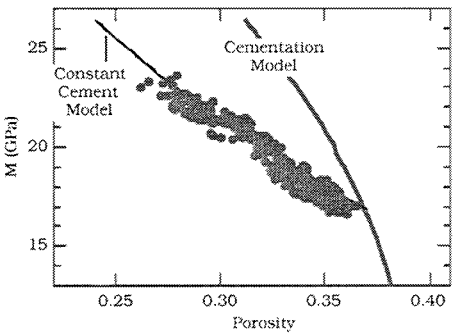

Figure A1.7. Example of adjusting constant cementation model (choosing appropriate cemented porosity) to well log data.

9. Unconsolidated Model (Friable Sand) of Dvorkin and Nur, 1996 (Theoretical)

This model assumes that sandstone starts as a pack of identical spherical grains at critical porosity, then porosity reduces due to the deposition of cement away from grain contacts. At critical porosity, the elastic moduli of the dry frame are calculated versus effective pressure from the Hertz-Mindlin equations. For smaller porosities, we connect the critical porosity point with the solid-phase modulus at 0% porosity (Figure A1.8).

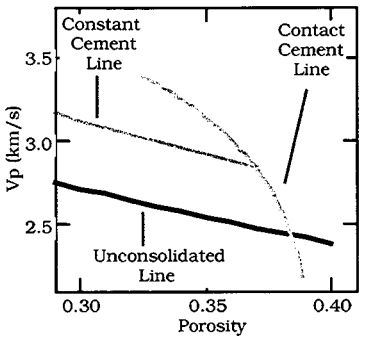

Figure A1.8. Unconsolidated model.

Inputs: critical porosity in fraction (ϕ_c);

bulk modulus of the solid phase in GPa ($K_{mineral}$);

shear modulus of the solid phase in GPa ($G_{mineral}$);

effective pressure in MPa (P);

coordination number (n) (number of contacts per grain: 6-9);

total porosity ϕ (varies between 0.1 and ϕ_c).

The effective bulk (K_{dry}) and shear (G_{dry}) moduli of dry rock are:

$$K_{dry} = [\frac{\phi / \phi_c}{K_{HM} + \frac{4}{3} G_{HM}} + \frac{1 - \phi / \phi_c}{K_{mineral} + \frac{4}{3} G_{HM}}]^{-1} - \frac{4}{3} G_{HM},$$

$$G_{dry} = [\frac{\phi / \phi_c}{G_{HM} + z} + \frac{1 - \phi / \phi_c}{G_{mineral} + z}]^{-1} - z, \quad z = \frac{G_{HM}}{6} \left(\frac{9K_{HM} + 8G_{HM}}{K_{HM} + 2G_{HM}} \right);$$

$$K_{HM} = [\frac{n^2 (1 - \phi_c)^2 G_{mineral}^{\ 2}}{18\pi^2 (1 - \nu_{mineral})^2} P]^{\frac{1}{3}}, \quad G_{HM} = \frac{5 - 4\nu_{mineral}}{5(2 - \nu_{mineral})} [\frac{3n^2 (1 - \phi_c)^2 G_{mineral}^{\ 2}}{2\pi^2 (1 - \nu_{mineral})^2} P]^{\frac{1}{3}};$$

$$\nu_{mineral} = 0.5(K_{mineral} / G_{mineral} - 2/3) / K_{mineral} / G_{mineral} + 1/3).$$

The bulk modulus K_{sat} of the rock saturated with common fluid is calculated from K_{dry} using Gassmann's equation. The bulk modulus of the solid phase for Gassmann's equation is $K_{mineral}$.

The desired compressional modulus is: $M_{common}^{unconsolid} = K_{sat} + 4G_{dry} / 3.$

Adjustable parameters in this model are: n (between 6 and 9), ϕ_c (between 0.35 and 0.42 for sandstones); as well as the elastic moduli of the mineral components that make up the grains and cement. An example is given in Figure A1.9.

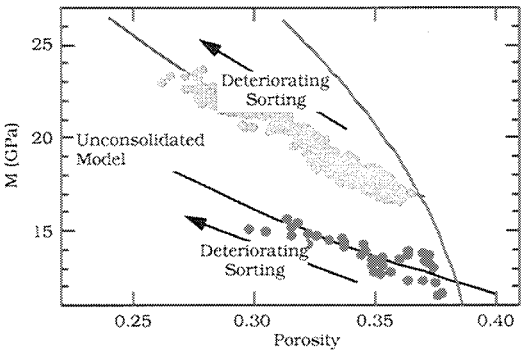

Figure A1.9. Example of fitting well log data with unconsolidated model curve. Constant cement data and curve are shown. Cementation model curve is shown as well.

11. Marine Sediment Model of Dvorkin and Prasad, 1999 (Theoretical):

This model is designed to describe unconsolidated ocean-bottom sediments and may be useful for modeling the seismic response of the very top part of the marine sediment column. It assumes that sediment starts as a pack of identical spherical grains at critical porosity, then porosity increases due to the insertion of voids in the sediment fabric. At critical porosity, the elastic moduli of the dry frame are calculated versus effective pressure by using the Hertz-Mindlin equations. For higher porosities, we connect the critical porosity point with zero modulus at 100% porosity. We connect these two points in the upper Hashin-Shtrikman fashion.

Inputs: critical porosity in fraction (ϕ_c);

bulk modulus of the solid phase in GPa ($K_{mineral}$);

shear modulus of the solid phase in GPa ($G_{mineral}$);

effective pressure in MPa (P);

coordination number (n) (number of contacts per grain: 6-9);

total porosity ϕ (varies between ϕ_c and 1).

The effective bulk (K_{dry}) and shear (G_{dry}) moduli of dry rock are:

$$K_{dry} = \left[\frac{(1-\phi)/(1-\phi_c)}{K_{HM}+\frac{4}{3}G_{HM}} + \frac{(\phi-\phi_c)/(1-\phi_c)}{\frac{4}{3}G_{HM}}\right]^{-1} - \frac{4}{3}G_{HM},$$

$$G_{dry} = \left[\frac{(1-\phi)/(1-\phi_c)}{G_{HM}+z} + \frac{(\phi-\phi_c)/(1-\phi_c)}{G+z}\right]^{-1} - z,$$

$$z = \frac{G_{HM}}{6}\left(\frac{9K_{HM}+8G_{HM}}{K_{HM}+2G_{HM}}\right); \quad K_{HM} = \left[\frac{n^2(1-\phi_c)^2 G_{mineral}^{\ 2}}{18\pi^2(1-\nu_{mineral})^2}P\right]^{\frac{1}{3}},$$

$$G_{HM} = \frac{5 - 4\nu_{mineral}}{5(2 - \nu_{mineral})}\left[\frac{3n^2(1-\phi_c)^2 G_{mineral}^{\ 2}}{2\pi^2(1-\nu_{mineral})^2} P\right]^{\frac{1}{3}};$$

$$\nu_{mineral} = 0.5(K_{mineral} / G_{mineral} - 2/3) / (K_{mineral} / G_{mineral} + 1/3).$$

The bulk modulus K_{sat} of the rock saturated with common fluid is calculated from K_{dry} using Gassmann's equation. The bulk modulus of the solid phase for Gassmann's equation is $K_{mineral}$. The desired compressional modulus is: $M_{common}^{marine} = K_{sat} + 4G_{dry} / 3.$

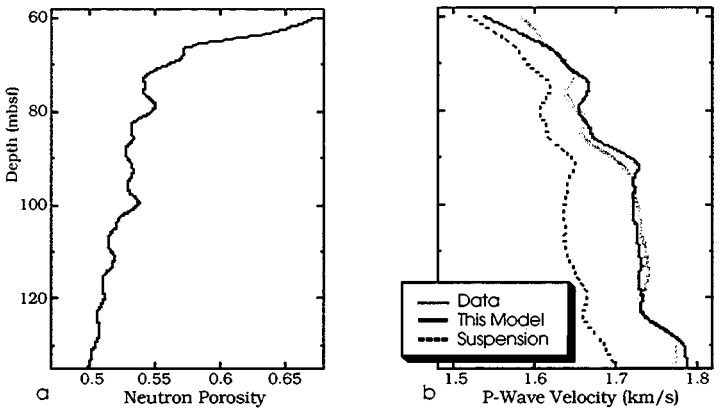

Figure A1.10. Well 974. a. Neutron porosity versus depth. b. Velocity versus depth: data, our model, and suspension model. All curves are smoothed.

Adjustable parameters in this model are the same as in the previous one.

An example of applying this model to log data is given below. The modeling results are compared with the sonic velocity data in Figure A1.10b where a good agreement between the model and the data is apparent.

12. Model for Chalks of Walls et al., 1998 (Theoretical):

Based on well-log data from Ekofisk. The model curve in the modulus-porosity plane connects the high-porosity point that has to be manually picked from the data to the zero-porosity point at which the moduli of the rock are those of the mineral phase. The high-porosity point has to is based on the dry-frame moduli. Use Gassmann's equation to calculate the dry-frame moduli from log data. Example is in Figures A1.11 – A1.13.

Inputs: initial (high) porosity chosen from the data, in fraction (ϕ_0);

bulk modulus at ϕ_0 in GPa (K_0);

shear modulus at ϕ_0 in GPa (G_0);

bulk modulus of the solid phase in GPa ($K_{mineral}$);

shear modulus of the solid phase in GPa ($G_{mineral}$);

total porosity ϕ (varies between ϕ_0 and zero).

The effective bulk (K_{dry}) and shear (G_{dry}) moduli of dry rock are:

$$K_{dry} = [\frac{\phi / \phi_0}{K_0 + \frac{4}{3} G_{mineral}} + \frac{1 - \phi / \phi_0}{K_{mineral} + \frac{4}{3} G_{mineral}}]^{-1} - \frac{4}{3} G_{mineral},$$

$$G_{dry} = [\frac{\phi / \phi_0}{G_0 + z} + \frac{1 - \phi / \phi_0}{G_{mineral} + z}]^{-1} - z, \quad z = \frac{G_{mineral}}{6} \frac{9K_{mineral} + 8G_{mineral}}{K_{mineral} + 2G_{mineral}}.$$

Adjustable parameters are: ϕ_0; K_0; G_0; $K_{mineral}$; and $G_{mineral}$.

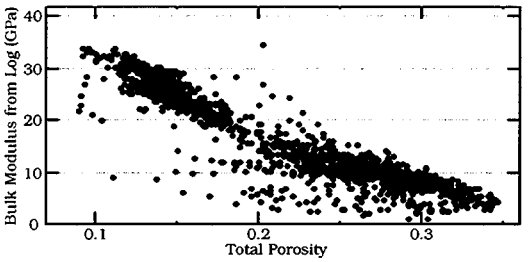

Figure A1.11. Chalk data. Bulk modulus (taken directly from log data) versus porosity.

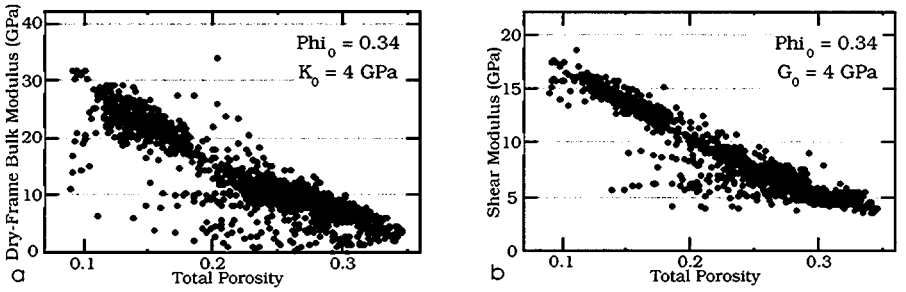

Figure A1.12. Dry-frame bulk modulus (a) and shear modulus (b). The initial (high) porosity and the corresponding moduli are picked from the plots.

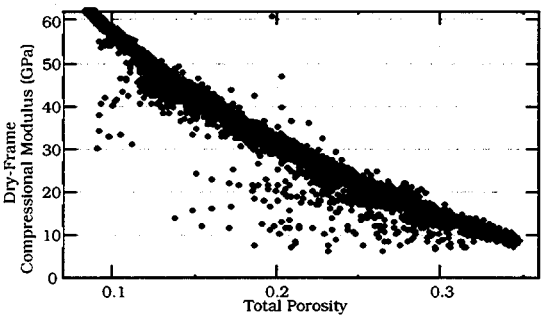

Figure A1.13. Dry-frame compressional modulus matched by the model curve.

13. Vp/Vs Models

The shear-wave velocity (or the shear modulus) is a necessary input parameter for full waveform elastic modeling of the seismic response. Some of the rock physics models discussed here provide both bulk and shear modulus. However, our experience shows that the shear-wave velocity theoretical curves often do not match the data (given that the rock physics diagnostic has been done using the compressional modulus).

For this reason, we present here Vp/Vs relations to be used for calculating Vs from the compressional-wave data (or theoretical curves). These models are discussed and analyzed in Mavko et al. (1998). Here we be briefly describe only several, most commonly used, of them.

13.1. Castagna et al. (1993) Mudrock Equation: $V_s = 0.862V_p - 1.172$ (km/s). This equation has been derived from in-situ data for water-saturated shales.

13.2. Castagna et al. (1993) Equations for Limestones and Dolomites:

Limestone: $V_s = -0.055V_p^2 + 1.017V_p - 1.031$ (km/s);

Dolomite: $V_s = 0.583V_p - 0.0789$ (km/s).

Both equations are based on laboratory measurements conducted on water-saturated samples.

13.3. Krief et al. (1990): $(V_{p-sat}^2 - V_{fl}^2)/V_{s-sat}^2 = (V_{p-mineral}^2 - V_{fl}^2)/V_{s-mineral}^2$, where V_{p-sat} and V_{s-sat} are the compressional- and shear-wave velocity in the saturated rock, respectively; $V_{p-mineral}$ and $V_{s-mineral}$ are the compressional- and shear-wave velocity in the mineral phase of the rock, respectively; and V_{fl} is the velocity in the fluid.

13.4. Greenberg and Castagna (1992) Method: This empirical formula (below) is based on a number of datasets where ultrasonic velocity measurements were conducted on pure water (the common saturation fluid) saturated rocks. To calculate V_s from V_p for other fluids use Gassmann's equation.

$$V_s = \frac{1}{2}\{(\sum_{i=1}^{4} X_i \sum_{j=0}^{2} a_{ij} V_p^{\,j}) + (\sum_{i=1}^{4} X_i (\sum_{j=0}^{2} a_{ij} V_p^{\,j})^{-1})^{-1}\}, \quad \sum_{i=1}^{4} X_i = 1;$$

where X_i is the volume fraction of pure mineral constituents in the mineral phase with "1" standing for sandstone (quartz); "2" for limestone (calcite); "3" for dolomite; and "4" for shale. The empirical coefficients a_{ij} are tabulated below:

i	Mineral	a_{i2}	a_{i1}	a_{i0}
1	Sandstone	0	0.80416	-0.85588

2	Limestone	-0.05508	1.01677	-1.03049
3	Dolomite	0	0.58321	-0.07775
4	Shale	0	0.76969	-0.86735

14. Velocity-Density Relations A velocity (V_p) versus bulk density (ρ_b) relation may be useful where only velocity data are available and there is a need to calculate the impedance.

14.1. Castagna, 1993: $\rho_b = aV_p^2 + bV_p + c$, where coefficients a, b, and c are tabulated below for various lithologies. Density is in g/cm^3 and velocity is in km/s.

Mineral	a	b	c
Shale	-0.0261	0.373	1.458
Sandstone	-0.0115	0.261	1.515
Limestone	-0.0296	0.461	0.963
Dolomite	-0.0235	0.390	1.242
Anhydrite	-0.0203	0.321	1.732

14.2. Gardner et al., 1974: $\rho_b = 1.741V_p^{.25}$. Density is in g/cm^3 and velocity is in km/s.

Appendix 1.2. Example 1 of Rock Physics Diagnostic: Competing Effects of Saturation and Rock Texture

Summary. In this example we analyze an interval in a vertical North Sea well that intersects oil-water and gas-oil contacts. Velocity in the gas zone appears to be higher that in the oil- and water zone, in spite of the high total porosity. This section of the interval corresponds to the constant and relatively low GR values. Therefore, this high-velocity effect is due to the texture of rock in the gas zone that is most likely to be connected with the depositional environment.

Introduction and Problem Formulation. It is generally expected that velocity in gas-saturated rock is smaller than in rock saturated with oil or water. However, in the well under examination, the opposite is true: the P-wave velocity increases across the gas-oil contact being larger in the gas zone (Figure A2.1b). This is in spite of the total porosity in the gas zone being much larger than porosity in the oil and water zones (Figure A2.1d). Our goal is to resolve this apparent inconsistency by the means of rock physics diagnostic.

Solution via Rock Diagnostic. Notice that in the well under examination, a low-GR (about 75 API) interval starts just above GOC and ends at about 1.53 km depth. In contrast, gamma-ray values between GOC and OWC reach 125 API. The low-GR interval corresponds to relatively high P-wave velocity (2.4 km/s) and high porosity (33% - 35%). Velocity above GOC is higher than below GOC. The shear-wave velocity also exceeds that below the gas-oil contact. This observation tells us that in addition to pore fluid, rock fabric may be also responsible for velocity-depth variations.

To approach this task we have to diagnose rocks in the interval under examination. To do so, we have to determine the elastic constants and densities of pore fluid components. We determine these properties using the Batzle-Wang (see in Mavko et al., 1998) formulas for reservoir temperature 70 ^{o}C and pore pressure 16 MPa. The results are given in Table A2.1 below.

The sonic data come from dipole measurements. We assume that there is no mud-filtrate invasion effect on the dipole and density data because porosity is high and, therefore, the invasion radius has to be small.

Therefore, we use the virgin saturation data to calculate the bulk modulus of the pore fluid that is a mixture of water, oil, and gas. When doing so, we assume that there is no oil above GOC and no gas below it. Obviously, such an assumption approximates the real situation. These fluid properties are used to calculate the compressional

modulus in the interval at 100% water saturation.

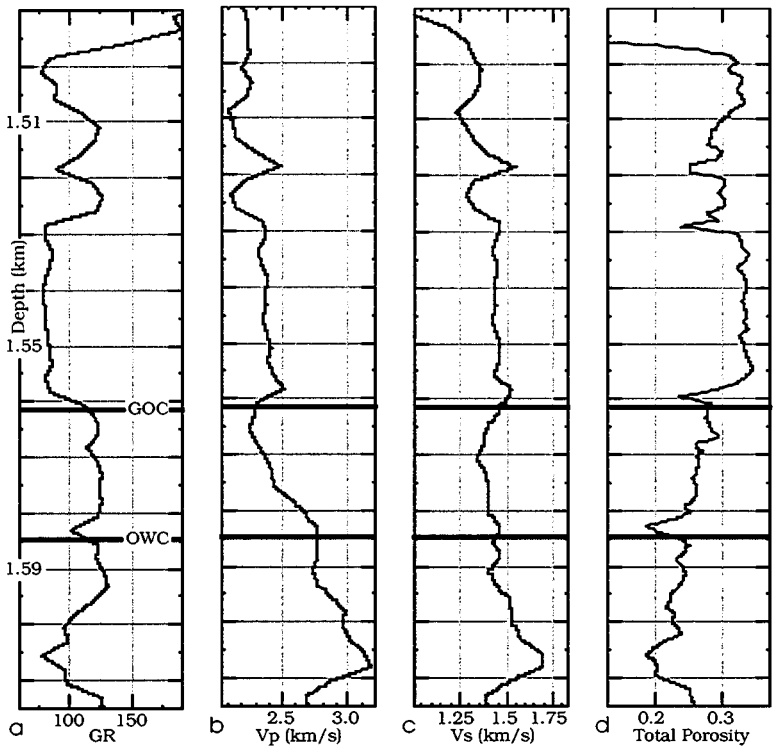

Figure A2.1. Gamma-ray, velocity, and total porosity versus depth. Velocity in the gas-saturated zone is higher than below it.

Table A2.1. Estimates for Pore Fluid Properties

Fluid	Density (g/cm^3)	Bulk Modulus (GPa)	Gravity (API)	Salinity (ppm)
Water	1.024	2.72		56,000
Oil	0.68	0.6	40 (GOR = 150)	
Gas	0.116	0.03	0.6	

Let us cross-plot the compressional (M) modulus versus porosity for the entire interval under examination (Figure A2.2a). The water and oil zones show clear modulus-porosity trends. The gas zone shows two trends: one for the interval above 1527 m, and the other for the interval between 1561 m and 1527 m. Notice that the latter interval corresponds to low gamma-ray readings (Figure A2.3).

In order to be able to compare gas to oil to water intervals, we theoretically resaturate the entire interval with 100% formation water. We crossplot the resulting compressional modulus versus porosity in Figure A2.2b. All parts of the interval,

except the low-GR interval in the gas zone between 1561 m and 1527 m appear to be on the same modulus-porosity trend that is the unconsolidated theoretical line of Dvorkin and Nur (1996). The low-GR gas interval stands out and lies on a constant-cement line (Avseth et al., 1998) with very small amounts of contact cement. The shear-modulus crossplot (Figure 3.4) further supports this hypothesis.

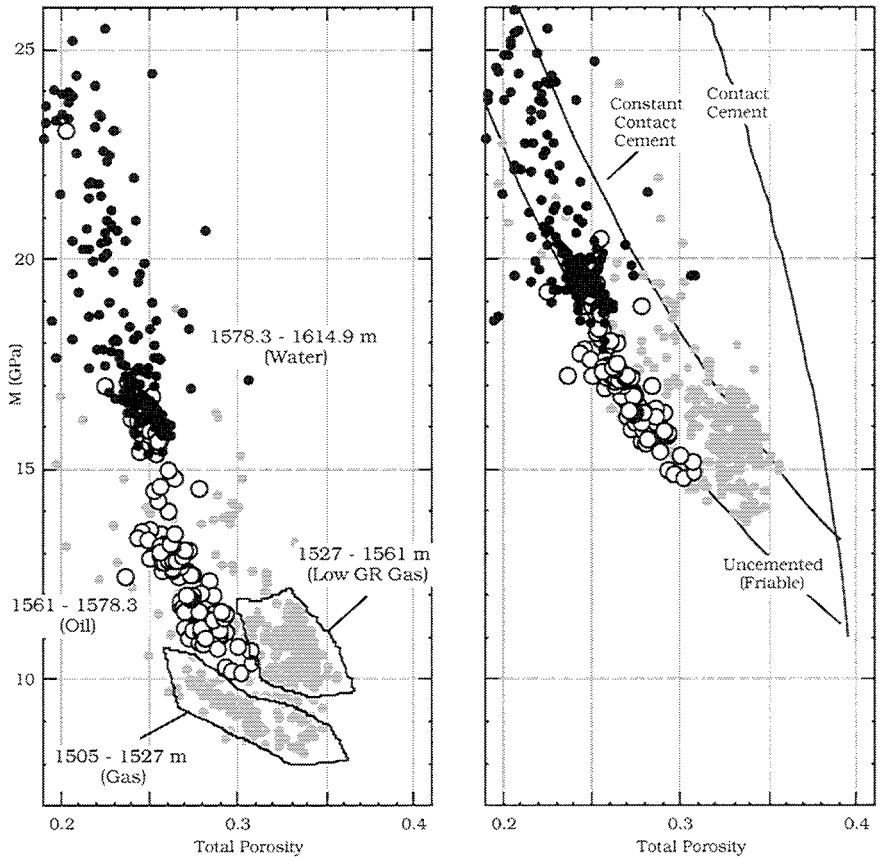

Figure A2.2. Compressional-modulus versus porosity below OWC, between OWC and GOC, and above GOC. Left: modulus as measured; right: modulus with uniform saturation (100% brine) with superimposed theoretical curves.

Conclusion. We conclude that it is rock texture rather than pore fluid that is responsible in this case for the observed vertical velocity variations and contrasts. The thin section images (Figure A2.5) do not directly show the presence of contact cement. However, the apparent angularity of the coarse grains corresponding to the low-gamma-ray gas-filled interval may indirectly indicate the presence of slight contact cementation.

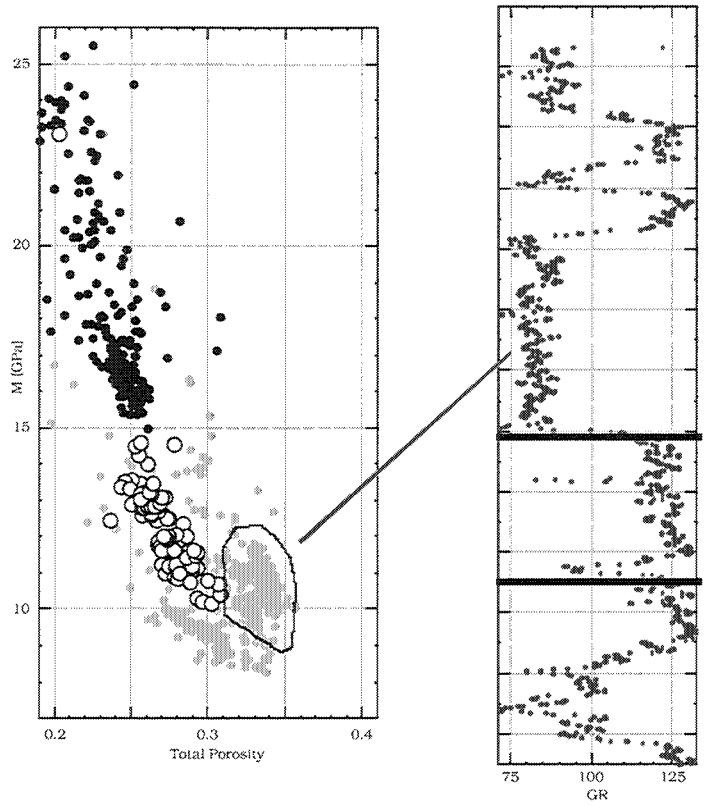

Figure A2.3. Anomalous velocity data correspond to the low-GR interval in gas zone.

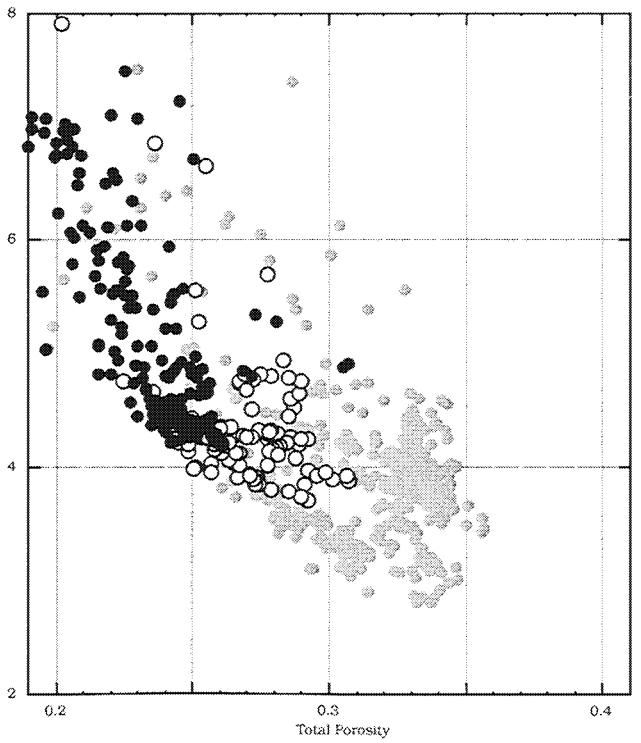

Figure A2.4. Shear modulus versus porosity. Symbols are same as in Figure A2.2.

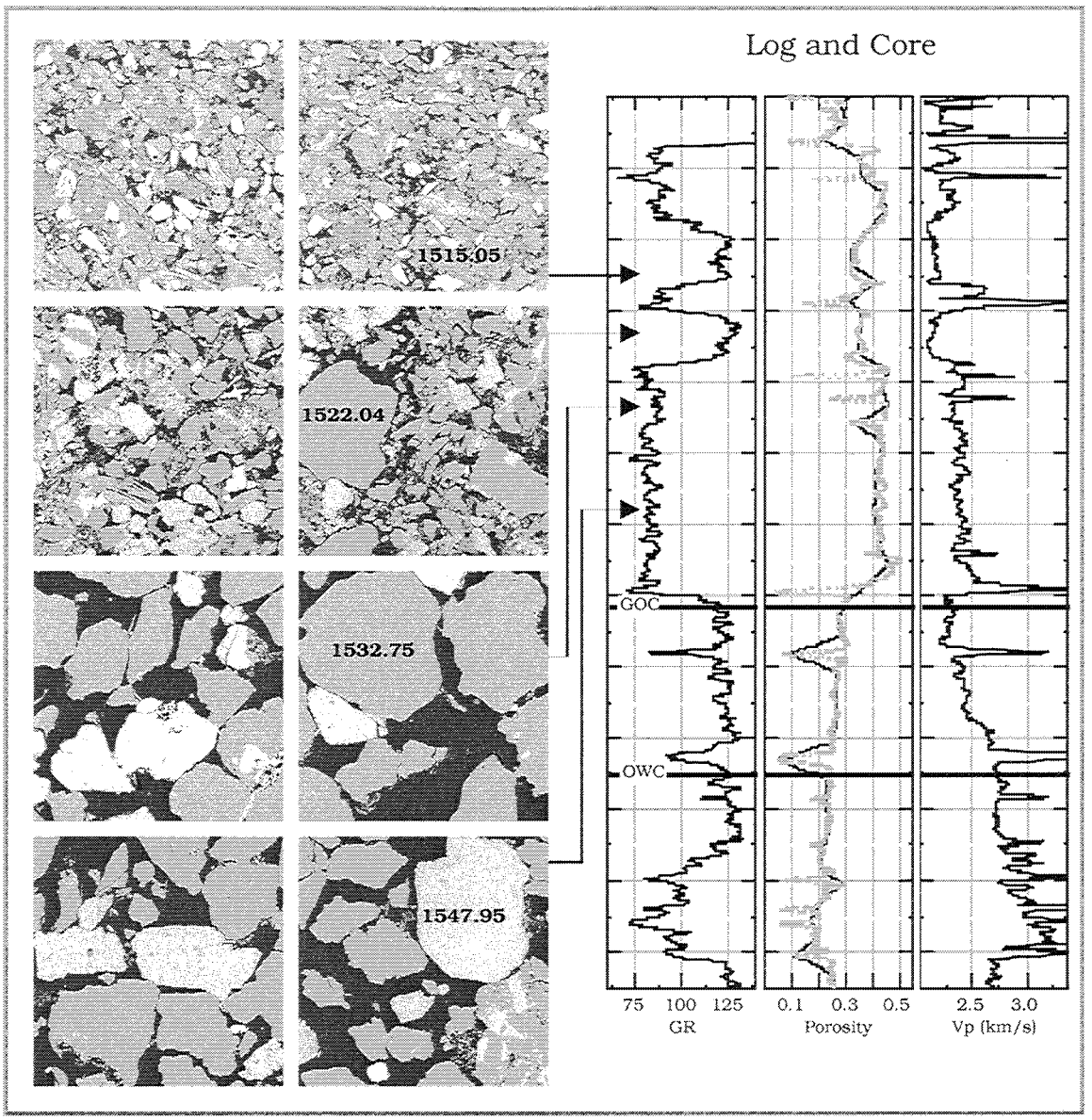

FigureA2.5. Thin sections and corresponding depth intervals.

Appendix 1.3. Example 2 of Rock Physics Diagnostic: Strength and Permeability from Porosity and Velocity for High-Porosity Sands

Summary. In high-porosity sandstones, permeability depends not only on porosity, but also on the location of the pore-filling minerals. It is affected mostly by the part of the pore-filling cement that is deposited away from grain contacts and clogs the pore space. On the other hand, the elasticity of sandstones (which determines the elastic-wave velocity) is affected mostly by the rest of the cement, i.e., by its part deposited at grain contacts. Then, by analyzing velocity data, one can estimate the volume of the contact cement. Once this quantity is known, porosity can be used to find the volume of the remaining, non-contact, cement whose effect on permeability is large. We offer a new rock physics theory to quantify the amount of the non-contact cement in sandstones from dry-rock velocity and porosity data. We apply this theory to field well-log data and show that by relating permeability to the volume of the non-contact cement a meaningful trend can be achieved, with much less scatter than the corresponding permeability-porosity trend. This success renders viable the approach where sonic and porosity logs are used together to diagnose the rock for its pore-scale structure and, based on this diagnostic, quantify properties that cannot be measured directly.

Introduction and Problem Formulation. Non-uniqueness in relating velocity to porosity in core and well-log data complicates interpretation of sonic and seismic measurements. One reason for this non-uniqueness in sandstones is clay (e.g., Han, 1986). Another reason is textural variability among samples. Dvorkin and Nur (1996) examine two relatively clay-free sandstone groups in the same porosity range, but whose velocities significantly differed (Figure A3.1a). By comparing the data with effective-medium theories they interpret this velocity difference as resulting from the difference in the position of diagenetic cement. The explanation is that in the "fast" (Oseberg) rocks (contact) cement is located predominantly at the grain contacts whereas in the "slow" (Troll) rocks (non-contact) cement is located predominantly away from these contacts.

Coincidentally, the permeability of the Troll rocks is smaller than that of the Oseberg rocks (Figure A3.1b). This fact allows us to assume that the position of the diagenetic cement affects not only velocity but also permeability. The assumption is supported by numerical simulations of Bosl et al. (1998). This effect has a simple physical explanation: the non-contact cement acts to increase the specific surface area (Figure A3.1b) and thus decrease permeability.

To do so, we use log-derived velocity and porosity together with rock physics theory to subdivide the

diagenetic cement into the contact and non-contact parts. Then by relating permeability to the volumetric fraction of the non-contract cement in the rock we obtain a usable trend. This non-contact cement fraction is the desired textural property. By quantifying the amount of contact and non-contact cement we diagnose sandstone's texture from well log data, similar to Dvorkin and Nur (1998). We show that such diagnostic is important not only for obtaining a high-correlation permeability trend but also for assessing the strength of the rock.

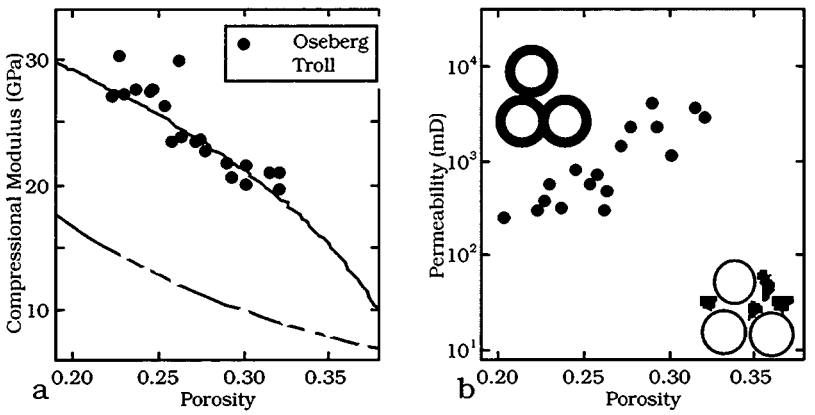

Figure A3.1. a. Compressional modulus (the product of bulk density and P-wave velocity squared) versus porosity for the Oseberg and Troll samples. The data displayed are for room-dry rocks at 30 MPa effective pressure (Strandenes, 1991; and Blangy, 1992). The upper curve is from the contact cement theory and the bottom curve is from the non-contact cement theory (Dvorkin and Nur, 1996). b. Permeability versus porosity for the same datasets (Strandenes, 1995). The cartoons schematically show the location of cement among grains (contact for Oseberg and non-contact for Troll).

North Sea Sleipner Field, Well 15/9-16. A vertical well, 15/9-16, penetrates the North Sea Sleipner gas/condensate reservoir comprised of Paleocene turbiditic sand. Porosity and permeability are available from about 60 plugs that evenly cover the interval from 2380 to 2460 m. The vertical and horizontal permeabilities are practically identical. The latter is used in this study. The sandstone is very well sorted with the average sorting coefficient of 1.7; grain size varies between 0.15 and 0.25 mm. The grains are predominantly quartz (average 80%) with the rest being feldspar (average 14%), mica (average 2.3%), and clay, mostly chlorite, (average 2.2%). Traces of calcite and other minerals are also present. The contact cement in these rocks is quartz (Nadeau, 1998). The upper part of the well is saturated with gas, with the gas-water contact at 2430 m. The bulk moduli and densities of the formation water and gas are

2.75 GPa and 1.02 g/cm^3, and 0.07 GPa and 0.27 g/cm^3, respectively (following Batzle and Wang, 1992).

The interval under investigation can be subdivided into a high-resistivity zone (HRZ) overlaying a low-resistivity zone (LRZ) with the transition at about 2410 m (Figure 4.2a). Nadeau (1998) shows that there is a diagenetic change associated with this transition. HRZ has a restricted distribution of diagenetic chlorite and up to 5% quartz cement. LRZ has a slightly larger content of chlorite and a smaller degree of cementation.

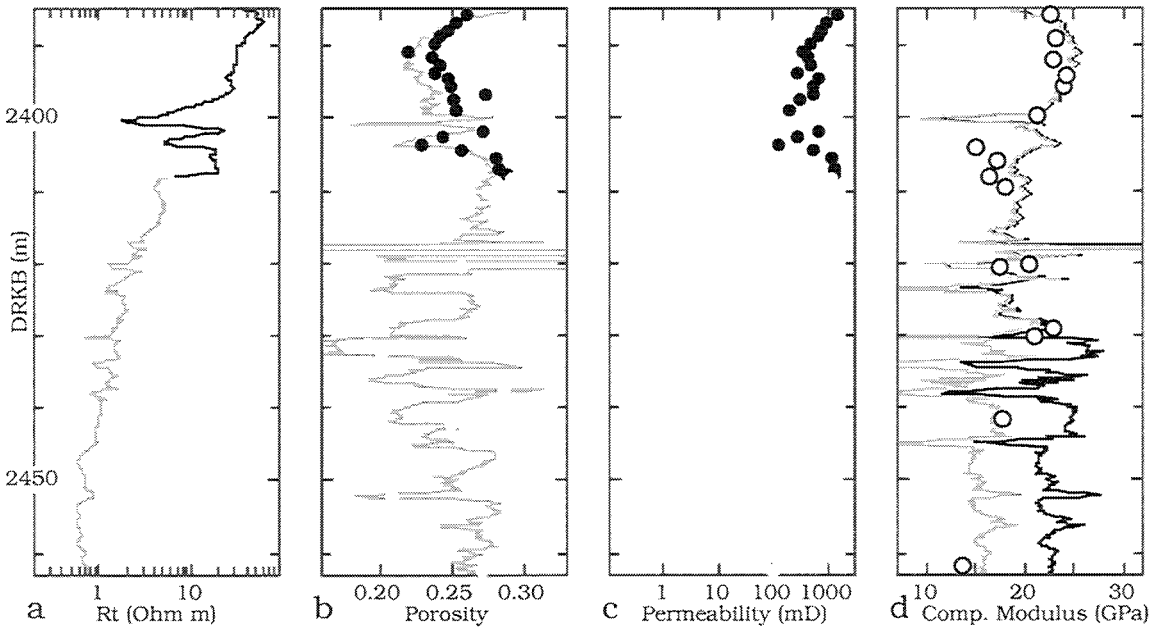

Figure A3.2. Various parameters versus depth in well 15/9-16. a. Far resistivity. Gray curve is for LRZ. b. Log-derived (gray curve) and core porosity. Open symbols are for LRZ. c. Permeability. Open symbols are for LRZ. d. Dry-rock (gray curve) and directly measured (black curve) compressional modulus. Symbols are from dry-rock lab measurements at 30 MPa.

Porosity in the interval is high. We calculate it from bulk density (Schlumberger, 1989). It's values do not differ much from those measured on cores except for a few points in LRZ (Figure 4.2b). The results of this study practically do not depend on what porosity (log-derived or core) we use. We relate all parameters to the log-derived porosity.

The log data contain only compressional-wave velocity. We calculate the dry-frame compressional modulus (the product of bulk density and P-wave velocity squared) by the V_p-only fluid substitution method (Mavko et al., 1995). The result is matched by

the values measured on several room-dry plugs (Figure A3.2d). The 30 MPa effective pressure for these datapoints equals the reservoir effective pressure (about 29 MPa).

Analysis of Data. There is a weak and not useful correlation between permeability and porosity (either log-derived or core) in well 15/9-16 (Figure A3.3). This fact can also be observed in Figures A3.2b and A3.2c where porosity and permeability are plotted versus depth. The lower-porosity sandstones in HRZ have permeability larger than that of the higher-porosity sandstones in LRZ. Notice also that the LRZ sandstones are softer than the HRZ sandstones (Figure A3.2d).

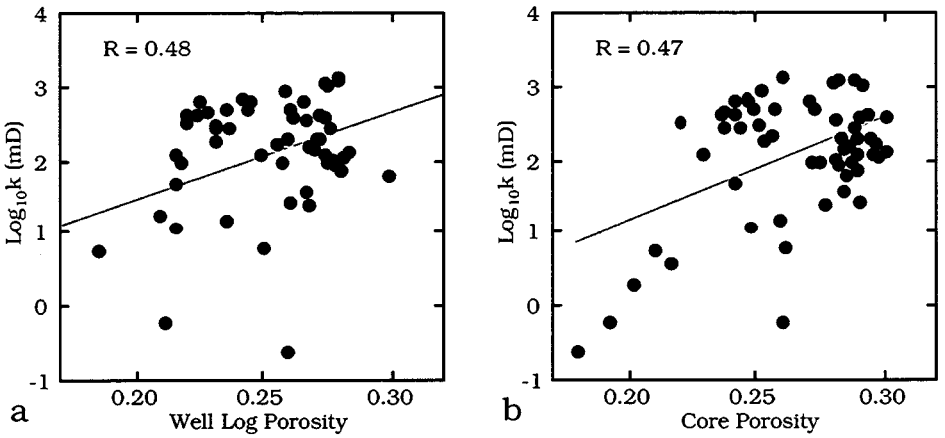

Figure A3.3. Horizontal permeability versus log-derived (a) and core (b) porosity. Gray lines show best linear fits. Correlation coefficients are given in the graphs.

The modulus-porosity and permeability-porosity trends for HRZ and LRZ are given in Figure A3.4. In the modulus-porosity plane (Figure A3.4a) the HRZ trend parallels that of the contact-cemented Oseberg rocks and the contact cement theoretical trajectory (the latter calculated for quartz grains with quartz cement). The HRZ rocks have a tight modulus-porosity trend. Remarkably, in the permeability-porosity plane (Figure A3.4b) the HRZ sandstones plot on top of the Oseberg data and also exhibit a noticeable permeability-porosity trend. The LRZ sandstones on the other hand do not show a modulus-porosity trend. These datapoints fill the space between the contact and non-contact cement theoretical trajectories (the latter calculated for quartz rock at 29 MPa effective pressure). Similarly, in the permeability-porosity plane these rocks fill the space between the Troll and Oseberg datapoints, and a permeability-porosity trend is absent. Both HRZ and LRZ rocks are quartz-cemented and have very close

mineralogy. Based on this, we assume that both the modulus- and permeability-porosity non-uniqueness (Figure A3.4) is due to the varying amounts of contact and non-contact cement.

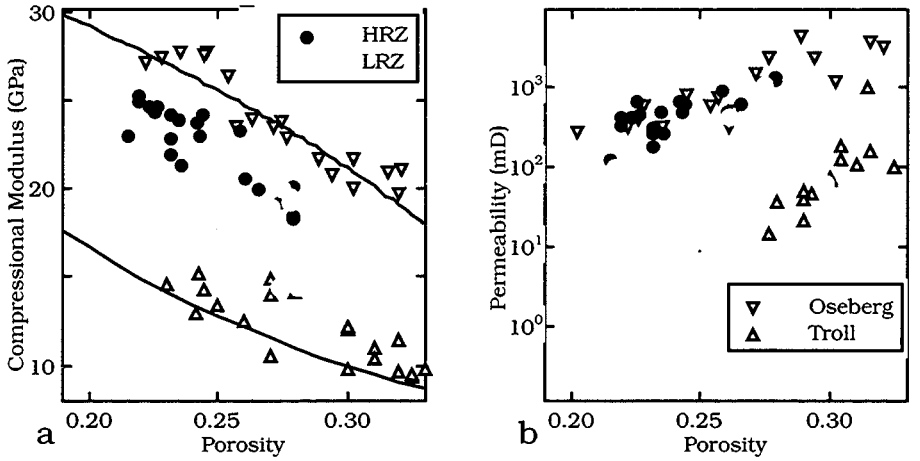

Figure A3.4. a. Dry-frame compressional modulus versus porosity for the Oseberg and Troll samples at 30 MPa, and HRZ and LRZ. The HRZ and LRZ data are selected at the depths of permeability datapoints. The upper curve is from the contact cement theory and the bottom curve is from the non-contact cement theory. b. Permeability versus porosity for the same datasets. The open triangles are for Oseberg and Troll. The filled circles are for HRZ and the open circles are for LRZ. The Oseberg and Troll data are plotted versus core porosity whereas the HRZ and LRZ data are plotted versus log-derived porosity.

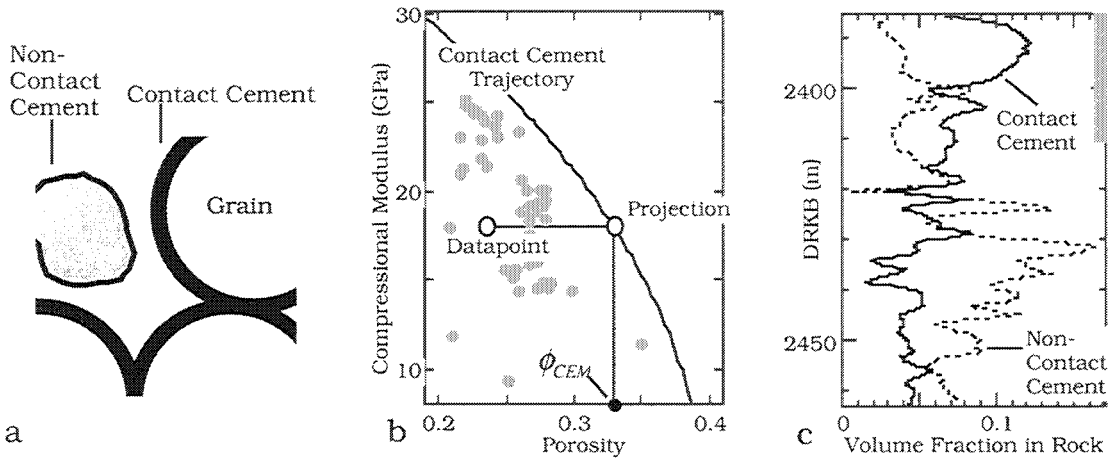

Figure A3.5. a. Idealized picture of granular rock with contact and non-contact cement. b. Calculating the amount of non-contact cement. Gray symbols show scattered datapoints. c. Volumetric fraction of contact (solid line) and non-contact (dotted line) cement versus depth in well 15/9-16. Gray vertical bar shows the extent of HRZ.

Diagnosing Rock for Non-Contact Cement. To calculate the amount of the non-

contact cement from sonic and porosity we use a model where a high-porosity sandstone has an idealized texture. Its basis is a random dense pack of identical spherical grains at some critical porosity ϕ_c which may vary between 0.36 and 0.4 (Nur et al., 1998). Every grain is identically and evenly enveloped by a layer of contact cement, and the rest of the solid phase (additional to the grains and contact cement) forms non-contact cement deposited in the pore space away from grain contacts (Figure A3.5a). One is unlikely to encounter such an idealized picture in a thin section. However, this is a way to build effective medium models, some of which have been effectively used to model granular rocks (e.g., Dvorkin and Nur, 1996; Moos et al., 1997).

Consider now a datapoint in the modulus-porosity plane that lies below a theoretical contact cement trajectory (Figure 4.5b). We assume that the non-contact cement does not contribute to the stiffness of this rock. Thus its modulus is identical to that of a higher porosity (ϕ_{cem}) rock of the same texture but without the non-contact cement. The corresponding datapoint is the horizontal projection (in the modulus-porosity plane) of the original one onto a contact-cement trajectory (Figure 4.5b). Volume balance gives the following relations between the porosity of the datapoint (ϕ), its projection on the contact-cement trajectory (ϕ_{cem}), critical porosity (ϕ_c), and the volume fractions of the contact (f_{cc}) and non-contact (f_{ncc}) cement in rock:

$$f_{cc} = \phi_c - \phi_{cem};\ f_{ncc} = \phi_c - \phi - f_{cc}. \qquad \text{(A3.1)}$$

The contact-cement trajectory can be plotted using equations in Dvorkin and Nur (1996); it depends on the elastic moduli of grains and cement, and on the chosen critical porosity value. An additional input parameter is the average number of contacts per grain in the original sphere pack (n). It may vary between 9 and 6. In the case under examination we choose ϕ_c = 0.38 (average between 0.36 and 0.4) and n = 8.5. Because the grains and contact cement are predominantly quartz, we plot the contact-cement trajectory for quartz-cemented quartz grains (Figure A3.5b). In calculating this trajectory, we use 38 GPa and 44 GPa for the bulk and shear moduli of quartz, respectively (Carmichael, 1990). This trajectory can be statistically fitted (with

correlation coefficient about 1) by equation

$$1.037\sqrt{0.38-\phi_{cem}} = -0.0013+0.0134M+4.3\cdot10^{-5}M^2, \qquad \text{(A3.2)}$$

where M is the compressional modulus of the dry contact-cemented rock. The contact-cement trajectory for any set of input parameters can be obtained from Dvorkin and Nur (1996). Then it can be statistically fitted by an equation similar to Equation (A3.2).

Now we can combine Equations (A3.1) and (A3.2) to arrive at a formula that relates the volumetric fractions of the contact and non-contact cement to the dry-frame compressional modulus and porosity:

$$f_{cc} = 0.93(-0.0013+0.0134M+4.3\cdot10^{-5}M^2)^2, f_{ncc} = 0.38-\phi-f_{cc}. \qquad \text{(A3.3)}$$

These fractions, as calculated for well 5/9-16 (using the dry-frame compressional modulus from fluid substitution) are given in Figure A3.5c. The contact cement dominates in HRZ whereas the non-contact cement is prevalent in LRZ.

This diagnostic can be immediately used to assess the strength of the rock: clearly the larger the amount of contact cement the stronger the rock (at the same porosity). This effect could be clearly seen in the Troll and Oseberg example (Figure A3.1). The Troll samples that do not have contact cement are friable sands (Blangy, 1992), whereas the Oseberg samples show significant structural integrity (Strandenes, 1991). In the case under examination, our diagnostic is also consistent with the rock's strength: Nadeau (1998) states that quartz cementation progressed more readily in HRZ and is associated with intervals less prone to sand production.

Permeability Trend. In Figure A3.6a we plot the logarithm of permeability (k) versus the volumetric fraction of the non-contact cement. A linear trend is evident (as opposed to the absence of such in Figure A3.3). The linear-fit equation for this trend is

$$\mathrm{Log}_{10}k = 3.3-19.46\,f_{ncc};\ R=0.85. \qquad \text{(A3.4)}$$

The correlation slightly improves if the permeability is normalized by the grain size (d) squared (Figure A3.6b):

$$\mathrm{Log}_{10}(k/d^2) = 4.8-20.47f_{ncc};\ R=0.86. \qquad \text{(A3.5)}$$

Such normalization is often used to improve permeability trends because permeability strongly depends on the grain size (e.g., Bourbie et al., 1987). In our case this improvement is small due to a relatively uniform grain size distribution in the interval (between 0.15 and 0.25 mm).

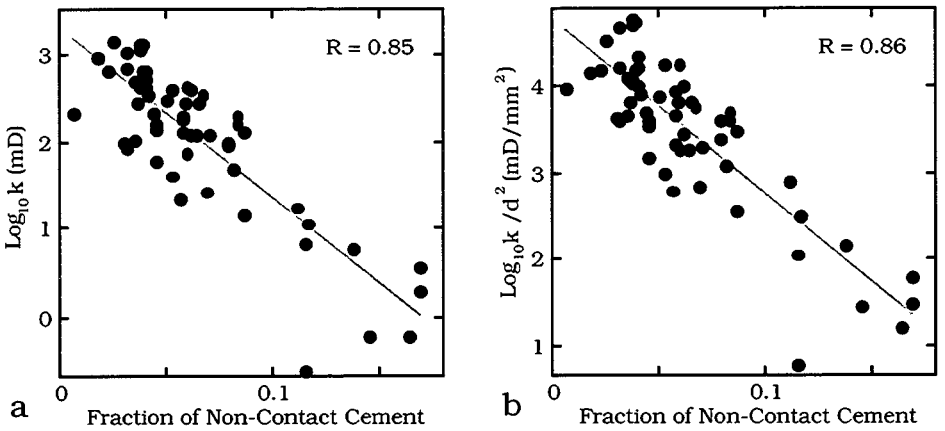

Figure A3.6. Permeability (a) and permeability normalized by grain size squared (b) versus the volumetric fraction of non-contact cement. Gray lines show best linear fits. Correlation coefficients are given in the graphs.

Conclusion and Recommendations. The high-correlation trends in Equations (A3.4) and (A3.5) can be used to predict permeability from sonic and porosity data. We obtained these trends by using the amount of non-contact cement to quantify the variability of rock texture. This confirms our initial hypothesis that textural variability in rock, specifically, the amount of the non-contact cement, can be responsible for non-uniqueness in permeability-porosity trends such as shown in Figure 4.3. To calculate the amount of the non-contact cement is a way of obtaining a meaningful correlation for permeability. The method of calculating the amount of contact and non-contact cement presented here is in fact a method of diagnosing the texture of high-porosity sandstone from well-log data. Such diagnostic is important not only for obtaining a usable correlation for permeability but also for assessing the strength of rock and its susceptibility to sanding.

Equation (A4.2) is not universal. In every separate case study it has to be re-derived from the appropriate contact-cement trajectory where the elastic moduli of the grains and cement are selected according to mineralogy or within reasonable ranges. The "free" parameters ϕ_c and n can be varied within reasonable (narrow) ranges until the

best correlation, such as Equation (A4.4), is obtained.

Appendix 1.4. Example 3 of Rock Physics Diagnostic: Diagnosing Sands for Reservoir Characterization from Sonic and Seismic

Summary. At high porosity, velocity in reservoir rocks strongly depends on the position of the intergranular material. Velocity is high if the original grains are cemented at their contacts. It is low if the pore-filling material is placed away from the contacts. In the latter case we have truly unconsolidated sediments. In the former case we have high-porosity cemented rocks. Separating these two rock types is important for hydrocarbon identification. Due to the difference in the rock frame stiffness between the unconsolidated and high-porosity cemented rocks, seismic signatures of the former filled with water can be very close to those of the latter filled with hydrocarbons. This may complicate direct hydrocarbon detection. We separate the two rock types by diagnosing sand using rock physics theory. We conduct such diagnostic on well log data from two wells that penetrate the Heimdal formation (North Sea). We show that the Heimdal formation reservoir is composed of both unconsolidated and cemented high-porosity sands. The initial quartz cementation present in the latter is clearly seen in the cathode-luminescent SEM images. These images, combined with point XRD analysis, confirm our diagnostic that the high-velocity high-porosity sands in Heimdal contain quartz grains surrounded by quartz-cement rims. We find that the two different types of sand which are capped by similar low-impedance shales produce drastically different AVO signatures. The oil-filled high-porosity cemented sand shows a relatively strong zero-offset reflectivity which becomes less positive with increasing offset, while the oil-filled uncemented sand shows a negative zero-offset reflectivity with increasingly negative far-offset response. These results show that (1) rock diagnostic can be conducted not only on the log scale but also on the seismic scale; and (2) taking into account the nature of the rock improves our ability to identify pore fluid from seismic.

Introduction and Problem Formulation. Quartz cementation of sands greatly affects porosity, permeability, and seismic properties. Sandstones in continuously subsiding sedimentary basins, such as in the North Sea and the Gulf Coast, tend to have poorly developed quartz cement down to a depth of 2.5 - 3.0 km (Bjørlykke and Egeberg, 1993). Hence, Tertiary sands in the North Sea are usually reported to be poorly consolidated with no (or insignificant quantities of) quartz cement. "Insignificant" is related to volume -- small amounts of quartz cement do not significantly affect porosity. However, only small amounts of cement at grain contacts are needed to considerably stiffen the frame of a rock (Dvorkin and Nur, 1996) and strongly increase velocity. We apply the contact cement concept to study two clean sandstone intervals, both representing the Palaeocene age Heimdal Formation in the North Sea. Both

intervals are oil-filled reservoir sands of commercial interest. We diagnose the rock using well log measurements and rock physics theory. We assume that if in the velocity-porosity plane a datapoint falls close to a theoretical line, the internal structure of the rock is similar to the idealized structure used in the model. We find from such diagnostic that one interval is composed of unconsolidated sand, while the other interval is composed of cemented high-porosity sand. Thin-section and SEM images confirm this diagnostic. By studying the seismic signatures of these two different types of clean sands we upscale the log-based diagnostic to the seismic scale.

Diagnostic and Confirmation. We examine two wells -- Well #1 and Well #2. Sonic velocity and gamma-ray are plotted versus depth for both wells in Figures A4.1a to A4.1d. Vp is plotted versus porosity in Figures 1d and 1f. Notice that in Well #2 a thick sand interval (gray bar in Figure A4.1c) is marked by extremely low and constant gamma-ray readings. This sand layer is surrounded by high-gamma-ray shale packages. In Figure A4.1f, these two lithologies fall into two distinctive velocity-porosity patterns. In Well #1, unlike in Well #2, we observe a gradual variation of clay content between very clean sand and shale. Only a relatively thin (10 m) sand interval (gray bar in Figure A4.1a) is identified as a practically clay-free reservoir sand. Because of the gradual variation of clay content in this well, we do not observe (Figure A4.1e) velocity-porosity patterns as distinctive as in Well #1. These two clean sand intervals (in both wells) represent the same stratigraphic level, although located in different oil fields. They are shown by bold black symbols in Figures A4.5.1e and A4.5.1f.

For the purpose of diagnostic, we plot together these two subsets of the data (Figure A4.2). We diagnose these rocks by superimposing theoretical rock physics curves (Dvorkin and Nur, 1996) on this plot. The contact cement line corresponds to the case where rock is formed by quartz-cement rims growing on sand grains. Here velocity drastically increases with only slightly decreasing porosity. The unconsolidated line corresponds to the case where porosity reduces not due to the growth of contact cement, but due to loose pore-filling material such as small grains, mica and detrital clay particles. Here velocity strongly depends on the effective pressure (about 20 MPa here) and only gradually increases with decreasing porosity. Notice that the Well #2 data points do not fall on the contact cement line. This is because the volumetric fraction of contact cement in these rocks, according to a thin section point-count analysis, is constant (about 2%) in the entire porosity range. Therefore this contact cement is responsible for the initial drastic velocity increase (as compared to uncemented sand) at 37% porosity, but the continuing porosity decrease is due to loose pore-filling material. This concept is represented by the

constant cement fraction line that has the shape of the unconsolidated line, but a different high-porosity end member. The two sand intervals can be diagnosed by rock physics theory as: (a) Well #1 -- unconsolidated quartz sand; and (b) Well #2 -- contact-cemented quartz sand with a constant fraction of cement in the whole rock.

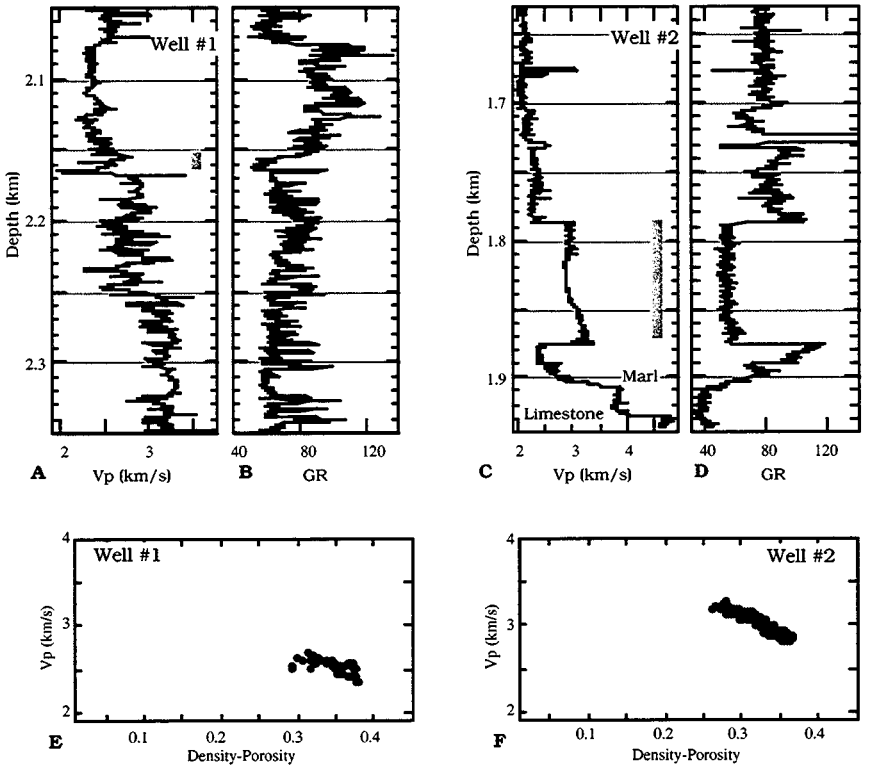

Figure A4.1. P-wave velocity and gamma-ray versus depth (a-d); and P-wave velocity versus porosity (e and f) for both wells.

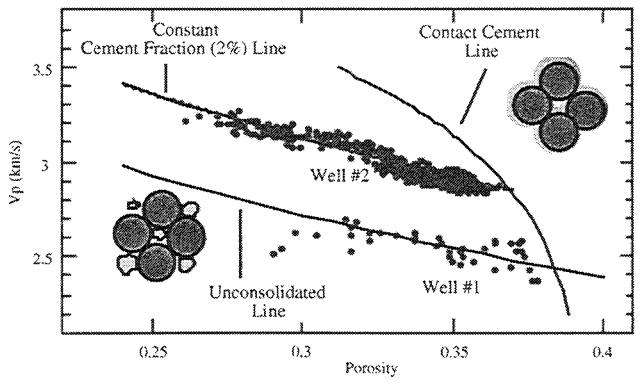

Figure A4.2. P-wave velocity versus porosity for sand intervals in both wells. Theoretical lines serve to diagnose the rocks.

To directly confirm this diagnostic, consider the thin sections of two samples from both intervals (Figure A4.3). The samples have approximately same porosity. They are predominantly quartz. No contact cementation is apparent in both images. The left image (Well #1) shows some organic coating around quartz grains. Consider now two SEM images of a sample from Well #2 (Figure A4.4). The left-hand image is in back-scatter light and the right-hand one is in cathode-luminescent light. Notice the V-shaped grain in the middle. No contact cement rim is apparent around this grain in back-scatter light. Cathode-luminescent light reveals a contact-cement rim around this grain. The point XRD analysis shows that both the grain and cement rim are pure quartz. This confirms our diagnostic that the Well #2 sand interval is contact-cemented. The hexagonal crystal shapes in the upper left corner also indicate diagenetic cementation. No cement rims or hexagonal crystal shapes have been found around grains in the sand interval from Well #1. Another direct proof of our diagnostic was that cores extracted from Well #1 appeared as piles of loose sand, whereas those from Well #2 supported external stress.

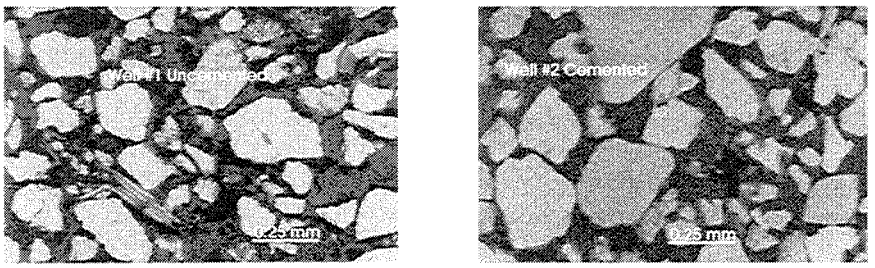

Figure A4.3. Thin sections of two selected samples from Well #1 (left) and #2 (right).

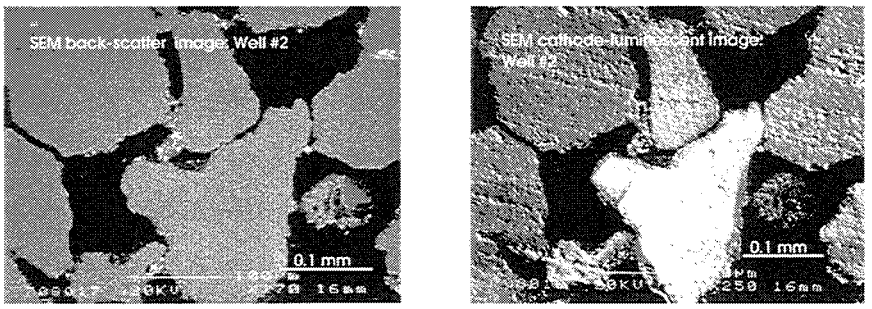

Figure A4.4. SEM images of a Well #2 sample in back scatter light (left) and cathode-luminescent light (right).

Seismic Response. To understand how the type of sand (unconsolidated versus

cemented) affects the seismic response, we analyze CDP gathers at the well locations.

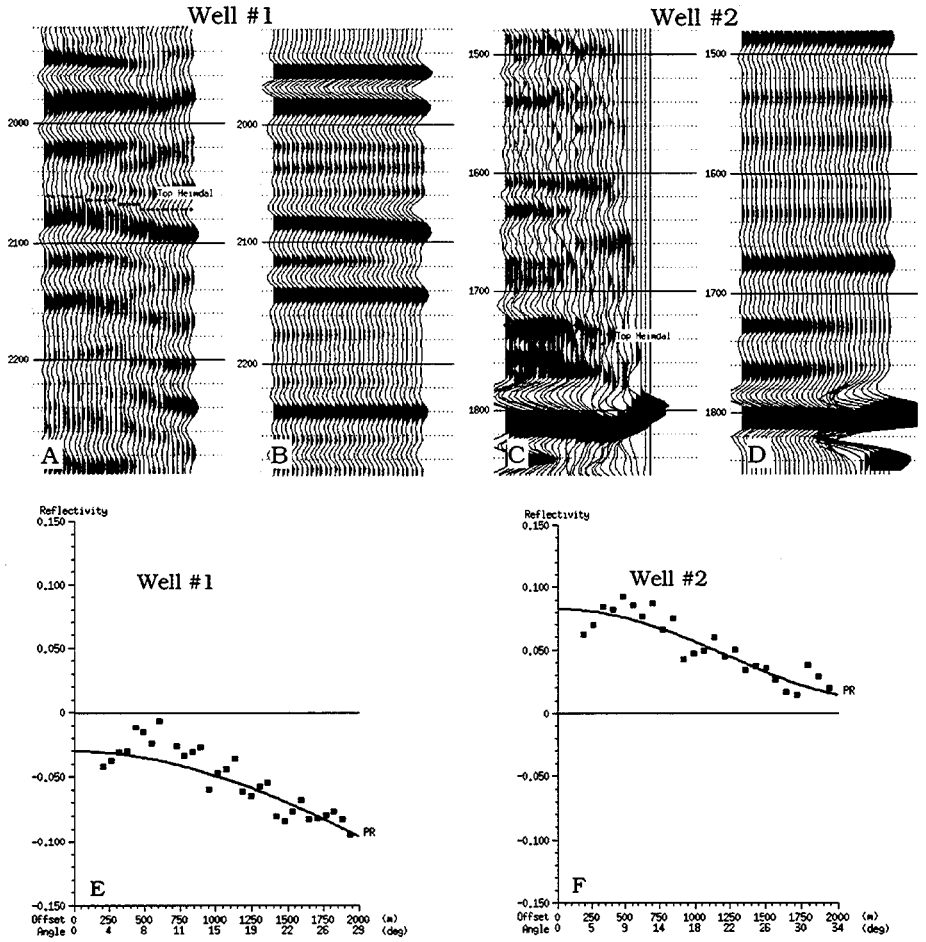

Figure A4.5. Top. Real (a and c) and synthetic (b and d) CDP gathers. In synthetic gathers, the AVO effect was modeled only at the target zones. Bottom. Real reflectivity versus offset and angle (symbols) and theoretical Zoeppritz lines.

Figure A4.5a shows the real CDP gather at Well #1 where the picked horizon is at the top of the Heimdal formation. Figure A4.5b gives a synthetic CDP gather for this well produced by using a 30 Hz zero-phase Ricker wavelet and a log-derived reflectivity series. Both the real and synthetic gathers show reflectivity increasingly negative with increasing offset at the picked horizon. This reflectivity is plotted versus offset (angle), together with the theoretical Zoeppritz line, in Figure A4.5e. Contrary to Well #1, the top of the Heimdal formation in Well #2 (which is capped by similar shales) produces a strong positive reflector with reflectivity decreasing with increasing offset (Figures A4.5c and A4.5d). For this well, the reflectivity is plotted versus offset (angle), together with

the theoretical Zoeppritz line, in Figure A4.5f. The synthetic response is very close to the real data in both wells which means that we can rely on well-log-based rock diagnostic to predict seismic response.

This offset-dependent reflectivity analysis shows that clean sands of the same formation, similar porosity, and with comparable oil saturation produce drastically different seismic response depending on whether they are truly unconsolidated or have initial quartz cementation. Therefore, we can use both normal-incidence and offset-dependent reflectivity to diagnose rock and characterize a reservoir from seismic. Such rock diagnostic may be of great importance because if high-porosity contact-cemented sands are not separated from truly unconsolidated sands, one may misinterpret a change in seismic signatures caused by this petrographic effect as a pore-fluid effect.

AVO Effect and Pore Fluid. It is very important to diagnose the texture of the rock not only for the purpose of strength estimation but also for reducing the risk of fluid identification from AVO data.

In Figure A4.6 we plot synthetic amplitude-versus-offset curves for a contact cemented and uncemented sandstone samples from the two wells under examination. We use Gassmann's fluid substitution equation to calculate the effective elastic properties of the samples with gas and water. In this model, the samples are overlaid with a shale layer. We can see from Figure A4.6 that the AVO signature of the uncemented sand with water may be very close to that of the cemented sand with gas. Only by understanding the texture of the rock, the interpreter will be able to reliably identify the pore fluid in this situation.

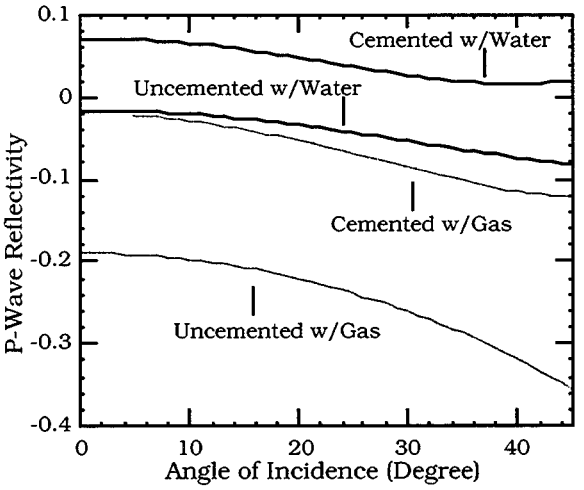

Figure A4.6. AVO signatures of sandstones with two different textures saturated with gas and water.

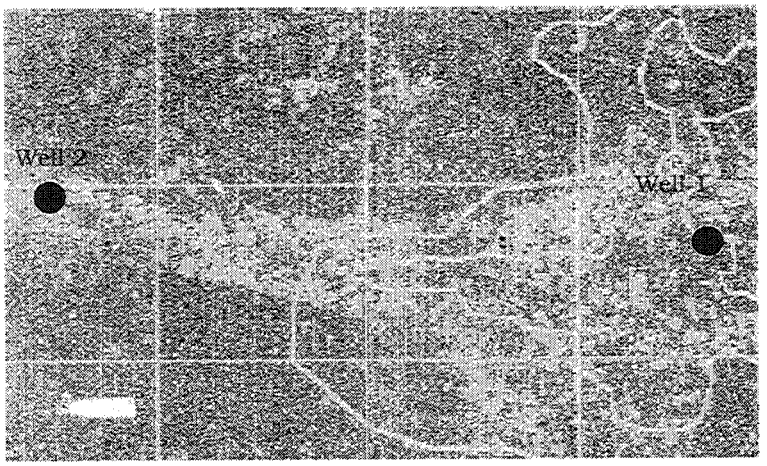

Figure A4.7. Amplitude map at the top of Heimdal formation with well location.

Relating Texture to Geology. A way of identifying rock texture is through comparing the hard velocity and porosity data to geology and depositional features.

It is evident from Figure A4.7 where the reflection amplitude map is shown at the top of the reservoir that is penetrated by the two wells under examination that Well #2, where the sandstone appears to have slight quartz cementation, is located in the high-energy depositional channel where the sand grains have been stripped of organic coating and grain sorting is good. We speculate that this is one reason for the generation of the contact cement. On the other hand, Well #1 is located in the low-energy lobe where the large quartz grains are likely to be covered by fines and organics

that prevent contact cementation. Therefore, by combining well log and core analysis with the geological knowledge and seismic imaging, we can tell the likelihood of the occurrence of a certain texture (cemented sand in the high-energy environment and friable sand in a lobe).

Conclusion. Rock diagnostic is important for correctly characterizing prospective reservoirs. Such diagnostic is based on rock physics theory and can be accomplished using well log data. The diagnostic features observed in well log data can be translated into distinctive seismic signatures. Therefore, seismic data can also be used for rock diagnostic given that the stratigraphic unit is resolvable at the seismic scale. In this paper we applied the diagnostic concept to the Heimdal formation, and were able to discriminate high-porosity cemented from unconsolidated sands both from well logs and seismic.

Appendix 1.5. Elastic Properties of Ottawa Sand - Kaolinite Mixtures

Summary. In this Appendix we display the measured properties of hand-made mixtures of Ottawa sand and kaolinite, following the data from Yin (1993). These hand-made mixtures have elastic properties analogous to those of unconsolidated Gulf of Mexico sediments (See Section 1). All data are for **room-dry** samples.

Volumetric and Transport Properties.

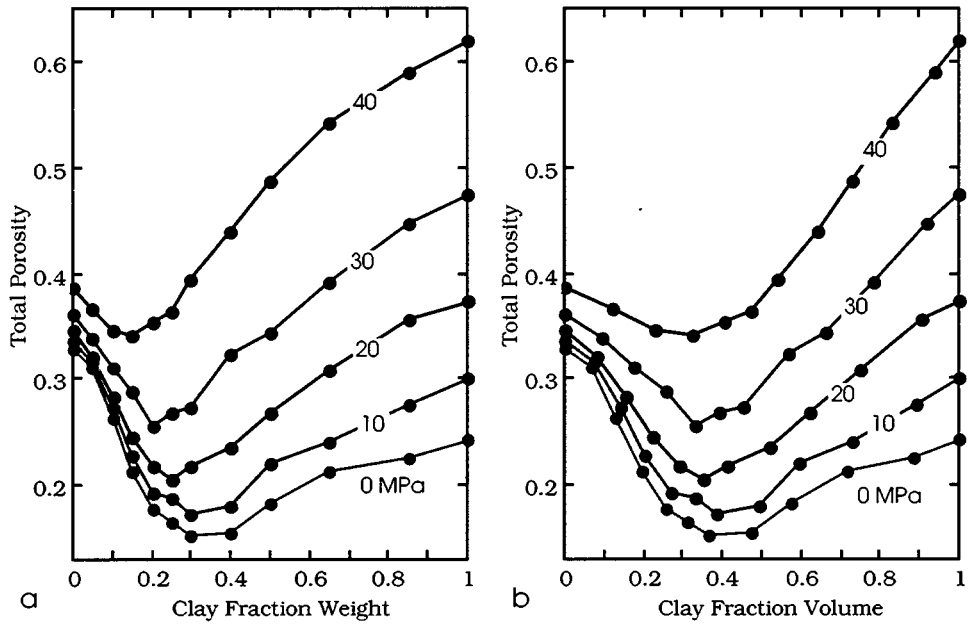

Figure A5.1. Total porosity versus (a) clay content by weight and (b) clay content by volume. The differential pressure of the measurement is given on the curves.

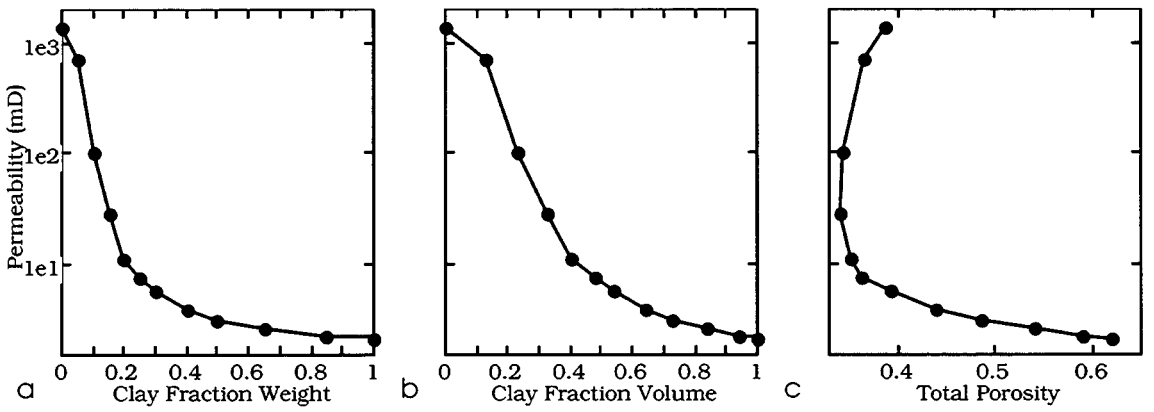

Figure A5.2. Permeability versus (a) clay content by weight; (b) clay content by volume; and (c) total porosity. measured at 0 MPa differential pressure.

Elastic-Wave Velocity.

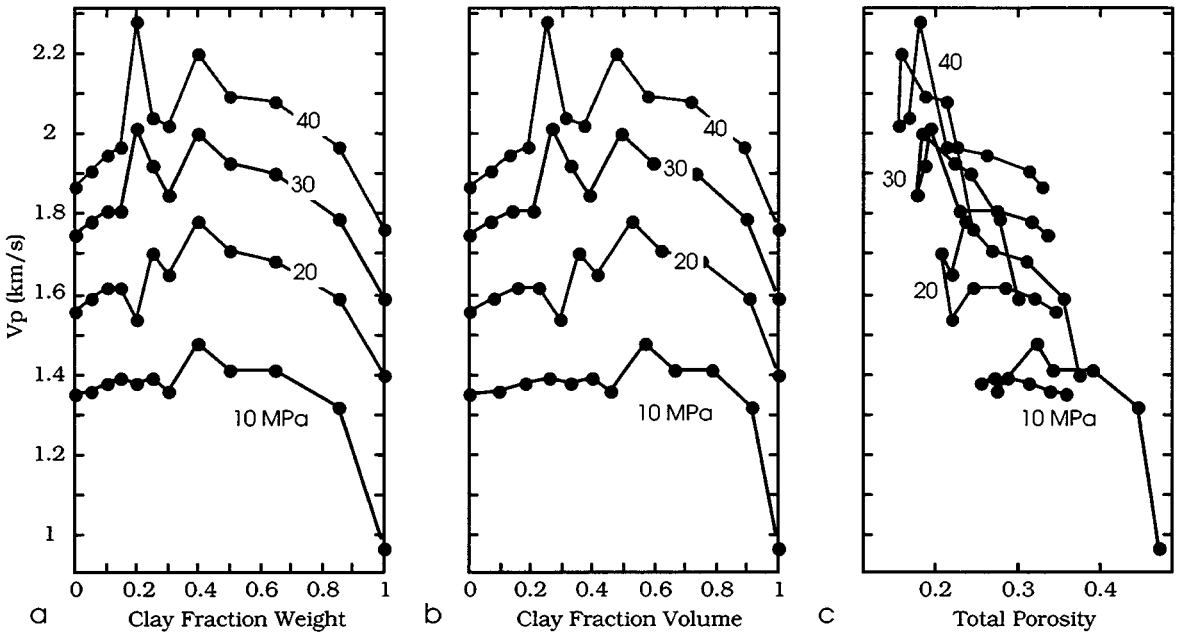

Figure A5.3. P-wave velocity versus (a) clay content by weight and (b) clay content by volume; and (c) total porosity. The differential pressure of the measurement is given on the curves.

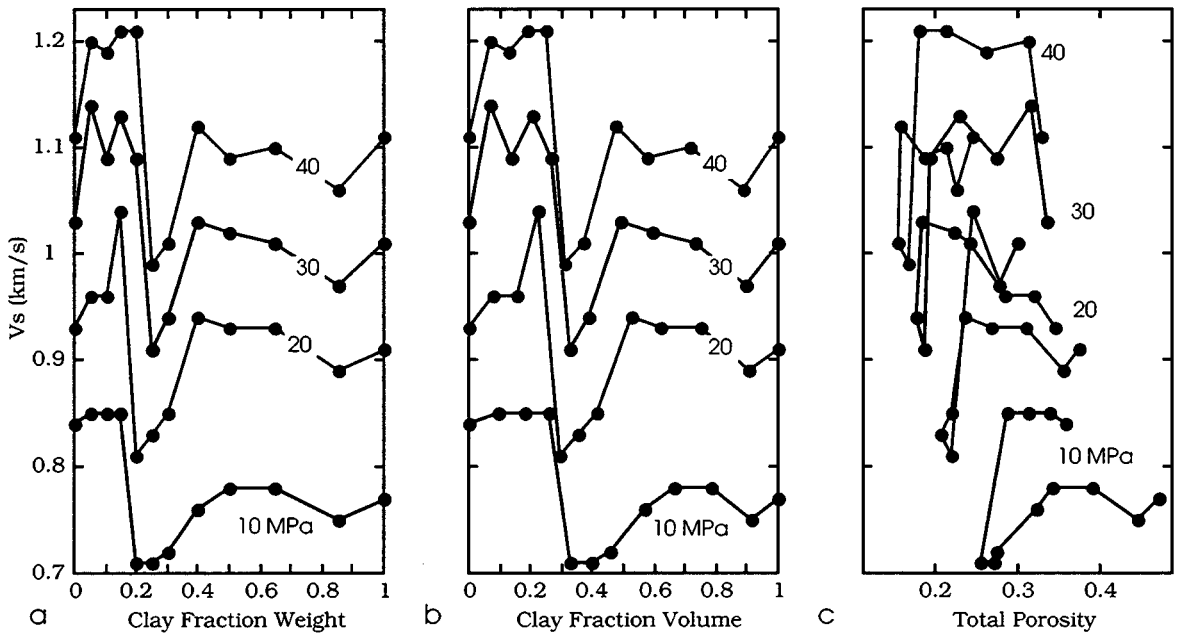

Figure A5.4. S-wave velocity versus (a) clay content by weight and (b) clay content by volume; and (c) total porosity. The differential pressure of the measurement is given on the curves.

Elastic Moduli.

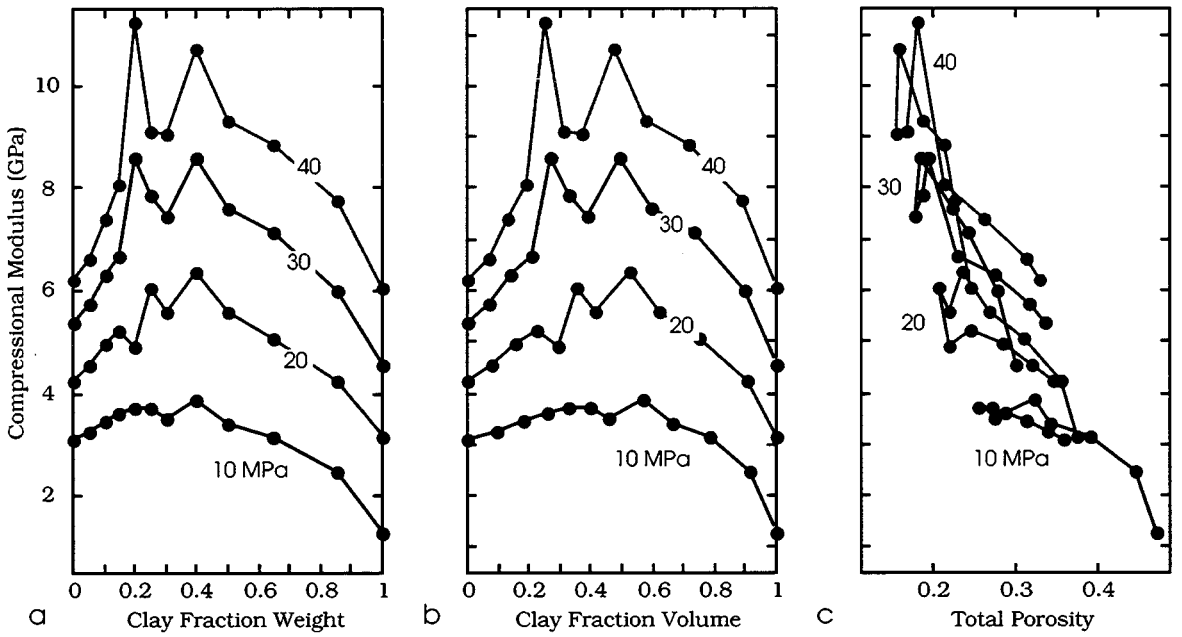

Figure A5.5. Compressional modulus versus (a) clay content by weight and (b) clay content by volume; and (c) total porosity. The differential pressure of the measurement is given on the curves.

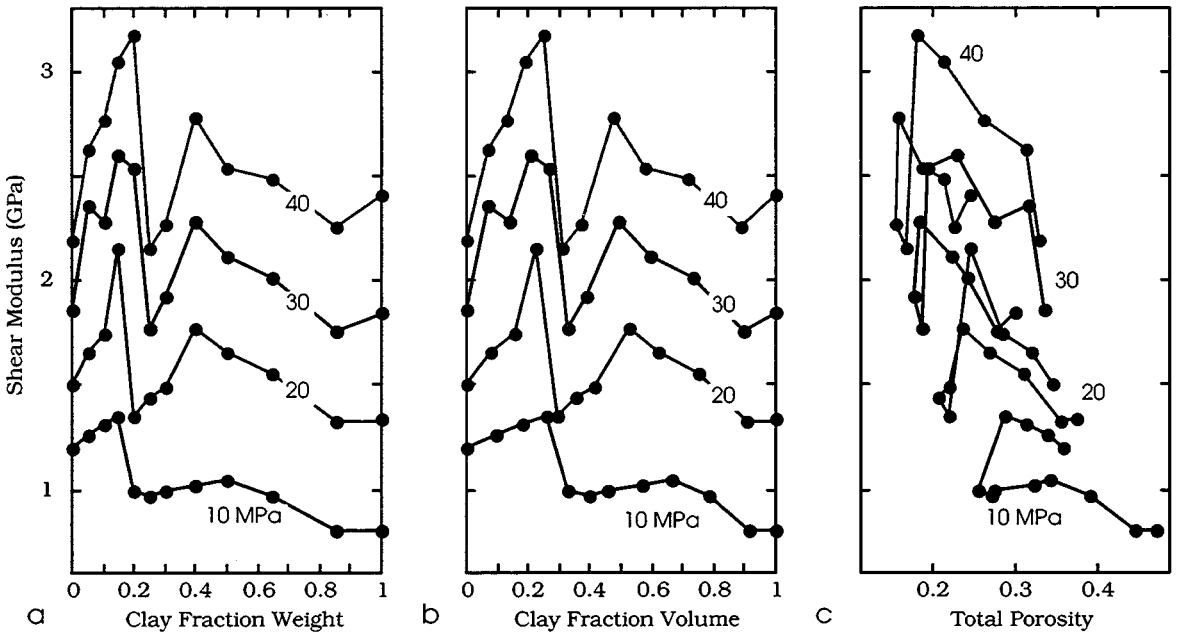

Figure A5.6. Shear modulus versus (a) clay content by weight and (b) clay content by volume; and (c) total porosity. The differential pressure of the measurement is given on the curves.